Single pulse studies of wide profile drifting pulsars — a probe of pulsar magnetospheres

A Thesis

Submitted For the Degree of

Doctor of Philosophy

in the Faculty of Science

by

Bhaswati Bhattacharyya

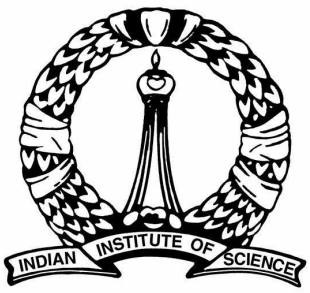

Department of Physics
Indian Institute of Science, Bangalore
Bangalore – 560 012

SEPTEMBER 2009

To my parents

DECLARATION

I hereby declare that the work presented in the thesis entitled "**Single pulse studies of wide profile drifting pulsars – a probe of pulsar magnetospheres**" is entirely original and has been carried out by me at the National Centre for Radio Astrophysics, Tata Institute of Fundamental Research, Pune, India, under the supervision of Prof. Yashwant Gupta under the Joint Astronomy Program. I further declare that this work has not formed the basis for any degree, diploma, fellowship.

Due acknowledgement has been made whenever any result/material of other investigators has been quoted. Any omission which might have occurred by oversight or error in judgment is regretted.

Bhaswati Bhattacharyya
March 16, 2009

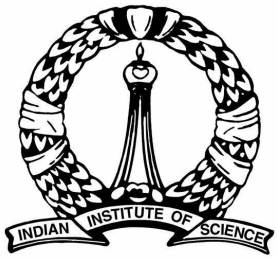

CERTIFICATE

We hereby certify that the matter embodied in this thesis entitled "**Single pulse studies of wide profile drifting pulsars – a probe of pulsar magnetospheres**" has been carried out by Ms. Bhaswati Bhattacharyya at the National Centre for Radio Astrophysics, Tata Institute of Fundamental Research, Pune, India, under our supervision and that it has not been submitted elsewhere for the award of any degree or diploma.

Prof. Yashwant Gupta	Prof. Arnab Rai Choudhuri
(Research Supervisor	(Advisor
NCRA-TIFR)	JAP-IISc)

Acknowledgements

This Ph.D. work was done as a part of the Joint Astronomy program (JAP) of the Indian Institute of Science (IISC). The thesis work was carried out in National centre for Radio Astro Physics (NCRA), Pune. After one year of course work in IISC under the JAP, I started research in the field of observational radio astronomy in NCRA under the guidance of Prof. Yashwant Gupta.

My supervisor, Prof. Yashwant Gupta has been a source of constant inspiration. His scientific attitude, critical views, urge for perfection added with hard work always motivated me. His reasoning in practical situations had helped to improve myself. I would like to thank him and Richa for providing generous supports whenever I required it. Their support in the crisis moments helped me to be able to face the life.

Part of the thesis work is done with Prof. Rajaram Nityanada. It was an exciting experience to work with him. His depth of understanding physics, capacity to grasp anything in less than a minute's time, was very encouraging. He has a unique way of solving problems which always astonished me. I have learned a lot while working with him. He also have given his valuable comments about parts of the thesis. I would like to express my sincere thanks for his supports.

I would take this opportunity to thank my collaborators, Prof. Janusz Gil and Dr. Marek Syndek. Janusz is a person with lots of enthusiasm. He used to inspire me a lot for all the results that I showed him. The pulsar group of University of Zielona Gora, Poland, was very supportive during my stay in Poland. They had made my first visit to Poland a nice memory.

I am thankful to my IISC co-guide Prof. Arnab Rai choudhuri for his support. I thank all the faculty members who offered JAP course work for us. I particularly enjoyed the courses offered by G. Srinibasan, P. Sreekumar, D. Bhattacharya and C. Jog. I also thank Meena and Rakma for their supports, regarding administrative matters.

I acknowledge the support from Dipanjan Mitra regarding the analysis of full polar data. Discussions with him in various topics related to my thesis work was very fruitful,

particularly one of his suggestion of trying out a different range of parameters for the PA fit worked very well.

I have discussed about my work with Ramesh Bhat, during his visits to NCRA and over emails. During the thesis period, he had guided me in many ways. I would like to thank him for his generous supports.

I would like to thank Roy Smits for the program for fluctuation spectrum analysis and also for being very friendly and cooperative. I also thank Paulo C. Freire for a very useful discussion during his visit to NCRA which lead to significant improvement in the method for determination of orbital parameters developed by us. I would also like to thank Joaana Rankin for always being very encouraging and friendly. I thank G. Wright for his comments on my work.

The observations presented in this thesis were done in the GMRT. I express my gratitude to Prof. Gobind Swarup, who had proposed the GMRT and had been the prime mentor in building it. I thank all the people who are associated in building and maintaining the telescope. I acknowledge the support of all the telescope operators who were with me at the time of pulsar observations.

I would like to thank the members of my review committee in NCRA for their advice. I would particularly thank Prof. Gopal Krisna for his comments on the introduction of this thesis. I thank all the academic and non-academic members of the NCRA for providing a nice atmosphere for doing research. My research work involves analysis of large volume of data sets. I thank the computer committee of NCRA specially, VVS and Shekar, for ensuing availability of large storage area and reasonable computing facility. I thank the library staffs particularly Sunita and Dalvi, for their help in library related issues.

I had lot of support from Subhasis Roy, during my initial days in NCRA. He helped me in learning Linux operating system. His comments on my work has been useful. I thank him for all the supports in personal as well as academic front. I thank Dharamjee and Babita for being so nice and supportive. Charanjib and Chandreyee had helped in formatting the thesis. I thank Chandreyee and Charanjib for being good friends. I thank Vishal for proof-reading part of the thesis. I also thank all the students and Postdocs of NCRA for their support in whatever aspects needed.

I would like to express my gratitude towards all my teachers in the schools and colleges, particularly to Ashoke Bhattacharyya, Ramesh Roy, Arun Chatterjee, Manoranjan Biswas, Manoranjan Saha, Budhadeb Bagchi and Subimal Sen. I would take this opportunity to thank Dr. Binayak Deb for his kind and generous help to our family. I had a nice time with my friends. I would particularly name, Gargi, Ishita, Moitrayee from the school days, Partha, Ananda, Sudipto, Kaustav, Somdeb, Sunanda, Prapti,

Deblina, Anasuya from the college days, and Lashmi, Harsha, Bishakha, Archana, Sutapa, Mausumi, Debbijoy, Malay and Jayanta Sarkar from the time I spent in IISC. I take this opportunity to thank Ranjan, for the thoughts that we shared.

My family provided constant encouragement and support during the thesis work. Ever since my child hood, my father used to think that his daughter will study physics. It is to fulfill his dreams, that motivated me to pursue careers in the field of scientific research. My mother has a very enthusiastic and energetic mind. She has a brave attitude to fight against the odds, which inspired me a lot. My brother is always with me in every step of life. His support played a vital role in during my research period. Being with me, Jayanta, shared all difficulties and supported me in every aspect possible. My in-laws were also very supportive during the thesis period. I would like to thank all my family members for always being supportive towards me.

At the end, I would like to express my sincere gratitude to Jocelyn Bell, without whose perceptiveness and persistence we might not yet have had the pleasure of studying the pulsars. I am thankful to all the researchers whose sincere efforts resulted in immense advancement in the field of of Astronomy.

This research has made use of

– NASA'a Astrophysics Data System Abstract Service
(http://adsabs.harvard.edu/abstract_service.html)

– European pulsar network
(http://www.mpifr-bonn.de/div/pulsar/data/browser.html)

– The Pulsar astronomy network
(http://www.pulsarastronomy.net/wiki/)

– ATNF Pulsar Catalog
(http://www.atnf.csiro.au/research/pulsar/psrcat/)

Synopsis

Thesis Title: Single pulse studies of wide profile drifting pulsars – a probe of pulsar magnetospheres

Research scholar: Bhaswati Bhattacharyya

Supervisor: Prof. Yashwant Gupta

Advisor from IISC: Prof. Arnab Rai Choudhuri

The detailed nature of radio emission processes of pulsars and the exact location and distribution of the pulse emitting regions are still shrouded with mystery. Pulsars with drifting subpulses are considered as an important key for unlocking the mystery of how radio pulsars work. The phenomenon of subpulse drifting (first reported by Drake & Craft (1968)) is manifested as an organized subpulse behavior – subpulses appear at progressively changing longitude in the pulse window following some particular path. The path followed by the subpulses is specific to the individual pulsar concerned and is known as drift band. Drifting is generally characterized by P_2^m (horizontal separation between the drift bands, i.e. in pulse longitude) and P_3^m (vertical separation between the drift bands, i.e. in pulse numbers). The subpulse drifting phenomenon finds a natural explanation in the model of Ruderman & Sutherland (1975). According to this model, the subpulse drifting is produced from a system of sub-beams (subpulse associated plasma columns). Sparks (sparking discharges within the vacuum gap) rotating around the magnetic axis under the action of an E x B drift, give rise to a circulating pattern of sub-beams, and the time for one full circulation is referred to as the carousel rotation period, which we designate as P_4. As pulsar radiation beams are widely believed to be arranged

in concentric cones, it is natural to expect the circulating sparks to be distributed in annular rings on the polar cap. Each of these rings gives rise to one cone in the nested cones of emission. It has been recently shown that, subpulse drift may be fairly common among pulsars (Weltevrede *et al.* (2006) and (2007)). Hence, the pulsar radio emission mechanism is most likely closely connected with mechanism for drifting. In spite of significant progress both in high quality observations of drifting (e.g. Weltevrede *et al.* (2006) and (2007)) and attempts for confronting the results from the observations with existing models (e.g. Deshpande & Rankin (1999) and Gupta *et al.* (2004) etc), the pulsar emission mechanism is still an unsolved puzzle.

Backer (1970*b*) first reported that emission from certain pulsars abruptly switches off for several periods, and suddenly comes back. This phenomenon is known as nulling. Nulling appears to be random, broadband and intrinsic to the concerned pulsar. Nulling is quite common in pulsars (Biggs, 1992). Although different aspects of the phenomenon of nulling are investigated in detail for many pulsars by several authors using high sensitivity observations, nulling is not yet explained by the existing theoretical models for pulsar radio radiation.

In this thesis, I have mainly studied phenomenon of subpulse drifting and nulling, with the aim to probe the radio emission processes of pulsars. Most of the pulsars have a narrow duty cycle of emission (5-10 % of pulsar period). This is generally consistent with the expectations of the angular width of the polar cap, for typical viewing geometries. However, there are small but significant number of pulsars with unusually wide profiles where the emission is seen for a wide range of longitude ($\geq$ 90 degrees). These are expected to be pulsars which are highly aligned, i.e. the magnetic dipole axis is almost parallel to the spin axis. In such a case, the line of sight (LOS) is very close to both the rotation and the magnetic axes, and consequently, we sample a large region of the polar cap. This has the exciting potential to allow a detailed study of the distribution and behavior of emission regions located in an annular ring around the magnetic axis. The study of pulsars showing systematic subpulse drift patterns provides important clues for the understanding of the unsolved problems of pulsar emission mechanism. Constraints provided by such observations can

have far reaching implications for the theoretical models, as exemplified by some of the recent results in this area (e.g. Deshpande & Rankin (1999) and Gupta *et al.* (2004)). In this context, wide profile drifting pulsars can provide extra insights because of the presence of simultaneous multiple drift bands. During the thesis period, I have mainly concentrated on the study of single pulse properties of two wide profile drifting pulsars, PSR B0818−41 and PSR B0826−34.

In depth study of PSR B0818−41

We have studied single pulse properties of a relatively less studied wide profile pulsar, B0818−41 using highly sensitive multi-frequency observations with the GMRT in full polar mode. Detailed investigation of PSR B0818−41 are reported in Chapters 2, 3 and 4 of this thesis. New results from our study are described in the following.

- We estimate the mean flux of PSR B0818−41 at 5 different frequencies and show that the spectrum flattens at frequencies lower than 325 MHz (at 244 or 157 MHz), providing indication of a low frequency turn-over.

- Significant linear polarization is observed at 325, 610 and 1060 MHz. Average linear polarization falls off much faster than the total intensity and decreases to zero near the outer edge of the profile. This can be explained by the orthogonal polarization mode jump at the edges of the profile observed at 325 MHz. Polarization angle sweep across the pulse profile evolves remarkably with frequency (between 325, 610 and 1060 MHz), which is not generally observed in other pulsars. Very less circular polarization without any signature of changing handedness is observed at 325 and 610 MHz. But circular polarization changes sign at the middle of the pulse profile at 1060 MHz.

- We report the discovery of a remarkable subpulse drift pattern in PSR B0818−41, using the high sensitivity GMRT observations. We find simultaneous occurrence of three drift regions with two different drift rates: an inner region with steeper apparent drift rate flanked on each side by a region of slower apparent drift rate.

- The closely spaced drift bands always maintain a constant phase relationship: the subpulse emission from the inner drift region is in phase with that from the outer drift region on the right hand side, and at the same time the emission in the inner drift region is out of phase with the outer drift region situated on the left hand side. This phase locked relationship (hereafter PLR) is maintained for the entire stretch of the data (for all the epochs of observations at 325 and 610 MHz) and does not appear to get perturbed after intermittent nulling or during changes in the drift rate.

- We observe frequent changes of drift rates. We see extreme examples of changing drift rates such as transitions from negative to stationary or stationary to negative drift rates, many of which appear to have some connection with nulls. We investigate changes in drift rates for about 10,000 pulses from two different epochs of observations at 325 MHz and observe frequent occurrences of small changes in the drift rate, seven transitions from negative to stationary drift rates, five transitions from stationary to negative drift rates, and two possible signatures of curved drift bands.

- In addition to the remarkable subpulse drift observed at 325 MHz, we report subpulse drifting at 244 and 610 MHz. At 244 MHz subpulse drifting is observed only in the leading and trailing outer regions, but not in the inner region. Though the drift bands are weaker, subpulse drifting is observed in both inner and outer region at 610 MHz.

- P_2^m, P_3^m and $\Delta\Phi_s$ (subpulse width) are determined for the inner and the outer drift regions for different frequencies. Though P_3^m is observed to be the same for the inner and outer drift regions, P_2^m and $\Delta\Phi_s$ are different for different drift regions.

- The unique drift pattern of this pulsar can be naturally explained as being created by the intersection of our LOS with two conal rings on the polar cap of a fairly aligned rotator. Based on the frequency evolution of the average profile, observed polarization angle (PA) swing and results from subpulse drifting, we converged on two possible choices of emission geometry: $\mathbf{G\text{-}1}$ (inclination angle $\alpha = 11$ deg

and impact angle $\beta = -5.4$ deg; which incidentally reproduces the middle part of the PA sweep at 610 MHz) and **G-2** ($\alpha = 175.4$ deg and $\beta = -6.9$ deg; geometry derived from RVM fit to 325 MHz PA sweep). Pulsar radiation pattern simulated with both the geometries reproduces the average profile as well as the observed features in the drift pattern quite well. However, **G-2** fits the PA sweep much better.

- We report that the peaks of the emission from the trailing and leading outer regions, as a function of the pulse number, are offset by a constant interval, $P_5 \sim 9P_1$. We also report a phase locked relation (PLR) between the inner and outer drift regions for PSR B0818$-$41. A new technique is introduced by us for resolving aliasing, using this constant offset ($P_5 \sim 9P_1$) between the peak emission from the leading and trailing outer regions. From the result of this technique, we propose that the subpulse drifting for PSR B0818$-$41 is most likely first order aliased, and the corresponding carousel rotation period $P_4 = 10$ s. This implies that PSR B0818$-$41 has the fastest known carousel.

- The drift pattern in the inner and outer rings are always phase locked for PSR B0818$-$41. This could be a significant constraint for the theoretical models of pulsar radio emission, and favors a pan magnetospheric emission mechanism.

- We observe frequent nulling for PSR B0818$-$41. We calculate a nulling fraction $\sim$ 30% at 325 MHz for this pulsar. Lengths of neighboring nulls and bursts are found to be independent.

- For the inner drift region, our investigations bring out the fact that the nature of the transitions from burst to null are different from the transitions from null to burst. Switching off of pulsar radiation during nulling for PSR B0818$-$41 is not abrupt, but is gradual, whereas the transitions from null to burst are found to be rather abrupt for the inner drift region. This effect is not prominent in the outer drift regions. Although, the inner region of the last active pulses before nulls are dimmer, the first active pulses after nulls outshines the normal ones.

- The intensity of the inner region is maximum for the average profile from the first active pulse immediately after the nulls and then gradually goes down. This is consistent with the behavior of the individual nulls described above. However, this is not the case for the leading and trailing outer regions.

- The average profiles from the first active pulse immediately after the nulls follows similar shape as the normal profile but shows an increased intensity (in the form of a bump) in the inner region which is not present in the normal average profile. In addition, the leading and the trailing peaks appear to be of similar intensity, while trailing peak is significantly more intense for the normal profile. The average profiles from the pulses immediately after the nulls are wider than the normal profile.

- The average profiles of the first active pulses after the nulls are drastically similar between two epochs of observations. This is a very unique result which is not reported for any other pulsar so far and may imply that the phenomenon of nulling is associated with some systematic energy re-distribution in the pulsar magnetosphere.

In depth study of PSR B0826$-$34

PSR B0826$-$34 is a pulsar with one of the widest known profile. The earlier studies of this pulsar (Durdin *et al.* (1979), Biggs *et al.* (1985) and Gupta *et al.* (2004)) have brought out some unique properties : strong evolution of the average profile with frequency, apparent nulling for 70% of time and a remarkable subpulse drift property $-$ multiple curved drift bands with frequent changes and sign reversals of drift rate. We studied PSR B0826$-$34 using the GMRT, simultaneously at 303 and 610 MHz, and individually at 157, 325, 610 and 1060 MHz. Detailed investigation of PSR B0826$-$34 are reported in Chapter 5 of this thesis. Some of the interesting new results from our work are,

- As a natural out-come of the simultaneous dual frequency observations, we obtain an accurate DM value, equal to 52.2(6) pc/cm^3, for this pulsar. Unlike most normal pulsars the DM determination for this pulsar is a difficult and trick exercise, mainly because the profile is

quite complex, very wide and strongly evolving with frequency. The advantage of our method of DM determination is that the observations at a single epoch are self sufficient for obtaining the DM value at that epoch.

- Contrary to the earlier study by Esamdin *et al.* (2005), we find no evidence of weak emission during the typical long null states of this pulsar, simultaneously at 303 and 610 MHz, as well as from non simultaneous observations at 157, 325, 610 and 1060 MHz at separate epochs. We have also obtained absolute flux limits for the non-detection at various frequencies, which should be a useful comparison standard for any more sensitive studies in the future.

- We present the average profiles at five different frequencies. Main pulse (MP) and inter pulse (IP) emission observed for this pulsar span over wide pulse longitude. There is a remarkable frequency-evolution of pulse profile: IP becomes stronger with increasing frequency.

- We estimated the mean flux of the MP, IP and the full pulse region of PSR B0826$-$34 at different frequencies of observation.

- Significant correlation in the total intensity of the individual pulses between 303 and 610 MHz is reported from the simultaneous dual frequency observations, which is indicative of the broad-band nature of the emission. The intensity correlations are positive for large lags, indicating that there is some kind of memory in the underlying structure. This memory is the longest for PSR B0826$-$34, amongst all known cases.

- Our study of this pulsar brings out insight into simultaneous behavior of the single pulses from PSR B0826$-$34 at 303 and 610 MHz, which has not been examined so far. We see about 6$-$7 drift bands in the MP region at 303 and at 610 MHz. At 610 MHz we see about 2$-$3 drift bands in the IP region. We observe wide variations in the drift rates, including positive and negative drift rates and curved drift bands, which are simultaneous for both frequencies. We have noticed coherence between simultaneous multiple drift bands $-$ at

some given instant of time all the drift bands (6$-$7 drift bands) under the MP window show similar kind of drift.

- Though we find the drift pattern to be very similar in the simultaneous 303 and 610 MHz data, we observe that the drift band separation (P_2^m) evolves significantly between these two frequencies, and in a manner opposite to the average profile evolution. In addition, we confirm the dependence of P_2^m on pulse longitude at 303 MHz and find indications for the same at 610 MHz.

- Significant linear polarization is observed in the MP region which drops abruptly at the edges of the pulse profile. Two orthogonal mode jumps are seen at the edges of the MP for both 325 and 610 MHz. We observe somewhat non orthogonal mode jump at the edges of IP for 610 MHz. Significant circular polarization in the MP along with the sense reversal near the center is observed for both the frequencies. The PA curve shows typical "S" shaped swing (though there is some hint of a kink in the central part of the PA curve). RVM fit (Radhakrishnan & Cooke, 1969) to the PA curve is obtained with $\alpha \sim 9.8$ deg, $\beta \sim 3.2$ deg, at both 325 and 610 MHz.

The detailed study of two unique wide profile pulsars, PSR B0818$-$41 and PSR B0826$-$34, was very rewarding and provided fair amount of insight towards the emission properties of pulsars. We broadly conclude that the emission from simultaneous multiple drift bands are coherent. In other words the emission mechanism responsible for generation of the drift bands is heavily correlated in the whole on pulse window. Also the equispaced sparks argues for a more isotropic arrangement of sparks which is favored by the conal model (Rankin, 1983). Drifting from more than one rings are observed only for two pulsars, PSR B0818$-$41 and PSR B0826$-$34. For PSR B0818$-$41 we observe that the emission from different rings are always locked in phase. This constant phase relation is maintained even during sequences of irregular drifting as well as after nulling. PSR B0826$-$34 is another wide profile pulsar for which presence of simultaneous multiple drift regions are observed. For this pulsar the MP and the IP emission are interpreted to be coming from two concentric rings of emission. The drift bands in these regions are locked in phase implying

that the emission from the inner and the outer rings are in phase. For PSR B0826−34 we observe frequent nulling and changes of drift rates which are simultaneous for both the inner and outer rings. Hence for all pulsars for which we know drifting from more than one ring, the drift pattern in the inner and outer rings are always phase locked. No counter example is observed. This requires common drift rate in the inner and outer rings, implying that emission in the two rings are not independent, and the conditions responsible for drifting are similar in both rings. Our finding of PLR between the emission from the inner and the outer rings puts constraints on the theoretical models of pulsar emission mechanism and favors a pan magnetospeheric radiation mechanism.

Preliminary study of single pulse properties of six other pulsars

Inspired by the success of our study of PSR B0818−41 and PSR B0826−34 we carried out single pulse study of few other pulsars with diverse profile. Preliminary results from this study are presented in Chapter 6. However, some of the new results form this work are highlighted in the following. We report occasional nulling for PSR B0540+23 which is important in the sense that nulls are not commonly seen in the core components. We observe simultaneous two drift bands for B1819−22 at 325 and 610 MHz. We observe some kind of mode changing between stronger and weaker modes with changes of drift rates, which are probably associated with occasional nulling observed in this pulsar. For PSR B1839−04 subpulse drifting is observed under the two peaks of the profile. The emission under the leading and trailing peaks appear to be in phase.

Determination of the orbital parameters of binary pulsars

Apart from the above work, I got interested in determination of the orbital parameters of the binary pulsars. This work was triggered by the discovery of a binary pulsar PSR J0514−4002 (the first known pulsar in the globular cluster NGC 1851) at the GMRT in 2004 (Freire *et al.*, 2004). We present a novel method for determination of the orbital parameters of binary pulsars, using data on the pulsar period at multiple observing epochs in contrast to the method described by Freire, Kramer & Lyne (2001) which requires both pulsar period and period derivatives at particular observing

epochs. This method uses the circular nature of the velocity space orbit of Keplerian motion and produces preliminary values based on two one dimensional searches. Preliminary orbital parameter values are then refined using a computationally efficient linear least square fit. This method works for random and sparse sampling of the binary orbit. Unlike the method used by Freire, Kramer & Lyne (2001), which works for nearly circular binary orbits, this method works for binary orbit with any eccentricity. We demonstrate the technique on (a) the highly eccentric binary pulsar PSR J0514−4002 (the first known pulsar in the globular cluster NGC 1851) and (b) 47 Tuc T, a binary pulsar with a nearly circular orbit. Our result agrees with the earlier determination of the orbital parameters of the binary pulsars done with coherent multi-epoch timing (Freire, Kramer & Lyne (2001) and Freire *et al.* (2007)). In our method the computation involves only one dimensional searches and linear least square fits. This study is reported in Chapter 7.

The main conclusions and the possible future works are presented in Chapter 8.

PUBLICATIONS

Refereed publications

- **Discovery of a remarkable subpulse drift pattern in PSR B0818−41**
  Bhattacharyya, B., Gupta, Y., Gil, J. & Sendyk, M., 2007, MNRAS, 377L, 10B

- **Determination of the orbital parameters of Binary pulsars**
  Bhattacharyya, B. & Nitayananda, R., 2008, MNRAS, 387, 273

- **Results from multi-frequency observations of PSR B0826−34**
  Bhattacharyya, B., Gupta, Y. & Gil, J., 2008, MNRAS, 383, 1538B

- **Exploration of the remarkable subpulse drift pattern and polarization properties of PSR B0818−41**
  Bhattacharyya, B., Gupta, Y. & Gil, J., MNRAS, 2009 (in press)

Papers in preparation

- **Investigation of the unique nulling properties of PSR B0818−41**
  Bhattacharyya et al.

- **Study of the polarization properties of PSR B0826−34**
  Bhattacharyya et al.

- **Study of single pulse properties of core and conal pulsars**
  Bhattacharyya et al.

Conference proceedings

- **Wide profile drifting pulsars : an elegant way to probe pulsar magnetosphere**
  Bhattacharyya, B., Gupta, Y. & Gil, J.
  A paper presented at an international workshop on Low-Frequency pulsar Science, University of Leiden, Netherlands, June 23 − 27, 2008.
  Low-Frequency Radio Universe, ASP Conference Series, Vol. LFRU, 2009.

- **Discovery of remarkable drift pattern in PSR B0818−41**
  Bhattacharyya, B., Gupta, Y. & Gil, J.
  A paper presented at the Annual meeting of the Astronomical Society of India, Hydrabad, India, February 7 − 9, 2007 (BASI, 2008, 25S, 34B).

- **PSR B0826−34: a unique wide profile drifting pulsar**
  Bhattacharyya, B. & Gupta, Y.
  A paper presented at the Annual meeting of the Astronomical Society of India Nainital, India, February 13 − 18, 2005 (BASI, 2005, 33, 383B).

- **A novel method for determination of orbital parameters of binary pulsars**
  Bhattacharyya, B. & Nityananda R.
  Presented at the Annual meeting of the Astronomical Society of India Nainital, India, February 13 − 18, 2005 (BASI, 2005, 33, 384B).

ABBREVIATIONS

P_1 : Period of the pulsar
P_2 : Horizontal separation between the drift bands (i.e. in pulse longitude)
P_2^m : Measured P_2
P_2^t : True P_2
P_3 : Vertical separation between the drift bands (i.e. in pulse numbers)
P_3^m : Measured P_3
P_3^t : True P_3
P_4 : Carousel rotation period
α : Inclination angle between the magnetic axis and the rotation axis
β : Impact angle between the rotation axis and the line of sight
η : Screening factor for the partially screened gap model (Gil *et al.*, 2006)
r_p : Polar cap radius
N_{sp} : Number of sparks in a conal ring
$\Delta\Phi$: Width of average pulse profile
$\Delta\Phi_s$: Subpulse width
DM : Dispersion measure
RM : Rotation measure
PA : Polarization position angle
OPM : Orthogonal polarization mode
LOS : Line of sight
PLR : Phase locked relation
RVM : Rotating Vector Model (Radhakrishnan & Cooke, 1969)
MP : Main pulse
IP : Inter pulse
OP : Off pulse
SNR : Signal to noise ratio

List of Figures

List of Tables

Contents

CHAPTER 1

Introduction

"Equipped with his five senses, man explores the universe around him and calls the adventure Science."
– Edwin Powell Hubble

1.1 Background

Pulsars emit extremely regular clock like pulses (e.g. Fig. 1.1) and have resulted in many applications in physics and astronomy. Pulsars were discovered in 1967 with the Mullarad Radio Astronomy Observatory array (rectangular array containing 2048 dipoles operating at 81.5 MHz, Fig. 1.2) by Anthony Hewish and Jocelyn Bell (Hewish *et al.*, 1968). The observed short periodicity of the pulses imply that the source must be very compact and sufficiently massive. The initial attempts to explain the periodicity considered three distinct mechanisms: radial pulsations, orbital motion and rotations. In radial pulsations, the observed pulse period is proportional to $\rho^{-0.5}$, ρ being the mean stellar density. To obtain the range of periodicity observed in pulsars the density range required is too high for a single class of objects. The models with orbital motion had serious difficulties in explaining the observed slowdown of the rotational period of the pulsars. Although there are still many open questions, the basic established model suggests that pulsars are rapidly rotating, highly magnetized neutron stars formed during the supernova explosions of massive stars (stars with zero age masses between about 10 to 40 Solar mass). Soon after the discovery of neutrons Baade & Zwicky (1934) had suggested a possible connection between the supernovae phenomenon and the formation of the neutron stars. The present understanding

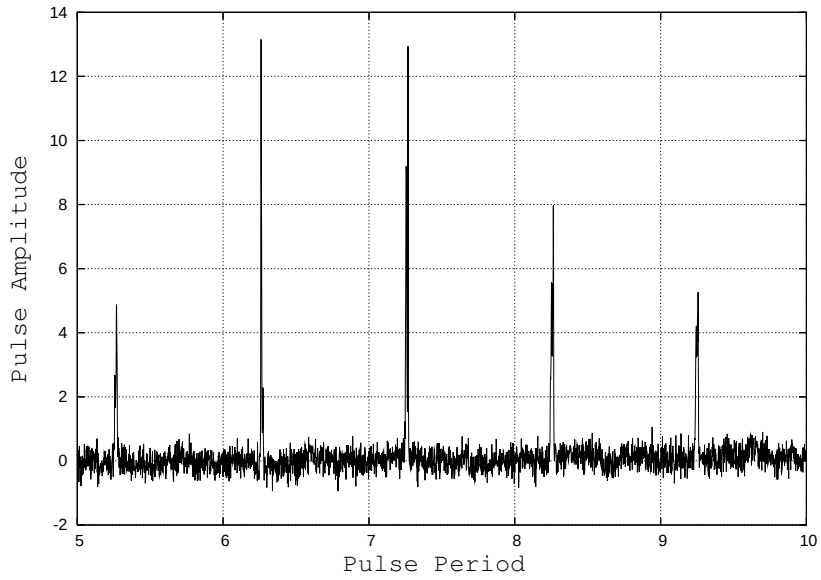

Figure 1.1: Periodic train of single pulses from PSR B0818−13 at 610 MHz observed by us with the GMRT. Pulse amplitude is in arbitrary units. (PSR stands for Pulsating Source of Radio, the numbers refer to the right ascension and declination of its position).

Figure 1.2: Mullard Radio Astronomy Observatory array (rectangular array containing 2048 dipoles operating at 81.5 MHz) used for the discovery of the pulsars in 1967 by Anthony Hewish and Jocelyn Bell (Hewish *et al.*, 1968). PSR B1919+21 is the first pulsar discovered by them. (Credit: http://www.mrao.cam.ac.uk/outreach/pulsars.html)

Figure 1.3: Light house model for pulsar emission. Beamed emission from pulsar (upper portion) is compared with the emission from a light house (lower portion). (Credit: Joe Bergeron @ 2001 Addison Wesley Longman)

is that, pulsars are the collapsed cores of massive stars, composed of an iron crust which covers incredibly dense neutron matter (average mass density $\sim 6.7 \times 10^{14}$ g/cm^3). Pulsars have very strong magnetic field, probably with a dipolar form. The typical field strength is 10^{11-12} Gauss and have a range from 10^8 to 10^{13} Gauss. Beams of radiation are formed at the magnetic poles, probably directed radially away from the star, as shown in Fig. 1.4. As the pulsar rotates, these beams sweep around 360 degrees like a lighthouse (Fig. 1.3). Radio telescopes thus receive a regular train of pulses, (example in Fig. 1.1) as the radiation beam of a pulsar repeatedly crosses the earth, making the pulsar appear to be a pulsating radio signal (with periods ranging from few milliseconds up to few seconds). These pulses are broadband, extending in some cases from low radio frequencies to high-energy gamma rays and are often highly polarized.

Sect. 1.2 of this chapter presents a brief overview of the different observed properties of pulses (both average and instantaneous). In Sect. 1.3 we discuss the binary pulsars and the orbits of the binary pulsars. Sect. 1.4 presents a

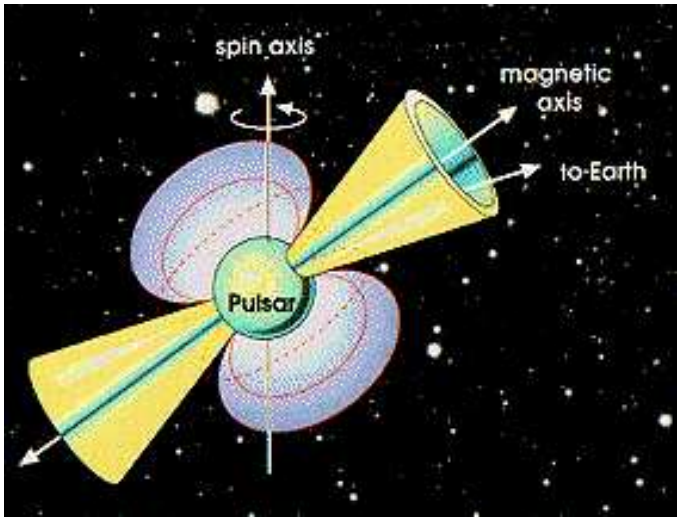

Figure 1.4: Schematic diagram for the beamed emission from a pulsar. The pulsar is rotating around the spin axis in anti-clockwise direction (for the anti-pulsars the rotation is in clock wise direction). The emission is beamed close to the direction of the magnetic axis. As the observers line of sight intersects the beam of emission, pulses of radiation from the pulsar are observed. (Credit: http://www.daviddarling.info/encyclopedia/P/pulsar.html)

brief discussion about the existing models explaining pulsar radio radiation. In Sect. 1.5 we describe pulsar observations with the GMRT. Motivations for this thesis are summarized in Sect. 1.6. Sect. 1.7 provides an outline of the thesis.

1.2 Observed properties of pulsars

Though many of the basic observational facts about radio pulsars were established shortly after their discovery in 1967, the detailed nature of radio emission processes of the pulsars, the exact location and distribution of the pulse emitting region are still not tightly pinned down. One can probe the details of pulsar magnetosphere using the observational results. In the following we provide a brief introduction to some of the observational characteristics of the pulsars.

(a) Integrated pulse profile

Pulsars are weak radio sources. Measured intensities, usually quoted in the literature for a radio frequency of 400 MHz, vary between 0.1 mJy and 5 Jy ($1\ Jy = 10^{-26}\,W\,m^{-2}\,Hz^{-1}$). As a result, even with a large radio telescope, the folding of many hundreds or even thousands of pulses is usually required, for the weaker pulsars, in order to produce a detectable integrated profile. The overall radio spectra of the total intensity of pulsars are quite steep ($E \propto \nu^{-2}$), although they often flatten or even turn over at lower frequencies (Malofeev *et al.*, 1994).

The integrated profile at any particular observing frequency is very stable and can be thought of as a "fingerprint" of the emission beam of the neutron star. A few pulsars display exceptional behavior in the form of mode changes which is discussed later in this section. Fig. 1.5 shows a rich diversity in the integrated profile including examples of inter pulses (PSR B1937+21 and PSR J1012+5307) − a secondary pulse separated by about 180 degrees (in longitude) from the main pulse. The interpretation for this phenomenon could be that the main pulse and inter pulse originate from opposite magnetic poles of the neutron star. However, it is possible to have both main pulse and inter pulse emission originated from the same pole (e.g. PSR B0826−34).

The shape and width of the integrated profiles of pulsars vary over the radio spectrum. The integrated profile usually get broader at lower frequencies which is interpreted as lower frequencies originating from a greater height at which the dipolar field lines diverge to larger angles, i.e a radius to frequency mapping. Hence this is generally accepted that the higher frequency radiation is emitted from lower altitudes (from the pole) than that of the lower frequencies. The emission altitude is described by a empirical relation proposed by Kijak & Gil (2003) (and the references therein),

$$r_{em} = (40 \pm 8) R \nu^{-0.26\pm0.09} {P_{-15}}^{0.07\pm0.03} {P_1}^{0.3\pm0.05} \tag{1.1}$$

It is now generally accepted that the radio radiation originates in the polar cap region − the part of the pulsar magnetosphere bounded by the open field line region. Observationally the occurrence of discrete emission components in pulsar average profiles indicates that the polar cap region consists of distinct active regions of emission (Backer, 1976). Each part of the

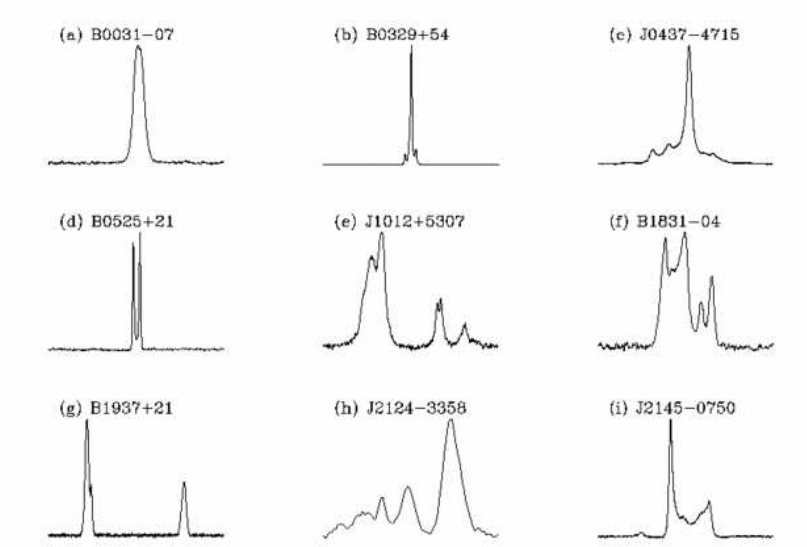

Figure 1.5: Integrated pulse profile for a variety of pulsars. Different profile shapes are observed (e.g. single − (a), double − (d), multiple − (f), (h), both main pulse and inter pulse − (g)). (Credit: "Handbook of Pulsar Astronomy" by Duncan Lorimer and Michael Kramer)

integrated profile is believed to originate in a small part of this polar region, so that the integrated profile represents a cut across the distributed source of emission. The average profiles are remarkably stable from one observation to another, and have provided the basis for studies of location of the emitting region within the light cylinder. There are two competing views about how these emitting regions could be arranged in the magnetosphere − the "conal" vs "patchy" beam models. The conal beam model (e.g Rankin (1993), Rankin (1990)) posits that the emitting region consists of two distinct kinds − core and conal − which have properties that are observationally distinguishable. The core radiation is thought to originate close to the magnetic axis of the pulsar and comes from lower altitudes in the pulsar magnetosphere than the conal emission, which is thought to originate in a series of concentric hollow cones centered on the magnetic axis.

Shape of the observed pulse profile depends on the actual cut that the observers line of sight (hereafter LOS) makes through such an emission beam.

The observed average profile of pulsars may consist of one or more components. It is observed that the pulsars with complex pulse shapes are noticeably slow rotators. On the average 3 ± 1 conal components are observed in normal pulsars and 4 ± 1 conal components are observed in millisecond pulsars (Kramer *et al.*, 1998). That is, the correlation between slowness and multiple components in the pulse profiles, applies to normal pulsars, and there is a general increase in the number of components for MSPs.

Fig. 1.6 explains how different LOS cuts through the concentric conal rings can give rise to the observed variety of pulse profiles, such as single, double, triple, multiple profiles. On the other hand, the patchy beam model (Lyne & Manchester, 1988), argues that the component locations within the beam are randomly distributed rather than organized in the form of one or more hollow cones (e.g. Fig. 1.7). However, the conal model is backed by recent claims of support from interpretations of observational data (e.g. Bhattacharyya *et al.* (2007), Gupta *et al.* (2004), Gupta & Gangadhara (2003), Kijak & Gil (2003), Mitra & Deshpande (1999), Gangadhara & Gupta (2001)), which is not true for the patchy beam model.

(b) Individual pulses

Individual pulses coming from the pulsars vary greatly from one pulse to another in terms of their shape, intensity and polarization properties. Left panel of Fig. 1.8 shows a sequence of individual pulses obtained from the GMRT observations of PSR B0950+08 at 610 MHz. Enormous variations in shape and intensity are observed among the single pulses.

Individual pulses are often composed of one or more narrower emission features (2 to 10 degrees), known as subpulses. Subpulses usually occur randomly in pulse phase. Though there are finner structures (called micro structures) detected in pulsars, subpulses are often considered as basic units of emission. Subpulses probe instantaneous changes in the emitting region and can provide useful clue about location and distribution of the same. Subpulse intensity modulation is manifested in the phenomena of drifting, nulling and mode changing.

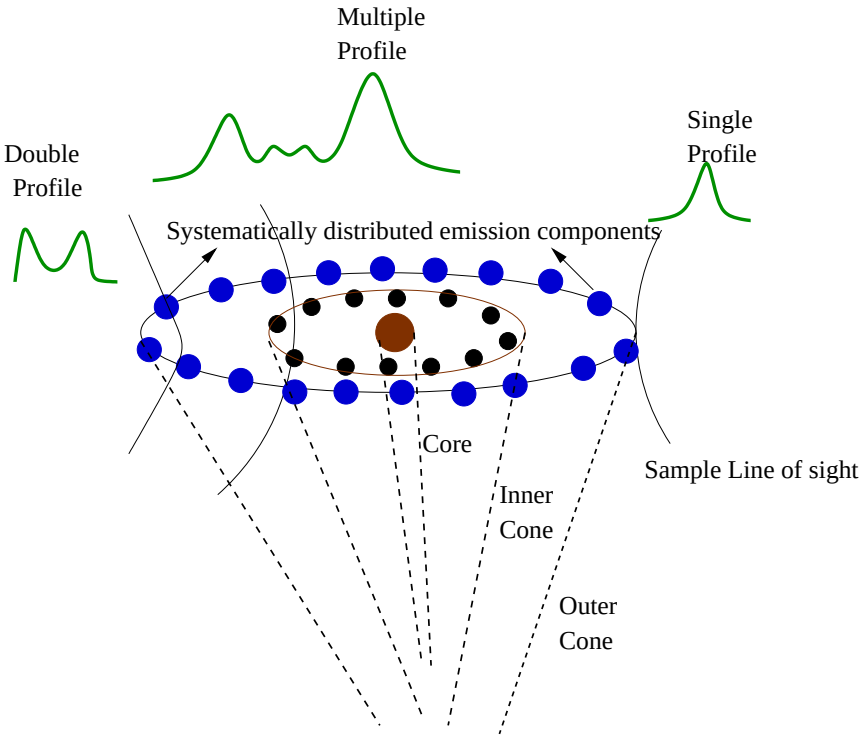

Figure 1.6: Phenomenological models for pulse shape produced by different LOS cuts across the beam in the core-conal model (Rankin, 1993).

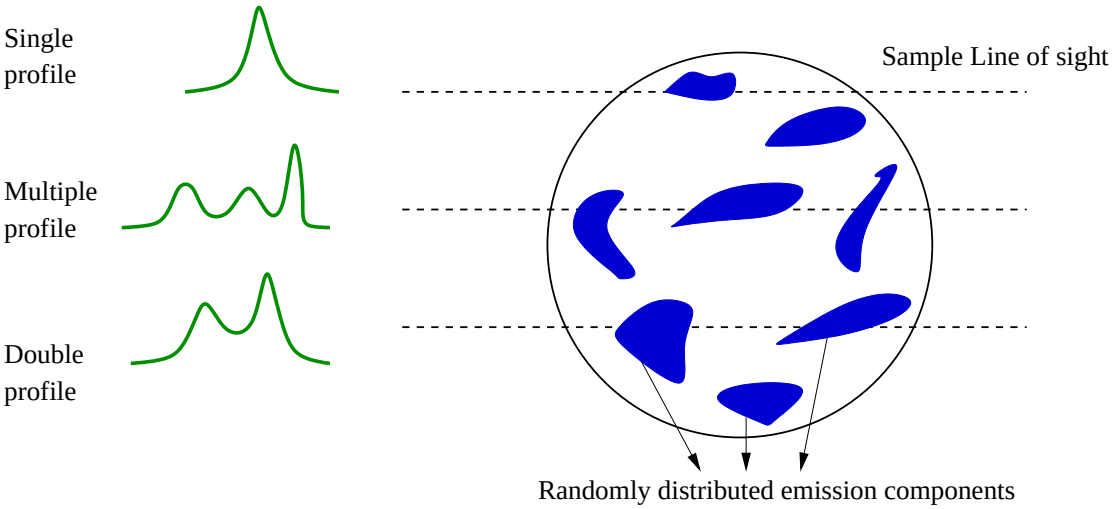

Figure 1.7: Phenomenological models for pulse shape produced by different LOS cuts across the beam in the patchy beam model (Lyne & Manchester, 1988).

Figure 1.8: Sequence of single pulses from PSR B0950+08 (left panel) and B0809+74 (Right panel) at 610 MHz observed by us with the GMRT.

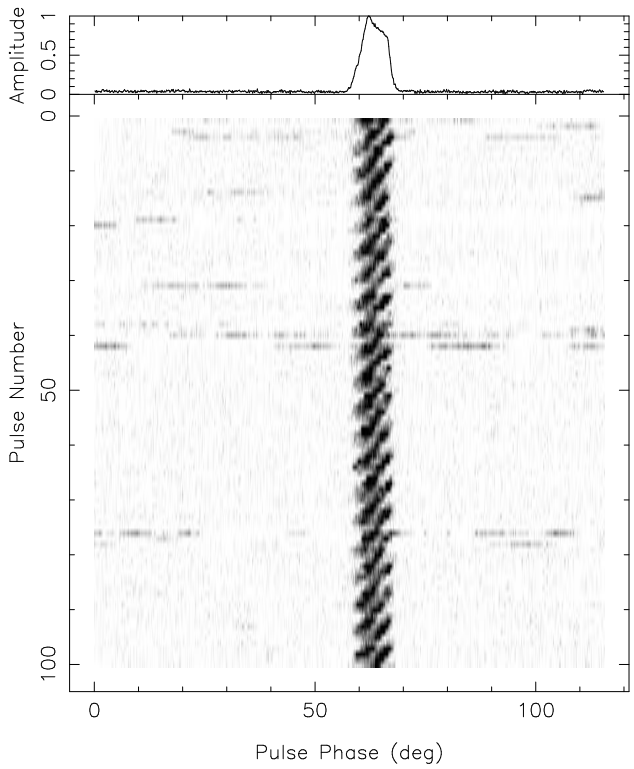

Figure 1.9: Gray scale plot of the single pulses from PSR B0818−13 at 610 MHz observed by us with the GMRT, with the average profile shown on the top.

(c) Subpulse Drifting

The phenomenon of drifting subpulses (first reported by Drake & Craft (1968)) is manifested as systematic subpulse behavior − subpulses appear at progressively changing longitude in the pulse window following some particular path. Over successive pulses the subpulses appear following some specific patterns, known as drift bands, which are characteristics of the particular pulsar. It has been recently shown that subpulse drifting may be fairly common among pulsars (Weltevrede *et al.* (2006) and (2007)). Hence, the emission mechanism is most likely quite closely connected with the mechanism for drifting.

Right panel of Fig. 1.8 presents the single pulses stacked on one another, from the GMRT observations of PSR B0809+74 at 610 MHz. We see that the individual subpulses vary greatly in the shape and intensity but follow specified drift bands. Two drift bands are simultaneously seen for this pulsar.

Fig. 1.9 is the gray scale plot of the single pulses from PSR B0818−13 at 610 MHz, with average profile plotted in the top. The phenomenon of drifting results in one or more drift bands spanning the pulse envelope. Subpulses are observed to drift, from leading to the trailing edge (conventionally called positive drift) or from trailing to the leading edge (negative drift as in Fig. 1.8). Pulsars are known with both kinds of drifting but for a given pulsar the direction of drift is usually fixed. However, there are few pulsars for which both directions of drift are seen but at different times (e.g. PSR B0826−34, Biggs *et al.* (1985)).

The intensity of the subpulses are systematically modulated as they move along the drift band. Generally the intensity peaks in the middle of the pulse envelope due to more central cut of the LOS and decreases towards the edges; opposite trend is also seen (Taylor *et al.*, 1975). Pulse to pulse intensity variations are analysed by using fluctuation spectrum method (Backer, 1973). Detailed study by Rankin (1986) reveal that the fluctuation properties of core and conal components are very different. Isolated core components of the pulsar with core single profiles rarely exhibit regular fluctuations and the drifting subpulses are generally observed in conal components.

Observed drifting can be characterized by two parameters P_3^m and P_2^m that decide the slope of the drift bands (Fig. 1.10). P_3^m is the time interval between the recurrence of successive drift bands at a given pulse longitude and P_2^m is the measured longitude separation between the adjacent drift bands. The observed drift parameters and the frequency evolution of those parameters can provide important clues towards the conditions of pulsar magnetosphere, gap height, possible arrangements of the emitting regions across the polar cap etc. High sensitivity single pulse observations are required for the above kind of study.

Determination of P_2^m and P_2^t:

P_2^m value in the inner drift region is calculated from the auto-correlation function of the single pulses and is averaged over the total number of available pulses. The secondary peak of the correlation function will correspond to the correlation between adjacent drift bands and in turn will give us the P_2^m value. The measured P_2^m does not corresponds to the true value, P_2^t, due to

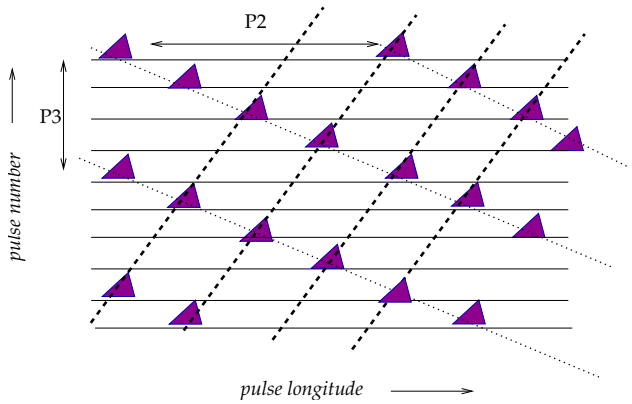

Figure 1.10: Schematic explanation of P_3^m, P_2^m and drift bands, Dashed lines indicate the drift bands for positive drifting and the dotted lines indicate the drift bands for negative drifting.

the following reasons (Gupta *et al.*, 2004).
(a) The LOS takes finite time to traverse the beam. By the time the line of sight moves from one subpulse longitude to the next one, the subpulse pattern drifts in longitude by a small amount. Hence the measured P_2^m value is a Doppler-shifted version of the actual subpulse separation P_2^t. P_2^m and P_2^t are related by,

$$P_2^t = (1 - D_p^t/360)P_2^m \tag{1.2}$$

Where D_p^t is the drift rate in degrees per period. The sign of D_p^t is positive for drift from leading to trailing longitude (i.e. along the direction of the LOS), and negative for the other direction.

(b) For the non aligned rotators the equal angular intervals along the LOS (P_2^m, measured with respect to rotation axis) do not map to equal angular intervals on the polar cap ring ($\Delta\sigma$) (refer to section 3.2.2 of Gupta *et al.* (2004) for a detailed discussion). The general formula that relates the azimuthal angles measured with respect to the magnetic axis (σ) with the rotational phase (ϕ) is,

$$\sin(\sigma) = \frac{\sin(\alpha+\beta)\ \sin(\phi)}{\sin(\Gamma)} \tag{1.3}$$

where Γ is the angle between the magnetic axis and the line of sight at the rotational phase (ϕ).

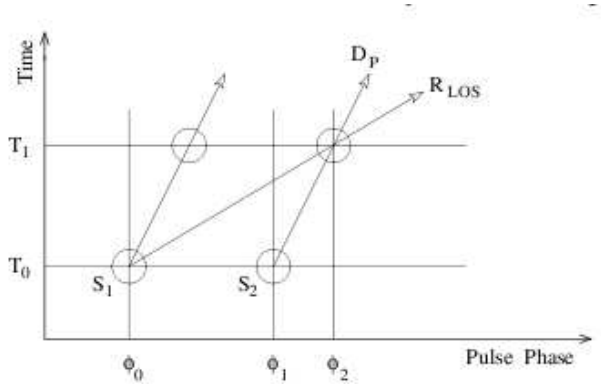

Figure 1.11: Drift induced modification of actual subpulse separation P_2^t. S_1 and S_2 are two sparks located at longitudes ϕ_0 and ϕ_1 at time T_0 (i.e. $P_2^t = \phi_1 - \phi_0$). At T_0, the LOS (moving along the R_{LOS}) is at ϕ_0, and sees S_1. At a later time T_1, the LOS is at ϕ_2, where it sees the spark S_2. Hence $P_2^m = \phi_2 - \phi_0$. During the interval $T_1 - T_0$, the sparks (moving along D_p) drift by an amount $\phi_2 - \phi_1$ (Credit: Gupta *et al.* (2004))

Determination of P_3^m and P_3^t:

Pulse to pulse intensity variations in pulsars can be studied by using the fluctuation spectrum method (Backer, 1973). To avoid the effects from temporal variation of drift rates, the sequences of pulses which show well defined drifting, should be considered. For each pulse in this sequence, we need to consider the flux at a fixed phase and the consequent absolute values of Fourier transform of this flux distribution should be calculated. This was done on each phase of pulsars "on" pulse. The resulting transforms were then averaged over phase, giving a phase averaged power spectrum from 0 Hz up to the reciprocal of twice of the pulsar period, with a frequency resolution given by the reciprocal of the total length of the time sequence. P_3^m can be determined for the cases where the drift rates are stable with time. But it is not clear whether P_3^m is equal to P_3^t or not. Since we observe the pulsar once in its period, the signal at any given pulse longitude is sampled only once per pulsar period (P_1). Any periodic signal measured (e.g. periodicity P_3^t) is subject to the constrains of the this sampling rate (Gupta *et al.*, 2004). There are following possibilities,

(1) $P_3^t > 2\ P_1$: Sufficiently slow drift rate and P_3^m is the same as P_3^t.

(2) $P_3^t = 2\ P_1$: In this case a subpulse drifts to the longitude of adjacent

subpulse in exactly two periods. This corresponds to the Nyquist periodicity, $f = 1/(2\ P_1)$ (even odd modulation).
(3) $P_3^t < 2\ P_1$: Drift rate is faster. Aliased version of periodicity is seen and the direction of drift depends on how fast the drift rate is.
(i) P_3^t slightly less than $2\ P_1$: P_3^m is slightly more than $2\ P_1$ and the apparent drift is of opposite sign to the true drift.
(ii) $P_3^t = P_1$: P_3^m is infinite ($f_3^t = 2\ f_N$, $f_3^m = 0$). This gives rise to longitude stationary subpulse patterns, with zero apparent drift rate.
(iii) $P_3^t < P_1$: Non zero drift rate is again observed but the drift direction is the same as the true drift direction. The apparent drift direction reverses sign every time the true drift rate crosses a multiple of the Nyquist boundary. The apparent drift amplitude goes through zero for every even crossing (n = even number) and through the maximum observable value for every odd crossing (n = odd number).

Though it has been recently shown that subpulse drifting may be fairly common among the pulsars (Weltevrede *et al.* (2006) and (2007)), a thorough study has not been done for a majority of them. In the following we list some of those along with a brief idea of present status of the investigation.

PSR B0031−07:
PSR B0031−07 is particularly interesting because it shows three distinct drift-modes with different P_3 values : drift modes A, B, C with corresponding P_3 of 13, 7, and 4 P_1, respectively. All the three drift modes are very stable. This pulsar has been studied at different observing frequencies in several works (Huguenin *et al.* (1970), Vivekanand (1995), Vivekanand & Joshi (1997), Vivekanand & Joshi (1999) etc). Izvekova *et al.* (1993) studied subpulse characteristics of this pulsar at 62, 102, 406 and 1412 MHz, and found that the switching between the different drift modes and the nulls occur simultaneously at all the frequencies. Smits *et al.* (2005) studied this pulsar simultaneously at 328 MHz and 4.85 GHz. They found that the mode A occurs simultaneously at these frequencies, while the modes B and C only occur at 328 MHz. They also establish that the modes A and B are associated with two orthogonal modes of polarization, respectively. Based on the observations, they suggested a geometrical model where the modes A and B

at a given frequency are emitted in two concentric rings around the magnetic axis with mode B being nested inside mode A. More recently Smits *et al.* (2007) made detailed multi-frequency study of this pulsar. They worked out a model that reproduces the observed polarization and intensity characteristics. The model further suggests that the emission heights of this pulsar range from a few km to a little over 10 km above the pulsar surface.

PSR B0809+74:
PSR B0809+74 shows subpulse drifting, nulling and mode changing. The drift rate occasionally changes with nulling as the trigger. van Leeuwen *et al.* (2003) studied drifting and nulling mechanism and their interactions in PSR B0809+74 in detail, and reported that the drift is not aliased but directly reflects the actual motion of the sub-beams. The drift pattern after null differs from the normal, and after nulls a quasi stable drift mode is started.

PSR B0818−13:
This pulsar exhibit very strong drift bands. Lyne & Ashworth (1983) studied drifting of this pulsar. Janssen & van Leeuwen (2004) investigated the drift null interaction for this pulsar and solved the aliasing for this pulsar.

PSR B0826−34:
This is a unique pulsar with simultaneous multiple drift bands. Biggs *et al.* (1985) have discovered drifting in this pulsar. This pulsar shows changing drift rates and curved drift bands, which is quite unique among drifting pulsars. Gupta *et al.* (2004) made a detailed investigation of the subpulse drifting of this pulsar at 318 MHz and provided a model that explains the observed subpulse drift properties of this pulsar, including the apparent reversals of the drift direction. According to them the observed drift rate is an aliased version of the true drift rate which is such that a subpulse drifts to the location of the adjacent subpulse (or a multiple of that) in about one pulse period. They showed that small variations of drift rates are enough to explain the apparent drift reversals seen in the data.

PSR B0834+06:

This pulsar displays strong, alternate-pulse intensity modulation without any significant drift at meter wavelengths. Asgekar & Deshpande (2005) determined the circulation time for the drift pattern. They used cartographic transform mapping technique to study the properties of the polar emission pattern.

PSR B0943+10:
Deshpande & Rankin (1999), Asgekar & Deshpande (2001), Deshpande & Rankin (2001) and Rankin *et al.* (2003) have reported detailed studies of drifting subpulses of PSR B0943+10 at frequencies in the range 35−430 MHz. These studies led to the identification of a system of sub-beams circulating around the magnetic axis of B0943+10 that was responsible for the observed steady drift pattern. Deshpande & Rankin (1999) introduced a cartographic transform (and its inverse), which relates the observed pulse sequence to a rotating frame around the magnetic axis in order to map the underlying pattern of emission.

(d) Nulling

Flux densities of pulsars vary on many timescales. Some of these variations result from scintillations due to scattering of ray paths by fluctuations in the interstellar electron density (Rickett, 1990). However, when averaged over timescales of many minutes, the intrinsic luminosity of most pulsars is apparently very stable (Kaspi & Stinebring, 1992). Pulsar often exhibit a different class of intensity fluctuation which is characterized by abrupt transition to null state (i.e. almost zero energy state). Backer (1970*b*) first reported that emission from certain pulsars abruptly switches off for several periods, and suddenly comes back. This random phenomenon is known as nulling.

Nulling is quite common in pulsars − investigating 72 well-observed pulsars Biggs (1992) found evidence for nulling for 43. Duration of nulling vary widely, from just a few pulses to many hours or even days. "Nulling fraction" is defined as the fraction of time that the pulsar is in null state and is different for different pulsars, ranging from about zero (for the Vela pulsar) to about 70% (for PSR B0826−34). In the most extreme cases, the pulsar may be visible only in short bursts in between the nulls making its detection

very difficult.

Ritchings (1976) determined the nulling fractions for many pulsars and found that nulling fraction is correlated with pulsar age, older pulsars are more likely to null. However, Biggs (1992) found an inverse correlation between the nulling fraction and pulsar period. These results suggests that the emission process becomes somewhat unsteady with age of the pulsar as discussed in Rankin (1986). There is a large scatter in the nulling fraction and so a clear nulling-age effect is not obvious. Interestingly, as yet no evidence of nulling is observed in millisecond pulsars.

Nulling appears to be broadband phenomenon and is intrinsic to the particular pulsar. Study of Bhat *et al.* (2007) reports that, for PSR B1133+16, the nulling is not exactly simultaneous between the observing frequencies, they have found about 6% excess in nulls which occurred at frequencies below or near 1.4 GHz.

Although it was commonly known that nulling occurs randomly, there are some recent studies (Herfindal & Rankin, 2007) which report periodicity in nulling for PSR B1133+16. By replacing each pulse with a scaled version of the average profile, they quenched all subpulse modulation and still the fluctuation feature was present. Hence, they concluded that nulls exhibit periodicity. With further investigation they have observed nulling in a few other Arecibo Pulsars. Rankin & Wright (2008) report that null pulses for PSR J1819+1305 bunch at periodic intervals of around 57 times of the pulsar period, which they explained by modeling a sparsely filled sub-beam carousel with nulls appearing whenever our LOS intersects a circulating empty region.

Interaction between nulls and emission was studied for PSR B0834+06 by Rankin & Wright (2007). According to them periodic modulation in pulsar's emission governs the occurrence of nulls. The nulls in PSR B0834+06 do not appear randomly in the pulse sequence, but are found to occur preferentially close to the minimum of the pulsars emission cycle. They also reported two distinct populations, nulls and the partial nulls, for PSR B0834+06. For some pulsars nulling is found to be related to drifting : van Leeuwen *et al.* (2003) investigated the interaction between drifting and nulling in PSR B0809+74. They found that the drift rate before nulls does not deviate much from the normal drift rate. However, drift rate after nulls are lower than the normal drift rate. For PSR B0818−13 the subpulse drift appears to increase during

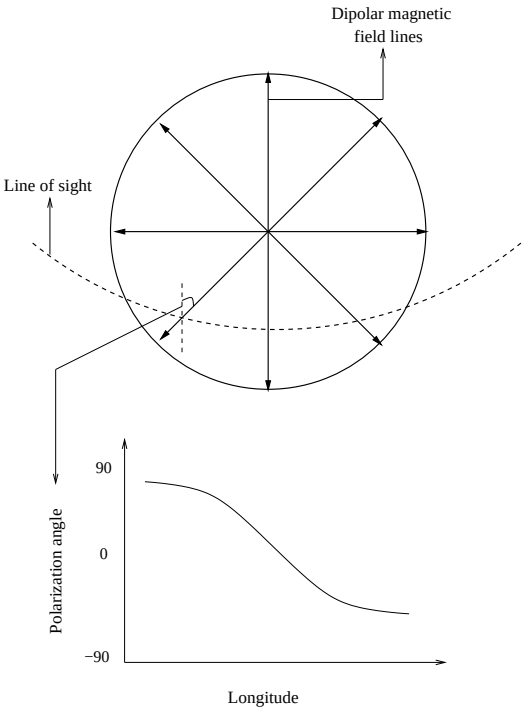

Figure 1.12: Schematic diagram showing polarization position angle (PA) as the line of sight (LOS) crosses the pulsar beam. Typical 'S' shaped PA curve due to the projected dipolar magnetic field lines is predicted by (Radhakrishnan & Cooke, 1969).

the nulls (Janssen & van Leeuwen, 2004).

Different aspects of the phenomenon of nulling are investigated in details for many pulsars by several authors using high sensitivity observations. However, nulling is not yet explained by the existing theoretical models for pulsar radio radiation. Nulling is supposed to be very closely associated with the emission mechanism, hence a thorough study may help to refine the emission models. Observations of nulling are often limited by signal to noise ratio and, in practice, null is only an absence of detectable emission.

(e) Mode changing

Backer (1970*a*) first observed mode changing in PSR B1257+25. Mode changing is a kind of discontinuous change where the mean pulse profile abruptly changes between two or more quasi-stable forms. The emission process usually favors one state (known as normal mode) for most of the time

and switches suddenly to the abnormal mode. For those pulsars exhibiting subpulse drifting, the drift rates clearly change when a mode switching occurs. While nulling are viewed as the transitions between an 'on' and 'off' state of pulsar emission, it is likely to be related to a similarly abrupt phenomenon known as mode changing. Drifting, micro-structure, polarization properties are effected by mode changing, showing that it represents a fundamental change in the emission process.

(f) Polarization properties

Polarization studies of radio pulsars can be used for, (a) classifying the different types of profiles, (b) understanding the underlying emission mechanism, (c) determining the geometry of the star, etc. The radiation is believed to originate from the particles streaming outward along the open field lines above the poles of an essentially dipolar magnetic field. The linear polarization at any point in the profile is related to the orientation of the magnetic field at the corresponding point of origin. The observed rotation of the plane of polarization through the profile can then be related to the geometry of the field lines above the pole.

Pulsars are highly polarized objects. Linear polarization is usually dominant, with the radiation from some pulsars being almost 100% polarised. Based on a sample of 300 pulsars studied at 600 and 1400 MHz by Gould & Lyne (1998), the average degree of linear polarization is found to be about 20 %. Some pulsars are known to change linear polarization angle abruptly by close to 90 degree, that is there are some pulses where the plane of polarization of the linearly polarized pulses is at right angles to the average. This phenomenon is known as orthogonal polarization mode jump. As a result the percentage of linear polarization drops to zero at the jumps of position angles. Circular polarization is also observed but usually with a significantly lower fractional polarization, typically 10 % (Gould & Lyne, 1998). Towards the center of the profiles of many pulsars, especially for those for which LOS cut is close to the center of the emitting cone, there is often a high degree of circular polarization. Frequently the circular polarization reverses hand. The degree of linear or circular polarization in individual pulses observed from the stronger pulsars often approaches 100%. But the inegrated profile represent the sum of pulses with different sense of circular or position angle

of linear polarization. Hence the integrated profile may be much less polarized. Towards the center of the profiles of many pulsars, especially for those for which LOS cut is close to the center of the emitting cone, there is often a high degree of circular polarization. Sense reversal of circular polarization are generally associated with core emission.

Viewing geometry and PA

The radiation is believed to originate from the particles streaming outward along the open field lines above the poles of an essentially dipolar magnetic field. The linear polarization at any point in the profile is related to the orientation of the magnetic field at the corresponding point of origin. The observed rotation of the plane of polarization through the profile can then be related to the geometry of the field lines above the poles. The position angle of the linear polarization within the pulse window rotates smoothly as a function of longitude in a "S" shaped fashion as shown in Fig. 1.12 (Radhakrishnan & Cooke, 1969). The polarization angle curve is a characteristic feature of all known pulsars and hints towards dipolar magnetic field (in presence of multi-polar field structure the "S" shaped curve is expected to develop kinkiness). According to rotating vector model(RVM) by Radhakrishnan & Cooke (1969), the polarization position angle (PA) as a function of pulse longitude (ϕ) can be expressed as,

$$PA = PA_0 + \arctan[\frac{\sin\alpha\ \sin(\phi-\phi_0)}{\sin(\alpha+\beta)\ \cos\alpha - \cos(\alpha+\beta)\ \sin\alpha\ \cos(\phi-\phi_0)}]; \tag{1.4}$$

Here ϕ_0 is the pulse longitude at which PA is PA_0, i.e. ϕ_0 is the PA of the rotation axis projected on to the plane of the sky, α, the angle between the spin and magnetic axes, and β, the minimum angle between the magnetic axis and the observers LOS. Determination of the geometry of radio pulsar is essential for understanding the emission mechanism and the distributions of the emitting regions of the neutron star. Fitting an RVM to the PA sweep can provide some estimate of α and β. For many of the pulsars it is difficult to determine α and β with any degree of accuracy, partly because the longitude range over which the pulsars emit is rather small and partly because strong deviations from a simple swing of PA are often observed.

1.3 Binary pulsars and their orbits

During 1974 Joseph Taylor and Russell Hulse were searching for new pulsars with the Arecibo telescope. They discovered 40, one of which was to be very important. When they were observing the new pulsar, PSR 1913+16, they found that the pulses arrived sometimes more often and sometimes less. The simplest interpretation was that the pulsar was orbiting another star very closely and at high velocity. The system is known as the Hulse-Taylor binary pulsar and comprises two neutron stars closely orbiting their common center of mass, one of these neutron stars being detected as a pulsar. The subsequent study of this binary has provided the strongest evidence to date for the existence of gravitational waves. General relativity predicts that such a system will radiate energy in the form of gravitational waves, causing the stars to slowly spiral towards each other. In 1982 Hulse and Taylor could report, after eight years of observations, that the system was losing energy and in-spiraling at the rate predicted by Einstein's general relativity. After the discovery of the first binary pulsars, over about a hundred binary pulsars have been discovered till now. A list of binary pulsars and their parameters till 2005 can be found in http://www.johnstonsarchive.net/relativity/binpulstable.html. These binary systems have different orbital periods (ranging from a few hours to several days), eccentricities (most of the orbits being nearly circular, but few have quite high eccentricity) and companions. Most of them have either a neutron star or a white dwarf as the companion. There is only one double pulsar system, PSR J0737−3039A and PSR J0737−3039B revolving around each other.

The discovery of a pulsar with a period that changes significantly and systematically indicates that it is a member of a binary system. For non-relativistic binary systems, the orbit can be described using Kepler's laws. Five orbital parameters that describe the Keplerian binary orbit uniquely are, the binary orbital period (P_b), orbital eccentricity (e), projection of the semi major axis on the LOS ($a_1 sin\ i$, i being the angle between the orbit and the sky plane), longitude of periastron (ω) and the epoch of periastron passage (T_o). Knowledge of the orbital parameters of binary pulsars is necessary for coherent timing and for investigation of different properties of the pulsar and the companion star. Determination of the orbital parameters is specially important for newly discovered pulsars, in order to plan follow up

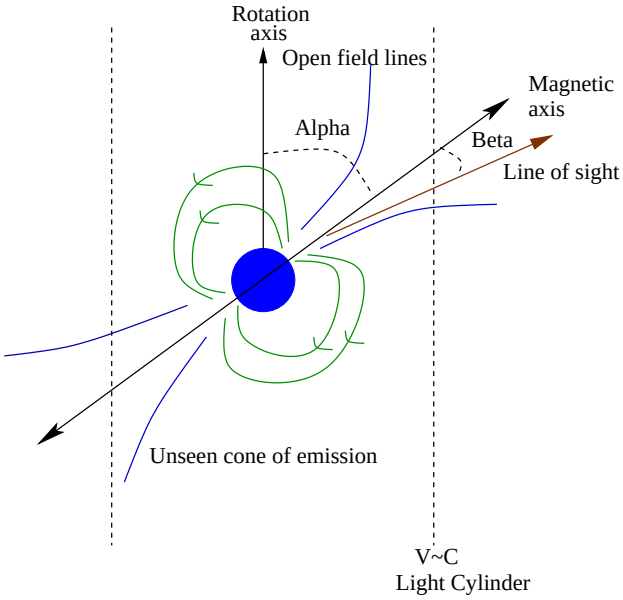

Figure 1.13: Emission geometry of pulsars, α is the angle between the spin and magnetic axes and β is the minimum angle between the magnetic axis and the observers LOS as the beam sweeps past the observer. The dashed line represents the light cylinder. (Credit: Lyne & Smith, 1998)

observations at different epochs.

1.4 Emission Models

Fig. 1.13 presents a schematic view of the emission geometry of pulsars. The orientation of any pulsar reduces basically to two angles: α, the angle between the spin and magnetic axes, and β, the minimum angle between the magnetic axis and the observers LOS as the beam sweeps past the observer. The magnetic field of the neutron star probably has significant multipolar structure within a few stellar radii of the surface, but further out it is assumed to be dipolar. Because of the strong magnetic field the charged particles are forced to move along the field lines and thus co-rotate with the star. But the co-rotation can not persist beyond the surface where the tangential velocity is equal to the speed of light. In Fig. 1.13, the dashed line represents the light cylinder, the point where the speed of the co-rotating particles in the pulsar magnetosphere reaches the speed of light ($R_L = c/\Omega$, Ω being the rotational frequency of the star and c being the speed of light). The closed

field lines are the dipolar field lines with radii less than the light cylinder radius, whereas the radius of the open field lines are more than the light cylinder radius.

Though quite a few observational characteristics are yet unexplained, Ruderman & Sutherland (1975) model (referred as RS model hereafter) for pulsar radio radiation provides acceptable explanations for a wide variety of observed pulsar characteristics. As a special case of Fig. 1.13, Ruderman & Sutherland (1975) considered a neutron star with anti parallel spin and magnetic axes. Charges are pulled out till the force-free condition is satisfied ($\vec{E}.\vec{B} = 0$), where $\vec{E}$ is the electric field and $\vec{B}$ is the magnetic field. Charges get trapped in the closed magnetic field lines and co-rotate with the star. The electrons which travel along the open field line (field lines whose radius is more than the light cylinder radius) do not return to the neutron star and hence neutron star continuously losses charge. Huge magnetic fields of the pulsars ($\sim 10^{12}G$) cause the nuclei of the stellar surface to form a tightly bound condensed state.

It is assumed that there is large enough potential drop along the open magnetic field lines of a rotating neutron star to produce an outflowing stream of relativistic electrons and positrons. In case of general pulsars the stellar surface is not hot enough to sustain an outflow of positive ions to balance the outflow of electrons as charges leave the magnetosphere through the light cylinder along the open magnetic field lines. Loss of charges in open field lines causes $\vec{E}.\vec{B} \neq 0$. Hence parallel component of $\vec{E}$ is generated along $\vec{B}$ and this $\vec{E}$ will try to pull positive ions from the neutron star surface. But since the surface binding energy of the ions in the star is high enough, the free outflow from the polar cap surface is strongly impeded, which leads to the formation of an empty gap just above the polar cap.

A strong potential difference is generated across the gap which vanishes essentially everywhere else in the near magnetosphere. According to Eqn. 15 of Ruderman & Sutherland (1975), potential difference $\Delta V = \Omega\ B\ h^2/c$, where h is the gap height and $h << r_p$, r_p being the radius of the polar cap. If not limited by a breakdown of the vacuum, the gap would grow until the entire available potential drop would develop along a field line traversing the gap. But before the gap grows to this extent the region within the gap becomes unstable against an avalanche growth of electron positron pairs.

The potential difference between the base and the top of the gap is around 10^{12} volts. For most of the pulsars the gap width is about $h \sim 10^4 cm$. When a discharge begins at some point on the polar cap, $\vec{E}.\vec{B}$ that had built up across the gap rapidly falls and this inhibits formation of another discharge within distance h. Thus the gap discharges through a group of localized sparks whose time scales are of microsecond order ($h/c \sim 10^{-6} s$). These sparks inject energetic positron beams into the magnetosphere beyond the gap. The location of sparks on a polar cap determines the geometrical pattern of instantaneous subpulses within a pulsar's integrated pulse profile. The intensity of the spark discharge may fluctuate as the electron positron plasma increases or the potential drop decreases but presumably only rarely turns off entirely. Hence the radio emission comes either from curvature radiation from the charge bunches moving along the curved field lines, or from acceleration along these lines caused by $\vec{E}.\vec{B} \neq 0$, or from both.

Electrons and positrons in a spark do not exactly co-rotate with the staller surface until $\vec{E}.\vec{B} = 0$ everywhere along it, which is not the case. In the absence of the gap the co-rotation prevailed and the electric field was tangent to the surface and had a magnitude $((\Omega \times r)/c) \times B$. The presence of the gap changes the tangential velocity within the gap and thus alters the co-rotational velocity given by,

$$v = \frac{E \times B}{B^2} c \tag{1.5}$$

Hence, according to the RS model the subpulses are expected to exhibit a similar drift which is indeed the case, as discussed in Sect. 1.2(c). Within the vacuum gap model, subpulses correspond to beams of particles (or sparks) produced in the vacuum gap over the polar cap and are thought to rotate around the magnetic axis due to perpendicular component of the electric field and the magnetic field ($E \times B$ drift). Each spark will correspond to one band of drifting subpulses. The drift rate is slower than the co-rotation rate and sparks lag behind with every rotation. The model predicts drift in only one direction depending on the relative orientation of rotation and magnetic axis and the observers LOS : for inner LOS one should observe negative drifting and for outer LOS one is expected to observe positive drifting (Ruderman, 1976). According to the RS model P_2^t is the distance between the sparks, P_3^t is the period of recurring of a particular subpulse distribution.

The time for a spark to make one complete revolution about the magnetic pole, or the carousel rotation period, P_4, is predicted by RS model which can be checked with observations. According to Eqn. (33) of Ruderman & Sutherland (1975),

$$P_4 = 5.6 \times 10^{12} \times \frac{B_{12}}{P_1} s \tag{1.6}$$

Where P_1 is the pulsar period in seconds, $B_{12} = B_s/10^{12}$ and B_s is the surface magnetic field in Gauss.

Though RS model had considerable success in explaining some of the observational properties of pulsars there are certain difficulties with this model. Following we list some of the limitations of RS model pointed out by later studies and the corresponding extensions of the model.

(i) The essential feature of the RS model is that the ions on the neutron star surface have strong binding energy, which helps to form the vacuum gap. If the ion (or electron) flow from the neutron star surface is not strongly inhibited by the surface binding effects, space charge limited potential drops near the star may not be sufficient to create the vacuum gap (Usov & Melrose, 1996). Cheng & Ruderman (1980) considered consequences of ion outflow from positively charged pulsar polar caps where this outflow coexists with the production of outflowing electron-positron plasmas. This model differs in critical details from the RS model but still many of the results of the RS model are retained in their model. Gil & Mitra (2001) revisited the binding energy problem and concluded that although the formation of the vacuum gap in RS model was in principle possible, it will require a very strong magnetic field, much stronger than the dipolar component inferred from the spin-down rate of the pulsar.

(ii) RS model can not explain certain details pertaining to drifting subpulses, nulling and mode changing. In particular the persistence of drifting subpulse phase memory after nulling and the phenomenon of nulling can not be explained in RS model (Usov & Melrose, 1996). Filippenko & Radhakrishnan (1982) attempted to reconcile these difficulties with some modifications of the standard model.

(iii) To account for the subpulse emission, they would have to repeat at approximately the same place for a time long relative to their lifetime. No clear explanation of such a surface memory was proposed by Ruderman & Sutherland (1975). RS model also does not distinguish between the core and conal

emissions. To overcome these limitations Gil & Sendyk (2000) proposed a modification of RS model.
(iv) RS model predict too fast a drift rate (Deshpande & Rankin, 1999) and also fails to explain the variation of drift rates, change of apparent drift direction, etc. Gil *et al.* (2003) developed the idea of the inner acceleration region above the polar cap by including the partial screening due to thermionic ions flow from the surface heated by sparks.
(v) Qiao *et al.* (2004) explain the bi-drifting phenomenon in PSR B0815+09 in the sparking gap model considering that the pulsars have both inner annular gap and inner core gap.

1.5 Pulsar Observations with the GMRT

We have conducted multifrequency observations of pulsars with the Giant Meterwave Radio Telescope (GMRT). The GMRT consists of an array of 30 antennas, each of 45 m diameter, spread over a region of 25 km diameter (Swarup *et al.*, 1997). At present the GMRT is operating at 5 different wave bands between 150 and 1450 MHz (150, 234, 325, 610 and 1280 MHz). Twelve antennas are randomly placed in a 1 km by 1 km square ("Central square") and the reminder form the irregularly shaped Y (6 on each arm) over a total extent of about 25 km. Detailed system specifications of the GMRT can be found in http://www.gmrt.ncra.tifr.res.in/. Though designed to function primarily as an aperture synthesis telescope, the GMRT can be used in an array mode by adding the signals from individual dishes, either coherently or incoherently. This configuration, referred to as the array mode of operation, is used primarily for observations of compact objects like pulsars. Furthermore, sub-sets of the 30 antennas can be configured completely independently in what is referred to as the sub-array mode, to effectively provide more than one "single dish", thereby enabling pulsars to be observed simultaneously at multiple frequencies.

(a) Phasing of the array

Before observing the target pulsars, all the antennas should be pointed to a phase calibrator. All the sub-arrays required to be individually "phased"

by estimating the phases with respect to a reference antenna in each sub-array (from the point source visibilities recorded on the calibrator by the correlator) and applying the corrections for these back into the correlator hardware. The phase calibrator should be close to the target pulsar and should act as a point source, even for the longest baseline used at the observing frequency and are generally chosen from the VLA calibrator manual (www.aoc.nrao.edu/ gtaylor/csource.html). Once the arrays are phased, target pulsars can be observed typically for 2 hrs at the higher frequencies (325, 610 and 1280 MHz), but for only about 1 hr at lower frequencies (150 and 234 MHz). Thereafter, one need to re-phase the arrays to proceed with further observations.

(b) Signal flow

The signals from different antennas and observing frequency bands are eventually converted to a base-band signal of 16 MHz bandwidth, which is then sampled at Nyquist rate. The signals are further processed through a receiver system consisting of a correlator and a pulsar back-end. In the coherent (or phased) array mode, the geometrical and instrumental delays between the antennas are corrected to the accuracy of 2 nano seconds. The observing bandwidth of 16 MHz is divided into 256 spectral channels in the FX correlator. These dual polarization voltage signals from all the antennas are then brought to the GMRT Array Combiner (GAC), where they are added coherently or incoherently to get the phased array or incoherent array outputs, respectively for each polarization (Gupta *et al.*, 2000). In case of the polarimetric observations, pulsar receiver computes both the auto and cross polarized powers for each of the 256 channels (Mitra *et al.*, 2007). The GAC has the facility of assigning different values of gains to each spectral channel of each polarization of each antenna, in a completely independent manner, before the addition. These data were of 16 micro second time resolution, which were further integrated in time and finally recorded on the disk. The sampling times supported by the current GMRT system are 128 μs, 256 μs, 512 μs and 1.024 ms. Data can be further integrated during the offline analysis.

(c) Strategy for simultaneous multifrequency observations: Band masking

In the simultaneous multi-frequency sub-array mode of pulsar observations, the base-band signals from antennas in different sub-arrays (operating at different radio frequencies) can be added together in the same GAC, and the data can be recorded as a single stream, after integration by the desired amount. The dedispersed data streams for the different frequencies are extracted from this single data stream during off-line processing. Such a technique was employed by Ahuja *et al.* (2005), who carried out simultaneous dual frequency observations using the incoherent array mode of operation of the GMRT. They utilised the fact that, while traversing the interstellar medium, different frequency signals suffer different amount of dispersion delay and as a result the pulses arrive at different times (and hence at different pulse phases) at different frequencies. Hence the on-pulse data from different frequencies can be recovered from appropriate phase windows in the pulse period, during the offline analysis. This scheme provides naturally synchronized data from all the sub-arrays, without the need for separate, synchronized receivers for each sub-array. However, as Ahuja *et al.* (2005) have pointed out that this technique works well only for cases where the dispersion curves for different radio frequencies, when mapped to the 16 MHz base-band, do not overlap with each other for all phases of the on-pulse signal. This criterion becomes difficult to meet for pulsars with large duty cycle pulses and for large DMs. Specifically, in the case of wide profile pulsars (e.g PSR B0826−34, PSR B0818−41) this scheme will definitely fail due to the fact that the pulses at both frequencies will overlap in the band and it will be impossible to extract the stream of single pulse separately at different frequencies.

For such pulsars, we have devised a new scheme to carry out simultaneous multi-frequency observations. As mentioned earlier, the GAC has the facility of assigning to each spectral channel, a different value of gain − including zero gain. This allows selectable parts of the band to be processed, while blocking the rest of the band, for each antenna. The setting can be done independently for each antenna. This technique, which we refer to as **"band masking"**, allows simultaneous multi-frequency observations of all types of pulsars, independent of the combination of values of period, pulse width and DM, without having the need for separate, synchronized pulsar receiver chain

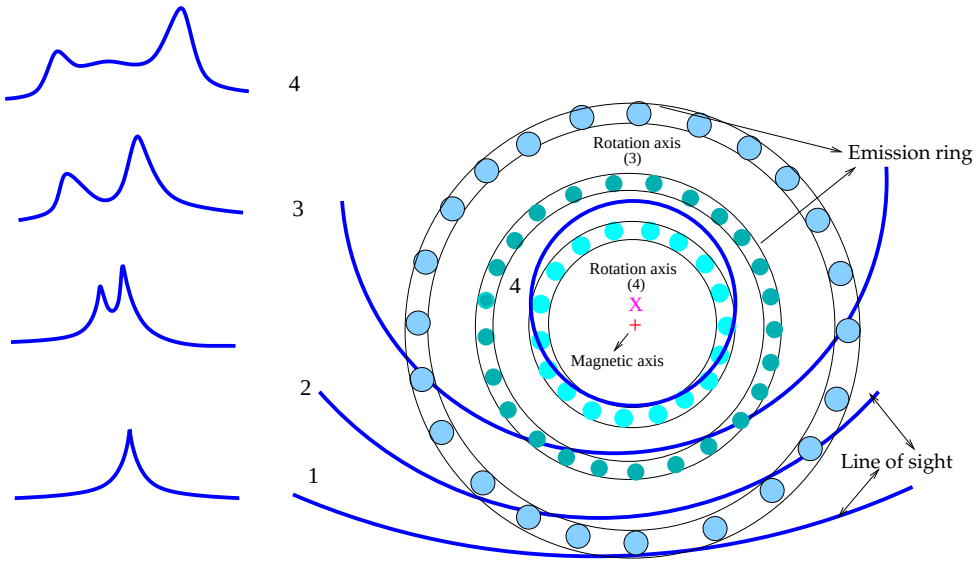

Figure 1.14: Different LOS cutting various parts of the beam giving rise to the observed pulse shapes for different pulsars considering the conal model; 1, 2, 3, 4 denote some sample LOS cut; 1, 2, 3 gives rise to the normal single, double pulse profiles, 4 will produce a very wide pulse profile and samples a large region of the polar cap.

for each sub array. The trick is to split the available base-band bandwidth into non-overlapping sub-bands, each of these parts being assigned to the antennas of one particular sub array, using appropriate band mask settings for each antenna. For the antennas of a given sub array, we apply nominal gain value for the typical GMRT pulsar observations in the chosen part of the band and the rest of the band is masked by applying zero gain value. During simultaneous dual frequency observations the available band is divided into two parts, each part being allotted to one of the observing frequencies. For example, we illustrate simultaneous observations at 325 and 610 MHz. Total number of antennas should be divided in two sub-arrays; antennas of sub-array#1 pointing at 325 MHz and those of sub-array#2 pointing at 610 MHz. The total bandwidth of 16 MHz, has to be divided between the two frequency bands by masking 8−16 MHz of the band for the antennas in sub-array#1 and 0−8 MHz of the band for the antennas in sub array#2. Both

the sub-arrays has to be individually "phased". The voltage outputs from the GAC will be passed to the phased array pulsar receiver where the data were converted to intensity values and intensities from the two polarizations will be added to obtain the total intensity for each of 256 spectral channels, containing information from the two sub-arrays.

Detailed observational requirements for individual works are described in the respective chapters of this thesis. However, the basic observing strategy illustrated above are alluded to at different stages of the thesis.

1.6 Motivation for this thesis

During the thesis period I was mostly involved in the study of wide profile drifting pulsars. Apart from this I also worked for the development of a simple method for determining the orbital parameters of a binary pulsar system. Motivations for the thesis are discussed in the following.

(a) Motivation for the study of wide profile drifting pulsars

Most of the pulsars have a narrow duty cycle of emission, about 5-10 % of pulsar period. This is generally consistent with the expectations of the angular width of the polar cap, for typical viewing geometries. However, there is a small but significant number of pulsars with unusually wide profiles, for which the observed emission is seen for a wide range of longitude. These are expected to be pulsars which are highly aligned, i.e. the magnetic dipole axis is almost parallel to the spin axis and the emission is coming from one magnetic pole of a highly aligned pulsar. In such a case, the LOS being very close to both the rotation and the magnetic axes samples a large region of the polar cap. This has the exciting potential to allow a detailed study of the distribution and behavior of emission regions located in a annular ring around the magnetic axis, thereby allowing for the most direct test of the conal (Rankin (1993), Rankin (1990)) versus patchy model (Lyne & Manchester, 1988), which are two competing views about how the emission could be arranged in the magnetosphere (discussed in detail in Sect. 1.2(a) of this thesis). Fig. 1.14 shows different LOS cuts to various parts of the beam

giving rise to the observed pulse shapes for different pulsars considering the conal model, where 1, 2, 3, 4 denote some sample LOS cuts. While 1 and 2 are examples of LOS cuts that will produce the single, double pulse profiles with narrow duty cycle, LOS cut like 3 or 4 will produce very wide pulse profiles and sample large regions of the polar cap.

The study of pulsars showing systematic subpulse drift patterns provides important clues for understanding the unsolved problems of pulsar emission mechanism. Constraints provided by such observations can have far reaching implications for the theoretical models, as exemplified by some of the recent results in this area (e.g. Deshpande & Rankin (1999) and Gupta *et al.* (2004)). Though there has been significant progress both in high quality observations of drifting subpulses and in confronting their observational properties with the existing models, the detailed nature of radio emission processes of pulsars and the exact location as well as distribution of the pulse emitting regions are still shrouded in mystery. It has been recently shown that subpulse drifting may be fairly common among the pulsars (Weltevrede *et al.* (2006) and (2007)) but a thorough study has not been done for a majority of them. In this context, pulsars with wide profiles can provide extra insights because of the presence of multiple drift bands.

Fig. 1.15 shows the single pulse gray scale plot of an unique wide profile pulsar PSR B0826−34 at 1060 MHz, obtained with the GMRT. Simultaneous multiple drift bands are observed. Upper panel of Fig. 1.15 shows the wide average profile of PSR B0826−34 at 1060 MHz. Since our LOS samples a large region of the polar cap in case of the wide profile pulsars, there is a high probability of intersection of LOS with multiple rings of emission. As a result simultaneous multiple drift regions will be observed. Hence the relation between the drifting in the multiple rings can be studied for wide profile pulsars and it will be possible to probe the nature of the distribution of electrodynamic control in the polar cap (i.e. distribution of electric and magnetic fields), which is responsible for drifting according to Ruderman & Sutherland (1975). Spark discharges occur in every place where the potential drop is high enough to ignite and develop pair production avalanche (Ruderman & Sutherland, 1975), so the sparks populate the polar cap as densely as possible. At the same time such arrangement of sparks should be quasi rigid, a property which should be reflected in the data. Therefore one can

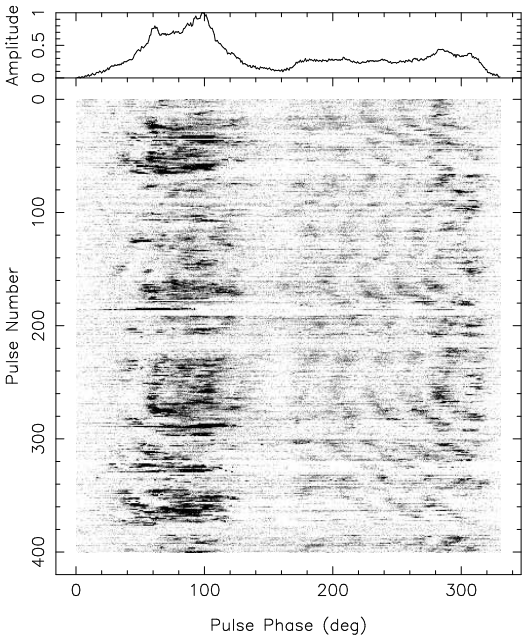

Figure 1.15: Gray scale plot of the single pulses from PSR B0826−34 at 1060 MHz observed with the GMRT by us, with the average profile shown on the top.

probe the dynamics and distribution of the emission regions in the polar-cap with the study of wide profile pulsar. With this as our motivation we study the following specific features for the wide profile pulsars.

(i) Since in case of wide profile pulsars we sample a large region of the polar cap, if the drift rate is similar for the entire pulse window then the mechanism that gives rise to subpulse drift is expected to be uniform across the polar-cap.

(ii) Because of the wide profile one is likely to observe emission from multiple cones. If multiple cones are visible, the relation between the drifting in the cones can be studied (e.g. coherent drifting between two rings will indicate towards a common electrodynamic control in the polar cap).

(iii) Multiple drift regions with their drift phase related to each other, are known only in a few pulsars, PSR B0815+09 (McLaughlin *et al.*, 2000), PSR B1839−04 Weltevrede *et al.* (2006). The phase relationship between the observed drift regions can provide clue towards the arrangements of the emission regions in the polar cap.

(iv) Exploring nulling properties for wide pulse longitude may provide extra

insight towards the emission mechanism.
(v) Because of the wide longitude coverage, it is easier to fit RVM model (Radhakrishnan & Cooke, 1969) to the polarization angle traverse for wide profile pulsars. Hence it will be easier to determine the emission geometry of the radiation beam which will help us in understanding the emission mechanism.
(vi) Frequency and longitude evolution of P_2^m, P_3^m, $\Delta\Phi$, $\Delta\Phi_s$ can be studied.

(b) Determination of orbital parameters of the binary pulsars

The orbital parameters of binary pulsar systems can be determined by fitting a Keplerian model to the pulsar period versus the epoch of observation. The usual methods require simultaneous fit to many parameters and need an initial guess. Such methods need dense sampling of period measurements at different epochs during the pulsar orbital period. Freire *et al.* (2001) proposed a new method for determination of the orbital parameters of binary pulsars. Their method require information on periods and period derivatives at multiple observing epochs. Their method worked only for nearly circular orbit.

This work was motivated by the discovery of a binary pulsar PSR J0514−4002, the first known pulsar in the globular cluster NGC 1851 at the GMRT by (Freire *et al.*, 2004). Orbit of this pulsar was found to be quite eccentric, and hence the method developed by Freire *et al.* (2001) was not useful in determination of orbital parameters of this pulsar. We felt the need for developing a method for determination of orbital parameters that will work for all types of orbits. It seemed to us that without requiring the information on period derivatives of the pulsars it is possible to develop a method for determining the Keplerian orbital parameters. Hence, I got motivated towards developing a simple method for determination of the orbital parameters of binary pulsars using pulsar period at multiple epochs.

1.7 An outline of this thesis

In the thesis period, I have thoroughly investigated drifting, nulling properties for two wide profile pulsars: PSR B0818−41 and PSR B0826−34. PSR B0818−41 is an unique wide profile pulsar for which remarkable drift pattern is discovered by us. PSR B0826−34 is a unique drifting pulsar with one of the widest known profile. Apart from this we have studied the single pulse properties for a sample of 6 more wide profile pulsars. The main aim of this dissertation is to investigate the single pulse properties of wide profile drifting pulsars to probe pulsar magnetosphere.

As part of a separate work we developed a simple method for determination of the orbital parameters of binary pulsars using the pulsar periods at multiple epochs.

The detailed results obtained from individual works and the possible implications for the pulsar emission physics are discussed in different chapters of this thesis.

A breakup of the contents of individual chapters of this thesis is as follows. Introduction is presented in Chapter 1. Chapter 2 describes average properties of unique wide profile drifting pulsar PSR B0818−41. Remarkable drifting properties of PSR B0818−41 are explored in Chapter 3. Our study reveal that PSR B0818−41 exhibits unique nulling properties which are investigated in Chapter 4. Multifrequency polarization study of single pulse properties of the unique wide profile pulsar PSR B0826−34 is reported in Chapter 5. Apart from PSR B0818−41 and PSR B0826−34 we investigated the single pulse properties of few other pulsars with a variety of pulse shapes, which is described in Chapter 6. In Chapter 7 we describe the method for determination of binary orbital parameters developed by us. The summary of the results presented in this thesis and the future prospects are presented in Chapter 8.

CHAPTER 2

PSR B0818−41 : an unique wide profile pulsar

"Imagination is more important than knowledge."
– Albert Einstein

2.1 Introduction

It is established that pulsars with wide profiles can provide extra insights about the magnetosphere because of the presence of simultaneous multiple drift bands, which is exemplified in the recent studies of PSR B0826−34 (Gupta *et al.* (2004) and Esamdin *et al.* (2005)) and PSR B0815+09 (Qiao *et al.*, 2004) and is discussed in details in Sect. 1.6 of Chapter 1. PSR B0818−41 is a less studied wide profile pulsar with emission occurring for more than 180 deg of pulse longitude. This pulsar was discovered during the second Molonglo pulsar survey (Manchester *et al.*, 1978). It has a period of 0.545 s and is relatively old, with a characteristic age of 4.57×10^8 years. The inferred dipolar magnetic field of this pulsar is 1.03×10^{11} G, which is a typical value for slow pulsars. Qiao *et al.* (1995) have studied the average polarization properties of this pulsar at 660 and 1440 MHz. Their study reports a steep-sided wide profile with modest amount of linear polarization (32% at 660 MHz and 31% at 1440 MHz). From the wide integrated profile, Qiao *et al.* (1995) also predicted that this pulsar must be a fairly aligned rotator.

Knowledge of pulsar flux and spectra provides idea about pulsars intrinsic brightness and helps to plan the observations. Pulsar average profile and its evolution with frequency gives information of average condition of pulsar

magnetosphere. Multifrequency observations offer insights into various aspects of frequency dependence of pulsar radiation, as exemplified by Taylor *et al.* (1975), Bartel & Sieber (1978), Bartel (1981), Bhat *et al.* (2007) etc.

We have carried out multi epoch observations of PSR B0818−41 at 157, 244, 325, 610 and 1060 MHz using the GMRT in full polar mode. We discover a remarkable pattern of subpulse drifting in this pulsar. We report unique drifting, nulling and polarization properties of PSR B0818−41. The remarkable drifting and nulling properties of this pulsar are investigated in Chapter 3 and 4 respectively. In this chapter we describe the observations of PSR B0818−41, and report new results from investigation of the average properties of the pulsar − spectrum, average profile and its evolution with frequency and the polarization properties. Sect. 2.2 describes the observations of PSR B0818−41 at multiple frequencies and multiple epochs. In Sect. 2.3 we investigate the average profile evolution with frequency. Flux calibration and determination of spectrum is detailed in Sect. 2.4. Sect. 2.5 describes the polarization properties at different frequencies. In Sect. 2.6, we summarize the main results presented in this chapter.

2.2 Observations and preliminary data analysis

We performed polarimetric observations of PSR B0818−41 at multiple frequencies (157, 244, 325, 610 and 1060 MHz), with the GMRT, using the phased array mode (Gupta *et al.*, 2000), at several epochs. The simultaneous dual frequency observations reported in this chapter were done using the "band masking" technique. Details of pulsar observations using the GMRT are described in Sect. 1.5 of Chapter 1. Data was recorded to the disk at a sampling rate of 0.512 ms. During the off-line analysis the raw data was further integrated to achieve the final resolution of 2.048 ms. Table 2.1 summarizes the observations.

Average pulse profiles at different observing frequencies were obtained by dedispersion with a DM of 113.4 pc/cm^3. Power line (50 Hz) and its harmonics were the major contributors to the radio frequency interferences present in the data. To remove power line related interferences, the dedispersed

Table 2.1: Details of the observations at different epochs and the corresponding flux measurements

Frequency (MHz)	Date of observation	No of pulses	No of antennas used	Flux of peak (mJy)	Mean Flux (mJy)
157	12 December 2005	2000	16	428^a 521^b	87^a 105^b
157	1 April 2006	3300	17	376^a	69^a
157	2 April 2006	4500	19	340^a	67^a
244	20 September 2007	9500	16	298^a 465^b	46^a 62^b
244	4 January 2008	9900	16	371^a 518^b	53^a 74^b
244	6 January 2008	4600	16	452^a 756^b	64^a 108^b
325	21 December 2005	6600	15	586^a 695^b	95^a 116^b
325	24 February 2004	3414	17	568^a	93^a
325	26 December 2004	1869	19	384^a	65^a
$325^\dagger$	10 March 2006	4300	8	548^a	92^a
$325^\dagger$	16 March 2006	6500	7	617^a	98^a
610	14 December 2005	9900	16	98^a 103^b	20^a 20^b
610	25 February 2004	1612	20	153^a	29^a
610	11 January 2005	6000	22	125^a	24^a
610	25 January 2005	7000	20	74^a	19^a
$610^\dagger$	10 March 2006	4300	8	75^a	17^a
$610^\dagger$	16 March 2006	6500	10	104^a	21^a
1060	22 November 2005	7800	22	33^a 36^b	7^a 7^b
1060	16 September 2006	6600	16	45^a 51^b	9^a 11^b
1060	13 January 2007	3000	27	32^a	7^a

a : relative calibration

b : absolute calibration

† : simultaneous dual frequency observations

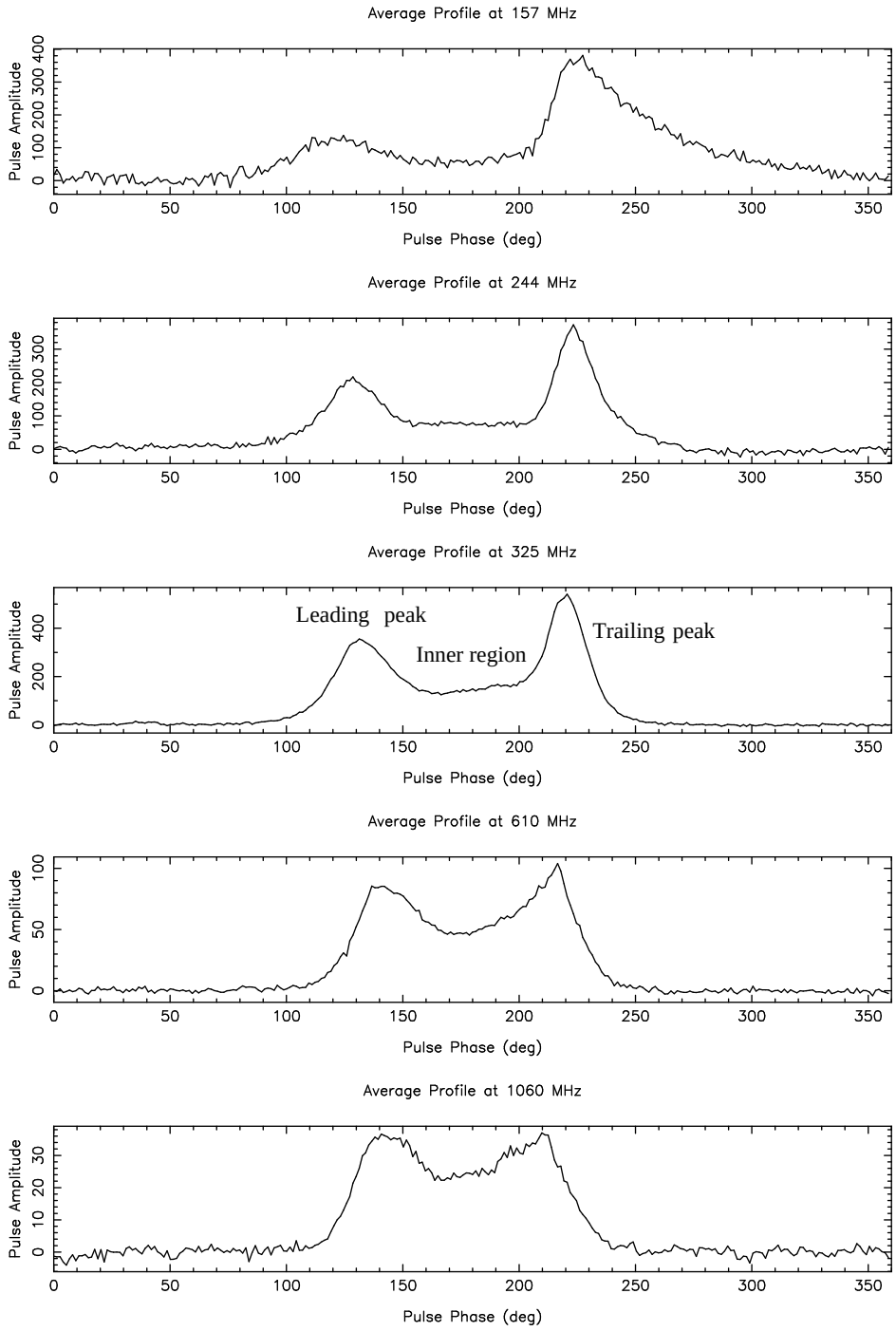

Figure 2.1: Frequency evolution of the average profile of PSR B0818−41. Different panels plot the average profiles obtained from the GMRT observations at different observing frequencies, 157, 244, 325, 610 and 1060 MHz respectively. Pulse amplitude is in mJy. The separation between two peaks of the double peaked pulse profile decreases with increasing frequency following the radius to frequency mapping.

data were put through a radio frequency interference filtering routine which detected most (but probably not all) of the power line interferences and replaced them by appropriate random noise. The dedispersed, interference free data stretch were synchronously folded with the topocentric pulsar period.

2.3 Average profile evolution with frequency

Fig. 2.1 presents the plot of the average profiles at five different observing frequencies. At 325 MHz, it shows a fairly steep sided double-peaked structure. The two components of the double-peaked profile are separated by 86.6±0.3 deg and are joined by a saddle region. The trailing peak is more intense than the leading one. The trailing peak is broadened at 157 MHz, probably because of scattering effects (which become more prominent at lower frequencies). The two peaks of the average profile, at 157 MHz, are of unequal intensity, leading peak having about half the intensity of the trailing peak. With increase in frequency, the leading peak becomes more intense and the saddle region joining the two peaks becomes more filled up. At 1060 MHz, both the peaks of the double peaked profile are of comparable intensity and the inner saddle region is quite filled up. Separation between the two peaks of the double peaked average profile ($\Delta\Phi$) reduces with increasing frequency (Table 2.2). $\Delta\Phi$ varies with frequency as $\Delta\Phi \propto \nu^{-p}$, with average p value of 0.2 (Table 2.2). This follows the general trend of the "radius to frequency mapping", seen in a majority of pulsars.

2.4 Flux at individual frequencies and spectrum

We determine the mean flux of PSR B0818−41 for all the observing frequencies at all the observing epochs. For some of the epochs we had observed flux calibrator sources and for these cases we determine the flux from absolute calibration. The calibrator fluxes at 90 and 20 cm available in the VLA catalog are used as the calibrator fluxes at 325 and 1060 MHz respectively. However, the calibrator flux at 610 MHz is obtained by interpolation between 90 and 20 cm fluxes from the VLA catalog and the calibrator fluxes at 157

Table 2.2: Frequency dependence of separation between the two peaks ($\Delta\Phi$)

Frequency (MHz)	$\Delta\Phi$ (deg)
157	105±0.3
244	96±0.3
325	86.6±0.3
610	75.7±0.3
1060	63±0.3

and 244 MHz are obtained by extrapolation of the 90 and 20 cm fluxes. For the epochs where we do not have any flux calibrator source observed, we follow a relative calibration procedure, using the knowledge of the observing parameters and the background sky temperature near the source. As a crosscheck we compare the fluxes where both absolute and relative calibrations were possible. The flux values determined from absolute and relative calibration are similar for all the frequencies, except at 157 and 244 MHz. The reason for the difference in flux values between absolute and relative calibration could be due to the error in the estimation of calibrator flux or inaccurate knowledge of the sky temperature at the position of the pulsar, at the lower frequencies. In Table 2.1 we list the mean flux, for all the five frequencies of observations.

Though the scintillation properties of PSR B0818−41 are not studied, still we try to understand the effect of scintillation on the observed flux, by comparing with two nearby pulsars for which the scintillation properties are known. The mean flux densities for two nearby pulsars, PSR B0628−28 and PSR B0834+06, are observed to change by $\sim$ 30% between the observing epochs (Bhat *et al.*, 2007). Between different observing sessions of PSR B0818−41, we observe 15 to 20% change of the mean flux, for a particular frequency (Table 2.1). Hence, it is likely that the estimated mean flux values of PSR B0818−41 are affected by the scintillation to a moderate extent. Fig. 2.2 presents the spectral behavior of the mean flux densities obtained from

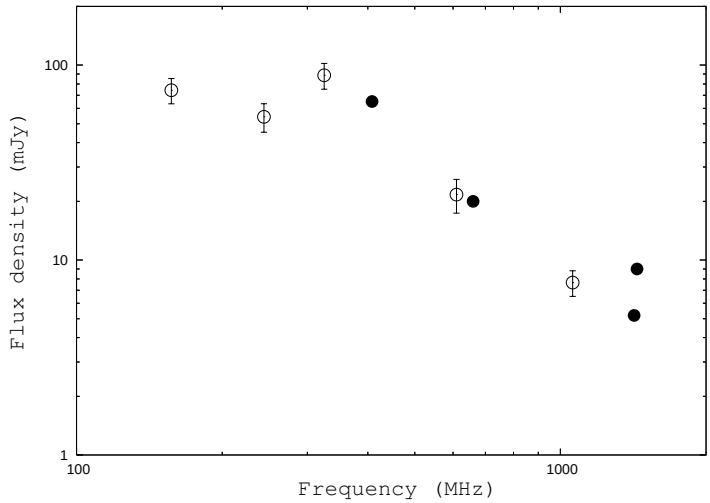

Figure 2.2: Spectra with the calculated mean flux densities from relative calibration (Table 2.1). Open circles with error bars represent the flux measurements from this work and the filled circles represents the flux values available in the literature. Spectra flattens below 325 MHz, at frequencies like 157 and 244 MHz. Known values of the mean flux of PSR B0818−41 at different frequencies are: 65 mJy at 400 MHz (Hobbs *et al.*, 2004), 20 mJy at 660 MHz (Qiao *et al.*, 1995), 5.2 mJy and 9 mJy at 1.4 GHz estimated by Taylor *et al.* (1993) and Qiao *et al.* (1995) respectively. The spectra from our work seems to disagree with mean flux of 9 mJy at 1.4 GHz (Qiao *et al.*, 1995) and agrees with mean flux of 5.2 mJy at 1.4 GHz (Taylor *et al.*, 1993).

relative calibration. The error in mean flux is calculated from the standard deviation of the available flux values at a given frequency. Our estimation of the mean flux values of PSR B0818−41 at different frequencies are in the same ballpark as the earlier results available at 400, 660 and 1400 MHz (Fig. 2.2). Monotonic increase in pulsar flux is observed with decreasing frequency starting from 1400 to 325 MHz with average value of spectral index $\alpha \sim -2$ (where α is defined as $I \propto \nu^{\alpha}$), which is similar to the mean value of the power law index for a typical pulsar spectrum (Maron *et al.*, 2000). However, we note that there is a tendency of flattening of the pulsar spectrum at frequencies lower than 325 MHz (at 244 or 157 MHz). We believe that this flattening of the spectrum is associated with the turn-over at low frequencies. But because of the uncertainty in the observed flux values, it is difficult to estimate the exact frequency of the turn-over. Usually pulsars exhibit such a power law spectrum with a low frequency turn-over near $\sim$ 100 MHz

(Malofeev *et al.*, 1994). For PSR B0818−41, the flux of leading outer, trailing outer and inner region evolve differently with frequency (Fig. 2.1). Relative strength of the leading peak as compared to the trailing peak increases with frequency. Inner saddle gets more filled with increasing frequency which is evident from the average profiles plotted in Fig. 2.1. Hence, spectral indices of different profile components are different for PSR B0818−41. Component dependent frequency evolution of flux is observed for many other pulsars (e.g. for PSR B1133+16 reported by Bhat *et al.* (2007)).

2.5 Polarization study

Fig. 2.3, 2.4 and 2.5 present the polarization profiles at 325, 610 and 1060 MHz. Polarization profiles at 610 and 1060 MHz have better signal to noise than the published polarization profiles at 660 and 1440 MHz by Qiao *et al.* (1995), and reproduce all the basic polarization features reported by them. We have observed PSR B0818−41 at several epochs. Analysis of the data from all the epochs produces self consistent polarization profiles. The polarization profiles with best signal to noise ratio available for a given frequency are presented in this work.

(a) Linear polarization

Significant amount of linear polarization is observed at all the frequencies (about 45% at 325 MHz, 32% at 610 MHz and 20% at 1060 MHz) : the percentage of linear polarization is more at 325 than at 610 and 1060 MHz. This agrees well with the percentage of linear polarization quoted by Qiao *et al.* (1995). The average profile for linear polarization follows the general double peaked structure of the total intensity profile. But the separations between the two peaks of the linearly polarized profile are, 79 deg at 325 MHz, 71 deg at 610 MHz and 60 deg at 1060 MHz, which are less than the separations between the total intensity peaks at individual frequencies. We note that this phenomenon appears to have a frequency dependence: width of linearly polarized and the total intensity profile differing by ∼10% at 325 MHz whereas by ∼5% at 610 and 1060 MHz. At 325 MHz the leading and the trailing peaks of the average linear polarization profile are of similar intensity, whereas in the total intensity profile the trailing peak is significantly more

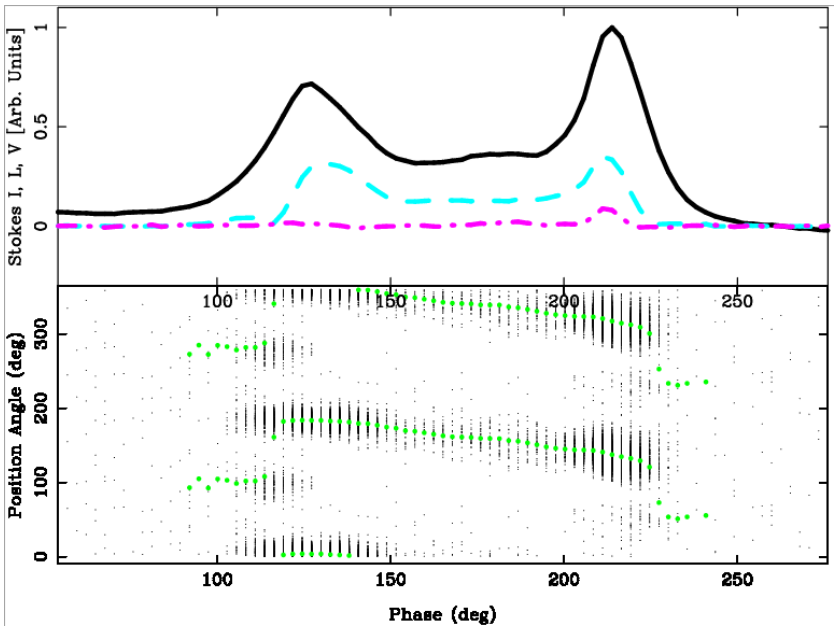

Figure 2.3: PA histogram for the 325 MHz pulse sequence on 21 December 2005. The upper panels show the average total power, total linear and circular polarizations and the lower panel gives the PA density. The PA values are plotted twice for clarity.

intense than that of the leading one. At 610 and 1060 MHz the leading and the trailing peaks of the linear polarization profile are of similar intensity, and the same is true for the total intensity profiles. Average linear polarization falls off much faster than the total intensity and decreases to zero near the outer edges of the profiles. This effect of edge depolarization is less in 1060 MHz as compared to 325 and 610 MHz.

Fig. 2.3, 2.4 and 2.5 show that the PA curve evolves significantly with frequency. In order to do a closer comparison, Fig. 2.6 shows the three PA curves in one plot. The PA curve shows linear monotonic variations (with some amount of irregularities) at 325 MHz. Total PA swing is about 69 deg at 325 and about 53 deg at 610 MHz. The PA curve at 610 MHz is quite different than that of 325 MHz. For the left half of the PA curve at 610 MHz, nearly linear PA variation with pulse longitude is observed, which is similar to 325 MHz. A different slope of the PA curve is seen at 610 MHz at the middle of the pulse profile. The other part of the PA curve at 610 MHz exhibits kinky structure and some signature of reversal of the slope of the

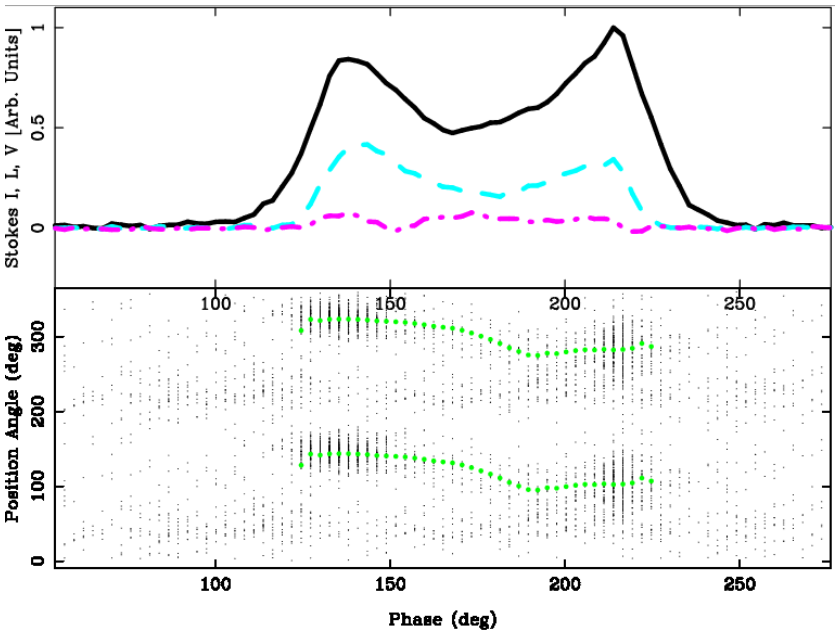

Figure 2.4: PA histogram for the 610 MHz pulse sequence on 14 December 2005. The upper panels show the average total power, total linear and circular polarizations and the lower panel gives the PA density. The PA values are plotted twice for clarity.

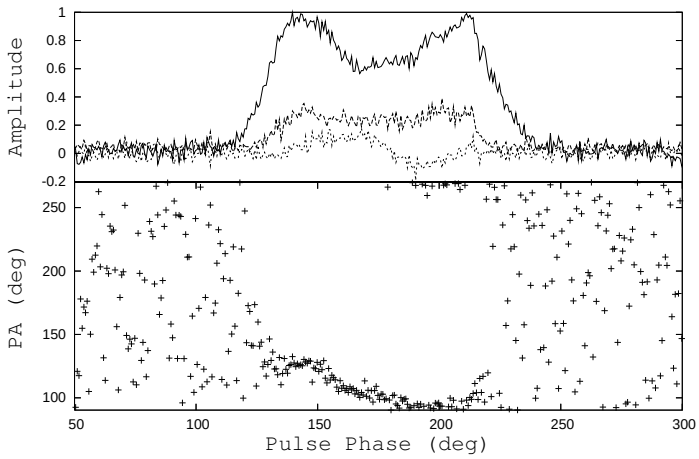

Figure 2.5: Polarization profile of PSR B0818−41 at 1060 MHz. The top panel shows the average profile in total intensity (solid line), linear polarization (dashed line) and circular polarization (dotted line). The lower panel shows the variation of PA as a function of longitude. The amplitude is in arbitrary units.

PA curve is observed at the edge of the profile. It is difficult to explain the total PA sweep at 610 MHz with the RVM (Radhakrishnan & Cooke, 1969), which is indicative of non dipolar emission geometry. Though the PA curve is quite noisy at 1060 MHz, we see a behavior intermediate to that at 325 and 610 MHz (Fig. 2.6).

Evidence of orthogonal polarization mode (OPM) jump is observed at the two edges of the profile at 325 MHz (Fig. 2.3). While investigating the single pulse PA using scatter plot, we observe OPM jump near two edges of the pulse profile at 325 MHz. At 610 MHz the signal to noise was not enough to see the OPM jump, and at 1060 MHz the signal to noise was not enough to observe single pulse PA. Orthogonal polarization mode jump observed at the edge of the profile at 325 MHz, can be the reason of the abrupt decrease of the linear polarization near the edge of profile. Presence of the secondary polarization mode at the edge of the profile can cause the observed reduced width of the linearly polarized profile compared to the total intensity profile. Strong OPM jump observed at 325 MHz, can explain the fact that observed differences between the separations between the peaks of linearly polarized and total intensity profile are more at 325 MHz.

(b) Circular polarization

Though circular polarization observed for PSR B0818−41 at 325 MHz is quite less, under the trailing component of the pulse profile there is a feature of increased circular polarization. Small amount of circular polarization is observed at 610 and 1060 MHz. Circular polarization changes sign at 1060 MHz near the middle of the pulse profile, which is also reported by Qiao *et al.* (1995) at 1440 MHz. We note that changing sign of circular polarization is not observed at 325, 610 (this work) and 660 MHz (Qiao *et al.*, 1995).

There are two possible origins of circular polarization of pulsars: either intrinsic to the emission properties and dependent on the emission mechanism (e.g. Michel (1987), Radhakrishnan & Rankin (1990), Gangadhara (1997)) or generated by propagation effects (e.g. Cheng & Ruderman (1979)). Circular polarization of some pulsars changes with frequency and the variation of degree of circular polarization with frequency is very different from pulsar to pulsar (e.g. refer to Table 5 of Han *et al.* (1998)). PSR J2053−7200 is an extreme example where sense reversal of circular polarization from the

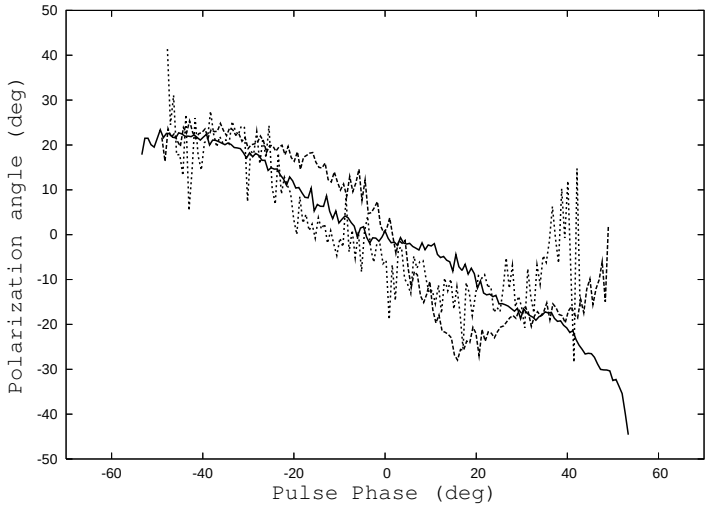

Figure 2.6: Observed PA curves at 325 (solid), 610 (doted line), 1060 (dash-dot).

positive to negative direction is observed near the intersection of two components, at low frequencies, whereas sense of circular polarization changes from negative to positive direction at high frequencies (Qiao *et al.*, 1995).

The feature of increased circular polarization near the trailing peak at 325 MHz, which is not observed at 610 and 1060 MHz, may contribute towards the more intense trailing peak than the leading one observed at 325 MHz. Sense reversals of the circular polarization are commonly associated with the core components. However, for PSR B0818−41, at 1060 MHz, it is associated with the conal components. There are some conal double pulsars such as PSR B0826−34, PSR B2048−72 which show a central reversal of circular PA but no core component at all (Biggs *et al.* (1985), Han *et al.* (1998)). In such cases the sense reversal is associated with conal components rather than the core components (Biggs *et al.*, 1985).

For PSR B0818−41 we observe a correlation between the sign change of circular polarization and the sense of PA sweep: with right hand (negative) circular polarization accompanying increasing PA. Han *et al.* (1998) reported similar correlation between the sense of PA sweep and the sense of circular polarization, using the polarization data of 20 conal-double pulsars.

2.6 Summary

Interesting new results from our investigation of average properties of PSR B0818−41 are highlighted in the following.
(1) We estimate the mean flux of PSR B0818−41 at 5 different frequencies and show that the spectrum flattens at frequencies lower than 325 MHz (at 244 or 157 MHz), providing indication of a low frequency turn-over.
(2) We present the average profiles at five different frequencies. The evolution of profile width with frequency follows "radius to frequency mapping".
(3) Significant linear polarization is observed at 325, 610 and 1060 MHz. Linear polarization profiles follow similar trend as the total intensity profile, but get depolarized at both edges of the profile. This is explained by the observed orthogonal polarization mode jump at the edges of the profile.
(4) Polarization angle sweep across the pulse profile evolves remarkably with frequency (at 325, 610 and 1060 MHz), which is not generally observed in other pulsars : at 325 MHz we observe linear monotonic variation consistent with RVM. For the left half of the PA curve at 610 MHz, nearly linear PA variation with pulse longitude is observed. But the other part exhibits completely different slope with kinky structure. To compare with 325 and 610 MHz we observe somewhat different PA swing at 1060 MHz. Origin of the observed frequency dependence of PA sweep as well as the non RVM PA sweep at 610 MHz require follow up investigation.
(5) Though very less circular polarization without any signature of changing handedness is observed at 325 and 610 MHz, circular polarization changes sign at the middle of the pulse profile at 1060 MHz.

CHAPTER 3

Exploration of the remarkable drifting properties of PSR B0818−41

"Joy in looking and comprehending is nature's most beautiful gift."
– Albert Einstein

3.1 Introduction

Pulsars with drifting subpulses are considered as an important key for unlocking the mystery of how radio pulsars work. Though there has been significant progress both in high quality observations of drifting subpulses and in confronting their observational properties with existing models (detailed in Chapter 1), the nature of radio emission processes of pulsars and the location, distribution of the pulse emitting regions are still not resolved.

Since our LOS samples a large region of the polar cap in case of wide profile pulsars, presence of simultaneous multiple drift regions is quite probable (sec Sect. 1.6 of Chapter 1 for illustration). Phase relationship between the drift regions can be used to probe the distribution and dynamics of the emission regions in the polar cap.

The average profile and polarization properties of PSR B0818−41 are reported in Chapter 2. High sensitivity GMRT observations of B0818−41 reported in Sect. 2.2 of Chapter 2, brings out a unique pattern of subpulse drift, which is hitherto not reported. In this chapter we will investigate the unique drifting properties of this pulsar. PSR B0818−41 is one of the few pulsars which show multiple drift regions having well defined phase relationship. Multi-frequency study of subpulse drifting is detailed in Sect. 3.2. It is essential to know the viewing geometry to understand the pulsar emission mechanism. The orientation of the pulsar radiation beam can be determined

by two angles, α and β. Possible geometry of a pulsar is determined by the "Rotating Vector Model (RVM)" (Radhakrishnan & Cooke, 1969) fit to the PA traverse as described Sect. 1.2(f) of Chapter 1. Our interpretation about the arrangements of sparks in polar cap for this pulsar are discussed in Sect. 3.3, which includes understanding of possible choices of viewing geometries and comparing those with results from simulations of the radiation pattern. Unique phase relationships between multiple drift regions observed for PSR B0818−41 are investigated in Sect. 3.4. In Sect. 3.5, we present a final summary of different aspects of the analysis results and the interpretations.

3.2 Subpulse drifting at multiple frequencies

Single pulse sequences from our data reveal an interesting pattern of drifting. Fig. 3.1 shows typical drift patterns over two sequences each with 200 pulses. We see three different drift regions with two different drift rates − an inner region with steeper apparent drift rate flanked on each side by a region of slower apparent drift rate. Multiple drift bands (typically 3 to 4) can be seen in the inner region for any single pulse, whereas the outer regions show only a single drift band. Fig. 3.2 shows an example of stack plot of the single pulse data of 200 pulses at 325 MHz. Individual pulses are seen over a wide longitude in the pulse window. Organized drifting near the two edges of the pulse profile is observed, in the form of linear drift bands going from the later to the earlier longitude, as the pulse number increases (we refer to this as negative drifting).

We note that the inner and the outer drift regions are quite closely spaced with almost no discontinuity between the drift bands of the two region. Furthermore, the two drift regions are clearly locked to each other in phase − the subpulse emission from the inner drift region is in phase with that from the outer drift region on the right side, and at the same time the emission in inner drift region is out of phase with the outer drift region situated on the left side. This phase locked relationship (hereafter PLR) is maintained for the entire stretch of the data and does not appear to get perturbed after intermittent nulling or during changes in the drift rate.

Though the regular drift patterns seen in Fig. 3.1 is quite common in the pulse sequences observed by us, there are regions of irregular drifting, as

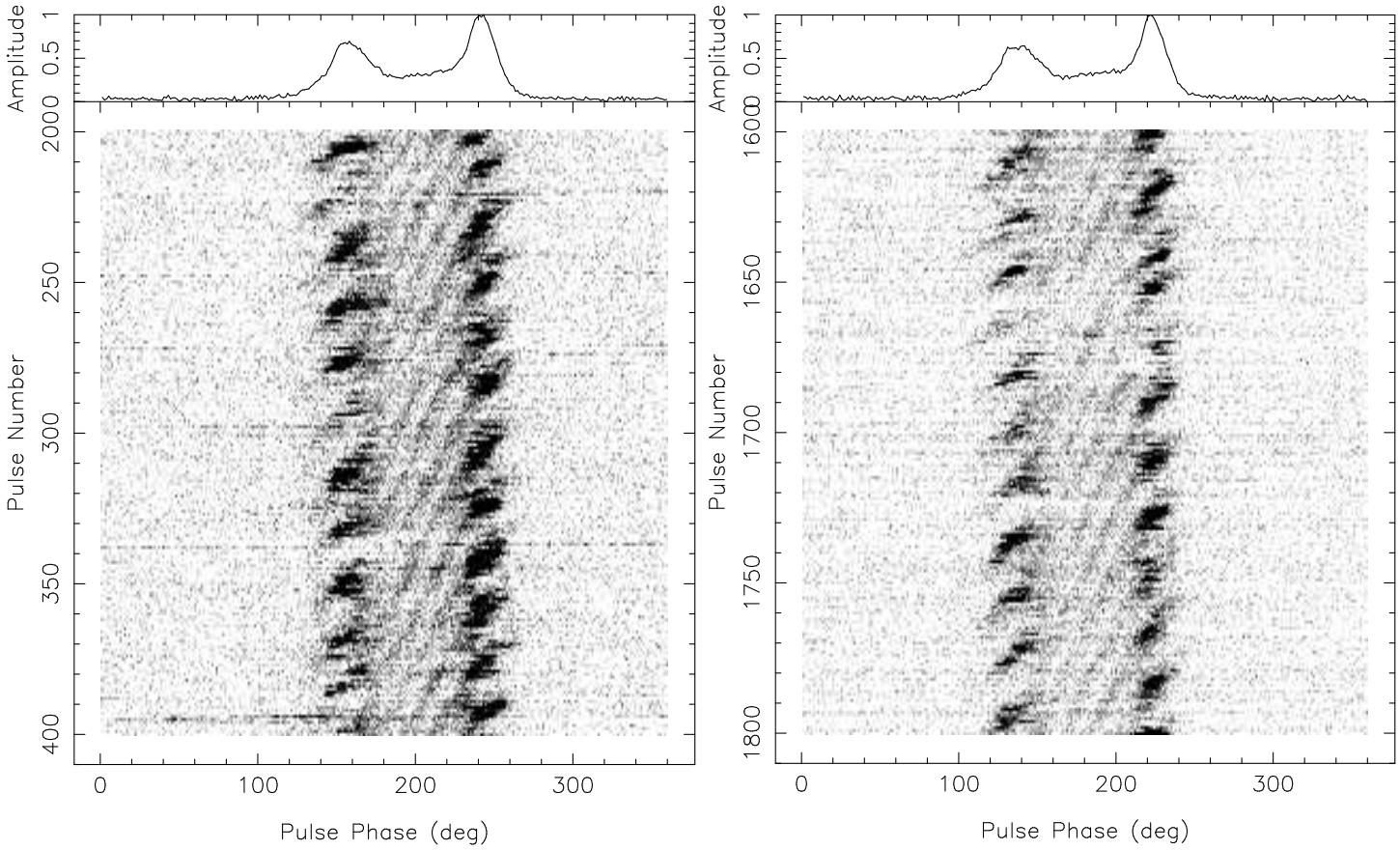

Figure 3.1: Gray scale plot of single pulse data of PSR B0818−41 from observations on 24 February 2004 at 325 MHz, with the average profile shown on top. Left panel: pulse # 200 to 400, signatures of radio frequency interference are present around pulse # 220, 298, 338 and 397, fading of the leading outer region is observed around pulse # 220 to 230 and pulse # 295 to 305. Right panel: pulse # 1600 to 1800, fading of the leading outer region near pulse # range 1655 to 1675, corresponding fading in the trailing outer region might be near pulse # 1670.

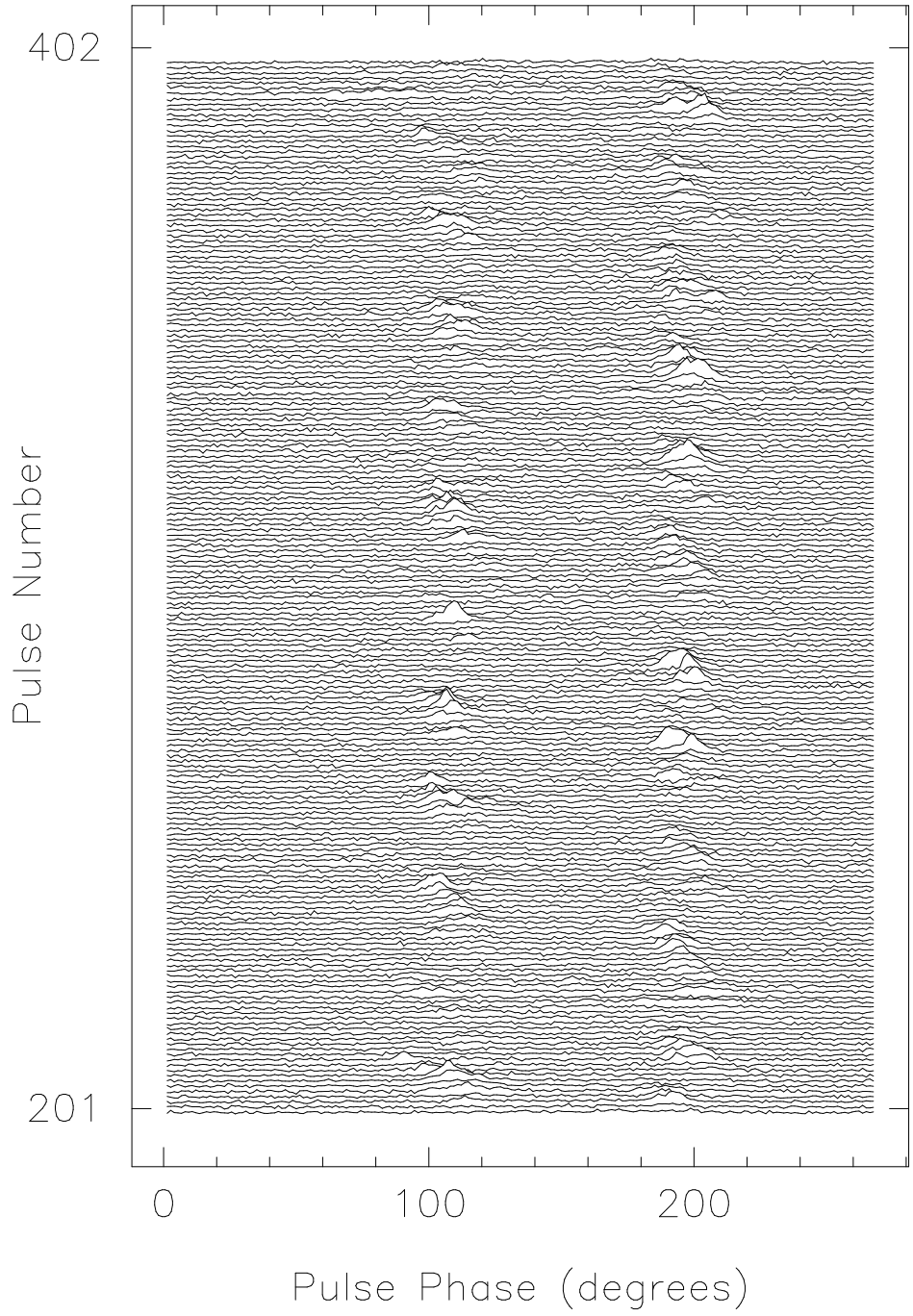

Figure 3.2: Single pulse sequence of 200 pulses (pulse # 200 to 400) of PSR B0818−41 from observations on 24 February 2004 at 325 MHz. Pulse emission is present for a wide longitude range ($\sim$ 180 deg). Drift bands in the leading and trailing outer regions are observed from the stack of single pulses. Modulations in the inner region are weaker and are indistinguishable in this plot in contrast to the outer regions.

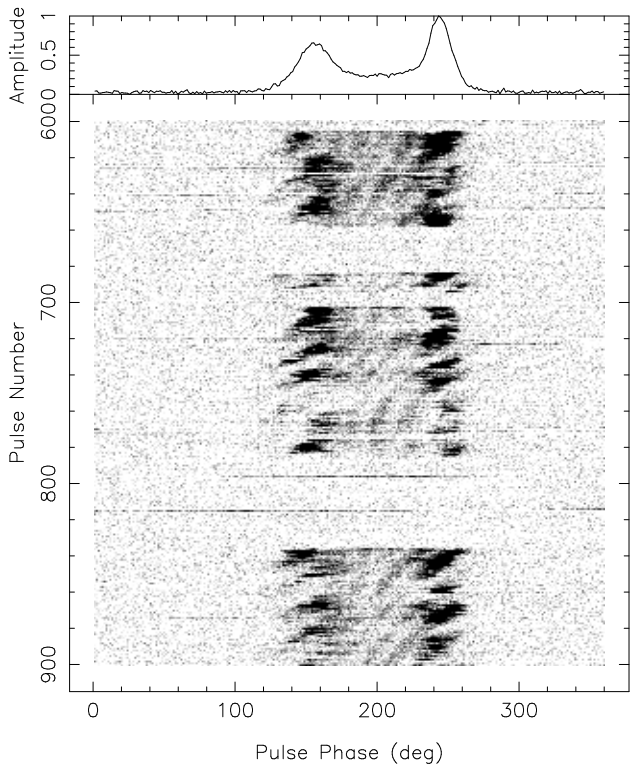

Figure 3.3: Same as Fig. 3.1, but for pulse # 600 to 900 of PSR B0818−41 from observations on 24 February 2004 at 325 MHz, with the average profile shown on the top. Signatures of radio frequency interference are present around pulse # 625, 720, 790 and 815.

well as significant sections of nulls. An illustrative 300 pulse sequence of this kind is shown in Fig. 3.3. Changes in drift rate, including curved drift bands (e.g. pulse # 720 to pulse # 780) are seen clearly. In this context this pulsar behaves similar to B0826−34. In Fig. 3.3 some instances of the pulsar in null state are also seen − pulse # 647 to 687, 693 to 705 and 780 to 835. We will discuss about the frequent change of drift rate later in this section. The unique nulling behavior of this pulsar is discussed in Chapter 4.

Though, simultaneous multiple drift regions are more prominent at 325 MHz, drifting is also observed at 150, 244 and 610 MHz. Right panel of Fig. 3.4 shows the gray scale plot of the single pulses at 610 MHz. Though the single pulses become quite weak at 610 MHz, drifting is clearly visible in the gray scale plot both in the inner and the outer region. In the inner region, 3 to 4 simultaneous drift bands are visible and faint single drift bands can be identified on both sides of the inner region. Left panel of Fig. 3.4 is the gray

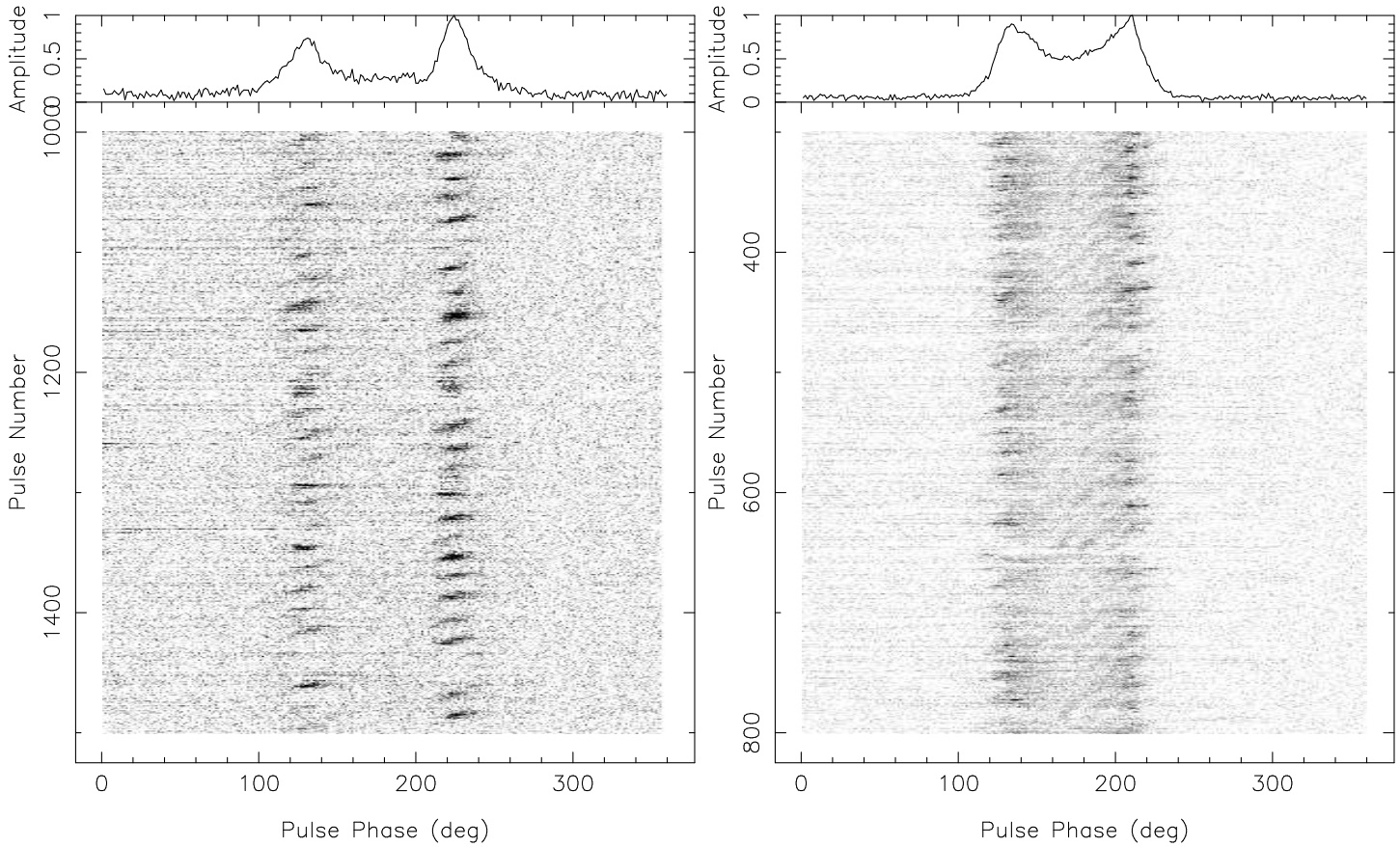

Figure 3.4: Gray scale plot of single pulse data of PSR B0818−41 from observations on at 244 and 610 MHz, with the average profile shown on top. Left panel: pulse # 1000 to 1500 from observations on 20 September 2007 at 244 MHz; drifting is observed in the leading outer and trailing outer regions, but not in the inner region; occasional fading of drift bands in the outer left region is seen. Right panel: pulse # 300 to 800 from observations on 25 February 2004 at 610 MHz showing regular drifting; drift bands are observed both in the inner and the outer regions.

scale plot of single pulses at 244 MHz. Drifting is observed in the leading and trailing outer regions, but no signature of drifting is present in the inner saddle region. Even after integrating the data up to a resolution of 8 ms to detect possible weak drift bands in the inner drift region, we do not see any evidence of that. At 157 MHz faint drift bands are observed in the trailing outer region, but no evidence of drifting is observed either in the inner region or in the leading outer region.

Occasionally, either leading or trailing outer region partially or totally disappears, while normal emission is observed from the other regions. Fading of the leading outer region is more commonly observed, e.g. around pulse # 220 to 230, pulse # 295 to 305 and pulse # 1655 to 1675 for 325 MHz as in Fig. 3.1; 1420 to 1440 for 244 MHz as in left panel of Fig. 3.4 and 470 to 490 for 610 MHz as in right panel of Fig. 3.4.

We can characterize the observed drift pattern by estimating P_3^m (the measured time interval between the recurrence of successive drift bands at a given pulse longitude) and P_2^m (the measured longitude separation between two adjacent drift bands). In practice, the P_3^m and P_2^m values need not correspond to the true values (P_3^t and P_2^t). For relation between the measured and true values, refer to Sect. 1.2(c) of Chapter 1.

(a) Determination of P_3^m :

For the determination of P_3^m, we use the fluctuation spectrum analysis technique (Backer, 1970*b*). Fig. 3.5 plots the phase resolved fluctuation spectrum for a sequence of 200 pulses showing regular drifting as in left panel of Fig. 3.1. The strong peak at 18.3 P_1 is identified as P_3^m. The value of P_3^m varies slightly for different pulse sequences with regular drifting, from minimum of about 16.7 P_1 to maximum of 21.4 P_1. For a given pulse sequence, P_3^m appears to be the same for leading outer region, inner saddle region and trailing outer region. This is true even for the pulse sequences showing irregular drifting.

Fig. 3.6 shows the fluctuation spectrum for the sequence of 800 pulses with regular drifting at 610 MHz shown in right panel of Fig. 3.4. We observe a strong peak corresponding to P_3^m at 18.6 P_1, which is the same for both the inner and the outer regions.

Fig. 3.7 shows the fluctuation spectrum at 244 MHz for the sequence

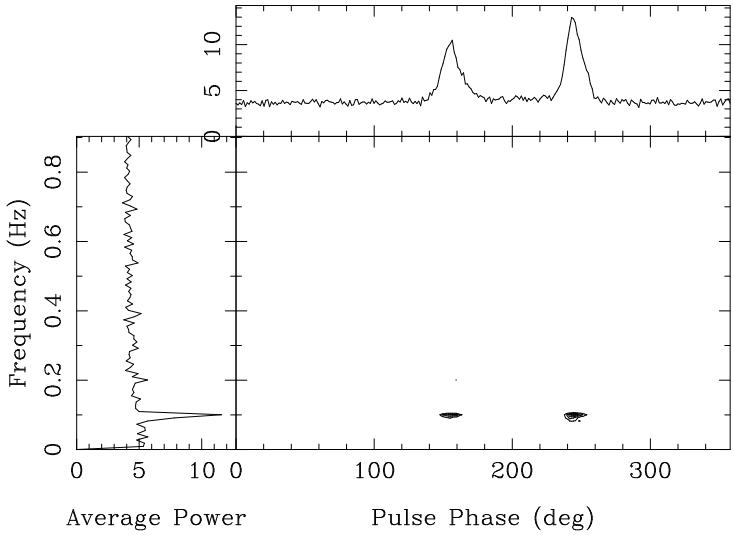

Figure 3.5: The contour plot of the power spectrum of the flux at 325 MHz as a function of pulse phase for the sequence of 200 pulses showing regular drifting as in left panel of Fig. 3.1. The left panel shows the power spectrum integrated over the entire pulse longitude. The upper panel shows the power integrated over fluctuation frequency. The peak fluctuation feature is at 18.3 P_1.

of 500 pulses shown in left panel of Fig. 3.4. We observe a strong peak corresponding to P_3^m at 18.6 P_1, for the leading outer and the trailing outer regions. Even after integrating the data up to 8 ms, the fluctuation spectrum analysis does not show any periodicity present in the inner region.

Table 3.1 lists the P_3^m values, at the individual frequencies, calculated for the pulse sequences with regular drifting. Within error bars, the value of P_3^m is the same at all the frequencies ($\sim 18P_1$). This supports the general result arrived at, for a larger sample of pulsars by Weltevrede *et al.* (2006) and (2007) at 20 and 92 cm respectively.

(b) Determination of P_2^m :

From the gray scale plot of the single pulses at 325 MHz (e.g. Fig. 3.1), it is evident that the P_2^m values for the outer regions are more than that of the inner region. Also it appears that the drift bands in the trailing outer region are somewhat steeper than the drift bands in the leading outer region. P_2^m value in the inner drift region at 325 MHz is calculated from

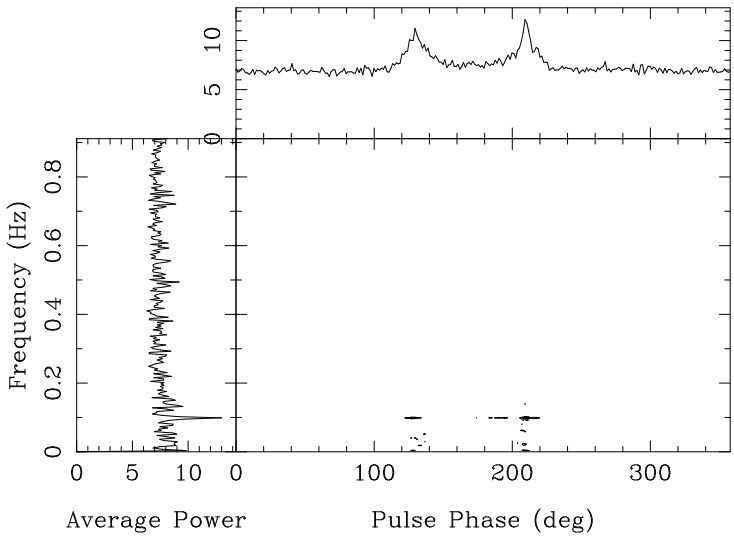

Figure 3.6: Same as Fig. 3.5, but at 610 MHz for the sequence of 500 pulses as in right panel of Fig. 3.4. The peak fluctuation feature is at around 18.6 P_1.

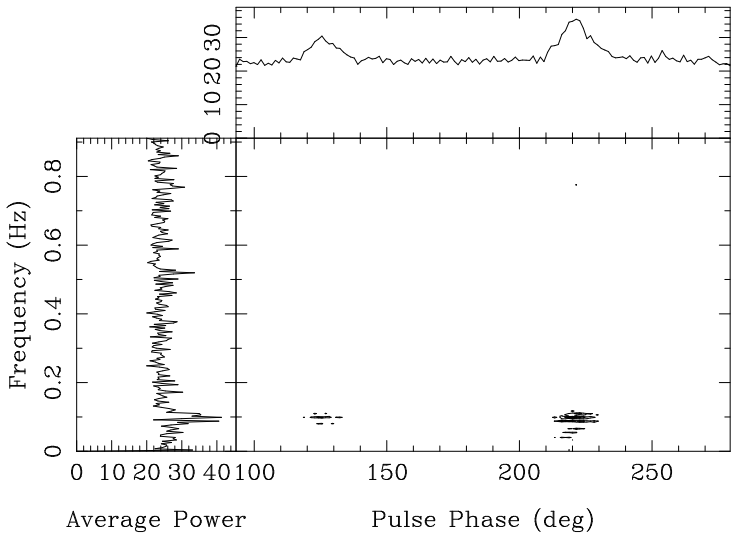

Figure 3.7: Same as Fig.3.5, but at 244 MHz for the sequence of 500 pulses as in left panel of Fig.3.4. The peak fluctuation feature is at 18.6 P_1.

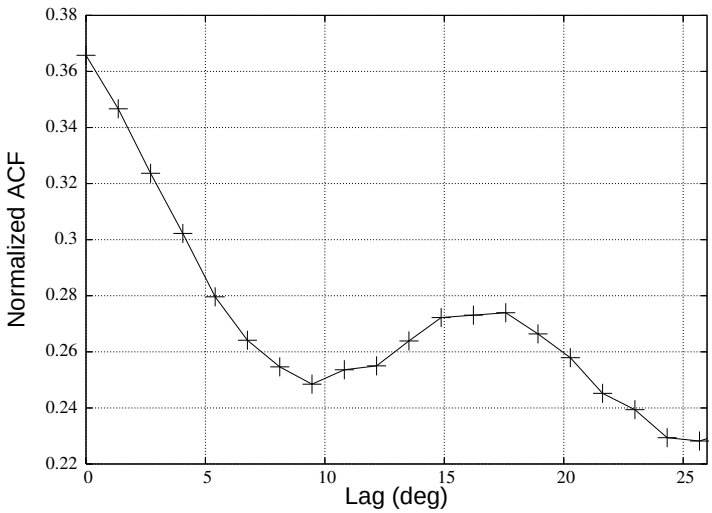

Figure 3.8: Figure for determination of P_2^m of inner region at 325 MHz. Auto correlation results for the inner region. Secondary maxima of the auto correlation function near the lag of 17.5 deg.

the auto correlation function of the single pulses averaged over the number of available pulses (Fig.3.8). The secondary peak of the correlation function will correspond to the correlation between adjacent drift bands and will give us the P_2^m value. From the location of this secondary peak, P_2^m value for the inner region is found to be 17.5±1.3 deg for 200 pulses (pulse # 1600 to 1800) showing regular drifting (right panel of Fig. 3.1). We determine similar P_2^m values, when calculated for another pulse sequence of 200 pulses showing regular drifting as well as for the full data set containing all the 6600 pulses. Similar correlation analysis performed for the inner region at 244 MHz, even with 8 ms integration, does not show any secondary peak. Due to poor signal to noise, the secondary peak position at 610 MHz can not be clearly determined from zero pulse offset correlation. From the one pulse offset correlation (while computing the auto correlation function we correlated each pulse to the adjacent pulse) we determine, P_2^m=16.5±1.3 deg for the inner drift region at 610 MHz.

Since simultaneous multiple drift bands are not visible in the outer regions, P_2^m values can not be estimated using the method described above. Instead we use the following technique to determine the P_2^m value of the outer regions.

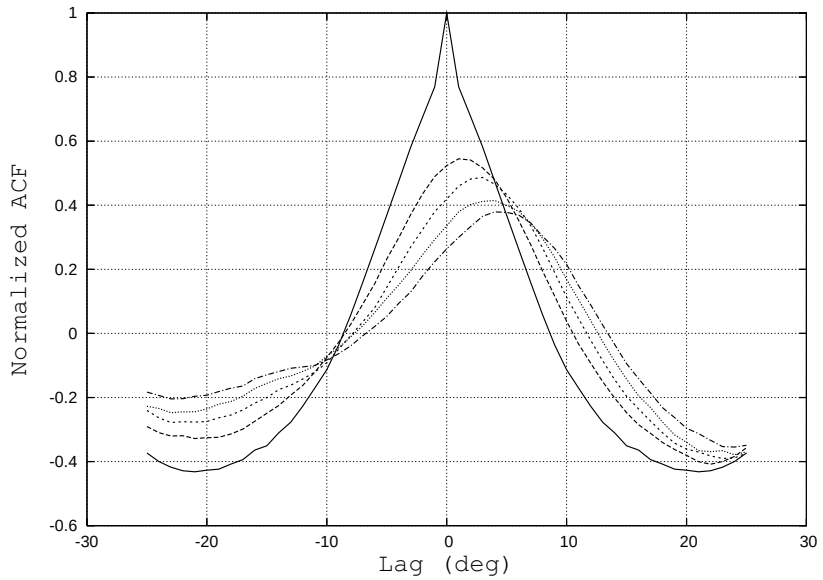

Figure 3.9: Determination of P_2^m of the leading outer region at 325 MHz : step 1. Auto correlation results for the leading outer region at 325 MHz. Curves are for 4 different pulse offsets : solid curve (pulse offset=0), long dash (pulse offset=-1), short dash (pulse offset=-2), dotted (pulse offset=-3), dash-dot (pulse offset=-4).

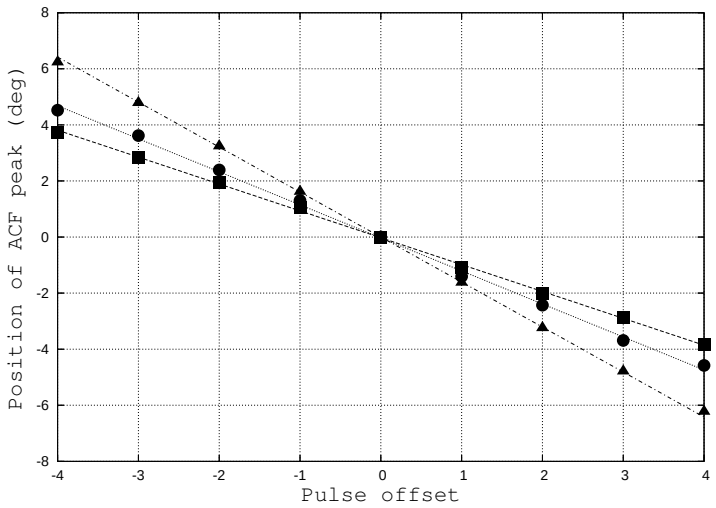

Figure 3.10: Determination of P_2^m of the leading outer region at 325 MHz: step 2. Plot of position of the peak of the correlation functions versus the corresponding pulse offsets. Squares and dashed line : for the inner region and the corresponding fitted straight line with slope -0.96 deg/P_1; circles and dotted line : for the trailing outer region and the corresponding fitted straight line with slope -1.2 deg/P_1; triangle and dash-dot line : for the leading outer region and the corresponding fitted straight line with slope -1.7 deg/P_1

The correlation function, as described above, is calculated for different pulse offsets. The peak of the correlation function with zero pulse offset is at zero lag and with increase in pulse offset the peak shifts to higher lags in pulse longitude (e.g. Fig. 3.9). We plot the position of the peak of the correlation function versus the pulse offset. This plot is a straight line whose slope should reproduce the slope of a drift band (e.g. Fig. 3.10). From the slope of the fitted straight line and the P_3^m values, one can estimate the P_2^m. We refer to this method as pulse offset correlation method (POCM hereafter).

A pulse sequence showing regular drifting (pulse # 1600 to 1800 shown in right panel of Fig. 3.1), is considered for determination of P_2^m values. As a crosscheck, we apply POCM to determine the P_2^m value of the inner region. The P_2^m values for the inner drift region at 325 and 610 MHz determined using POCM are identical to the respective values determined from the secondary peaks of the correlation function. Fig. 3.9 is the plot of the auto correlation functions of the leading outer region calculated for different pulse offsets at 325 MHz. The peak of the correlation function shifts with increasing pulse offsets. The positions of the peaks of the correlation function versus the pulse offset are plotted for the leading outer, inner and trailing outer drift regions in Fig. 3.10. From the slopes of the straight lines fitted to those, we determine P_2^m=21.6 deg for the trailing outer region and P_2^m=31 deg for the leading outer region. Determined P_2^m values for leading outer, inner and trailing outer regions calculated for another sequence of 200 pulses showing regular drifting, are also in the same ballpark. We apply this method for determination P_2^m at 244 and 610 MHz, and obtain, P_2^m=16.9 deg for the leading outer, P_2^m=29.8 deg for the trailing outer regions at 244 MHz and P_2^m=16.5 deg for the inner region at 610 MHz. But surprisingly, when calculated for different pulse offsets for the outer regions at 610 MHz, very less shift (for trailing outer region) or almost no shift (for leading outer region) of the peak of the correlation function is observed which may imply rather flatter drift bands in the outer region. So we were unable to determine P_2^m values for the outer regions at 610 MHz. The P_2^m values for the leading outer and the trailing outer region at different frequencies are listed in Table 3.1.

The absence of the inner drift region at 244 MHz can be interpreted as, the LOS missing the emission from the inner ring, which is supported by the

results from the simulations (Sect. 3.3(b)). P_2^m in the outer regions are more than that of the inner region, which is also evident from the visual inspection of the drift pattern at 325 MHz. The P_2^m for the leading outer drift region is more than the P_2^m for the trailing outer region, both at 244 and 325 MHz (Table 3.1). This is difficult to explain with a concept of circular outer ring around the magnetic pole with isotropic distribution of sparks. With the simulations (Sect. 3.3(b)), we obtain identical P_2^m values for the leading and trailing outer regions as well as for the inner region. Spark patterns centered around a local pole rather than the magnetic dipole axis may provide a possible explanation.

(c) Determination of the subpulse width ($\Delta\Phi_s$)

To determine the subpulse width ($\Delta\Phi_s$), we compute the auto correlation function, with zero pulse offset, and find the full width at half maximum (FWHM). Values of $\Delta\Phi_s$, calculated for a pulse sequence with 200 pulses showing regular drifting at 325 MHz, are equal to 12.3 deg, 6.3 deg and 10.8 deg for the leading outer, inner and trailing outer regions respectively. $\Delta\Phi_s$ values calculated for another pulse sequence with 200 pulses showing regular drifting, as well as for the full data set containing 6600 pulses at 325 MHz, are identical.

We calculate the $\Delta\Phi_s$ values for the inner and the outer regions at 610 MHz and for the outer regions at 244 MHz. Table 3.1 lists the values of $\Delta\Phi_s$ for all the three drift regions determined from our observations at different frequencies. For both 325 and 610 MHz, $\Delta\Phi_s$ values in the inner region are less than that of the outer regions. $\Delta\Phi_s$ values in leading outer region are more than that of trailing outer region at 325 and 610 MHz. However, at 244 MHz, $\Delta\Phi_s$ values for the leading outer and trailing outer regions are comparable and more than the corresponding values at 325 MHz. Evolution of $\Delta\Phi_s$ values with pulse longitude follows the trend of evolution of P_2^m. Though within error bars, $\Delta\Phi_s$ value, for the inner drift region at 610 MHz is less than the corresponding value at 325 MHz, which is expected by the radius to frequency mapping. Hence, evolution of $\Delta\Phi_s$ and P_2^m values with frequency and longitude mostly follow similar trend.

Table 3.1: Frequency dependence of $\Delta\Phi$, P_3^m, P_2^m and $\Delta\Phi_s$

Frequency (MHz)	$\Delta\Phi$ (deg) observation	simulation[a]	simulation[b]	P_3^m	$(P_2^m)^c$ (deg) inner outer	trailing outer	leading	$(\Delta\Phi_s)^c$ (deg) inner	trailing outer	leading outer
157	105±0.3	104	104	$18.6\pm1.6P_1$	–	–	–	–	–	–
244	96±0.3	93	94	$18.6\pm1.6P_1$	–	16.9	29.8	–	13.5	13.3
325	86.6±0.3	88	88	$18.3\pm1.4P_1$	17.6	21.5	31	6.3	10.8	12.3
610	75.7±0.3	74.6	75	$18.6\pm1.5P_1$	16.5	–	–	4.3	10.8	14.1
1060	63±0.3	64	65	–	–	–	–	–	–	–

a : simulation is done with **G-1** (α =11 deg and $\beta = -5.4$ deg)
b : simulation is done with **G-2** (α =175.4 deg and $\beta = -6.9$ deg)
c : error associated in determination of $\Delta\Phi_s$ is ±1.3 deg

(d) Frequent change of drift rates :

Though the regular drift patterns observed in Fig. 3.1 are quite common for this pulsar, we observe frequent changes of the drift rates. Some extreme examples of changing drift rates such as transitions from negative to phase stationary or phase stationary to negative drifting are also observed. Because of the observability of simultaneous multiple drift regions with good signal to noise, changing drift rates are more prominently seen at 325 MHz. The apparent phase stationary intensity modulations (phase stationary drift) are quite frequently observed for this pulsar. Due to the absence of drifting in the inner region at 244 MHz and weaker drift bands at 610 MHz, such regions are harder to identify at these frequencies. We investigate changes in drift rates for about 10,000 pulses from two different epochs of observations at 325 MHz. In addition to frequent occurrences of small changes in the drift rate, we could find, seven transitions from the negative to phase stationary drift rates, five transitions from phase stationary to negative drift rates, and two possible signatures of curved drift bands. We also observe one pulse sequence showing phase stationary drifting interleaved between nulling regions.

Fig. 3.11 and 3.12 illustrate some extreme examples of changing drift rates, such as transitions from negative to stationary and stationary to negative drifting. Left panel of Fig. 3.11 shows the single pulse gray scale plot for pulse # 2800 to 3200. Almost phase stationary drift is observed around pulse # 2870 to 2920 after which the regular negative drifting starts. Irregular drifting is observed again around pulse # 3107. Right panel of Fig. 3.11 presents the single pulse gray scale plot for pulse # 3600 to 4000. Stationary drift bands are observed from pulse # 3665 to 3698 after which regular negative drifting starts from pulse # 3702. The apparent drift rate again slows down around pulse # 3900, phase stationary drifting is observed in following few pulses and then the pulsar starts nulling around 3913. Left panel of Fig. 3.12 presents the single pulse gray scale plot for pulse # 4500 to 4900. Transition from negative to phase stationary drift rate is observed around pulse # 4545. Stationary drifting is observed from pulse # 4545 to 4595, after which the pulsar starts nulling and becomes active again at pulse # 4603. Right panel of Fig. 3.12 presents the single pulse gray scale plot for pulse # 5600 to 6000. Indication of curved drift bands is seen around pulse # 5660 to 5720. For the sequences showing transitions from negative to phase

stationary drift, nulling starts immediately after the phase stationary drifting. Similarly for the sequences showing transitions of phase stationary to negative drift, the phase stationary drifting follows just after nulling. Almost no situation is seen (apart from some indication in curved drift bands) where the drift direction is positive. Possible negative-phase stationary-negative or negative-phase stationary-positive transitions are generally interrupted by nulls.

To summarize, frequent changes of drift rates − including transitions from negative to phase stationary and phase stationary to negative drift rates − are observed for PSR B0818−41. We observe transitions from negative to phase stationary drift or phase stationary to the negative drift in different pulse sequences at 325 MHz. Such transitions of negative to phase stationary drift are always followed by nulling. After nulls the drifting is phase stationary (or irregular) for few pulse and then the transition from phase stationary to negative drift is observed.

Interpretations with aliasing: Observed phase stationary drifting and the transitions from negative to phase stationary drift rates can not be explained without aliasing. According to Ruderman (1976), for the case of unaliased drifting one should observe negative drifting for inner LOS geometry and positive drifting for outer LOS geometry. Although, for **G-1** the observed negative drift, can be explained either by unaliased drifting or by aliased drifting with even alias order, observed occasional changes of drift rates can be easily understood with aliased drifting. Observed negative drift is explained if, $0 < P_3^t < P_1$, and the transitions from negative to phase stationary drift rates can be explained by slight decrease of the drift rate, so that P_3^t is equal to P_1. The intrinsic drift rate for the unaliased case is positive for **G-2**. Thus to reproduce the observed negative drifting for **G-2**, we need to consider aliased drifting so that $P_1 < P_3^t < 2P_1$ and the apparent drift is of opposite sign than that of the true drift rate i.e. the true positive drift rate will appear as negative drift rate to the observer. Occasionally drift rate slightly increases so that P_3^t is equal to P_1, and we observe phase stationary drift bands. Hence for **G-1**, P_3^t is slightly less than P_1 will give rise to aliased negative drifting and transition from the negative to the phase stationary drifting means slowing down of the carousel so that $P_3^t = P_1$. For

G-2, P_3^t is slightly more than P_1 will give rise to aliased negative drifting and transition from the negative to the phase stationary drifting means speeding up of the carousel. Similarly the observed phase stationary to negative drift rate transitions can be interpreted as speeding up of carousel for **G-1** and slowing down of the carousel for **G-2**.

Frequent occurrence of nulling either before or after phase stationary drifting indicates that somehow nulling is associated with the condition $P_3^t = P_1$. After transitions of apparent drift rate from negative-phase stationary direction, we generally observe nulling, implying that, pulsar stops emitting after carousel slows down for **G-1** and after the carousel speeds up for **G-2** to satisfy $P_3^t = P_1$. Quite often, recovery of pulsar emission after null, starts from phase stationary drifting ($P_3^t = P_1$) and then the regular negative drifting follows. Association of phase stationary drifting and nulling indicates that the mechanism responsible for pulsar drifting is closely associated with the pulsar emission mechanism.

Sign reversals of drifting and curved drift bands are observed for PSR B0826−34 (Biggs *et al.*, 1985), unlike PSR B0818−41 where we do not observe positive drifting (except for some indications of curved drift bands interrupted by nulling, e.g. Fig. 3.12). Similar to our interpretations for explaining the observed transitions of negative to phase stationary drift rates in B0818−41, Gupta *et al.* (2004) proposed that the observed drift rate for PSR B0826−34 is aliased version of the true drift rate which is such that a subpulse drifts to the location of the adjacent subpulse (or a multiple thereof) in about one pulse period. They showed that small variations in the mean drift rate are enough to explain the apparent reversal of drift directions seen in the data.

Gupta *et al.* (2004) proposed that the small variations in the mean drift rate caused by very small heating and cooling effects of the polar cap can explain the apparent reversals of drift directions observed for PSR B0826−34. Similarly, the slight change of the drift rate required for transition form negative to stationary directions of apparent drifting for PSR B0818−41 can be explained by very small heating and cooling effects in the surface temperature of the polar cap (Gil *et al.*, 2003). We note that the transitions of drift rates are rather abrupt for quite a few sequences. Which can be interpreted by means of quantum jump or quite fast change in polar cap

temperature, causing P_3^t slightly less than P_1 (giving rise to observed negative drift) to $P_3^t = P_1$ (giving rise to phase stationary drifting) for **G-1**, and vice verse.

3.3 Interpretation & Modeling

We interpret our observations and analysis results within the frame work of Ruderman & Sutherland (1975) model and improved versions of the same (e.g. Gil *et al.* (2003) and the references therein), which is detailed in Sect. 1.4 of Chapter 1. According to these, subpulse drifting is produced from a system of sub-beams (subpulse associated plasma columns). Sparks (sparking discharges within the vacuum gap), rotating around the magnetic axis under the action of an E x B drift, gives rise to a circulating pattern of sub-beams, and the time for one full circulation is referred to as the carousel rotation period, which we designate as P_4. As pulsar radiation beams are widely believed to be arranged in concentric cones, it it natural to expect the circulating sparks to be distributed in annular rings on the polar cap (e.g. Gil & Sendyk (2000)), each ring giving rise to one cone in the nested cones of emission. To confirm and support our interpretations, we have carried out simulations of the expected radiation pattern for this pulsar. These are described at the end of this section, but their results are alluded to at the different stages of our interpretation, which are as follows.

(1) The possibility that the observed drift pattern could be produced from sparks circulating in one ring can be ruled out on the basis of the large difference in P_2^m values and the pattern of intensity distribution between the drift regions. A simple interpretation of the observed drift pattern is that the inner saddle region corresponds to an inner conal ring that is somewhat tangentially grazed by the observer's line of sight (LOS), while the outer drift regions are produced by the intersection of the LOS with an outer conal ring. The simulation results show that the inner drift region can be produced by the intersection of the LOS with three/four neighboring sparks of the inner ring, whereas the outer drift region can be created by the intersection of the LOS with one spark of the outer ring, on each side of the inner ring.

(2) The closely spaced inner and outer drift regions can be explained with a rapid transition of the LOS from one ring to the other. For the inner

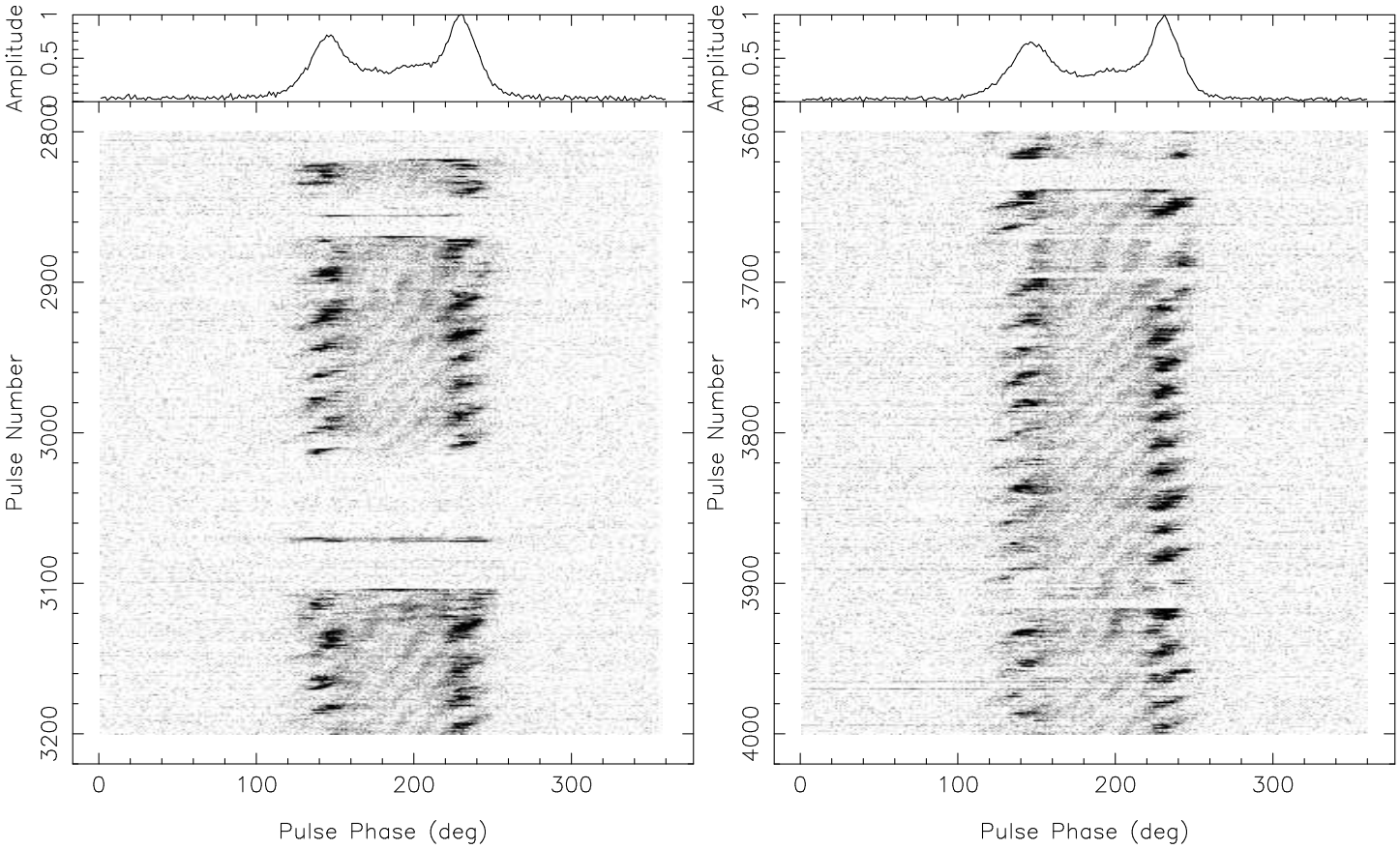

Figure 3.11: Same as Fig. 3.1, but from observations on 21 December 2005 at 325 MHz. Left panel: pulse # 2800 to 3200; almost phase stationary drift is observed around pulse # 2870 to 2920, then the regular negative drifting starts, frequent nulling is observed. Right panel: pulse # 3600 to 4000; transition from negative to phase stationary drift rate around pulse # 3665, almost phase stationary drifting from pulse # 3665 to 3698, regular drift starts from pulse # 3702. Drift rate again slows down around pulse # 3900, phase stationary drifting is observed in following few pulses and then the pulsar starts nulling around 3900. Pulsar becomes active at around pulse # 3920.

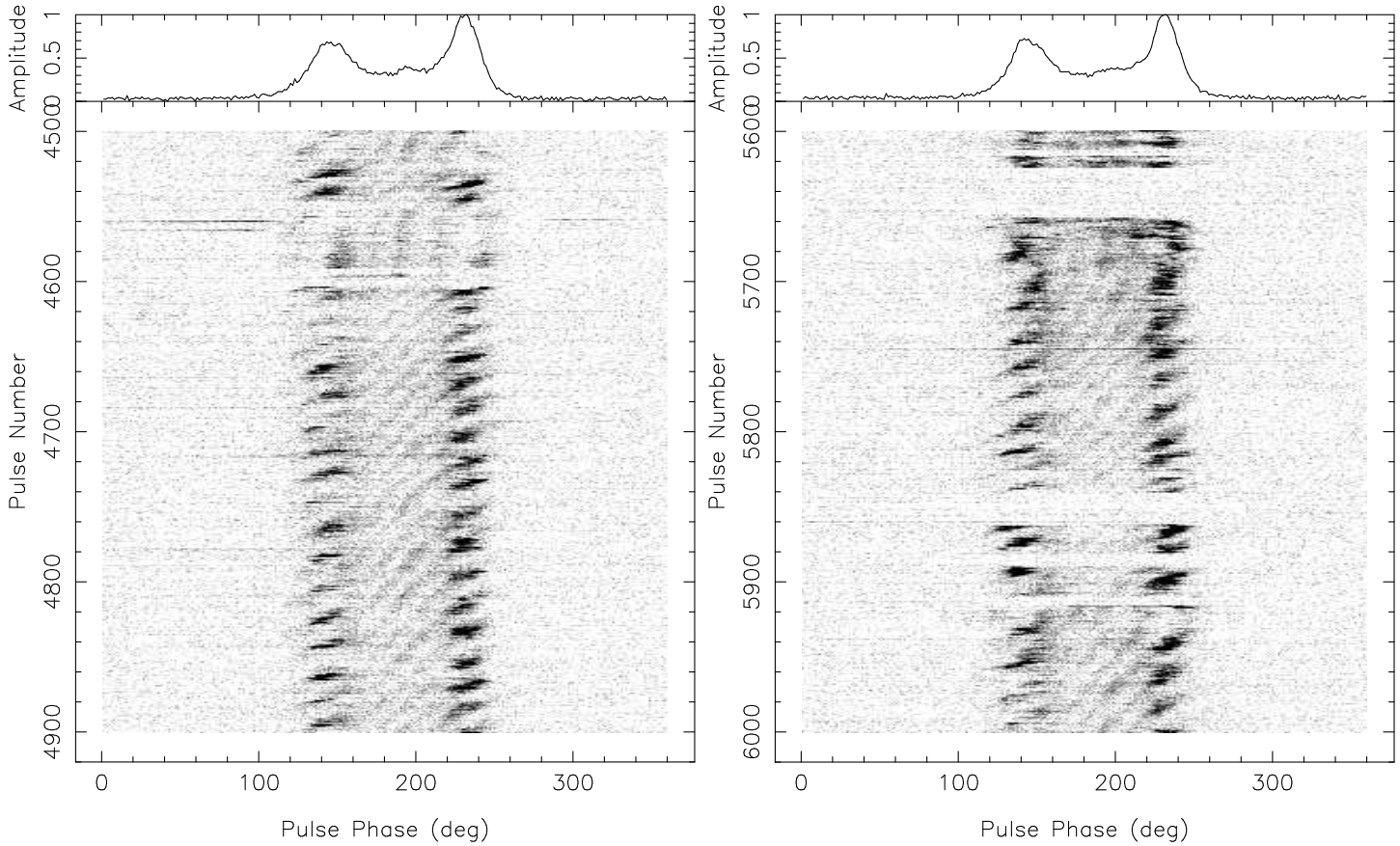

Figure 3.12: Same as Fig. 3.1, but from observations on 21 December 2005 at 325 MHz. Left panel: pulse # 4500 to 4900; transition from negative to phase stationary drift rate is observed around pulse # 4545. Stationary drifting is observed from pulse # 4545 to 4595, after which the pulsar starts nulling and becomes active again at pulse # 4603. Right panel: pulse # 5600 to 6000; there is some indication of curved drift band around pulse # 5660 to 5720.

LOS geometry (negative β), the LOS traverses the region between the inner and the outer region almost perpendicularly and as a consequence one can achieve quite closely spaced drift regions with reasonably well separated rings of emission. This is borne out by the simulation results (see Fig. 3.16).

(3) The observed PLR implies that the apparent angular drift rate is the same for both the inner and the outer rings. This can be achieved with two possibilities: different parts of polar cap plasma rotating at the same rate (i.e. the rotation is quasi-rigid), or different parts of the polar cap plasma circulating with different speeds which are fine tuned to maintain the apparent PLR. We do not see a natural way to achieve the later and hence, we suggest that the carousel rotation period, P_4, and the number of sparks, N_{sp}, are the same for both the inner and the outer ring. The simulations with two rings of emission with same P_4 and N_{sp}, with 180 deg out of phase emission between the rings, successfully reproduces the PLR.

(4) What are the likely values for N_{sp}, P_3^t (and hence P_4), for this pulsar? To start with, we note that for a LOS grazing the inner ring, the P_2^m is expected to be close to P_2^t. So, $N_{sp} = 360/P_2^t \approx 19 - 22$. Now, for P_3^t, there are two possibilities : (i) The P_3^m represents an unaliased true drift rate; i.e., in successive pulses, the observer sees the same spark, shifted to a nearby longitude. In this case, $P_3^t = P_3^m = 18.3\,P_1$ and $P_4 = N_{sp} \times P_3^m \approx 370\,P_1$. (ii) The P_3^m is an aliased version of P_3^t; i.e., in successive pulses, a given spark drifts by an amount very close to the separation between adjacent sparks (or a multiple thereof, depending on the order of the aliasing). As shown by Gupta *et al.* (2004), under the effect of aliasing, P_3^t and P_3^m are related as,

$$\frac{1}{P_3^t} = k\frac{1}{P_1} + (-1)^l \frac{1}{P_3^m} \quad , \tag{3.1}$$

where $k = INT[(n+1)/2]$ and $l = mod(n, 2)$ depend on the alias order, n. Note that we observe a negative drift rate for this pulsar. For an inner LOS geometry, this can happen for the case of an unaliased drift (as in case (i) above) – the ExB drift of the spark plasma is slower than the rotation of the star (Ruderman (1976)). For an aliased drift, this can happen when $n = 2, 4, 6 \ldots$ (i.e $k = 1, 2, 3 \ldots; l = 0$). Taking the case for the lowest possible alias order ($n = 2, k = 1, l = 0$), and using $P_3^m = 18.3\,P_1$, we obtain $P_3^t = 18.3/19.3\,P_1 = 0.95\,P_1$ and $P_4 = N_{sp}\,P_3^t = (18 - 21)\,P_1 \approx P_3^m$. This

leads to the interesting result that the carousel rotation rate is the same as the measured P_3^m. For this scenario, the entire spark pattern rotates with an angular velocity of 360 deg/P_4 ≈20 deg/P_1.

(a) Understanding the emission geometry of PSR B0818−41

The possible choices of the emission geometries are constrained by the following observed characteristics:
(i) Observed profile width at individual frequencies (Table 3.1) as well as the profile evolution with frequency(shown in Fig. 2.1).
(ii) Overall pattern of drifting with simultaneous multiple drift regions (e.g. Fig. 3.1), P_2^m, P_3^m values and the relative intensities of the drift regions.
(iii) Observed PA curves.

RVM fit to PA sweep :
RVM (Radhakrishnan & Cooke, 1969) is fitted to the PA curve of PSR B0818−41 at 325 MHz. While fitting we used symmetry about magnetic axis, i.e. $0 < \alpha < 180$ deg (e.g Everett & Weisberg (2001) and Johnston & Weisberg (2006)), rather than symmetry about the magnetic equator, i.e. $0 < \alpha < 90$ deg (e.g. Lyne & Manchester (1988), Narayan & Vivekanand (1982), Rankin (1990), Rankin (1993) etc). Our attempt to fit RVM to the PA curve at 325 MHz gives best fit values of $\alpha \sim 175.4$ deg and $\beta \sim -6.9$ deg, which is an outer LOS geometry. This means that the spin axis is anti aligned to the magnetic axis. The angle between the spin axis and the magnetic axis is, 180−175.4∼5.6 deg, and the LOS makes a circle of radius $5.6 + \beta$=12 deg around the spin axis. Fig. 3.13 presents a plot of the observed PA sweep at 325 and 610 MHz and the RVM curves for two possible geometries : $\alpha \sim 11$ deg, $\beta \sim -5.4$ deg (which incidentally reproduces the middle part of PA sweep at 610 MHz) and $\alpha \sim 175.4$ deg, $\beta \sim -6.9$ deg (the geometry derived from the RVM fit to 325 MHz PA sweep).

The observed drift pattern for PSR B0818−41 can be interpreted as being created by the intersection of our LOS with two conal rings on the polar cap of a fairly aligned rotator (α ∼11 deg), with an inner LOS geometry ($\beta \sim -5.4$ deg). This geometry was developed to give best fit to profile shape and drift pattern at 325 MHz (at that time polarization information

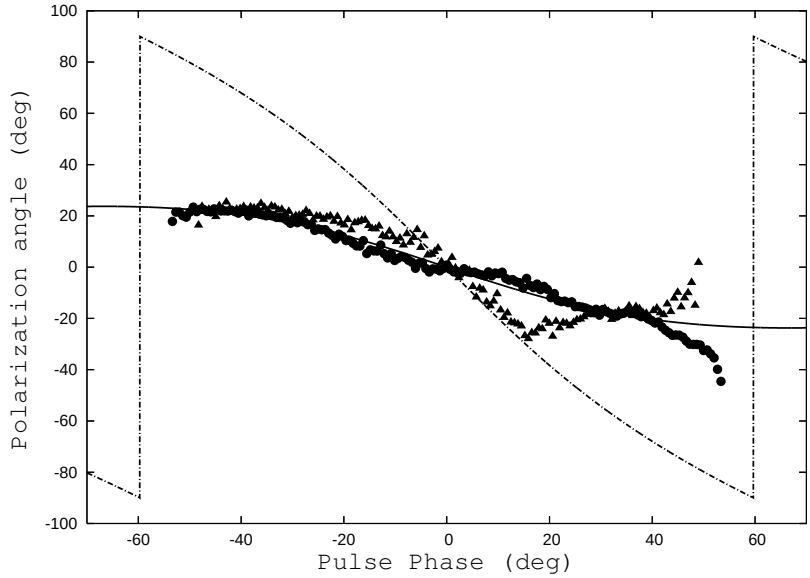

Figure 3.13: Observed PA curves at 325 (solid circles), 610 MHz (solid triangles) and the RVM curve for $\alpha \sim 175.4$ deg and $\beta \sim -6.9$ deg (dotted line) and for $\alpha \sim 11$ deg, $\beta \sim -5.4$ deg (dashed line).

was not available to us). But later we found that the PA traverse at 325 MHz can not be explained by this geometry, but surprisingly the middle part of the PA swing at 610 MHz is satisfied by this geometry (Fig. 3.13). However, best RVM fit to the PA curve at 325 MHz as well as left half of PA sweep at 610 MHz is obtained with $\alpha \sim$175.4 deg and $\beta \sim -6.9$ deg. Therefore, we have two competing geometries,

G-1 (α =11 deg and $\beta = -5.4$ deg) : geometry that gives best fit to profile shape and drift pattern at 325 MHz. This geometry incidentally produces reasonable fit to the middle part of PA sweep at 610 MHz.

G-2 (α =175.4 deg and $\beta = -6.9$ deg) : geometry obtained by RVM fitting to the PA curve at 325 MHz.

In order to investigate how well these two geometries satisfy the above constraints we have exhaustively used the simulation techniques as described below.

(b) Simulation

The simulations with two rings of emission having same carousel rotation period (P_4) and the number of sparks (N_{sp}), with 180 deg out of phase emission between the rings, successfully reproduces the PLR in the observed drift pattern. Considering the measured P_2^m =17.5 deg for the inner region and assuming $P_2^m \sim P_2^t$ (true longitude separation between adjacent drift bands) for nearly aligned rotator, we have, $N_{sp} \sim 19 - 22$. We simulate the radiation from PSR B0818−41 using the method described in Gil & Sendyk (2000) for both **G-1** and **G-2**. While doing the simulation we use 20 equispaced sparks in each of the two concentric rings, rotating with a drift rate of 19.05 deg/P_1 (as $P_3^m \sim 18P_1$, Sect. 3.2(a)). The empirical emission altitude formula by Kijak & Gil (2003) is used for determining the LOS cut through the beam at different frequencies.

The gray scale plots of the simulated single pulses for **G-1** and **G-2** (Fig. 3.14 and Fig. 3.16) reproduces the overall pattern of drifting. Radii of the inner and outer rings in Fig. 3.14 (simulated with **G-1**) are 0.6 r_p and 0.8 r_p. However, for Fig. 3.16 (simulated with **G-2**) radii of the inner and outer rings are 0.7 r_p and 0.9 r_p respectively. Ratio of spark intensities of the inner and outer rings, required to reproduce the relative intensities of the inner saddle region and the trailing peak, is ~ 3. This is identical to the relative intensities of the inner saddle region and the trailing peak of the observed pulse profile at 325 MHz (Fig. 2.1). From the simulated single pulses with **G-1**, we calculate $P_2^m \sim 16$ deg for both inner and outer regions, which is close to the observed P_2^m in the inner region ($P_2^m \sim 17.5$ deg in Sect. 3.2(b)) whereas for **G-2**, $P_2^m \sim 14$ deg for the inner and outer regions, which is a bit lower than the observed P_2^m for the inner region. Fluctuation spectrum of the single pulses generated from both the geometries exhibits a strong feature at $\sim 18P_1$, which is identical to the determined P_3^m value. Simulated single pulse drift pattern with **G-1** in Fig. 3.14 have single drift bands in the outer drift region on both sides of the inner region, which matches with observation. But for the simulated single pulse drift pattern with **G-2**, at times, two drift bands in the outer region on both sides of the inner region are observed. The simulated average profiles for both the geometries and the observed average profiles at 325 MHz are over plotted in Fig. 3.15 and 3.17. In the simulated average profiles the inner saddle region get more filled at higher frequencies,

which reproduces the observations (Fig. 2.1). Though, general double peaked structure of the profiles, profile width at individual frequencies as well as the profile evolution with frequency are well reproduced by the simulations with both the geometries (Table 3.1), features like differences in amplitude of the leading and trailing peaks are not achieved with simulations. We note that the presence of closely spaced drift regions with widely different P_2^m values, and our inference that the LOS intersects only one spark from the outer ring, all favor an inner LOS geometry (**G-1**) over an outer LOS geometry (**G-2**).

As can be seen, most of the observed features of the average profile and the drift bands are well reproduced, including the significant change of P_2^m between the inner and the outer drift regions, which is clearly a geometrical effect. Interestingly, a 180 deg phase shift between the spark locations on the inner and outer rings is needed to match the PLR of the observed drift pattern (see Fig. 3.1).

Finally, to investigate the relationship between P_4 and P_3^m, simulations have been tried using sparks of unequal intensities to bring out the presence of P_4 explicitly in the fluctuation spectrum. Different values of P_4 are achieved by using slightly different values of the drift rate. In the general case, two different features can be seen in the spectrum, corresponding to P_3^m (caused by periodic drifting features) and P_4 (caused by the amplitude modulation due to the unequal sparks). For the appropriate choice of drift rate (equal to 20 deg/P_1), these two features merge/overlap in the spectrum to produce the measured P_3^m signal. For the real data, we believe that if the P_4 is present in the spectrum, it is co-located with the aliased P_3 signal, at P_3^m.

To summarize, we have simulated the radiation pattern of the pulsar for both **G-1** and **G-2**. Both the geometry satisfy constraints (i), (ii) and (iii) discussed in Sect. 3.3(a). Though the overall PA curve at 325 MHz, and left half of the PA curve at 610 MHz is fitted with **G-2**, only the middle part of the PA curve at 610 MHz is fitted with **G-1**. On the other hand, **G-1** appears to give a better match to the observed P_2^m values in the inner region. We will refer to the simulation results at different stages of this chapter.

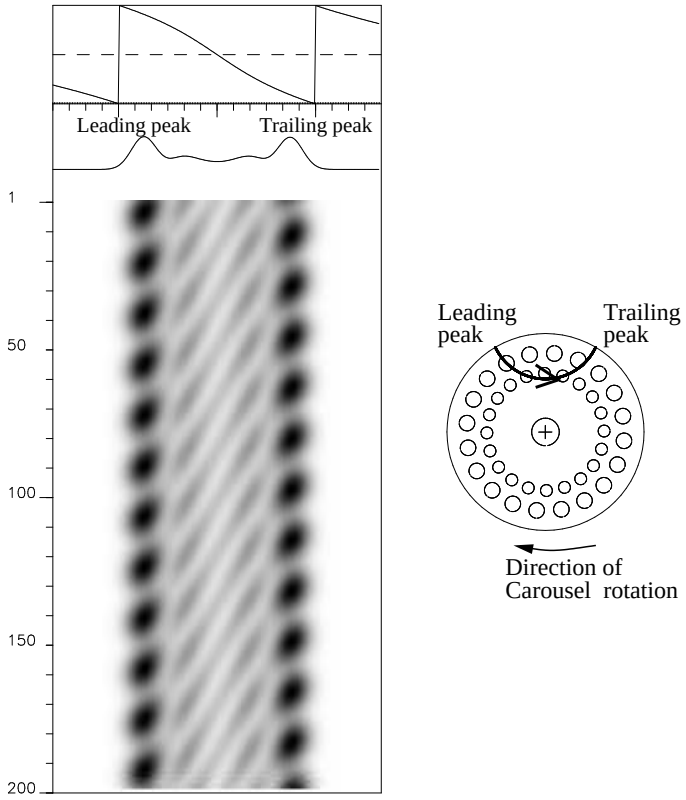

Figure 3.14: Simulation of the subpulse drift pattern with simple dipolar geometry for the case: **G-1** ($\alpha = 11$ deg, $\beta = -5.4$ deg); drift rate $D = 19.05$ deg/P_1, $Nsp = 20$. Corresponding $P_5 = 8.7\,P_1$.

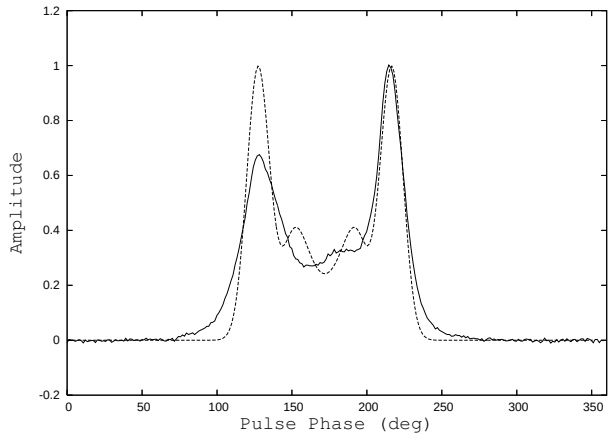

Figure 3.15: Observed and simulated pulse profile at 325 MHz with simple dipolar geometry for the case: **G-1** ($\alpha = 11$ deg, $\beta = -5.4$ deg); drift rate$D = 19.05$ deg/P_1.

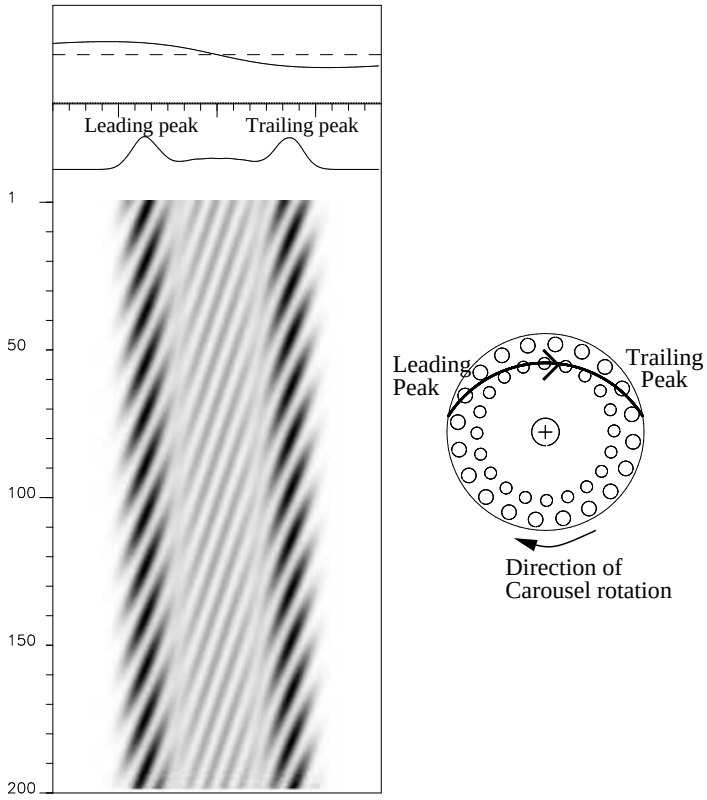

Figure 3.16: Simulation of the subpulse drift pattern with simple dipolar geometry for the case: **G-2** (α = 175.4 deg, β = −6.9 deg); drift rate $D = 19.05\text{deg}/P_1$, $Nsp = 20$, Corresponding $P_5 = 8.7\,P_1$.

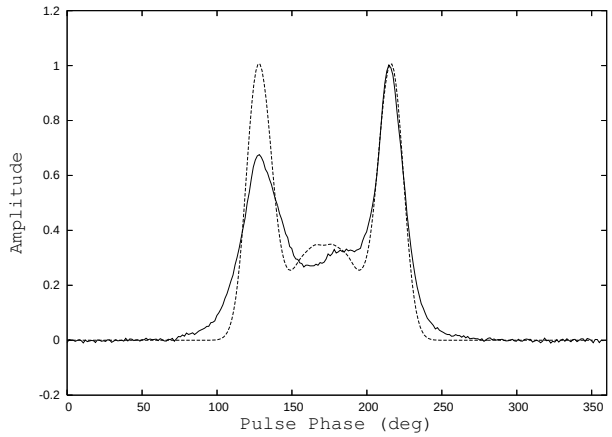

Figure 3.17: Observed and simulated pulse profile at 325 MHz with simple dipolar geometry for the case: **G-2** (α = 175.4 deg, β = −6.9 deg); drift rate$D = 19.05$ deg$/P_1$.

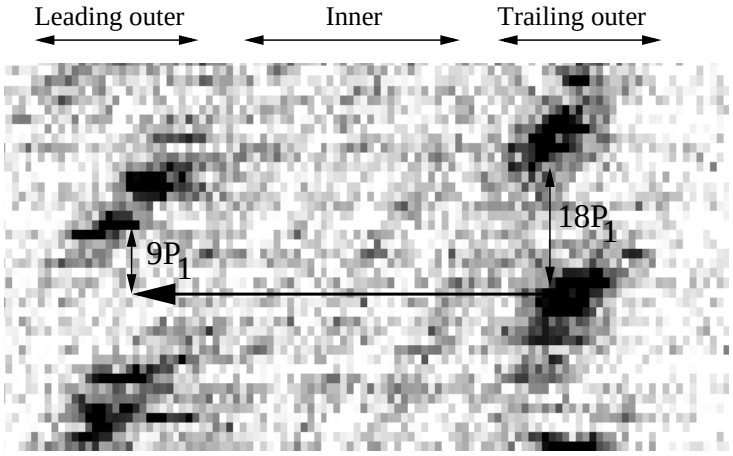

Figure 3.18: Gray scale plot of 27 single pulses from PSR B0818−41 at 325 MHz. The horizontal arrow is drawn to illustrate that the peak emission from trailing outer and leading outer region are not in phase (offset by ~ 9 P_1).

3.4 Phase relation between multiple drift regions

Simultaneous multiple drift regions maintain unique phase relationship for PSR B0818−41 : (1) peaks of the emission from outer leading and trailing regions are at constant phase offset (observed at 244, 325 and 610 MHz) and (2) emission from the inner and outer regions are always locked in phase (observed at 325 and 610 MHz). These phase relationships are clearly observed in Fig. 3.18, a zoomed plot of 27 single pulses at 325 MHz.

(a) Investigation of the constant phase offset between the peaks of emission from leading and trailing outer regions

As seen in the single pulse gray scale plots (e.g. Fig. 3.18), the peaks of emission from the leading and trailing outer regions as a function of pulse number are not in phase and are offset by a constant pulse period, which we denote as, $P_5 \sim 9P_1$ from eye estimation. We use the following procedure to study this phase relation more quantitatively. For each pulse we compute the total energy under the trailing and the leading peaks (up to a point where the energy goes down to 50% of the peak value on both sides of the peak). Fig.

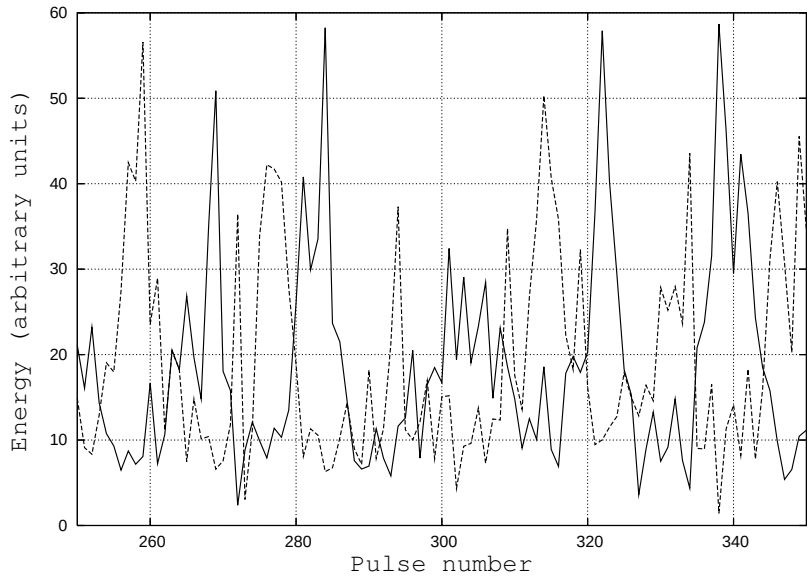

Figure 3.19: Pulse energy under the trailing outer region (solid line) and the leading outer region (dashed line) for pulse # 250−350 at 325 MHz.

3.19 shows the variation of the energy of the leading and the trailing peaks with pulse number, for a sequence of 100 pulses showing regular drifting. Peaks of the emission for leading and trailing outer regions are observed to be offset by $P_5 \sim 9P_1$. To get a more accurate estimation of P_5, we cross correlate the energy under the trailing and leading peaks for different pulse lags. A similar exercise is performed at 244 and 610 MHz. Fig. 3.20 presents the plot of the correlation between the energy of trailing and leading outer regions as a function of pulse lag, for 244, 325 and 610 MHz. Initially, the emissions from leading and trailing peaks are anti correlated; the correlation builds up with increasing pulse offsets and reaches to maximum value near $\sim 9P_1$, after which the secondary peaks are observed at $18P_1$ interval. To avoid contributions from frequent nulls and irregular drifting, this exercise was performed on sequences of pulses showing regular drifting (e.g. Fig. 3.1). We repeat this exercise for 13 such pulse sequences, each containing about 200 pulses showing regular drifting. P_5 varies slightly, from minimum of $6P_1$ to maximum of $10P_1$, with an average of $9.2P_1$. No apparent frequency dependence of P_5 is observed.

Solution of the aliasing problem : Drifting subpulses are an excellent example of under sampling. The aliasing problem is solved for only a few

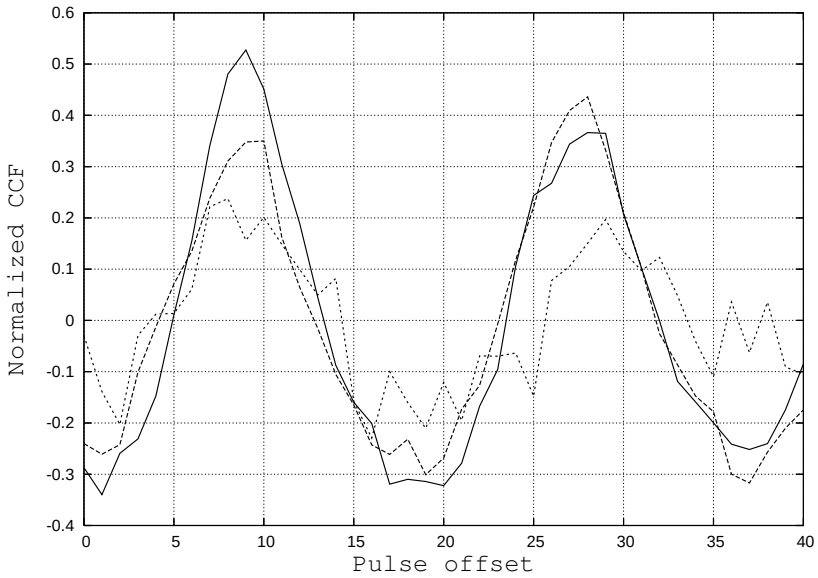

Figure 3.20: Cross correlation of pulse energy in the leading and trailing outer regions as a function of pulse offset, calculated for pulse sequences showing regular drifting. Solid line (325 MHz), long-dash (610 MHz), short-dash (244 MHz).

drifting pulsars (e.g. PSR B0809+74, B0943+10 etc) using extra information from specific features present in the data. In the following we describe a scheme for solving the aliasing problem using knowledge of P_5.

Fig. 3.21 illustrates the configuration of sparks in two concentric polar rings and the possible LOS cuts, for both **G-1** and **G-2**. Here $\Delta\sigma$ is the profile width measured with respect to magnetic axis and $\Delta s = 360/N_{sp}$, is the angular separation between two consecutive sparks measured around the magnetic axis. Now we consider the ratio,

$$\frac{\Delta\sigma}{\Delta s} = I_1 + f_1 \tag{3.2}$$

where I_1 and f_1 denote the integer and fractional parts of the ratio. This gives the total number of sparks occupying the outer ring between the points of intersection with the leading and trailing peaks of the profile. Here, f_1 is a measure of observed phase offset : $f_1 = 0$ will give drift bands which are in phase, whereas $f_1 = 0.5$ will produce a phase offset of $9P_1$. The above analysis assumes that the spark pattern drifts by a negligible amount in the duration of the LOS traverse from the leading to trailing peak. In reality, the spark pattern will drift by $\Delta\phi\, D/360$ deg during this interval, where D

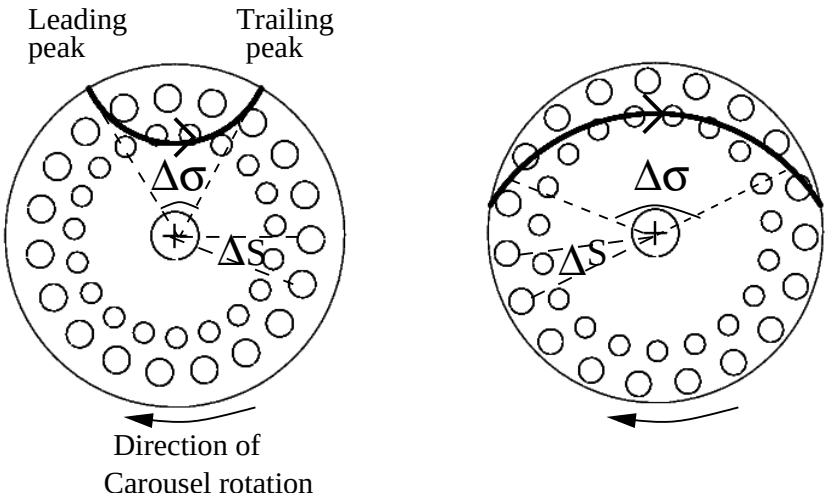

Figure 3.21: Arrangements of sparks in two rings in the polar cap and possible LOS cuts for **G-1** (left panel) and **G-2** (right panel).

is the amount by which the sparks drift in one pulse period ($P_3^m = 360/D$) and $\Delta\phi$ is the separation between two peaks of pulse profile.

$$\frac{\Delta\sigma}{\Delta s} + \frac{\frac{\Delta\phi\, D}{360}}{\Delta s} = I_2 + f_2 \tag{3.3}$$

For a finite f_2, the peak emission from leading and trailing outer regions will be out of phase by a constant pulse offset (P_5), which will be determined by the time taken by the sparks to traverse $(1 - f_2)\Delta s$ deg.

$$P_5 = \frac{(1 - f_2)\Delta s}{D_{ap}} \tag{3.4}$$

where, D_{ap} (apparent drift rate) is the amount by which a spark pattern with drift rate D will appear to move in one pulse period and is given by $D_{ap} = \mathrm{mod}(k\, D - \Delta s)$, $k = INT(n+1)/2$, n being the alias order. With the knowledge of viewing geometry, N_{sp}, alias order n and drift rate D, one can easily calculate the expected P_5 using Eqn. 3.4; which can then be compared with the observed value. Therefore, knowing viewing geometry, N_{sp} and observed value of P_5, it is possible to constrain drift rate D and possible alias order. This technique can solve the aliasing problem and will provide an independent estimation of P_3^t and P_4. The only missing term is an estimate for $\Delta\sigma$. This is obtained from the pulse width $\Delta\phi$, using the known geometry. The general formula that relates the azimuthal angle measured

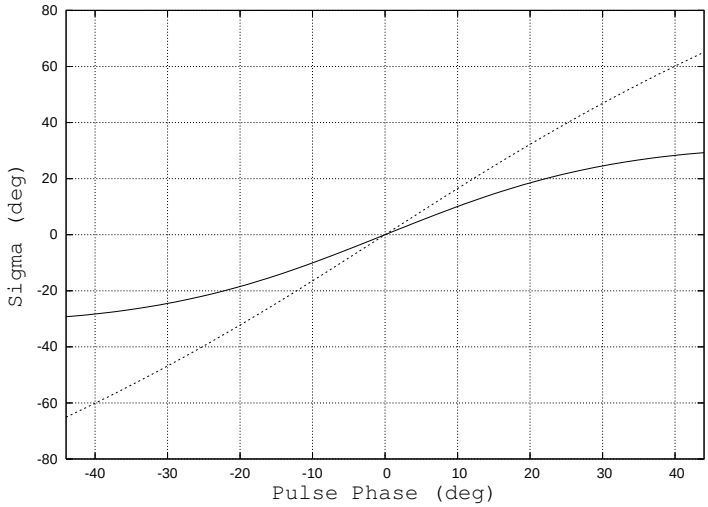

Figure 3.22: Variation of σ with ϕ (see Eqn.3.5 of text) for **G-1** ($\alpha = 11$ deg, $\beta = -5.4$ deg, solid curve) and **G-2** ($\alpha = 175.4$ deg, $\beta = -6.9$ deg, dashed curve).

with respect to the magnetic axis (σ) with the rotational phase (ϕ) is,

$$\sin(\sigma) = \frac{\sin(\alpha + \beta)\ \sin(\phi)}{\sin(\Gamma)} \tag{3.5}$$

where Γ is the angle between the magnetic axis and the LOS at the rotational phase ϕ (Gupta *et al.*, 2004). Fig. 3.22 shows the variation of σ as a function of ϕ around the magnetic meridian (ϕ=0 and σ=0) for **G-1** (solid curve) and **G-2** (dashed curve). For both **G-1** and **G-2**, $\Delta\Phi$ is equal to 88 deg at 325 MHz (Table 3.1). This corresponds to $\Delta\sigma \sim 58$ deg for **G-1** and $\Delta\sigma \sim 130$ deg for the **G-2** (Fig. 3.22). We consider two concentric rings each with 19 sparks. Using Eqn. 3.2 for **G-1**, we have $\Delta\sigma/\Delta s = 3.08$, i.e. $I_1 = 3$ and $f_1 = 0.08$. Fractional part f_1 is very small. Therefore, for negligible drifting, as the LOS passes from the first to the third spark, it traverses from the leading to the trailing peaks. In this case the peak emission from the leading and trailing outer regions will be in phase, which is also reproduced with simulations with **G-1**. Similarly for **G-2**, $\Delta\sigma/\Delta s = 6.86$ i.e. $I_1 = 6$ and $f_1 = 0.86$. Therefore, with negligible drifting, passage of LOS from the first to the sixth pulse and an extra amount, $f_1\Delta s$ deg, will imply the traverse from the leading to the trailing peak which is also reproduced in simulations with **G-2**.

We calculate pulse offset P_5 from Eqn. 3.4 for both the geometries for the cases of unaliased drifting and aliased drifting with different N_{sp} values ranging from 17 to 22. Table 3.2 lists different combinations of D, n, N_{sp} values required to reproduce the observed drift pattern and the corresponding estimations of P_5 for **G-1**. Table 3.3 lists the same for **G-2**. The results presented in Tables 3.2 and 3.3 illustrate that it is not possible to reproduce the observed phase relationship between the leading and the trailing peak with unaliased drifting − it is too slow to move the spark pattern so much that the emission is correlated after $\sim 9P_1$. Hence, the drifting is aliased for PSR B0818−41. For a particular geometry and a choice of N_{sp}, observed P_5 can be reproduced with certain choice of D and n. Knowing D and n, one can calculate the P_3^t using Eqn. 3.1. Since $P_4 = N_{sp}\, P_3^t$; P_4 is automatically constrained for all the cases considered in Table 3.2 and 3.3. Cases for which P_5 is close to the observationally estimated value ($P_5 = 9 \pm 2$) are indicated by bold face in Table 3.2 and 3.3. For **G-1**, $P_5 = 9 \pm 2$ is satisfied for the following choices,
(1) $N_{sp} = 20$, 1st order alias ($n = 2$, $k = 1$), $D = 19.05$ deg/P_1, $P_5 = 8.69P_1$, $P_4 \sim 18P_1 \sim 10$ s
(2) $N_{sp} = 19$, 2nd order alias ($n = 4$, $k = 2$), $D = 38.95$ deg/P_1, $P_5 = 7.40P_1$, $P_4 \sim 9P_1 \sim 5$ s
(3) $N_{sp} = 18$, 2nd order alias ($n = 4$, $k = 2$), $D = 41.05$ deg/P_1, $P_5 = 10.89P_1$, $P_4 \sim 9P_1 \sim 5$ s
For **G-2**, $P_5 = 9 \pm 2$ is satisfied for the following choices,
(1) $N_{sp} = 20$, 1st order alias ($n = 1$, $k = 1$), $D = 19.05$ deg/P_1, $P_5 = 8.74P_1$, $P_4 \sim 18P_1 \sim 10$ s
(2) $N_{sp} = 17$, 2nd order alias ($n = 3$, $k = 2$), $D = 43.40$ deg/P_1, $P_5 = 7.11P_1$, $P_4 \sim 9P_1 \sim 5$ s
According to the above analysis, 1st order aliasing with $D = 19.05$ deg/P_1 and $N_{sp} = 20$ give the best match of P_5 with observations, for both **G-1** and **G-2**, which is rather coincidental to us. Hence, it does not help to distinguish between **G-1** and **G-2**. We note that P_4 determined in this work is identical to the estimation in Sect. 3.3 and supports the interesting result that the carousel rotation rate is the same as the measured P_3^m.

We simulate the radiation for each geometry for different combinations of N_{sp} and D (refer to Sect. 3.3(b)). Next we correlate the emission under

the leading and trailing peaks of the simulated single pulses at different pulse lags (as is done for the real data). P_5 determined from the simulated data is found to be identical to that calculated from Eqn. 3.4 (listed in Tables 3.2 and 3.3). Hence, our methodology for determining P_5 is confirmed by simulations.

To summarize, the observed phase relationship between the peak emission from the leading and trailing outer region is an unique feature of PSR B0818−41 and acts as an additional information other than P_1, P_2, P_3 and P_4. Investigation of this unique phase relationship can solve the aliasing problem for this pulsar. It shows that drifting has to be aliased in PSR B0818−41. We provide a few combinations of feasible values of the N_{sp}, D and n that can produce the observed out of phase relation. The results from the corresponding simulations support our arguments. We propose, $P_4 \sim 18P_1 \sim 10$ s (for $n = 2$ for **G-1** and $n = 1$ for **G-2**). The attempt to determine n and P_4 has been successful only for a few other pulsars : PSR B0809+74 ($P_4 = 165$ $P_1 \sim 200$ s, $n = 2$, van Leeuwen *et al.* (2003)), PSR B0818−13 ($P_4 = 30$ s, Janssen & van Leeuwen (2004)), PSR B0826−34 ($P_4 = 14$ $P_1 \sim 25.9$ s, $n = 2$, Gupta *et al.* (2004)), PSR B0834+06 ($P_4 = 14.8$ $P_1 \sim 18.9$ s, Asgekar & Deshpande (2005)), PSR B0943+10 ($P_4 = 37$ $P_1 \sim 40$ s, $n = 0$, Deshpande & Rankin (1999)) and PSR B1857−26 ($P_4 = 147$ $P_1 \sim 89.9$ s, $n = 0$, Mitra & Rankin (2008)). Hence, PSR B0818−41 has the fastest known P_4, faster than PSR B0834+06.

(b) Phase locked relation (PLR) between inner and outer ring

From the gray scale plot of the single pulses (e.g. Fig. 3.1) it is evident that inner and outer drift regions are locked in phase : inner drift bands start from almost halfway between two drift bands in the leading outer region and always remain connected with the drift bands from the trailing outer region. This constant phase relation does not get perturbed by nulling or irregular drifting and is maintained even during the sequences of irregular drifting as well as after nulling. The PLR implies that the emission from the inner and the outer rings are always in fixed phase. Furthermore, nulling and changing drift rates are observed to be simultaneous in both the rings. Interestingly, a 180 deg phase shift between the spark locations on the inner and the outer

Table 3.2: Calculation of P_5 for **G-1** (the inner geometry) for different spark arrangements

Drift rate (deg/P_1)	Number of sparks (N_{sp})	Azimuthal separation between sparks (Δs)	$\Delta\sigma/\Delta s$	Apparent drift (D_{ap})	Alias order order (n,k)	f_2	Pulse offset (P_5)
0.95	19	18.95	3.09	0.95	0	0.10	17.86
20	19	18.95	3.09	1.05	2, 1	0.34	11.82
38.95	19	18.95	3.09	1.05	4, 2	0.50	**7.40**
57.89	19	18.95	3.09	1.05	6, 3	0.83	3.15
76.84	19	18.95	3.09	1.05	8, 4	1.08	17.46
21.05	18	20	2.92	1.05	2, 1	1.18	15.53
41.05	18	20	2.92	1.05	4, 2	1.43	**10.89**
22.23	17	21.18	2.76	1.05	2, 1	1.02	19.72
43.40	17	21.18	2.76	1.05	4, 2	1.26	14.81
19.05	20	18	3.25	1.05	2, 1	0.51	**8.69**
37.05	20	18	3.25	1.05	4, 2	0.75	4.22
18.17	21	17.14	3.41	1.05	2, 1	0.67	5.34
35.34	21	17.14	3.41	1.05	4, 2	0.92	1.36

†: combinations producing, $P_5 = 9 \pm 2$ are indicated by bold face.

Table 3.3: Calculation of P_5 for **G-2** (the outer geometry) for different spark arrangements

Drift rate (deg/P_1)	Number of sparks (N_{sp})	Azimuthal separation between sparks (Δs)	$\Delta\sigma/\Delta s$	Apparent drift (D_{ap})	Alias order order (n, k)	f_2	Pulse offset (P_5)
1.05	19	18.95	6.87	1.05	0	0.88	2.25
20	19	18.95	6.87	1.05	1, 1	1.13	15.71
38.95	19	18.95	6.87	1.05	3, 2	1.37	11.32
57.89	19	18.95	6.87	1.05	5, 3	1.62	6.92
76.84	19	18.95	6.87	1.05	7, 4	1.86	2.52
21.05	18	20	6.51	1.05	1, 1	0.76	4.48
41.05	18	20	6.51	1.05	3, 2	1.00	18.83
22.23	17	21.18	6.14	1.05	1, 1	0.40	12.02
43.40	17	21.18	6.14	1.05	3, 2	0.65	**7.11**
19.05	20	18	7.23	1.05	1, 1	0.49	**8.74**
37.05	20	18	7.23	1.05	3, 2	0.73	4.56
18.17	21	17.14	7.59	1.05	1, 1	0.85	2.43
35.34	21	17.14	7.59	1.05	3, 2	1.09	14.73

†: combinations producing, $P_5 = 9 \pm 2$ are indicated by bold face.

rings is needed in the simulation to match the PLR of the observed drift pattern of PSR B0818−41. Such an arrangement of sparks corresponds to a maximally packed structure on the polar cap. Spark discharges occur in every place where the potential drop is high enough to ignite and develop pair production avalanche Ruderman & Sutherland (1975), so sparks populate the polar cap as densely as possible. At the same time, such an arrangement of sparks should be quasi rigid, a property which is also suggested by the data.

PSR B0826−34 is another wide profile pulsar for which presence of simultaneous multiple drift regions are observed (Biggs *et al.* (1985), Esamdin *et al.* (2005)). The phase locked relation between the drift regions of this pulsar are discussed in Sect. 5.4(e) of Chapter 5.

Some pulsars − e.g. PSR B1237+25, B1857−26 − clearly shows multiple components in their profile (mostly five components, denoted by "M"). Rankin (1993) have recognized these pulsars as a distinct observational class of objects, where the emission is coming from the core and two concentric conal rings. No signature of drifting is detected in the inner ring for these pulsars, possibly because of the fact that the inner ring is too weak to detect any single pulse behavior.

To summarize, signatures of drifting from more than one ring are observed for only a few pulsars and for all of those pulsars, emission from inner and outer rings are locked in phase. No counter example is observed. This requires common drift rate in the outer and inner rings, implying that emission in the two rings are not independent, and that the conditions responsible for drifting are similar in both rings. This demands that the conditions are similar everywhere in the magnetosphere, which can in turn put constraints on the theoretical models attempting to explain the pulsar emission mechanism. Our finding of PLR between the emission from the inner and the outer rings can be explained considering the pulsar emission as a pan magnetospheric phenomenon.

According to Gil & Sendyk (2000), at any given time, the polar cap is populated as densely as possible. They consider, characteristic dimension of a spark and typical distance between sparks being equal to polar cap height h. They do not distinguish between the radial and the azimuthal directions, which may favor similar conditions (electric field and magnetic field) for both the rings of emission, leading to pan magnetospheric conditions across

the polar gap. Wright (2003) proposed an alternative model for the pulsar magnetosphere which considers the magnetosphere as an integral whole, and suggests that the inner and outer cones found in integrated profiles reflect the two intersections of the null surface with the light cylinder and the co-rotating dead zones respectively. They consider the pulsar radio emission phenomenon as a global pan magnetospheric phenomenon. Our results are consistent with these kinds of models.

3.5 Discussions and Summary

The remarkable subpulse drift pattern of B0818−41 can be interpreted as being due to an unaliased drift with a $P_4 \approx 370\,P_1 \approx 200s$, or an aliased drift with $P_4 \approx 18.3\,P_1 \approx 10s$. We believe that the latter is a more likely scenario for this pulsar. An unaliased drift can not explain the occurrence of longitude stationary sub-pulses and sense reversal of the drift rate that is seen in our data. For an aliased drift rate, this can be explained by small variations of the drift rate that move the P_3 across the nearest Nyquist boundary (Gupta *et al.* (2004)). Though it is rare for the signature of carousel rotation period to be directly present as a low frequency feature in the fluctuation spectrum, we note that this has been claimed for at least two other cases : B0834+06 (Asgekar & Deshpande (2005)) and B0943+10 in Q mode (Asgekar & Deshpande (2001) and Rankin & Suleymanova (2006)). This is supported by a new technique, introduced in this chapter for resolving aliasing (Sect. 3.4).

It is interesting to compare our results with the theoretical models for $E \times B$ drift, such as that given by Gil & Sendyk (2000). According to their equations (12) and (13), the complexity parameter a (which can be represented as $Int(a) \approx 2\nu + 1$, with ν being the putative number of cones), can be used to estimate the number of sparks in a ring as $N_{sp} = \pi a = P_4/P_3^t$. Taking $P_4 = m\,P_1$, we get : $P_3^t/P_1 = m\,\pi\,(2\nu+1)$. Further, if $P_4 = P_3^m$, then from Eqn. 1 we obtain, $P_3^t/P_1 = m\,(k\,m \pm 1)$. Hence, $\pi\,(2\nu+1) = (k\,m \pm 1)$, which relates the number of cones to the measured periodicity and the alias order. Here, the plus sign applies for even alias orders, i.e. $n = 2, 4, 6 \cdots$, $l = 0$ and the minus sign for the odd alias orders, i.e. $n = 1, 3, 5 \cdots$, $l = 1$. Thus, for our measured periodicity of $18.3 \pm 1.6\ P_1$, the right hand side evaluates to 19.3 ± 1.6 for the inner LOS solution and first allowed alias

order ($n = 2$). For the outer LOS solution, it evaluates to 17.3 ± 1.6 for the first allowed alias order ($n = 1$). The left hand side evaluates to 15.7 ± 1.6 for $\nu = 2$ and to 21.9 ± 1.6 for $\nu = 3$. Thus, the outer LOS solution is more compatible with the pulsar having two cones, whereas the inner LOS solution is in closer agreement with a three cone model. It is quite likely that the LOS misses the third innermost cone in this pulsar. Note that drift with higher alias orders (e.g. $n = 3, 4$) is incompatible with the above picture : either the number of sparks has to be twice as many (which is unlikely), or the P_4 has to be shorter by a factor of 2.

Furthermore, the complexity parameter can be used to estimate the screening factor η for the partially screened gap model, which describe the inner acceleration region in pulsars (Gil *et al.*, 2003). From equation (2) of Gil *et al.* (2006), $P_4/P_1 = a/2\eta$. For unaliased drifting ($P_4 \approx 370\ P_1$), $\eta \approx 0.016$ and $\eta \approx 0.023$ for $\nu = 2$ and $\nu = 3$, respectively. For aliased drifting with $P_4 = 18.3\ P_1$, the corresponding estimates for η are 0.14 and 0.19. In Gil *et al.* (2003), calculated η values for different pulsars range from 0.032 to 0.36, with a typical value of ≈ 0.2 meaning that on the average the actual potential drop is of the order of 10% of the pure vacuum gap (Ruderman & Sutherland, 1975). The η value for the aliased drift case for B0818−14 is comparable to this, whereas for the unaliased drift case it will be the lowest amongst the known values of η. This lends further support to our preference for aliased drift in the case of this pulsar.

The permanent PLR between the inner and the outer drift regions is a unique feature in B0818−41. It suggests that the relative location of the circulating spark pattern in the two rings is strongly correlated, rather than being independent. Furthermore, the circulation rate is the same for both the rings, indicating a common electrodynamic control in the entire polar cap. Arrangement of sparks located 180 deg phase shifted in the inner and the outer rings would correspond to the sparks that are maximally packed on the polar cap. Spark discharges occur in every place where the potential drop is high enough to ignite and develop pair production avalanche (Ruderman & Sutherland, 1975), so sparks populate the polar cap as densely as possible. At the same time such arrangement of sparks should be quasi rigid, a property which is also suggested by the data. These results could be of significant implication for the physics of the polar cap. Multiple drift regions, with

their drifts phase related to each other, are known in only a few pulsars, e.g. B0815+09 by McLaughlin *et al.* (2000), and B1839−04 by Weltevrede *et al.* (2006). The mirrored drift bands for B0815+09 are explained in the sparking gap model as emission coming from an inner core gap (we refer as vacuum gap) and inner annular gap (Qiao *et al.*, 2004). The closely spaced inner and the outer drift regions can constrain the radial distances between the rings of emission in the polar cap of B0818−41. The radius of the inner and the outer ring from the simulation (Fig. 3.16) are, $0.6\,r_p$ and $0.8\,r_p$ − are roughly in the range predicted for other pulsars by Gupta & Gangadhara (2003) with a separate investigation method.

Following are the interesting new results from our investigation of subpulse drifting,

(1) Discovery of a remarkable drift pattern at 325 MHz characterized by simultaneous occurrence of three drift regions: an inner region with flatter apparent drift rate flanked on each side by a region of steeper apparent apparent drift rate. Though these drift regions have significantly different values for the measured P_2, the measured P_3 value is the same and equal to $18.6\,P_1$.

(2) We also report a phase locked relation between the inner and outer drift regions for PSR B0818−41. The PLR is maintained even after irregular drifting or nulling.

(3) We report that the peaks of the emission from the trailing and leading outer regions, as a function of the pulse number, are offset by a constant interval, $P_5{\sim}9P_1$.

(4) Frequent changes of drift rates, including transitions of drift rates from negative to phase stationary and vice verse, are observed for this pulsar. Such transitions of drift rates appear to have some connection with nulling.

(5) In addition to the remarkable subpulse drift observed at 325 MHz, we report subpulse drifting at 244, and 610 MHz. At 244 MHz subpulse drifting is observed only in the leading and trailing outer regions and not in the inner region. Though the drift bands are weaker, subpulse drifting is observed in both inner and outer region at 610 MHz. P_2^m, P_3^m and $\Delta\Phi_s$ are determined for the inner and the outer drift regions. Though P_3^m is observed to be the same for the inner and outer drift regions, P_2^m and $\Delta\Phi_s$ are different for different drift regions.

Interpretations of the analysis results, aided by the simulations, lead to following new outcomes,

(1) We interpret that the observed drifting is created by intersection of the LOS with two concentric rings of an nearly aligned rotator. Inner and outer drift regions are originated by intersection of the LOS with the inner and the outer rings respectively.

(2) Based on the frequency evolution of the average profile, observed PA swing and results from subpulse drifting, we converged on two possible choices of emission geometry: **G-1** (α = 11 deg and β = $-$5.4 deg) and **G-2** (α = 175.4 deg and β = $-$6.9 deg). Pulsar radiation pattern simulated with both the geometries reproduces the observed features, except for some differences. Rather surprisingly, all other observed properties are found to be satisfied for both these geometries.

(3) We explain the observed subpulse drifting and transitions of apparent drift rates from negative to phase stationary as being due to aliasing. The frequent transitions from negative to phase stationary drift rates observed for PSR B0818$-$41 can be understood by slight changes in polar cap temperature leading to change in the drift rate so that $P_3^t = P_1$ is satisfied and longitude phase stationary drifting is observed.

(4) The absence of the inner drift region at 244 MHz is interpreted as, the LOS missing the emission from the inner ring. This is supported by the results from the simulations.

(5) A new technique is introduced in this chapter for resolving aliasing, using the constant offset ($P_5 \sim 9P_1$) between the peak emission from the leading and trailing outer regions. From the result of this technique, we propose that the subpulse drifting for PSR B0818$-$41 is most likely first order aliased, and the corresponding carousel rotation period $P_4 = 10$ s. This implies that PSR B0818$-$41 has the fastest known carousel.

(6) 180 deg phase shift between the spark locations on the inner and the outer rings is needed in the simulation to match the observed PLR of the drift pattern, which implies that the sparks that are maximally packed on the polar cap.

(7) For all pulsars for which we know drifting from more than one ring (e.g. PSR B0826$-$34 and possibly PSR B0815+09), the drift pattern in the inner and outer rings are always phase locked. This could be a significant

constraint for the theoretical models of pulsar radio emission, and favors an emission model that considers pulsar radio emission as a pan magnetospheric phenomenon.

Hence, the results from the observations, simulations and the follow up interpretations, enable fair amount of insight towards the emission properties of the unique drifting pulsar B0818−41. This study will also have significant contribution to constrain the theoretical models explaining the possible emission mechanism of pulsars.

CHAPTER 4

Investigation of the unique nulling properties of PSR B0818−41

"I do not feel obligated to believe that the same God who has endowed us with sense, reasons, and intellect has intended us to forgo their use."
– Galileo Galilei

4.1 Introduction

In the previous chapters (Chapter 2 and 3) we investigated the remarkable drifting and polarization properties of PSR B0818−41. We solved aliasing problem for this pulsar and determined the corresponding carousel rotation period (P_4) which makes it the fastest rotating carousel. We argued that, all the pulsars showing drifting in multiple rings of emission exhibit phase locked drifting between the rings. This puts constraints to the theoretical models of pulsar emission mechanism. In this chapter, we will investigate the unique nulling properties of PSR B0818−41.

Nulling is considered as an important clue to unravel the mystery of the pulsar emission mechanism. Detailed investigation of nulling for many pulsars by several works (e.g. Ritchings (1976), Rankin (1986), Biggs (1992)), as described in Sect. 1.2(d) of Chapter 1, establish that the phenomenon is possibly broadband and is intrinsic to individual pulsars. Though, nulling is known to occur randomly, there are some recent studies by Rankin & Wright (2008) and Herfindal & Rankin (2007) which report periodicity in nulling for quite a few pulsars. It is generally believed that onset of nulling is abrupt, i.e. pulse intensity abruptly goes down before the nulls. However, for PSR B0809+74 and PSR B1944+17, it is reported that the transitions from burst to null is slow while the transitions from null to burst are abrupt (Lyne &

Ashworth (1983), Deich *et al.* (1986)). For PSR B0031−07, onset of the nulls are found to be abrupt (Vivekanand, 1995). Lyne & Ashworth (1983) investigated the nulls and the post null drift behavior for PSR B0809+74. They reported a relative dimness of last pulses before the nulls, whereas the first active pulses immediately after the nulls appear to outshine the normal pulses. van Leeuwen *et al.* (2003) confirmed their results and also investigated the interaction between drifting and nulling in PSR B0809+74. They concluded that the drift pattern immediately after the nulls differs from the normal one. They commented that, beside its normal and most common mode, the pulsar emits in a significantly different quasi-stable mode immediately after most or possibly all the nulls. In this mode the pulsar is brighter and the subpulse separation is less. The subpulses drift more slowly and the pulse window is shifted towards the earlier longitudes. Investigating the interaction between drifting and nulling, Janssen & van Leeuwen (2004) determined the alias order for drifting of PSR B0818−13. The unique nulling properties of PSR B0818−41 are hitherto unexplored. We have carried out a detailed investigation of this pulsar in null state at 325 and 610 MHz. The analysis and results are described in Sect. 4.2. In Sect. 4.3 we discuss the implications of our findings.

4.2 Analysis and Results

For the investigation of nulling behavior of PSR B0818−41, we used data from single pulse observations at 325 MHz for two epochs (on 24 February 2004 and 21 December 2005, containing 3414 and 6600 pulses respectively) and at 610 MHz for two epochs (on 25 February 2004 and 11 January 2005, containing 1612 and 3600 pulses respectively). Details of the observations have already been described in Sect. 2.2 and summarized in Table 2.1.

We observe frequent nulling for PSR B0818−41. Duration of the nulls varies from few tens of pulses to about hundred pulses. Left panel of Fig. 4.1 plots the single pulse gray scale plot for pulse # 1000 to 1200 from the GMRT observations on 24 February 2004 at 325 MHz. Some instances of the pulsar in the null state are seen for pulse # 1000 to 1020, 1028 to 1061, 1070 to 1088 and 1153 to 1176. Right panel of Fig. 4.1 plots the same, but for pulse # 1400 to 1600, where instances of pulsar in null state are seen for pulse

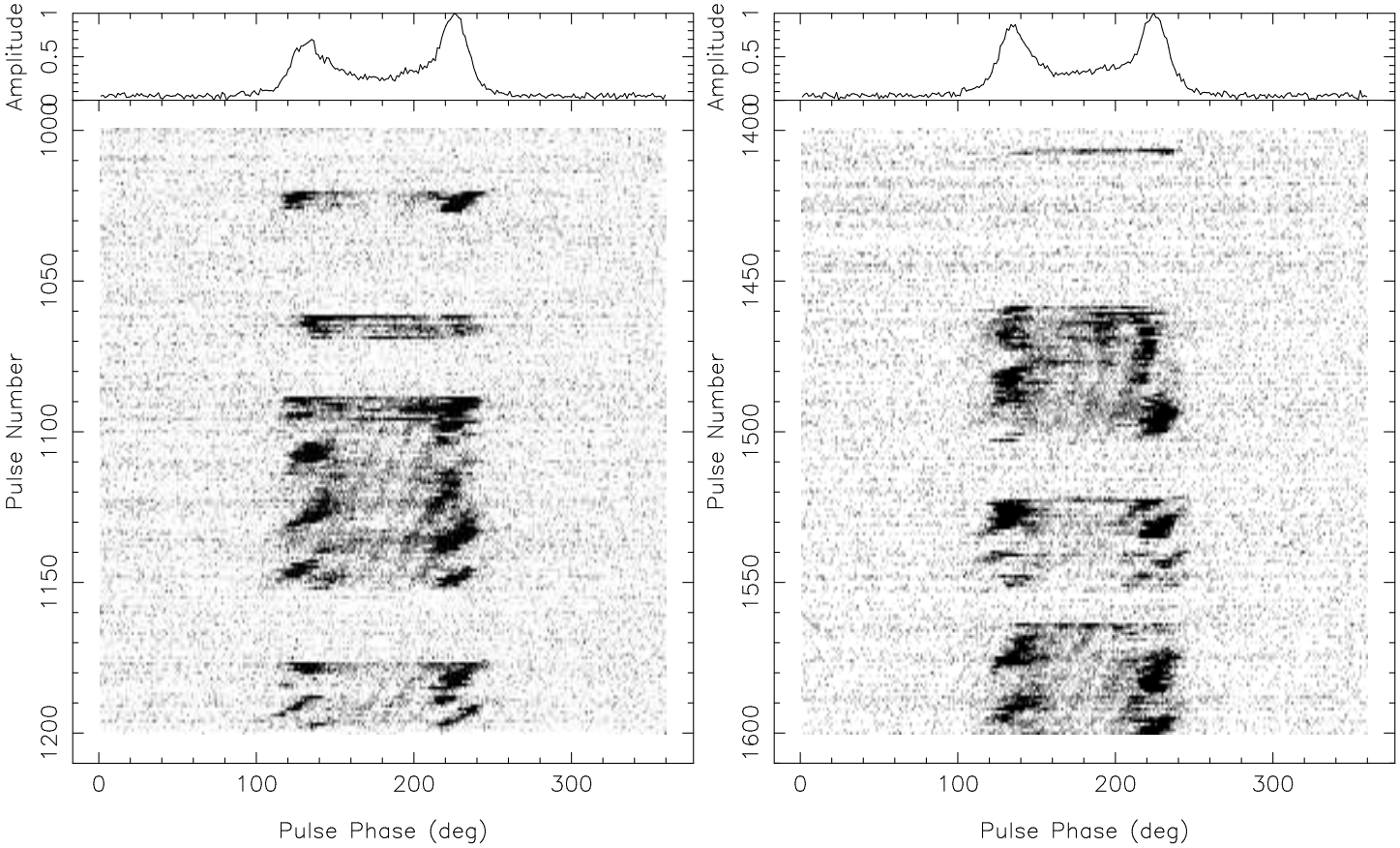

Figure 4.1: Gray scale plot of single pulses from PSR B0818−41 from observations on 24 February 2004 at 325 MHz. Left panel: for pulse # 1000 to 1200, pulsar nulls from pulse # 1000 to 1020, pulse # 1028 to 1061, pulse # 1070 to 1088 and pulse # 1153 to 1176. Right panel: for pulse # 1400 to 1600, pulsar nulls from pulse # 1409 to 1458, pulse # 1504 to 1521 and pulse # 1552 to 1563.

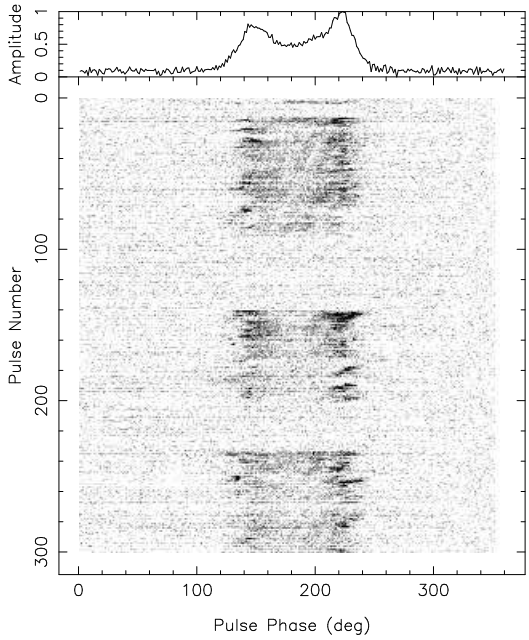

Figure 4.2: Same as Fig. 4.1, but for pulse # 1 to 300 from observations on 25 February 2004 at 610 MHz. Pulsar nulls from pulse # 3 to 13, pulse # 92 to 141 and pulse # 202 to 234.

#, 1409 to 1458, 1504 to 1521 and 1552 to 1563. Fig. 4.2 plots the same as Fig. 4.1, but for pulse # 1 to 300 from observations on 25 February 2004 at 610 MHz, with sequences of nulls observed from pulse # 3 to 13, pulse # 92 to 141 and pulse # 202 to 234. Investigating the single pulse gray scale plots (e.g. Fig. 4.1 and 4.2), we observe that the active pulses immediately after the nulls look different from the normal pulses. For these pulses, the inner region (refer to Fig. 2.1 of Chapter 3 for the definition of the inner region) appears more filled and is significantly more intense than that of the normal pulses. For example the inner regions of pulse # 1021, 1062, 1089 and 1177 (Fig. 4.1) are more filled and outshine the average ones. However, from visual inspection of the gray scale plot the inner regions of the pulses immediately before the nulls (e.g. pulse # 999, 1027, 1060, 1069 and 1087 in Fig. 4.1) appear less bright. Association of changing drift rates with the nulls (also discussed in Sect. 3.2(d)) are quite evident in the single pulse gray scale plots (see Fig. 4.1). For example, irregular drifting is observed before the nulls, around pulse # 1070, and after the end of the nulls, around pulse # 1088. Different aspects of the unique nulling properties of PSR B0818−41 are detailed in the following.

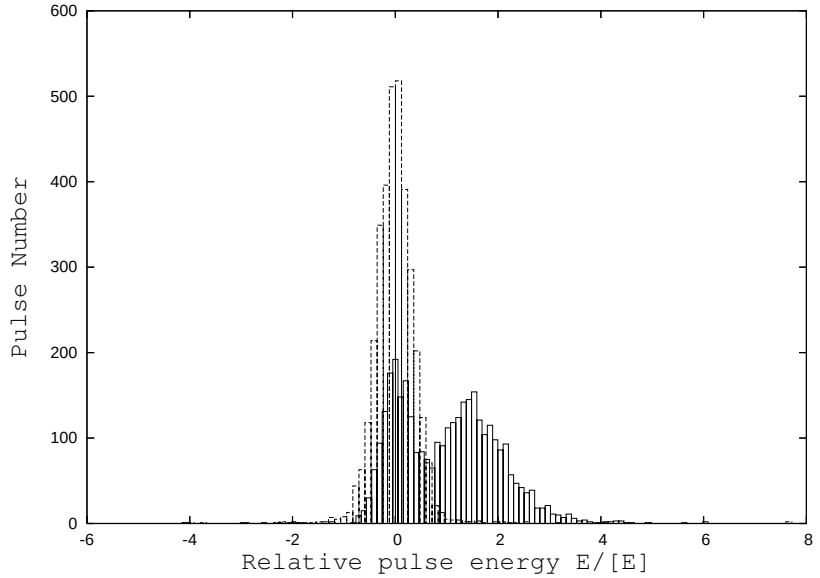

Figure 4.3: Energy histogram for PSR B0818−41 at 325 MHz with 3414 pulses, from observations on 24 February 2004. The energy distribution in the on pulse window are indicated by solid line and the same for the off pulse window are indicated by the dotted line.

(a) Identification of active and null state and calculation of nulling fraction

Identification of the active and the null states depends on the sensitivity limit of the telescope. Highly sensitive single pulse observations are required for accurate characterization of pulsar nulling properties. Very good signal to noise single pulse data, obtained from the GMRT observations allow us to explore the unique nulling properties of PSR B0818−41. Ritchings (1976) and Biggs (1992) investigated the statistics of pulse energy distributions for characterizing the phenomenon of nulling. We follow similar procedure for PSR B0818−41 and the corresponding ON pulse as well as OFF pulse energy histograms at 325 MHz from the observations on 24 February 2004, are plotted in Fig. 4.3. At 325 MHz the ON pulse histogram has two components corresponding to active and null pulses. We note, (i) strong presence of pulses with zero or near zero aggregate intensity, (ii) distribution is continuous between the pulses and the nulls, making it difficult to separate out the populations. At 610 MHz, the distribution tend to merge with each other as a consequence of lower SNR (Fig.4.4). Using the method described in Ritchings (1976) we calculate nulling fraction ∼30% at 325 MHz from the

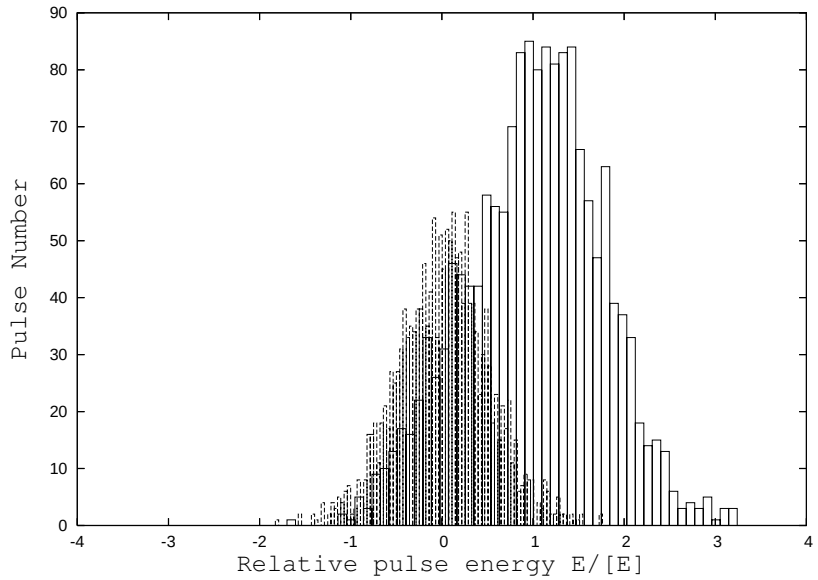

Figure 4.4: Energy histogram for PSR B0818−41 at 610 MHz with 1612 pulses, from observations on 25 February 2004. The energy distribution in the on pulse window are indicated by solid line and the same for the off pulse window are indicated by the dotted line.

observations on 24 February 2004. Calculated nulling fraction is 28% from the 325 MHz observations on 21 December 2005. This method does not yield meaningful estimates for 610 MHz, as the ON and OFF distributions merge at this frequency.

Although, pulse energy distributions provide statistical information about the nulling phenomenon, identifying individual nulls at each frequency is required for more detailed investigation. This is done by comparing the ON pulse energy estimate with a threshold based on the system noise level. The uncertainty in the pulse energy estimate $\sigma_{ep,on}$ is given by $\sqrt{n_{on}}\sigma_{off}$, where n_{on} is the number of ON pulse bins and σ_{off} is the rms of the OFF pulse region. Using this as a threshold, we consider pulses with ON pulse energy smaller than $3 \times \sigma_{ep,on}$ as null pulses.

(b) Intensity distribution of the inner region before and after individual nulls

Since both the leading and trailing outer regions have single drift bands which are strongly modulated by the 18.3 P_1 periodicity (the P_3^m for this pulsar),

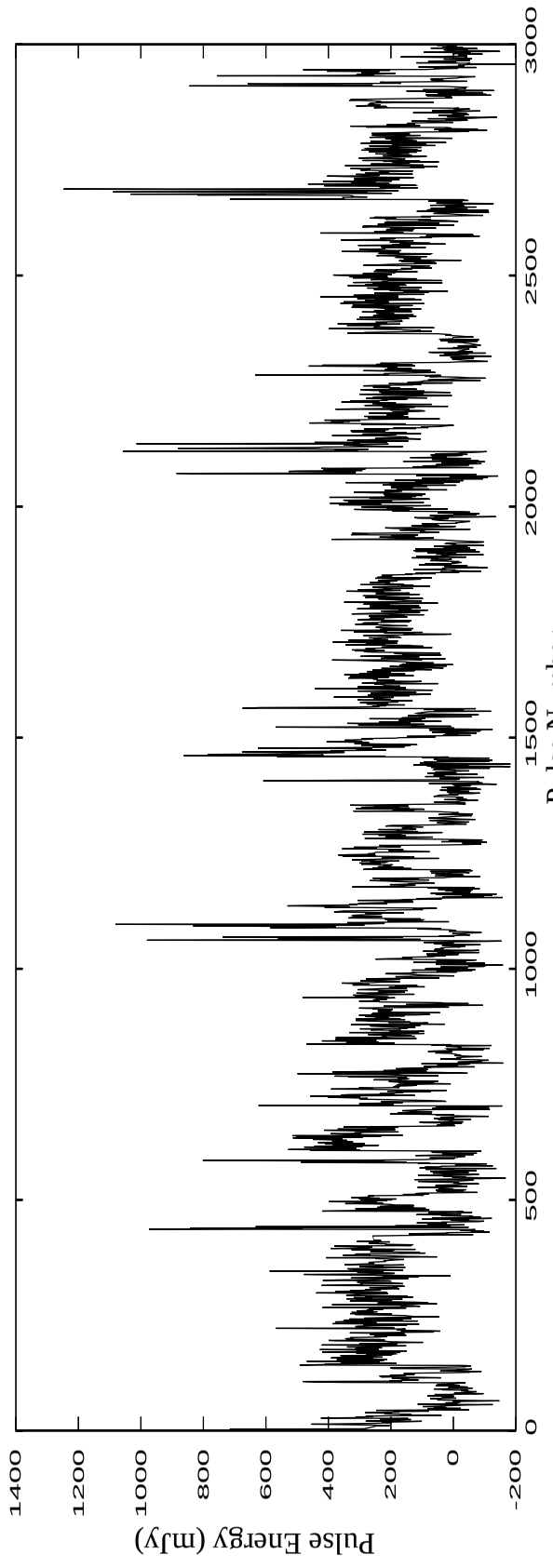

Figure 4.5: Total energy of the inner region versus pulse number for the 325 MHz from observations on 24 February 2004. Note that the pulse energy gradually decreases before the pulsar stars nulling. First few active pulses immediately after the nulls are stronger.

Figure 4.6: Total energy of the inner region versus pulse number for the 325 MHz from observations on 21 December 2005. Note that the pulse energy gradually decreases before the pulsar stars nulling. First few active pulses immediately after the nulls are stronger.

the intensity modulations around the nulls are more prominent in the inner region. Consequently, we choose the inner region for initial investigation of the intensity modulation before and after the nulls. Fig. 4.5 plots the pulse energy of the inner region versus the pulse number (for pulse # 1 to 3000) from observations on 24 February 2004 at 325 MHz. Fig. 4.6 plots the same (for pulse # 1 to 6000) from observations on 21 December 2005. The pulse intensity gradually goes down before the nulls and suddenly shoots up for the first few active pulses after the nulls. From investigation of the gradual fall of energy of the inner region before the nulls at 325 MHz, for about 10,000 pulses (from observations on 24 February 2004 and 21 December 2005) having about 40 null occurrences, we observe that the time taken for transition from the active to null state varies somewhat, with a minimum of about 5 pulses, maximum of about 13 pulses, and a mean of about 10 pulses.

We select the sequences of nulls for which pulsar is active for at least 10 pulses before the null and stays in active state for more than 10 pulses after the null. We will concentrate on these selected nulls for the rest of the analysis presented in this chapter. For the selected nulls, we compute the following quantities for the inner region,

• $\langle I_b(1p:10p)\rangle$: mean intensity of 10 active pulses immediately before the nulls.

• I_a: intensity of the first active pulse immediately after the end of the nulls.

• $\langle I_a(4p:10p)\rangle$: mean intensity of the 4th to 10th active pulses immediately after the end of the nulls [1]

• $I_a/\langle I_b(1p:10p)\rangle$: ratio of I_a to $\langle I_b(1p:10p)\rangle$ which will provide a comparison of the strength of the first active pulse immediately after the nulls to the mean strength of the last ten active pulses before the nulls.

• $I_a/\langle I_a(4p:10p)\rangle$: ratio of I_a to $\langle I_a(4p:10p)\rangle$ which will provide a comparison of the strength of the first active pulse immediately after the nulls to the mean strength from the fourth pulse onwards and up to the tenth active pulses after the end of the nulls.

• $\langle I_a(4p:10p)\rangle/\langle I_b(1p:10p)\rangle$: ratio of $\langle I_a(4p:10p)\rangle$ to $\langle I_b(1p:10p)\rangle$ which will provide a comparison of the strength of the active pulses after the end of the null (from the fourth pulse onwards and up to the tenth pulse) to the

[1]First three active pulses are generally stronger than the rest. So we considered the mean intensity of fourth pulse onwards for comparison of intensities just after the nulls to sufficiently after the nulls.

mean of the last ten active pulses before the nulls.

Table 4.1 lists the null occurrence numbers and corresponding durations of the nulls, durations of the active state before and after the nulls, $I_a/\langle I_b(1p:10p)\rangle$, $\langle I_a(4p:10p)\rangle/\langle I_b(1p:10p)\rangle$ and $I_a/\langle I_a(4p:10p)\rangle$ for observations of PSR B0818−41 at 325 MHz on 24 February 2004[2]. We find that $I_a/\langle I_b(1p:10p)\rangle$ is always greater than unity with a mean of 2.84, confirming that first active pulse just after the nulls outshine the pulses just before the nulls. $\langle I_a(4p:10p)\rangle/\langle I_b(1p:10p)\rangle$ is comparatively less and oscillates around unity, with the mean being 1.46. $I_a/\langle I_a(4p:10p)\rangle$ is always greater than unity (mean value ~ 2.05) implying that the first few active pulses immediately after the nulls are brighter than the following pulses. Table 4.2 lists the same as Table 4.1, but for observations at 325 MHz on 21 December 2005. All the three ratios computed in Table 4.1 and 4.2 have similar values. Table 4.3 and 4.4 lists the same as Table 4.1, but for observations at 610 MHz on 25 February 2004 and 11 January 2005. $I_a/\langle I_b(1p:10p)\rangle$ is almost always more than unity with mean of 2.29 for 25 February 2004 and 2.18 for 11 January 2005, which are bit lower than the ratios obtained at 325 MHz. Same is true for the comparison of $I_a/\langle I_a(4p:10p)\rangle$ values between 325 and 610 MHz. However, mean value of $\langle I_a(4p:10p)\rangle/\langle I_b(1p:10p)\rangle$ at 610 MHz is comparable or greater than the mean values at 325 MHz.

Left panel of Fig. 4.7 is the plot of $I_a/\langle I_b(1p:10p)\rangle$ versus null number for all the epochs at 325 and 610 MHz, with the mean for all the null occurrences for both the frequencies being 2.88 and median being 2.33. Right panel of Fig. 4.7 plots $I_a/\langle I_a(4p:10p)\rangle$ versus null number for all the epochs, with mean value for all the null occurrences at 325 and 610 MHz being 2.05 and median being 1.95. The implications of the above findings are discussed in Sect. 4.3.

[2]Same exercise tried with $\langle I_a(1p:3p)\rangle$ or $\langle I_a(1p:2p)\rangle$ in place of I_a produces similar ratios.

Table 4.1: Investigation of the intensity distribution of the inner region immediately before and after the nulls (from observations at 325 MHz on 24 February 2004)

Serial Number	Duration of null	Duration of burst after null	Duration of burst before null	$\frac{I_a}{\langle I_b(1p{:}10p)\rangle}$	$\frac{\langle I_a(4p{:}10p)\rangle}{\langle I_b(1p{:}10p)\rangle}$	$\frac{I_a}{\langle I_a(4p{:}10p)\rangle}$
1	59	20	>46	1.89	0.86	2.19
2	5	276	21	3.12	1.94	1.61
3	50	33	282	1.73	0.62	2.81
4	92	52	39	2.11	1.73	1.21
5	25	10	54	1.78	1.46	1.21
6	49	83	83	2.93	1.87	1.57
7	27	10	35	1.85	0.61	3.01
8	33	10	10	5.97	3.43	3.12
9	18	64	10	1.28	1.12	1.15
10	23	21	64	1.83	0.71	2.55
11	14	52	21	2.07	1.52	1.35
12	12	31	52	1.02	0.69	1.46
13	28	17	31	1.49	0.85	1.76
14	17	31	40	1.67	0.99	1.69
15	11	294	31	5.56	1.89	2.95
16	17	14	64	5.52	2.70	2.04
17	34	150	14	3.07	1.47	2.09
18	8	28	150	6.99	2.36	2.97
19	62	207	28	1.43	0.62	2.28
20	10	35	207	2.11	0.91	2.32
21	37	148	35	5.20	3.01	1.73
22	10	11	10	1.75	0.87	2.02
Mean value	–	–	–	2.84	1.46	2.05
Median Value	–	–	–	1.98	1.29	2.03

Table 4.2: Same as Table 4.1, but from another epoch at 325 MHz on 21 December 2005

Serial Number	Duration of null	Duration of burst after null	Duration of burst before null	$\frac{I_a}{\langle I_b(1p{:}10p)\rangle}$	$\frac{\langle I_a(4p{:}10p)\rangle}{\langle I_b(1p{:}10p)\rangle}$	$\frac{I_a}{\langle I_a(4p{:}10p)\rangle}$
1	46	30	>46	2.25	1.67	1.53
2	83	203	474	5.95	2.10	2.84
3	28	202	185	2.18	1.02	2.15
4	10	250	202	2.25	1.31	1.71
5	268	145	103	6.83	1.96	3.48
6	86	150	145	9.28	2.20	4.21
7	22	51	150	2.91	1.38	2.11
8	10	125	56	2.39	1.83	1.31
9	104	47	120	1.84	0.55	3.35
10	48	49	274	2.34	0.80	2.90
11	23	17	49	2.38	1.08	2.20
12	50	105	17	1.87	1.24	1.50
13	41	15	370	1.82	1.84	0.99
14	330	109	15	1.01	0.71	1.42
15	8	50	109	1.26	0.96	1.30
16	159	184	50	3.06	2.33	1.31
17	23	22	184	1.56	0.93	1.67
18	103	33	199	4.39	2.02	2.18
19	22	73	30	1.67	0.76	2.19
Mean value	–	–	–	3.03	1.40	2.12
Median value	–	–	–	2.33	1.31	2.11

Table 4.3: Same as Table 4.1, but at 610 MHz on 25 February 2004

Serial Number	Duration of null	Duration of burst after null	Duration of burst before null	$\frac{I_a}{\langle I_b(1p{:}10p)\rangle}$	$\frac{\langle I_a(4p{:}10p)\rangle}{\langle I_b(1p{:}10p)\rangle}$	$\frac{I_a}{\langle I_a(4p{:}10p)\rangle}$
1	8	81	>5	1.88	0.52	3.64
2	47	61	81	2.15	0.76	2.85
3	32	793	61	3.32	2.59	1.28
4	98	24	793	3.19	1.19	2.66
5	33	78	24	1.53	0.97	1.58
6	28	15	78	2.44	0.81	3.02
7	19	48	15	1.51	1.25	1.21
8	37	47	48	2.29	1.73	1.33
9	18	115	47	2.26	1.81	1.24
Mean value	–	–	–	2.29	1.43	1.81
Median value	–	–	–	2.26	1.35	1.36

Table 4.4: Same as Table 4.1, but at 610 MHz on 11 January 2005

Serial Number	Duration of null	Duration of burst after null	Duration of burst before null	$\frac{I_a}{\langle I_b(1p{:}10p)\rangle}$	$\frac{\langle I_a(4p{:}10p)\rangle}{\langle I_b(1p{:}10p)\rangle}$	$\frac{I_a}{\langle I_a(4p{:}10p)\rangle}$
1	200	400	725	2.51	1.70	1.47
2	60	113	96	2.95	3.93	0.75
3	73	55	113	1.42	1.15	1.24
4	31	164	55	2.51	2.13	1.18
5	86	130	164	2.88	2.42	1.19
6	40	15	130	1.80	0.84	2.13
7	94	220	405	0.90	1.03	0.87
8	128	103	202	2.47	1.26	1.96
Mean value	–	–	–	2.18	1.81	1.35
Median value	–	–	–	2.49	1.48	1.21

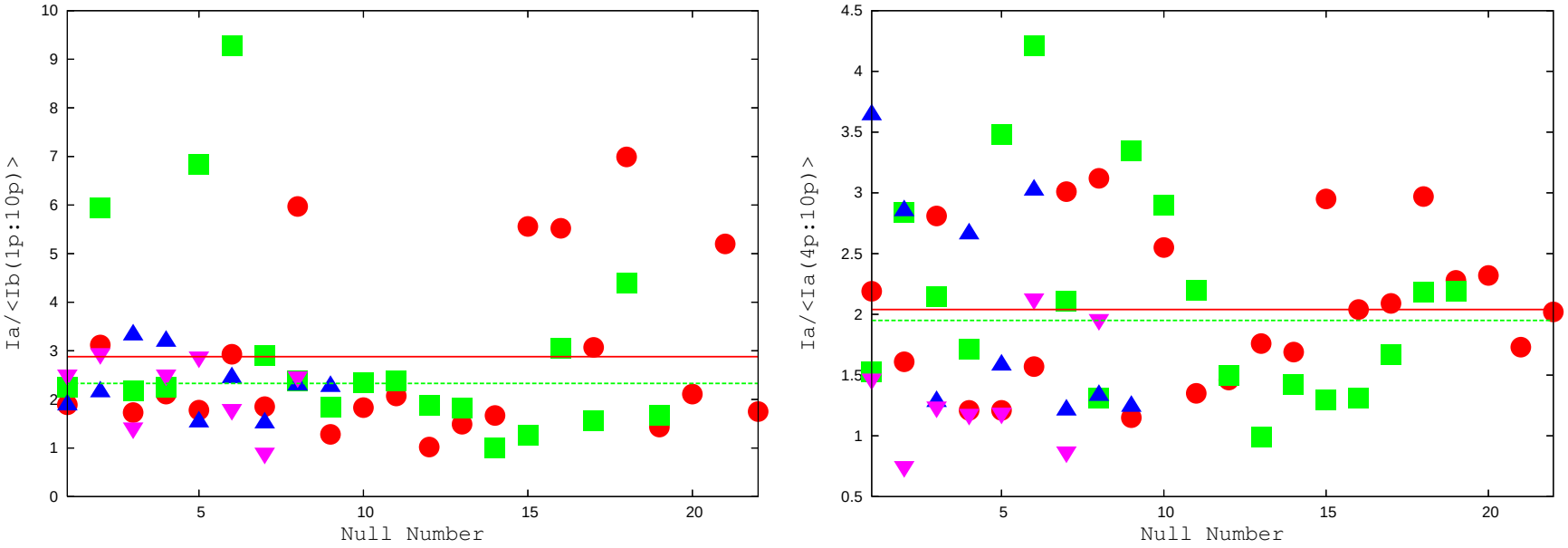

Figure 4.7: Relative strength of the first active pulse just after the nulls to the pulses before and after the nulls for the 325 and 610 MHz observations. $I_a/\langle I_b(1p:10p)\rangle$ is plotted against the null occurrence number (left panel) and $I_a/\langle I_a(4p:10p)\rangle$ is plotted against the null occurrence number (right panel). Solid red circles (325 MHz on 24 February 2004, Table 4.1), solid green squares (325 MHz on 21 December 2005 Table 4.2), solid blue triangles (610 MHz on 25 February 2004, Table 4.3) and inverted pink triangles (610 MHz on 11 January 2005, Table 4.4). The solid and dashed lines denote the mean and median values for all the null occurrences.

(c) Null versus burst length

We aim to investigate any possible connection between the intervals of the adjacent nulls (so called bursts), and the duration of the nulls. Does waiting longer for a null mean that it will last longer too? The durations of the nulls and the bursts immediately before and after the nulls are tabulated in Tables 4.1, 4.2, 4.3 and 4.4. Fig. 4.8 plots the duration of the nulls versus duration of the corresponding bursts after the nulls for all the 58 occurrences of nulls considering all the observing epochs together. This plot does not show any trend. Same is true for Fig. 4.9, which plots the durations of the nulls versus the corresponding durations of the bursts before the nulls.

We also wanted to check if there is any relation between the length of the null/burst and the relative strength of the pulses before and after the nulls. $I_a/\langle I_b(1p:10p)\rangle$ as a function of corresponding null durations are plotted in Fig. 4.10. No obvious correlation is observed. Similarly we do not see any correlation between $I_a/\langle I_a(4p:10p)\rangle$ and the corresponding null durations. These ratios when plotted as a function of the duration of the bursts before or after the nulls do not show any systematic trend. Hence, we do not see any obvious correlation between the lengths of the nulls and the corresponding bursts as well as between the null or burst length and the relative strength of the pulses just before and after the nulls.

(d) Average profile from the pulses immediately before and after the nulls

Analysis presented in Sect. 4.2(b) brings out the fact that the pulses immediately before and after the nulls have different characteristics than the normal pulses. To study this in more detail, we construct the average profiles of the pulses immediately before and after the nulls, for the nulls that satisfy the criterion described in Sect. 4.2(b). We have considered around 10,000 pulses from two epochs of observations at 325 MHz for the analysis presented here and hence the results may have some effect of small number statics.

Left panel of Fig. 4.11 presents the average pulse profile of PSR B0818−41 at 325 MHz on 24 February 2004, (a) from a sequence of 200 pulses showing regular drifting (referred to as normal profile hereafter), (b) from the last active pulse immediately before the nulls and (c) from the first active pulse

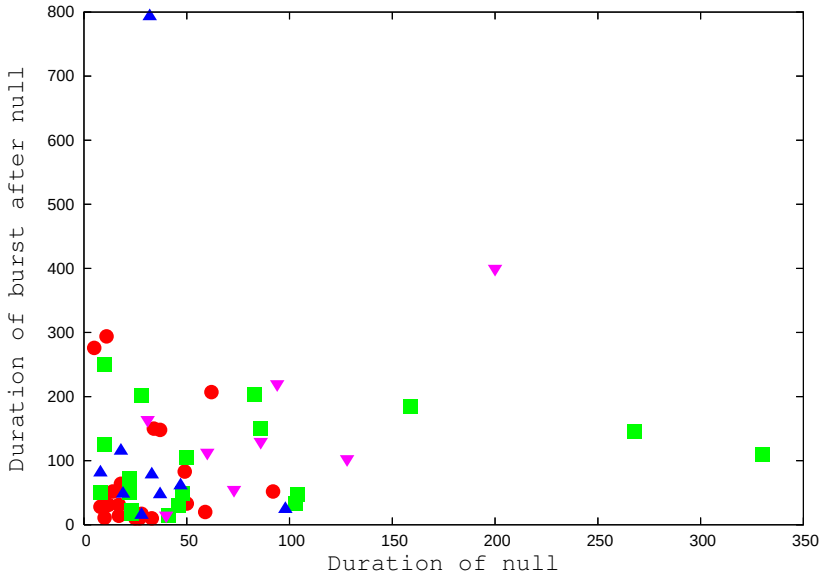

Figure 4.8: Durations of the nulls are plotted against the durations of bursts after nulls. Solid red circles (325 MHz on 24 February 2004, Table 4.1), solid green squares (325 MHz on 21 December 2005 Table 4.2), solid blue triangles (610 MHz on 25 February 2004, Table 4.3) and inverted pink triangles (610 MHz on 11 January 2005, Table 4.4).

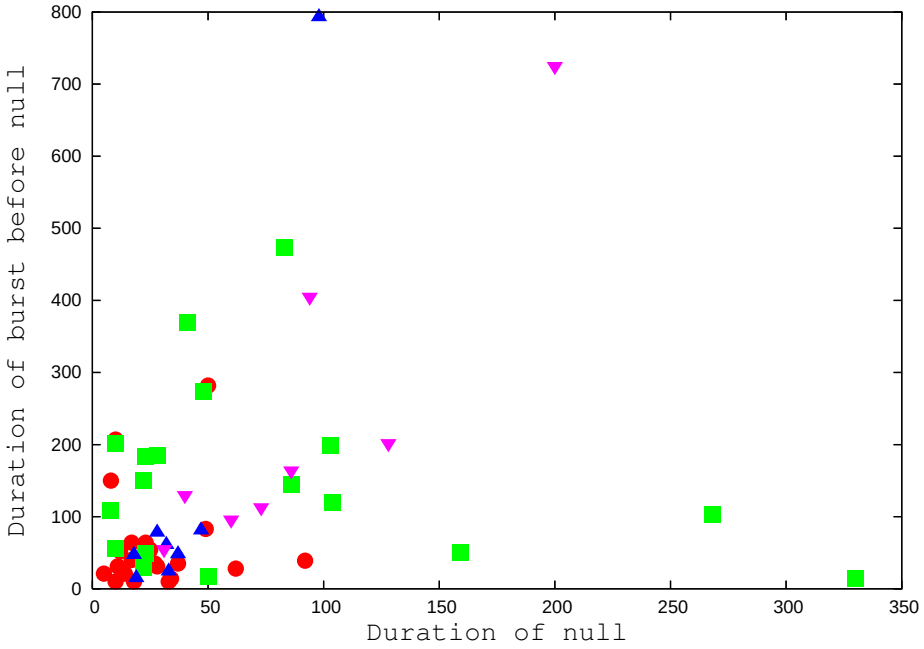

Figure 4.9: Same as Fig. 4.8, but with duration of the nulls plotted against the durations of bursts before the nulls.

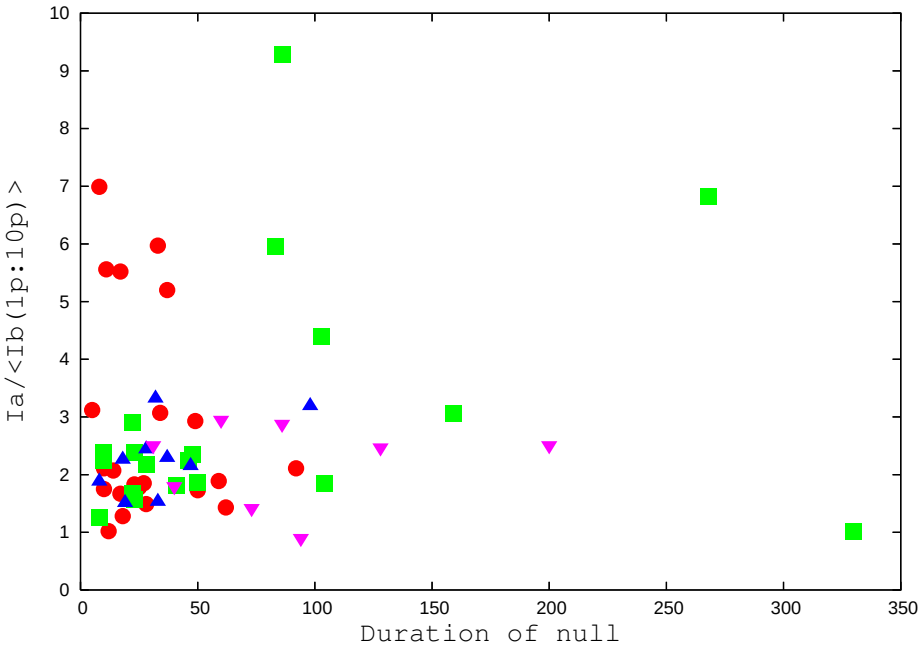

Figure 4.10: Same as Fig. 4.8, but with duration of the nulls plotted against $I_a/\langle I_b(1p:10p)\rangle$.

immediately after the nulls. Right panel of Fig. 4.11 plots the same at 325 MHz for the observations on 21 December 2005. Though, the average profile from the last active pulse immediately before the nulls has similar shape to the normal profile, it is much weaker than the normal profile. This profile has relatively less intensity in leading outer region and more intensity in the inner saddle region compared to the normal profile. On the other hand, the average profile constructed from the first active pulse immediately after the nulls is more intense than the normal average profile. It has increased intensity (in the form of a bump) in the inner region as compared to the normal average profile. The leading and trailing peaks are of similar intensity for this profile, whereas in the normal profile the trailing peak is significantly more intense. More interestingly, these characteristics of the average profiles constructed from the first active pulse after the nulls are similar for both the epochs of observations at 325 MHz (Fig. 4.13). We also note that there are some strong pulses (more than 2 times the strength of average pulses) which appear immediately after the nulls (within 5 to 6 pulses) when the pulsar goes to active state. Fig. 4.12 plots the average of the first active pulses immediately after the nulls and the profile for a sequence of 300 pulses

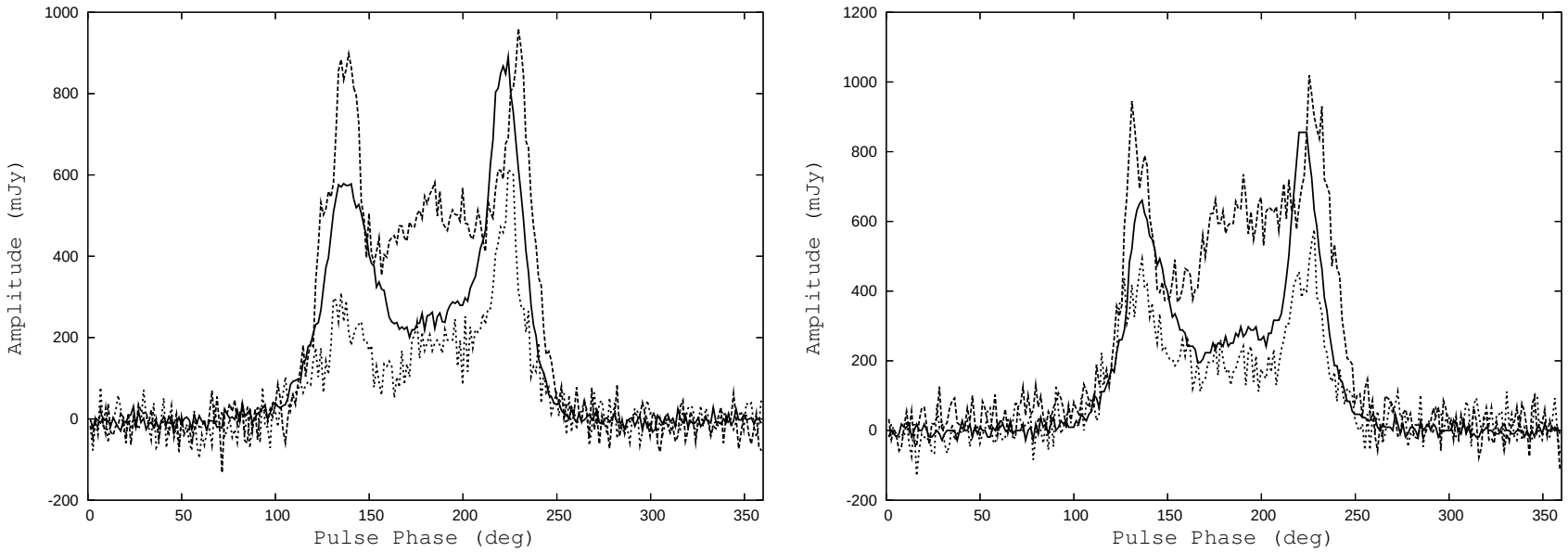

Figure 4.11: Left panel: The average profiles for regular drifting mode (solid line), first active pulses immediately after the nulls (dashed line), last active pulses immediately before the nulls (dotted line), at 325 MHz from the observations at the epoch on 24 February 2004. Right panel: same as the left panel, but on 21 December 2005.

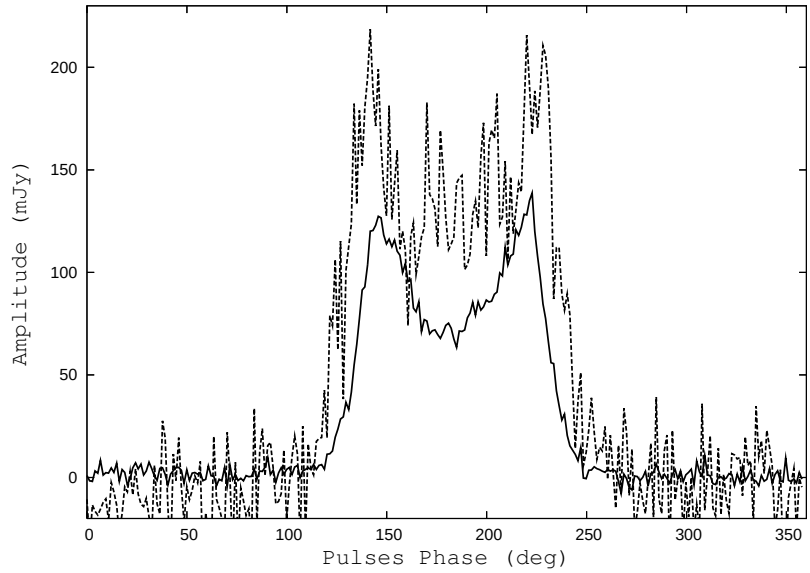

Figure 4.12: Normal average profile (dashed line) and the average profile from the first active pulses after the nulls (solid line) at 610 MHz. Amplitude is in arbitrary units which is same for both the profiles.

showing regular drifting at 610 MHz (for the observations on 25 February 2004), for comparison. Average profile from the pulses immediately after the nulls is stronger than the normal profile, which is similar to what is observed at 325 MHz. Shape of the average profile from pulses immediately after the nulls resembles with that of the normal profile except for the increased intensity in the middle of the profile as is observed at 325 MHz.

As noted above, the average profiles from the first active pulse immediately after the nulls for two epochs of observations on 24 February 2004 and on 21 December 2005 at 325 MHz, are surprisingly similar (Fig. 4.13). To investigate this further, we wanted to compare the corresponding average profiles immediately before and after the nulls for the two epochs of observations at 325 MHz. Thus, we construct the average profiles from the first, second, third, fourth, fifth and so on active pulses immediately after the nulls and the last, second last, third last, fourth last, fifth last and so on active pulses immediately before the nulls, for the selected null occurrences on 24 February 2004 and on 21 December 2005. In addition, we construct average profiles from the first two, first three, first five and so on active pulses after the nulls to achieve increased sensitivity. Fig. 4.14 plots the average profiles from the first, third, fifth and tenth active pulses immediately after

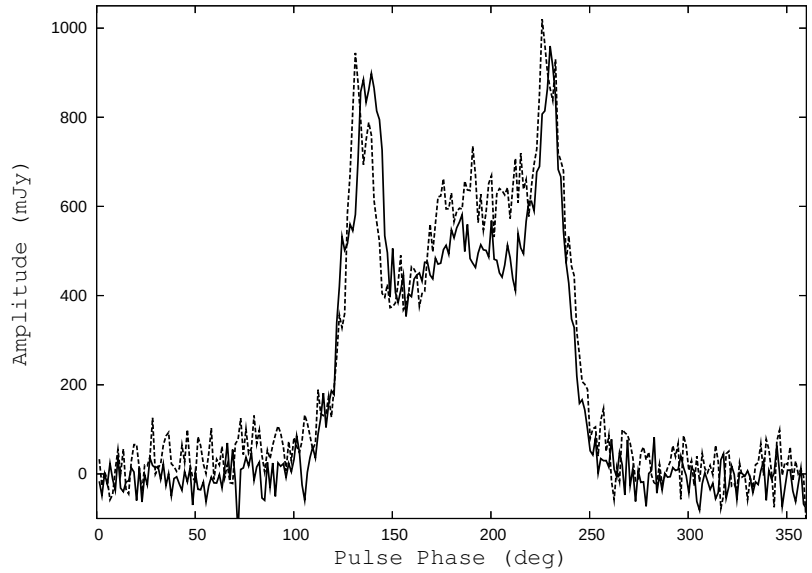

Figure 4.13: Comparison of the average profile for first active pulses immediately after the nulls at 325 MHz from observations on 24 February 2004 (solid line) and on 21 December 2005 (dashed line).

the nulls for the two epochs of observations, with calibrated amplitude in Jy. The regular average profile is plotted in the top panel to provide a scale for comparison. Remarkable similarity is observed between the corresponding average profiles from the two epochs of observations. Fig. 4.15 plots the average profiles from the first three, five, ten and twenty active pulses immediately after null with calibrated amplitude in Jy. However, the similarity between the corresponding profiles for the two epochs are more evident in Fig. 4.15 (than Fig. 4.14). Fig. 4.16 plots the average profiles from the first, third, fifth and tenth last active pulses immediately before the null, for the two epochs of observations with calibrated amplitude in Jy. The similarity between the corresponding average profiles, from the pulses immediately before the nulls, made from two epochs of observations is less compared to that for the average profiles immediately after the nulls. In the following we report the unique properties from the investigation of the average profiles of the active pulses immediately after the nulls.

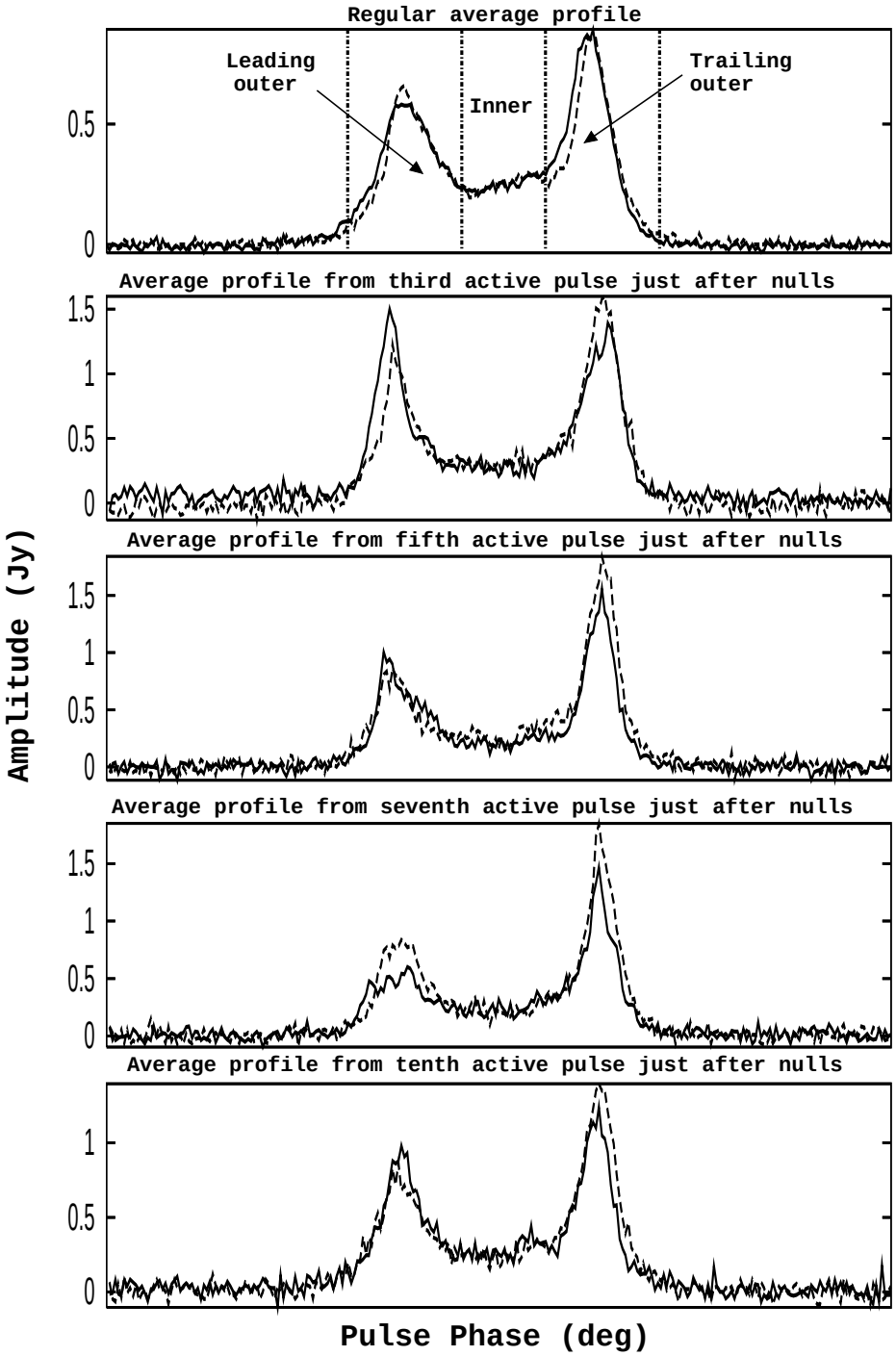

Figure 4.14: Comparison of the average profile from first few active pulses immediately after the nulls at 325 MHz from observations on 24 February 2004 (solid line) and on 21 December 2005 (dashed line).

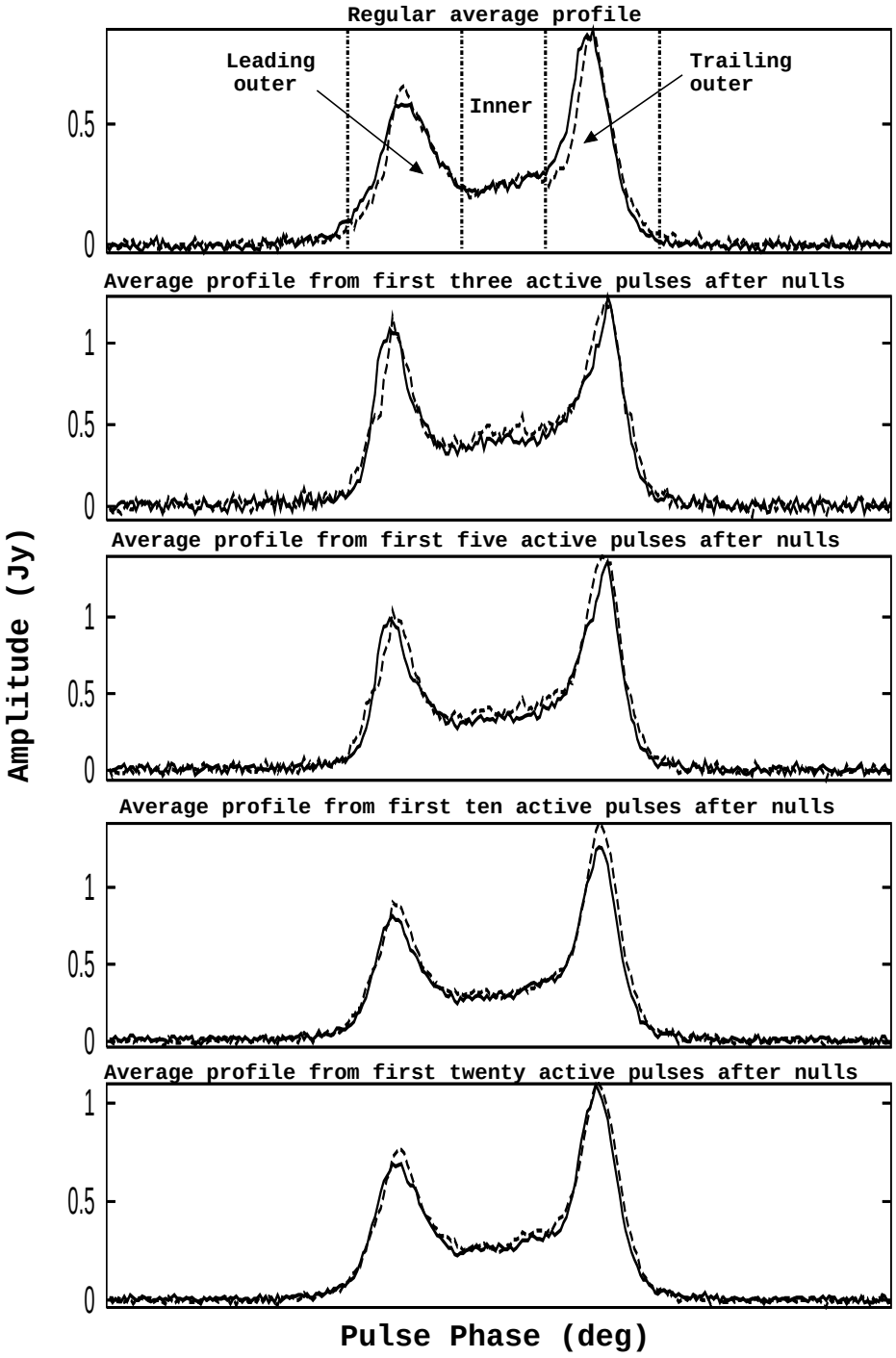

Figure 4.15: Comparison of the average profile for first few active pulses immediately after the nulls at 325 MHz from observations on 24 February 2004 (solid line) and on 21 December 2005 (dashed line).

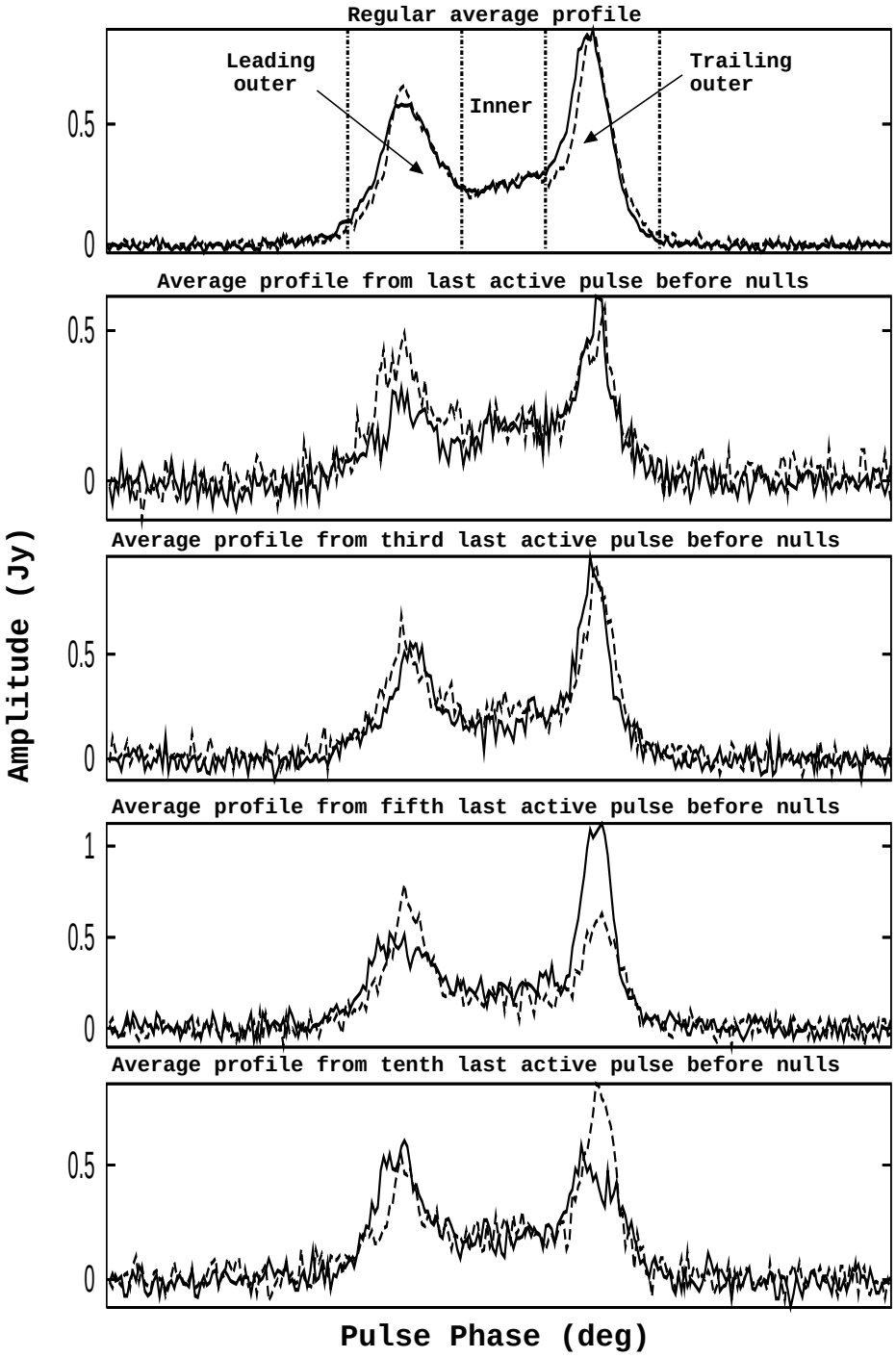

Figure 4.16: Comparison of the average profiles from first few active pulses immediately before the nulls at 325 MHz from observations on 24 February 2004 (solid line) and on 21 December 2005 (dashed line).

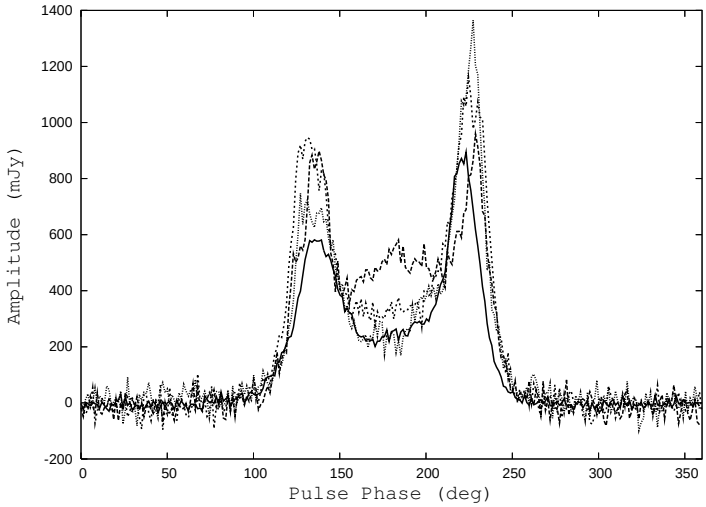

Figure 4.17: Normal average profile (solid line), average profile from the first active pulses after the nulls (long dashed line), third active pulses after the nulls (short dashed line), fifth active pulses after the nulls (dotted line) at 325 MHz on 24 February 2004.

(i) Intensity of the inner region as a function of pulse number immediately after the nulls:

We observe that the average profile constructed from the first active pulse immediately after the nulls has increased intensity in the inner region. In this context, we wanted to investigate the evolution of the intensity of the inner region as a function of the pulse number immediately after the nulls. Fig. 4.17 plots the average profiles from the first, third, fifth active pulses after the nulls, and the normal average profile for comparison. We observe that inner saddle region becomes relatively less intense (but still intensity level is more than the normal value) for the average profile from the third active pulses after the nulls. For the average profile from the fifth active pulse after the nulls the inner saddle region has almost similar shape and intensity as the normal profile.

To investigate this apparently systematic behavior in detail, we calculate the mean and the maximum intensity of the inner region of the average profiles from the active pulses immediately after the nulls. Fig. 4.18 plots the mean intensity of the inner region versus the pulse number immediately after the nulls at 325 MHz for the epochs of observations on 24 February 2004 and on 21 December 2005. Fig. 4.19 plots the maximum intensity of the inner region versus the pulse number immediately after the nulls. Mean

and maximum intensities of the inner region follow similar trend : they are maximum for the first active pulse after the nulls (mean intensity $\sim$ 520 mJy on 24 February 2004 and $\sim$ 650 mJy on 21 December 2005), and then gradually go down. So mean intensity of the inner region for the first active pulse is 1.2 times more for the epoch on 21 December 2005 than for the epoch on 24 February 2004. This coincides with the fact that, intrinsically the pulsar was slightly stronger for the epoch on 21 December 2005 than the epoch on 24 February 2004 (Table 2.1). Intensity of the inner region reaches the value observed for the normal profile ($\sim$ 220 mJy for the epoch on 24 February 2004 and $\sim$ 260 mJy for the epoch on 21 December 2005) after about first 20 active pulses from the end of nulls. It is very striking that the, intensity of the inner region versus pulse number immediately after the nulls follows identical trend for two different epochs of observations. Fig. 4.20 plots the mean intensity of the inner region versus the pulse number, calculated from average profiles of the pulses immediately before the nulls, at 325 MHz. The mean intensity of the inner region is less for the average profiles from the pulses immediately before the nulls : around 164 mJy for the epoch on 24 February 2004 and 187 mJy for the epoch on 21 December 2005. The mean intensity of the inner region increases and for twentieth last pulse immediately before the nulls this becomes around 214 mJy for the epoch on 24 February 2004 and 224 mJy for the epoch on 21 December 2005. This is consistent with the behavior of individual nulls described in Sect. 4.2(b), that the mean intensity of inner region is less before the nulls and it suddenly increases after the nulls by about a factor of 3. More interestingly, we note that, though the mean (and maximum) intensity of the inner region systematically decreases from its value at the first active pulse after the nulls (as in Fig. 4.18), no systematic trend is observed in increase of the mean intensity from the last active pulse onwards before the nulls (as in Fig. 4.20). This indicate that for the active pulses immediately after the nulls the conditions in the magnetosphere are very similar between different nulls and the intensity decrease follow a regular and systematic trend. On the other hand, the conditions may be very different for the active pulses before the nulls and the gradual decrease of intensity before the nulls happens over different timescales (as is reported in Sect. 4.2(b)), and hence we do not see any trend after averaging all the selected nulls present in the data. The above

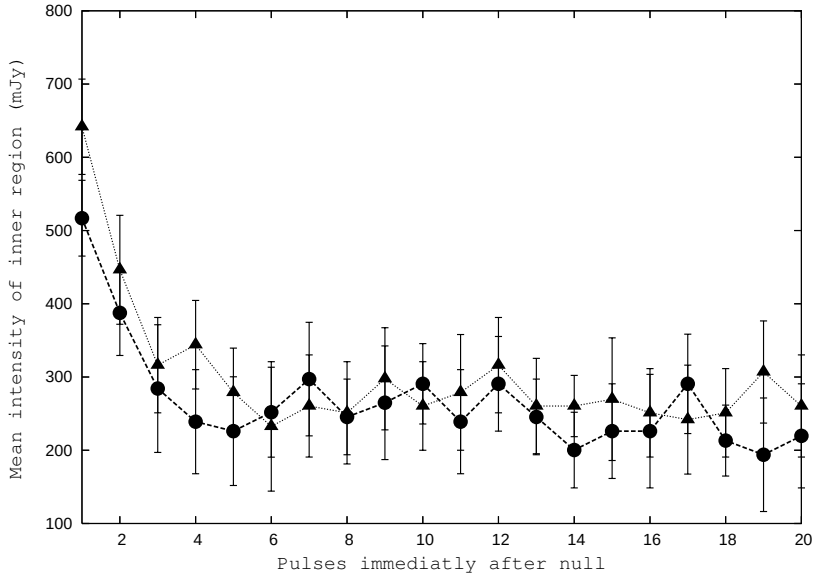

Figure 4.18: Mean intensity of inner region of the average profile from the pulses immediately after the nulls versus the corresponding pulse number at 325 MHz. Results for the epoch on 24 February 2004 are denoted by dashed line and for the epoch on 21 December 2005 are denoted by dotted line.

results shows that the emission has similar characteristics immediately after all the nulls, but the emission characteristics are not similar immediately before the nulls.

(ii) Intensity of the leading and trailing peaks as a function of pulse number immediately after the nulls

Fig. 4.21 and 4.22 plots the intensities of the leading and the trailing peaks (mean of 5 bins on each side of the concerned peak, 1 bin ∼1.35 deg) of the average profiles versus the corresponding pulse number immediately after the nulls. Both the peaks are of increased intensity after the nulls. Intensity of the leading peak becomes maximum for the average profile from the second active pulses immediately after the nulls for 24 February 2004, and for the average profile from the third active pulses immediately after the nulls for 21 December 2005, and then gradually falls. However, the trailing peak attains its maximum intensity for the average profile from the fourth active pulse immediately after the nulls for both 24 February 2004 and 21 December 2005.

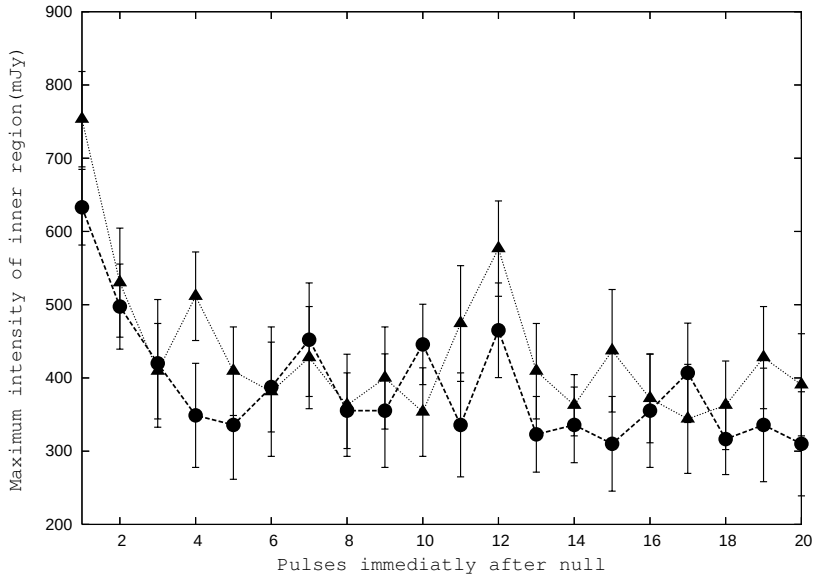

Figure 4.19: Maximum intensity of inner region of the average profile from the pulses immediately after the nulls versus the corresponding pulse number at 325 MHz. Results for the epoch on 24 February 2004 are denoted by dashed line and for the epoch on 21 December 2005 are denoted by dotted line.

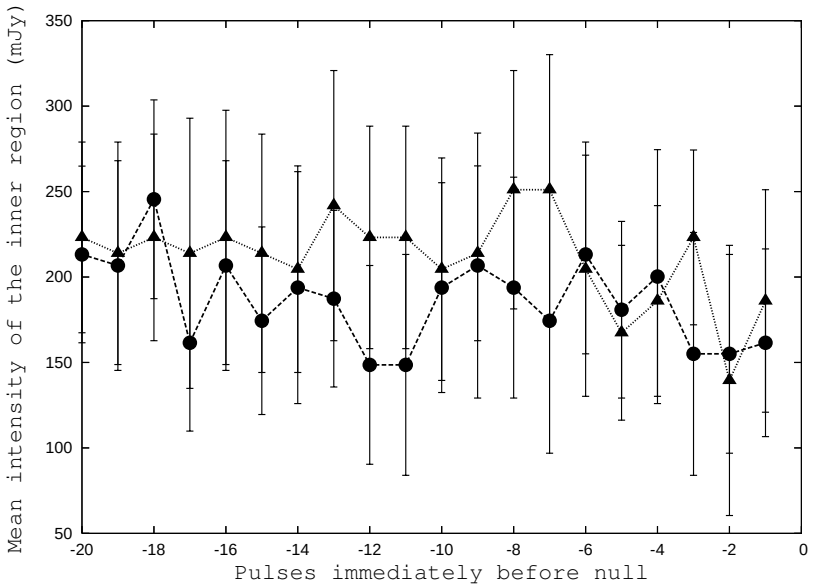

Figure 4.20: Mean intensity of inner region of the average profile from the pulses immediately before the nulls versus the corresponding pulse number at 325 MHz. Results for the epoch on 24 February 2004 are denoted by dashed line and for the epoch on 21 December 2005 are denoted by dotted line.

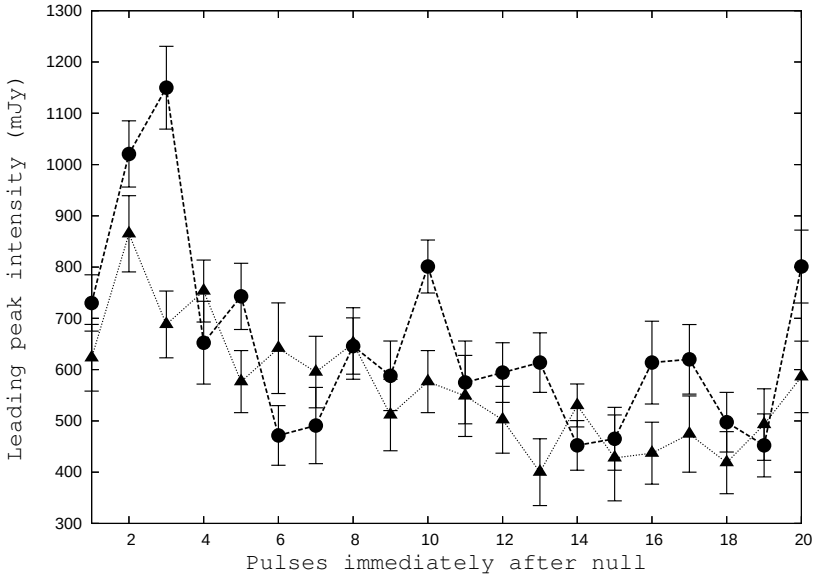

Figure 4.21: Mean intensity of the leading peak of the average profile from the pulses immediately after the nulls versus the corresponding pulse number at 325 MHz. Results for the epoch on 24 February 2004 are denoted by dashed line and for the epoch on 21 December 2005 are denoted by dotted line.

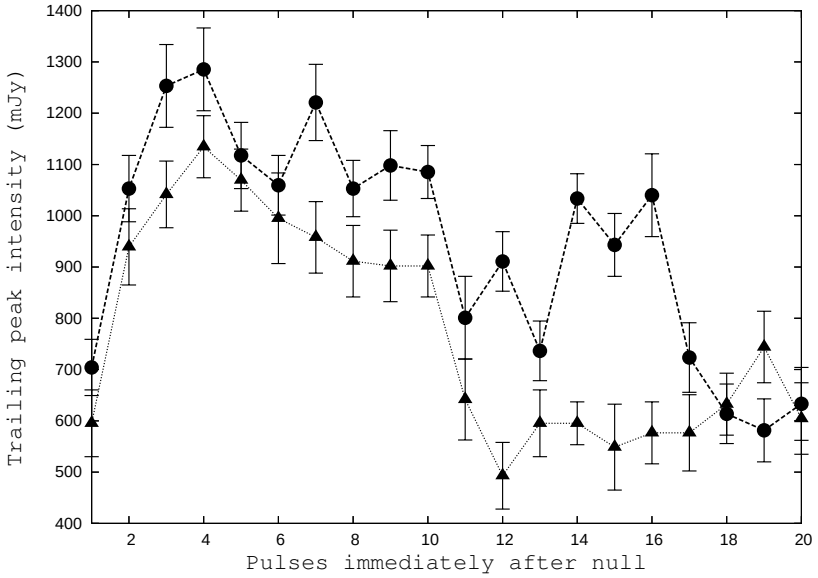

Figure 4.22: Mean intensity of the trailing peak of the average profile from the pulses immediately after the nulls versus the corresponding pulse number at 325 MHz. Results for the epoch on 24 February 2004 are denoted by dashed line and for the epoch on 21 December 2005 are denoted by dotted line.

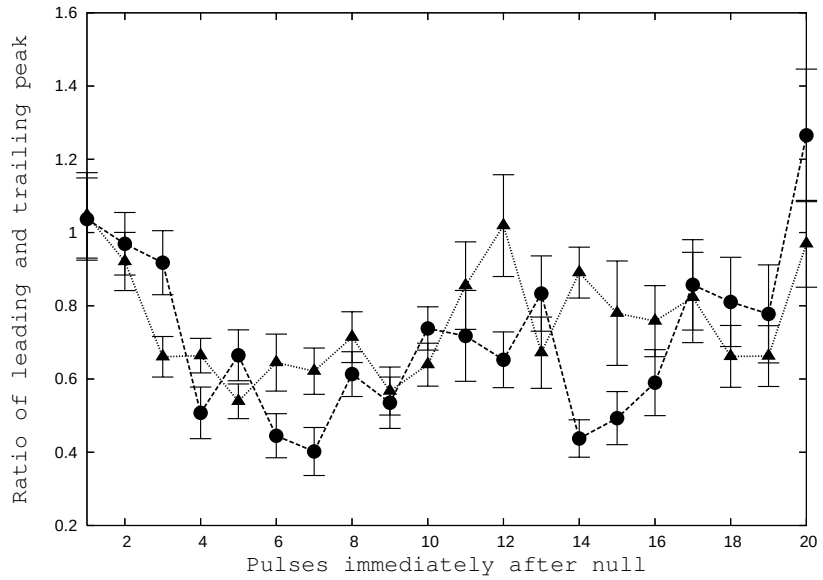

Figure 4.23: Ratio of mean intensities of leading and trailing peaks of the average profile from the pulses immediately after the nulls versus the corresponding pulse number at 325 MHz. Results for the epoch on 24 February 2004 are denoted by dashed line and for the epoch on 21 December 2005 are denoted by dotted line.

Similar trend is followed in the evolution of leading or trailing peak with pulse number after the nulls for both the epochs. Fig. 4.23 plots the ratios of the leading and the trailing peak intensities as a function of pulse number immediately after the nulls. For the average profile from the first active pulse immediately after the nulls, this ratio becomes maximum, and the leading and trailing peaks are of similar intensity, as is also seen in Fig. 4.13. For the average profiles of the next few active pulses immediately after the nulls this ratio goes down and eventually goes up. For the normal average profile this ratio of the leading to the trailing peak is around 0.6.

(iii) Width of the average profiles as a function of pulse number immediately after the nulls

Fig. 4.11 shows that the positions of the leading and the trailing peaks of the pulses just after the nulls are shifted from the normal. In the following we investigate this in details. We took two consecutive active pulses after the nulls for all the null occurrences for a given epoch and calculated the mean average profile (e.g. average profiles are constructed from first and second active pulses; third and fourth active pulses and so on). The positions of the

leading and the trailing peaks are calculated for each of these mean profiles by fitting second order polynomials to the peaks. We construct the average profiles of two consecutive pulses after the nulls, instead of single pulses to increase signal to noise of the resultant profile which helps us to fit a function to the peak to determine its position. Fig. 4.24 plots the positions of the leading peaks for the average profiles after the nulls versus the corresponding pulse numbers immediately after the nulls. The leading peak is shifted more in the leading side immediately after the nulls (around 132 deg for the first active pulse immediately after the nulls) and comes back to the position in normal profile (around 135 deg) with increasing pulse number. Fig. 4.25 plots the positions of the trailing peaks for the average profiles immediately after the nulls versus the corresponding pulse numbers : the trailing peak is shifted more in the trailing side (around 228 deg for first active pulse after the nulls) and then comes back to the normal position (around 222 deg) with increasing pulse number. As is evident from Fig. 4.24 and Fig. 4.25, the evolution of leading and trailing peak positions, with increasing pulse number immediately after the nulls, is similar for both the epochs of observations. As a result of the shift of the leading peak to the leading side and the trailing peak to the trailing side, the profile immediately after null becomes wider than normal profile. However, the profiles after the nulls are not symmetrically wider in the leading and the trailing sides, but get more wide in the trailing side. Fig. 4.26 plots the separation between the leading and the trailing peaks as a function of pulses immediately after the nulls. Immediately after the nulls this separation is more and goes down with increasing pulse number.

We calculate the positions of the midpoint of the average profile from the pulses immediately after the nulls. Fig. 4.27 plots the position of the profile mid point as a function of the null occurrence number. Solid line indicates the position of profile mid point for the normal profile. Position of profile mid point changes significantly immediately after the nulls.

(e) Drift rate around null

In Sect. 3.2(d), we have discussed about the changes in apparent drift rates and transitions of the apparent drift rates from negative to stationary or

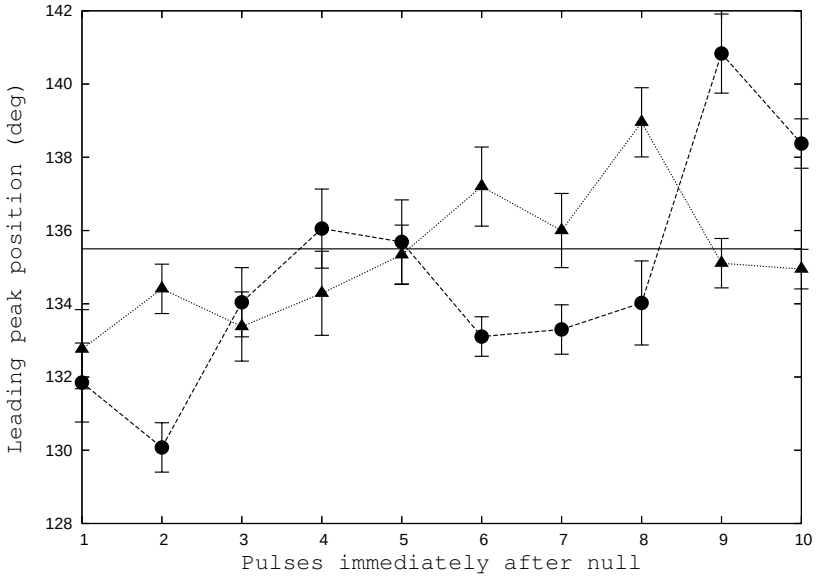

Figure 4.24: Position of the leading peak of the average profiles from the pulses immediately after the nulls versus the corresponding pulse number at 325 MHz. Results for the epoch on 24 February 2004 are denoted by dashed line and for the epoch on 21 December 2005 are denoted by dotted line. Solid line indicates the position of the leading peak for the normal profile ($\sim$ 135 deg).

stationary to negative directions. Fig. 3.11, 3.12 of Chapter 3 exhibit that change in drift rates are generally associated with nulls. We investigated the drift rates around the nulls. Most of the times the apparent drift rate becomes slower before the nulls, often transitions from negative to stationary drifting is observed before nulling starts. But there are times when it seemed that drift rate just before the nulls does not deviate much from the normal drift rate and the visual inspections of the drift bands is not enough to verify the slow down of the apparent drift rate. However, after the nulls, the apparent drifting is either stationary or irregular for initial few active pulses and then the regular negative drift starts.

4.3 Discussion and summary

In the following we discuss the interesting new results from our study of unique nulling properties of PSR B0818−41, and compare these with the similar results reported in the literature for other pulsars.

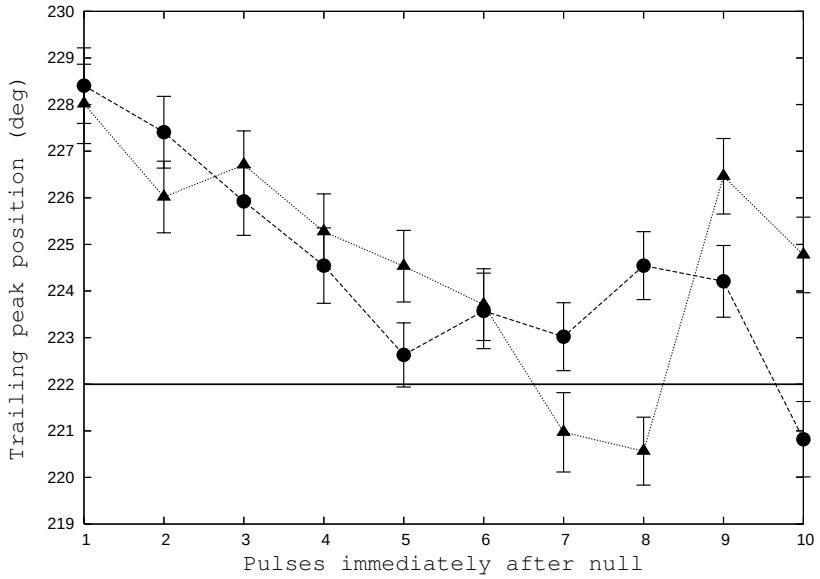

Figure 4.25: Position of the trailing peak of the average profiles from the pulses immediately after the nulls versus the corresponding pulse number at 325 MHz. Results for the epoch on 24 February 2004 are denoted by dashed line and for the epoch on 21 December 2005 are denoted by dotted line. Solid line indicates the position of the trailing peak for the normal profile ($\sim$ 222 deg).

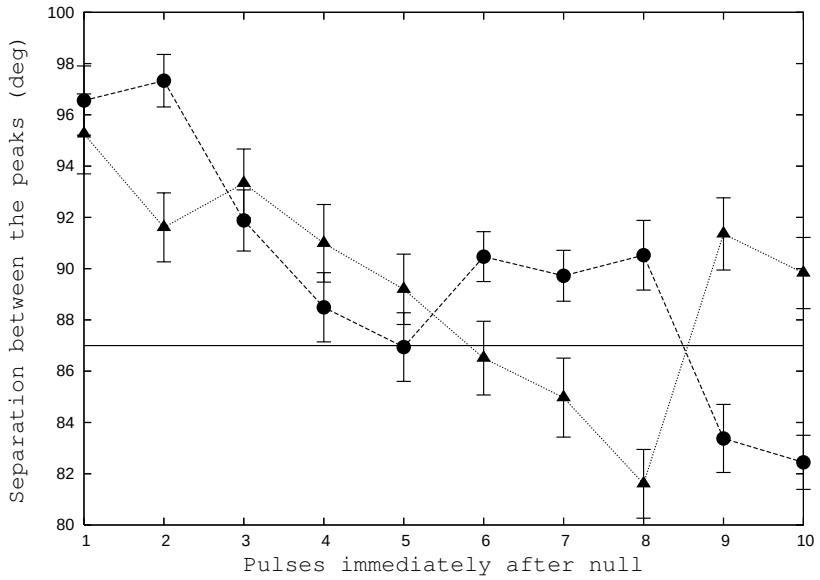

Figure 4.26: Separations between leading and trailing peaks of the average profiles from the pulses immediately after the nulls versus the corresponding pulse number at 325 MHz. Results for the epoch on 24 February 2004 are denoted by dashed line and for the epoch on 21 December 2005 are denoted by dotted line. Solid line indicates the separation between the leading and trailing peaks for normal profile ($\sim$ 86.8 deg).

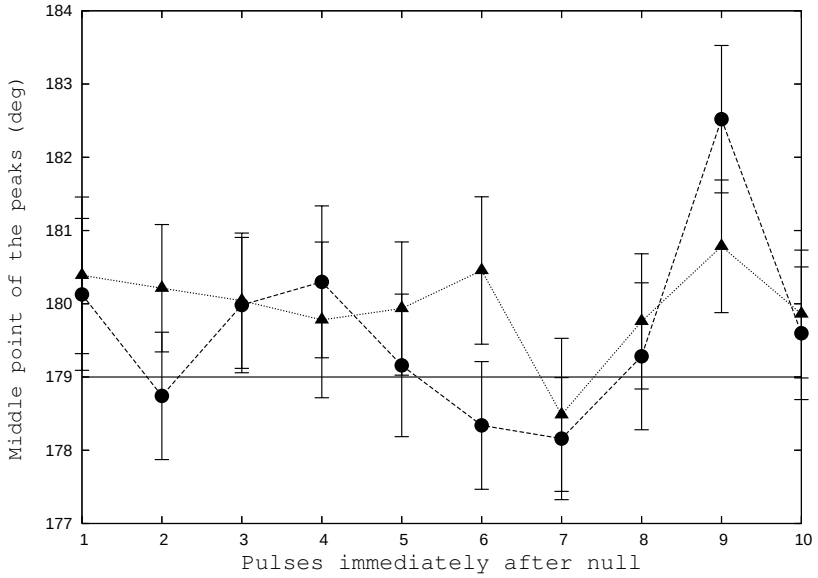

Figure 4.27: Position of middle point of the leading and the trailing peaks of the average profiles from the pulses immediately after the nulls versus the corresponding pulse number at 325 MHz. Results for the epoch on 24 February 2004 are denoted by dashed line and for the epoch on 21 December 2005 are denoted by dotted line.

(a) Nature of transitions from the bursts to the nulls and vice verse

Our investigations reveal the fact that for the inner region of PSR B0818−41, the nature of the transitions from the bursts to the nulls are different from the transitions from the nulls to the bursts. For the inner region, the switching off of pulsar radiation at the beginning of the nulls are not abrupt, but are gradual. The time spent in this gradual switching off of pulsar radiation varies with a mean of 10 pulse periods. The transitions from the nulls to the bursts are found to be rather abrupt for the inner region. This imply that, due to some reason, the energy of magnetosphere decreases gradually and the pulsar starts nulling, during the nulls the pulsar regains the energy and the emission abruptly comes back. Hence, the mechanism that cause the nulls is associated with fast rise and slow fall time. However, the intensity modulations before and after the nulls, are observed only for the inner region, but not evident for the leading and the trailing outer regions.

It would be important to know if PSR B0818−41 is a unique pulsar to show such gradual decrease of pulse intensity before the nulls and abrupt

rise of the same after the nulls. Detailed investigation of PSR B0031−07 by Vivekanand (1995) reports that most of the time bursts and nulls are abrupt, but in ≈ 20% of cases the onset of nulling is slow, occurring over one to several periods. Fig. 4 of Rankin & Wright (2008) plots pulse energy versus pulse number for PSR J1819+1305. For this pulsar, we note a clear signature of gradual decrease in energy in last active pulses before the nulls and sharp transition from null to burst state with outshining first active pulses after the nulls, which is however not mentioned by the authors in the paper. PSR B1944+17 is the only other pulsar for which the transitions from the nulls to the bursts are quite different in character from the transitions from the bursts to nulls. Deich *et al.* (1986) reported that the switching off of this pulsar is preceded by a slow ($\sim 3\ P_1$) decay in average intensity. Here, we also make a note of the fact that unlike the inner region, intensity modulations before and after the nulls are not evident for the outer regions of PSR B0818−41. This is possibly because of the central line of sight cut and presence of strong modulation at 18.3 P_1 periodicity for the outer regions. This helps us to postulate that, although the intensity modulation around nulls are present for all the pulsars, we do detect them only for the favorable cases with grazing LOS cuts. However, this warrants detailed investigation of the intensity modulation around the nulls for other pulsars for which the LOS grazes the emission rings.

(b) Intensity modulation around the nulls

For PSR B0818−41, the inner region of the last active pulse before the nulls are dimmer and the first active pulse after the nulls outshines the normal ones. On the average, at 325 MHz, the inner region of pulses immediately after the nulls are about a factor ~ 3 more intense than that before the nulls. At 610 MHz this ratio goes down to ~ 2.2, indicating some frequency dependence of this ratio. We report that, the intensity of the inner region of first few active pulses immediately after the nulls outshines the normal pulses. In other words, the first few active pulses immediately after the nulls have brighter inner region than the pulses sufficiently after : $I_a/\langle I_a(4p:10p)\rangle$ has a mean of about 2 for 325 MHz and about 1.4 for 610 MHz. This imply a systematic trend of energy fluctuation of the pulsar magnetosphere − before all the nulls the energy of the magnetosphere is less and after all the nulls

energy becomes more. Evidently, the mechanism which is responsible for the nulls also regulates intensity in the pulse beam.

Though, quantitative study of relative dimness is lacking in either case, last active pulse before the nulls are reported to be dimmer than the normal pulses for PSR B0809+74 (Lyne & Ashworth, 1983) and PSR B1944+17 (Deich *et al.*, 1986). Whereas for PSR B0031−07 no significant decrease in the brightness of the last active pulse before the nulls is observed (Vivekanand, 1995). Relative brightness of the first active pulse after the nulls are reported to be more for PSR B0809+74 and PSR B1944+17, but for PSR B0031−07 no significant increase in energy of the first active pulse after the nulls is observed.

(c) Null versus burst length

We found that lengths of the neighboring nulls and bursts are independent for PSR B0818−41. We do not observe any correlation between the intensities around nulls (both before and after) with the duration of the neighboring nulls and bursts. Our result is similar to the study of PSR B0809+74 by van Leeuwen *et al.* (2003), who found that the lengths of neighboring nulls and bursts are independent. This may indicate that there is no systematic dependence between the mechanism for nulling and the duration of nulls and bursts.

(d) Average profile from pulses around the nulls

The average profile from the first active pulse immediately after the nulls follows similar shape as the normal profile but with a increased intensity (in the form of a bump) in the inner region which is not present in the normal average profile. In addition, the leading and the trailing peaks appear to be of similar intensity, whereas for the normal profile the trailing peak is significantly more intense. The average profile of the last active pulse before the nulls are less intense than the normal profile but with similar shape. From the change of profile shape around the nulls, it is evident that the mechanism which is responsible for the nulls also changes the intensity distribution in the pulse beam.

In this context, we review the existing study regarding the shape of the

average profiles around the nulls for the other pulsars. For PSR B0031−07, Vivekanand (1995) did not find any significant difference in the average profiles from the first active pulse after the nulls, last active pulse before the nulls and the normal average profiles. van Leeuwen *et al.* (2003) reported that the average profile from the first active pulse after the nulls is stronger and the last active pulse before the nulls is weaker than the normal profile for PSR B0809+74. However, the average profiles of the pulses immediately before and after the nulls have similar shape to the normal profile for this pulsar. Janssen & van Leeuwen (2004) reported significantly different shapes of the average profiles of the pulses before and after the nulls for PSR B0818−13 − the average profile of the last and first active pulses are observed to be double peaked, whereas the normal average profile are observed to be single peaked. For PSR B1944+17, Deich *et al.* (1986) reported that the last pulse before null has a shape that is quantitatively different and more variable than the shapes of other pulses. Hence for the majority of pulsars, for which average profiles around the nulls are investigated, exhibits evidences for association of nulls with the changes the intensity distribution in the pulse beam.

Investigating the average profiles from the pulses immediately after the nulls we observe − for the average profile from the first active pulse after the nulls the inner region is of increased intensity and this intensity rapidly goes down for average profile from the second active pulse after the nulls, up til around the average profile from sixth pulse after the nulls. After that the intensity of inner region decreases slowly and around the average profile from twentieth pulse the intensity reaches to the normal value. However, the leading peak attains its maximum value for the average profile from the second or third active pulse after the nulls and the trailing peak attains its maximum for average profile from fourth active pulses after the nulls. The average profile from the first active pulse after the nulls has equally intense leading and trailing peaks. The ratio of the leading to trailing peak decreases from 1 to the normal value of 0.6 by around fourth active pulse after the nulls. Immediately after the nulls the intensity difference between the leading and the trailing peaks and the inner region is least. This imply that, just after the nulls the magnetosphere is more uniformly illuminated.

The average profiles from the active pulses immediately after the nulls are wider than that of the normal profiles of PSR B0818−41. The profiles after

the nulls are wider in the trailing side than in the leading side, i.e. the shift of the trailing peak, of the average profiles from the pulses immediately after the nulls, from its normal position is more than the shift of the leading peak. The mid point of the profile (which is believed to indicate the position of the magnetic meridian) appear to be shifted towards the trailing side for the first few active pulses immediately after the nulls. Observed wider profiles from the pulses immediately after the nulls can be explained by considering the emission to be coming from higher height in the magnetosphere or from outer field lines.

Only other pulsar for which it is reported that the nulls are associated with the changing width of the average profile is PSR B0809+74. For this pulsar, van Leeuwen *et al.* (2003) found that peaks of average profile from the first active pulse after the nulls are shifted towards earlier longitudes. As an explanation to this, van Leeuwen *et al.* (2003) proposed that after the nulls sub beam carousel is smaller, indicating that we are looking deeper in the pulsar magnetosphere than we do normally.

(e) Drift rate around the nulls

Beside its normal and most common mode, the pulsar emits in a significantly different quasi-stable mode before (most) and after (all) the nulls. There is quite close interaction between the phenomenon of drifting and nulling for PSR B0818−41: generally the apparent drift rate decreases (some times the apparent drift rate goes to zero and stationary drift bands are observed) and then the pulsar starts nulling. After the nulls the pulsar shows either stationary or irregular drifting and it takes a while for the pulsar to resume the normal drifting.

van Leeuwen *et al.* (2003) investigated drifting around the null for PSR B0809+74, and found that drift rate just before a null does not deviate from the normal drift rate. However, drift rate after nulls is different from the normal drift rate. After the nulls PSR B0809+74 goes to a quasi-stable mode. van Leeuwen *et al.* (2003) also found that drift rates after longer nulls are lower than the normal average drift rate.

(f) Similar post-null properties for the two epochs

Strikingly, all the above results are remarkably similar (almost identical) between different epochs of observations. For example,

• The ratios, $I_a/\langle I_b(1p:10p)\rangle$ and $I_a/\langle I_a(4p:10p)\rangle$, are identical between the epochs of observations, for a given frequency.

• Corresponding average profiles from the active pulses immediately after the nulls are drastically similar between two epochs of observations.

• The intensity of the inner region (and also of the leading and trailing outer regions) of the average profiles from the active pulses immediately after the nulls versus the corresponding pulse numbers follows very similar trend for the two epochs of observations.

• Width of the average profile from the pulses immediately after the nulls versus the corresponding pulse numbers follows identical pattern for both the epochs.

Above mentioned similarities between the null state properties of the two epochs of observations demands that the conditions of the magnetosphere immediately after the nulls are very similar between different nulls. This favors some mechanism enabling persistent memory of the condition of the magnetosphere after the nulls (even if separated by widely spaced epochs), as part of the pulsar radio radiation process. Hence, the phenomenon of nulling is not abrupt or random but some systematic energy re-distribution is happening in the magnetosphere immediately before and after the nulls. This unique result, have the potential to provide further insight to pulsar radio emission mechanism and its connection to the phenomenon of nulling, but is not reported (and may not even be investigated) for any other pulsar so far.

Hence, our study of unique nulling properties of PSR B0818−41 emphasizes that nulling provides an useful tool to understand the emission of PSR B0818−41 in particular and of the pulsar population in general. Our results favors that pulsar emission is systematically ceased due to some reason during the nulls. Study of Rankin & Wright (2008) provided evidences that pulsar nulling is not random but is periodic. This combined with our result demands some systematic characteristics of the nulls.

CHAPTER 5

Results from multi-frequency study of PSR B0826−34

"As far as the laws of mathematics refer to reality, they are not certain; as far as they are certain, they do not refer to reality."
– Albert Einstein

5.1 Introduction

We described the unique drifting and nulling properties of PSR B0818−41 in Chapters 2, 3 and 4. In this chapter we present detailed multi-frequency study of PSR B0826−34, which has the widest pulse profile among the known pulsars. The earlier studies of this pulsar (Durdin *et al.* (1979), Biggs *et al.* (1985), Gupta *et al.* (2004)) have brought out some unique properties : strong evolution of the average profile with frequency, apparent nulling for 70% of time and a remarkable subpulse drift property − multiple, curved drift bands with frequent changes and sign reversals of drift rate.

Multi-frequency observations, especially when done simultaneously at the different frequencies, are very useful for the study of various aspects of the frequency dependence of pulsar radiation (see Taylor *et al.* (1975), Bartel & Sieber (1978), Bartel (1981), Bhat *et al.* (2007) etc).
(i) Average profile evolution with frequency: Each part of the average pulse profile is believed to originate in a small part of the polar region, so that the average profile represents a cut across the distributed source of emission (refer to Sect. 1.2 (a) of Chapter 1). The average profile usually get broader at lower frequencies which is called "radius to frequency mapping". Multi-frequency study of the average profiles will give us idea about the LOS cut and its evolution with frequency.

(ii) Polarization study: Polarization studies of the radio pulsars at multiple frequencies can be utilised for classification of the different types of profiles, understanding the underlying emission mechanism, determination of the geometry of the star etc (refer to Sect. 1.2 (f) of Chapter 1).
(iii) Determination of accurate DM: Dispersion measure (DM) of pulsars can be determined from single epoch simultaneous dual frequency observations (Ahuja *et al.*, 2005). Investigating the literature we notice that the DM values, reported and used for PSR B0826−34, span a fairly wide range, from 47 to 65 pc/cm^3. In this context an accurate estimation of the DM of PSR B0826−34 assumes importance. In the usual method of DM determination using multi epoch timing data, the DM value is obtained as one of the parameters of the multi epoch timing solution. Using simultaneous dual frequency observations we propose a straight forward and simple method for determination of DM value of PSR B0826−34.
(iv) Study of the pulsar in the null state: Durdin *et al.* (1979) reported that PSR B0826−34 exhibits pulse nulling (no detectable emission for the entire pulse) for at least 70% of the time. Esamdin *et al.* (2005) claim the presence of weak emission, at 1374 MHz, during the long duration nulls of this pulsar. They identify these null states as some weak mode of emission where the pulse intensity is 2% of that of the regular, strong mode, with a pulse profile that is similar to the strong mode at lower frequencies. Sensitive, multi-frequency observations at the lower frequencies should provide useful information about the behavior in the null state.
(v) Study of simultaneous subpulses: Correlated behavior of subpulses at different frequencies are reported by several studies (e.g. Taylor *et al.* (1975), Bartel & Sieber (1978), Bartel *et al.* (1981), Izvekova *et al.* (1993)), and is useful to probe the broadband nature of the emission mechanism. Furthermore, for pulsars with drifting subpulses, evolution of P_2^m (longitude separation between adjacent drift bands) with frequency can also be significant and a comparison of this with the frequency evolution of other profile parameters can be useful (e.g. Smits *et al.* (2005), Izvekova *et al.* (1993) and Rankin *et al.* (2005)). Earlier study of drift properties of PSR B0826−34 (Biggs *et al.* (1985), Gupta *et al.* (2004) and Esamdin *et al.* (2005)) report different P_2^m values at various individual frequencies which do not follow the trend predicted by profile evolution with frequency. In addition, for PSR

B0826−34, the intricate nature of the multiple drift bands itself deserves a broadband study.

For several pulsars (e.g. PSR B0329+54, PSR B1133+16, PSR B1919+21) a significant evolution of subpulse width ($\Delta\Phi_s$) with frequency is reported by Taylor *et al.* (1975). Biggs *et al.* (1985) determined $\Delta\Phi_s$ for PSR B0826−34 at 645 MHz and observed that, $\Delta\Phi_s$ is longitude dependent. We plan to measure $\Delta\Phi_s$ simultaneously at 303 and 610 MHz and non simultaneously at 157, 610 and 1060 MHz to study the frequency evolution of $\Delta\Phi_s$. We also aim to study variation $\Delta\Phi_s$ with pulse longitude, at individual frequencies.

We observed PSR B0826−34 using the GMRT, simultaneously at 303 and 610 MHz, and individually at 157, 325, 610 and 1060 MHz in total intensity mode. In this chapter we concentrate on the results from the simultaneous dual frequency observations, and supplement these, where necessary, with the results from the single frequency observations. Pulsar observations using the GMRT is detailed in Sect. 1.5 of Chapter 1. In Sect. 5.2 we cover the observations. Different sub-sections of Sect. 5.3 describe the data analysis and results for (1) average profile evolution with frequency, (2) polarization study, (3) determination of DM value from simultaneous dual frequency observations, (4) study of the pulsar in its null state and (5) subpulse studies. In Sect. 5.4 we discuss the implications of our findings.

5.2 Observations

(a) Simultaneous dual frequency observations

Using the technique of "band masking" described in Sect. 1.5 Chapter 1, we observed PSR B0826−34, simultaneously at 303 and 610 MHz with the GMRT, on October 26, 2003. We used two sub arrays, one with 5 antennas (sub array#1), operating at 303 MHz, and the other with 10 antennas (sub array#2), operating at 610 MHz. We put more antennas at 610 MHz to get desired sensitivity, because of the fact that the pulsar is weaker at 610 than at 303 MHz. The signals coming from the antennas of each sub array were added coherently in the GAC. The total bandwidth used for the observations was 16 MHz, which was divided equally between the two frequency bands by masking 8−16 MHz of the band for the antennas in sub array#1 and 0−8 MHz of the band for the antennas in sub array#2. Before observing the pulsar,

both the sub-arrays were individually "phased-up" by estimating the phases with respect to a reference antenna in each sub-array (from the correlator visibilities recorded on a point source calibrator) and applying the corrections for these back into the correlator hardware. The voltage outputs from the GAC were passed to the phased array pulsar receiver where the data were converted to intensity values and intensities from the two polarizations added to obtain the total intensity for each of 256 spectral channels, containing information from the two sub-arrays. These data were further integrated in time and finally recorded to disk at a sampling rate of 1.024 ms. During the off-line analysis we further integrated these data to a final time resolution of 4.096 ms, as this was adequate to study this wide profile pulsar. The duration of the pulsar observation was about 1 hr, in which we recorded a data stretch of 2123 pulses from PSR B0826−34, simultaneously at 303 and 610 MHz. In the first 750 of these pulses, the pulsar was in the active state and for the remaining time it was in one of its long duration null states.

(b) Single frequency observations

We observed PSR B0826−34 using a large number of GMRT antennas in phased array mode at 157, 325, 610 and 1060 MHz individually at separate epochs. These observations have significantly higher sensitivity (by a factor of 2 or more) compared to the corresponding observations from the dual frequency effort, and were carried out primarily to supplement and improve the conclusions obtained from the simultaneous dual frequency data set. In addition, some of these observations were accompanied with flux calibration observations using known point sources, which allows for absolute calibration of the pulsar's flux. A summary of the main parameters of each observing session is given in Table 5.1.

5.3 Data Analysis and Results

A suitable calibration procedure as described by Mitra *et al.* (2007) was applied to the observations which were done in full polar mode to recover the stokes parameters I, Q, U, V. The simultaneous dual frequency data for PSR B0826−34 were dedispersed separately for 303 and 610 MHz, using only the respective non-masked parts of the base-band signal. The data

Table 5.1: Table containing, (a) summary of all the observations presented in this chapter, (b) rms values for pulsar active and null state, (c) the flux of the peak of the pulsar active state and the non-detection limit for null state and (d) the mean flux for the FP, MP and IP regions of pulsar active state for all the observing sessions (see Fig. 5.1 for the positions of the MP, OP and IP windows).

Frequency (MHz)	State (Active/Null)	Date of obs	No of pulses analysed	No of antennas used	rms$^{\bullet}$ (mJy)		Flux of peak (mJy)	Non-detection limit$^{\diamond}$ (mJy)	Mean Flux (mJy)		
					MP	OP			FP	MP$^{\odot}$	IP$^{\odot}$
303†	Active	26 October 2003	750	5	371	28	1687*	-	443*	754 *	99*
	Null	-	750	5	28	28	-	31*			
610†	Active	26 October 2003	750	10	57	5	250*	-	119*	178*	123*
	Null	-	750	10	4	4	-	5*			
157‡	Active	12 December 2006	970	16	427	13	1780*	-	370*	656*	42*
	Null	-	970	16	13	13	-	23*			
325§ (*polar*)	Active	12 January 2005	940	21	304	5	1330*	-	393*	763*	62*
	Null	13 January 2005	487	17	5	5	-	7*$^{\circ}$			
610‡ (*polar*)	Active	13 December 2006	705	17	85	2	410*$^{\circ}$	-	156*$^{\circ}$	248*$^{\circ}$	166*$^{\circ}$
	Null	-	705	17	2	2	-	2*$^{\circ}$			
1060‡	Active	18 November 2006	2900	21	120	10	1310*	-	479*	485*	989*
	Null	-	2900	21	10	10	-	15*			

† : Active and null state data recorded from same simultaneous dual frequency observing session, ‡ : Active and null state data recorded from same single frequency observing session, § : Active and null data recorded from single frequency observations from different days, • : Value quoted for profile data with time resolution of 4.096 ms, ◇ : 3-sigma Non-detection limit for the null state, for profile data with time resolution of 20.048 ms, ∗ : Flux estimated using standard GMRT system parameters using relative calibration procedure, ○ : Flux estimated using absolute calibration with a flux calibrator source, ⊙ : Mean flux is calculated up to 50% intensity lavel for MP and IP, *polar* : Observations were performed in full polar mode

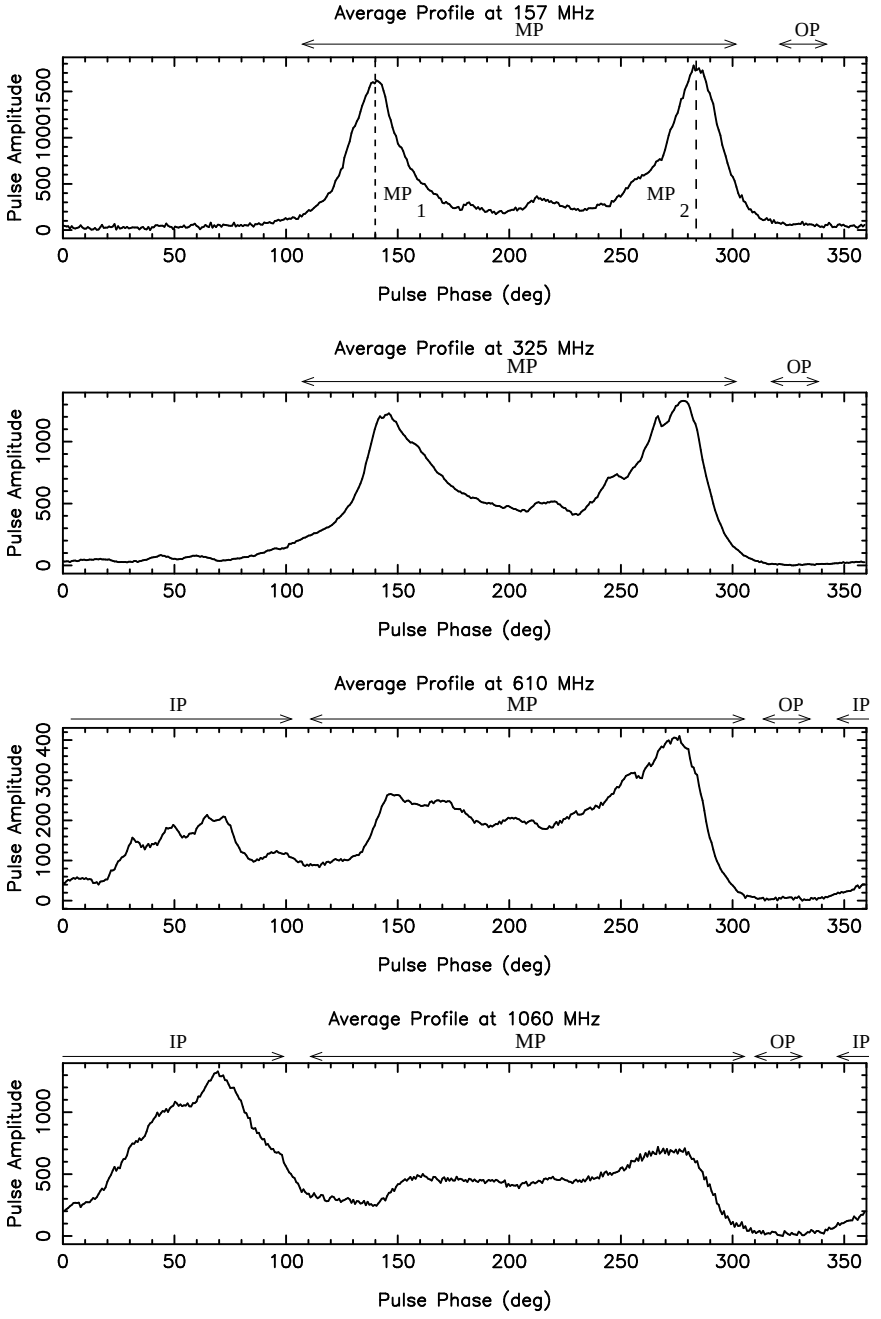

Figure 5.1: Frequency evolution of average profile of PSR B0826−34. Different panels plot the average profiles obtained from the GMRT observations at different observing frequencies, 157, 325, 610 and 1060 MHz respectively. MP, IP and OP refer to main pulse, inter pulse and off pulse, respectively (as described in the text). MP_1 and MP_2 refer to the two peaks of the MP. IP becomes stronger at high frequencies. Separation between two peaks of the MP decreases with frequency. Pulse amplitude is in mJy.

from the non-simultaneous observations at 157, 325, 610 and 1060 MHz were also dedispersed. The DM value used was 52.0, which is close to the final DM value determined by us (see Sect. 5.3(c)). The dedispersed data were put through a radio frequency interference filtering routine which detected and flagged most (but probably not all) of the instances of interference. The resulting time series were then synchronously folded with the Doppler corrected pulsar period to generate the average pulse profiles at all the radio frequency bands, which are shown in different panels of Fig.5.1.

(a) Average Profile evolution with frequency

Fig. 5.1 presents the average profiles at four different observing frequencies. Emission is present over a wide longitude range in the profile. We identify two emission regions of the pulse profiles, main pulse (MP) and inter pulse (IP). These two emission regions of the pulse profiles are labeled as MP − roughly from 120 deg to 300 deg of pulse longitude, and IP − roughly form 10 deg to 100 deg, as marked in the panels of Fig. 5.1. In addition, we identify an off pulse region (OP) in Fig. 5.1 − roughly from 310 deg to 350 deg pulse longitude. With frequency there is a remarkable evolution of the pulse profile observed for this pulsar. Though, only MP emission and no IP emission is observed at 157 MHz, with increase of frequency the IP becomes stronger. It appears that the MP reduces in strength relative to the IP as one goes from lower to higher frequencies, and IP actually dominates over the MP at frequencies above 1 GHz. Frequency evolution of the average profile is in accordance with the earlier studies of this pulsar by Durdin *et al.* (1979), Biggs *et al.* (1985) and Gupta *et al.* (2004). The MP consists of two distinct peaks (denoted by MP_1 and MP_2 in Fig. 5.1). The component separation between these two peaks ($\Delta\Phi$), listed in Table 5.4, reduces with increasing frequencies.

(b) Polarization study

Fig. 5.2 and 5.3 present the polarization profiles of PSR B0826−34 at 325 and 610 MHz. Polarization profiles at 325 and 610 MHz have better signal to noise than the published average profiles at 408 and 610 MHz by Biggs *et al.* (1985), and reproduces the basic features reported by them. Significant

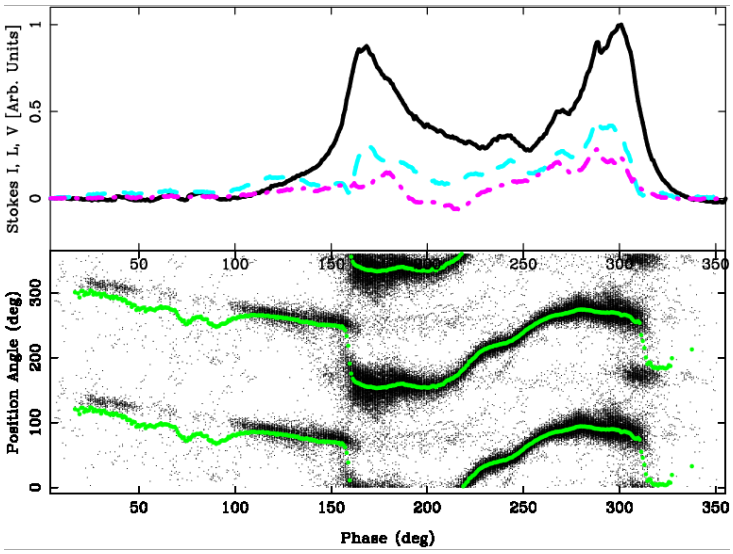

Figure 5.2: PA histogram for the 325 MHz pulse sequence for the observations on 12 January 2005. The upper panels show the average total power, total linear and circular polarizations and the lower panel gives the PA density. The PA values are plotted twice for clarity.

amount of linear polarization is observed in the main pulse region ($\sim$ 38% at 325 MHz and $\sim$ 36% at 610 MHz). The average profile for the linear polarization follows the general shape of the total intensity profile. However, in the inner region of the MP, most of the power in total intensity is linearly polarized which is not true for the outer edges. Maximum linear polarization is around 70%, near the inner part of the MP at 325 MHz (Fig. 5.2). At 610 MHz, the percentage of linear polarization is observed to be less for the leading side. Average linear polarization falls off faster at the edges of the profile and depolarization is observed at the outside edges of the profile. For the 610 MHz observations, linear polarization is also observed in the IP region. Interestingly, the region joining the MP and the IP emission has maximum of about 90% linear polarization. Fig. 5.2 and 5.3 shows that the PA roughly follows typical "S" shaped curve across the MP at both 325 and 610 MHz. In Fig. 5.4, we plot the average PA sweep under the MP for 325 and 610 MHz, for a closer comparison. We observe that the slope of the PA curve is flatter in the central region of the profile, steeper in the outer regions and even more flatter (almost horizontal) under the peaks. Although, PA sweep under the MP are quite similar for 325 and 610 MHz, the PA sweep

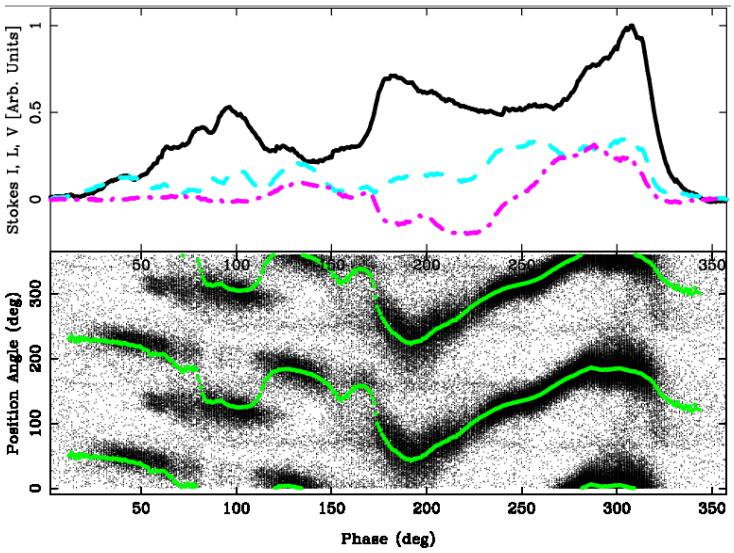

Figure 5.3: PA histogram for the 610 MHz pulse sequence for the observations on 13 December 2006. The upper panels show the average total power, total linear and circular polarizations and the lower panel gives the PA density. The PA values are plotted twice for clarity.

at 325 MHz near the leading edge of MP is flatter than that of 610 MHz (Fig. 5.4). From the PA histograms plotted in Fig. 5.2 and 5.3, we observe OPM jumps at the edges of the MP at 325 and 610 MHz, which explains the observed depolarization at the outside edges of the MP. Near the edges of the IP we observe somewhat non orthogonal mode jumps ($\sim$ 70 deg jumps), at 610 MHz.

Significant circular polarization is observed ($\sim$ 15%) in the MP region. Circular polarization changes sign near the center of the MP for both 325 and 610 MHz.

RVM fit to the PA sweep:

While fitting RVM (Radhakrishnan & Cooke, 1969) to the PA sweep at 325 and 610 MHz, we used the symmetry about magnetic axis i.e 0$<\alpha<$180 deg (e.g. Everett & Weisberg (2001) and Johnston & Weisberg (2006)), rather than symmetry about the magnetic equator, i.e. $0 < \alpha < 90$ deg (e.g. Lyne & Manchester (1988), Narayan & Vivekanand (1982), Rankin (1990), Rankin (1993) etc), as is also used for PSR B0818−41 in Chapter 3. Our attempt to fit RVM to the PA curve corresponding to the MP region at 325 MHz gives

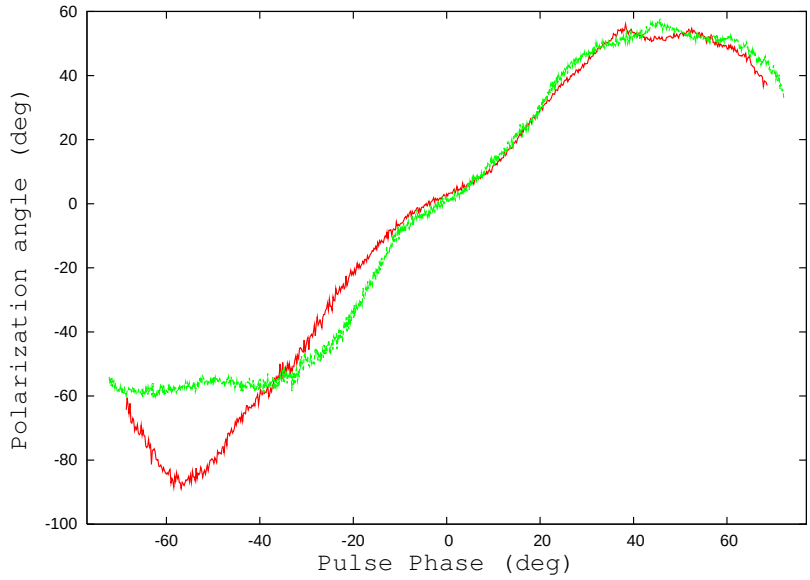

Figure 5.4: PA under the main pulse for 325 (red) and 610 (green) MHz.

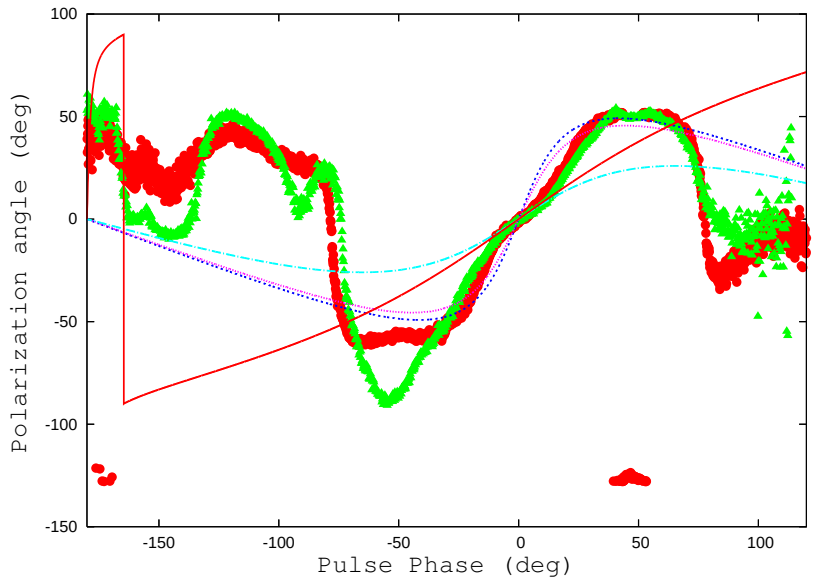

Figure 5.5: PA under the main pulse for 325 (red circles) and 610 (green triangles) MHz, and the RVM curve for $\alpha \sim 53$ deg and $\beta \sim 75$ deg from Biggs *et al.* (1985) (red solid line), $\alpha \sim 7.6$ deg and $\beta \sim 10$ deg from Biggs *et al.* (1985) (pink dotted line), $\alpha \sim 2.5$ deg and $\beta \sim 1$ deg from Gupta *et al.* (2004) (sky-blue dash-dot),$\alpha \sim 9.8$ deg and $\beta \sim 3.2$ deg from one of the trial fit from this work (dark blue short dash).

reasonable fit with $\alpha \sim 9.8$ deg and $\beta \sim 3.2$ deg, which is an outer LOS geometry. Since the PA curve is flatter in the central region and relatively steeper in the outer region and even more flatter under the profile peaks, it is difficult to have an unique fit to the PA sweep that satisfy the entire sweep corresponding to the MP equally well (Fig. 5.5). We note that the simulated RVM sweep for $\alpha \sim 9.8$ deg and $\beta \sim 3.2$ deg, when extended to the IP, satisfy part of the PA sweep under the IP. However, this does not satisfy part of PA sweep with somewhat non orthogonal jump under the IP. This geometry is compared to the geometries suggested by other studies of this pulsar in the literature in Sect. 5.4(b).

(c) Determination of accurate DM

A method of DM determination using simultaneous dual frequency observations is described by Ahuja *et al.* (2005). In that method, the amount of delay within a pulse period is estimated by cross correlating the average pulse profiles of different frequency bands for different values of sample lags. The value of lag, at which the cross correlation function peaks, will correspond to the time delay of pulse arrival between the two observing frequencies. They estimated the DM value from this time delay. But the method of DM determination followed by Ahuja *et al.* (2005), is unlikely to work for wide profile pulsars, like PSR B0826−34. Moreover, the DM determination becomes tricky for PSR B0826−34, because of complex and strong frequency evolving pulse profile. In the following we determine the DM value of PSR B0826−34 using single epoch simultaneous dual frequency observations.

In order to compute the dispersion delay between the profiles at the two frequencies, we need to establish a fiducial point that is expected to remain intrinsically fixed at a pulse longitude, even as the pulse profile evolves with frequency. For PSR B0826−34, we choose the mid-point of the two peaks of the MP of the average profile as the fiducial point. The DM is estimated from the well known formula that relates the difference in travel time Δt (in s) at the two radio frequencies, f_1 and f_2 (in MHz), as follows:

$$\Delta t = K\left(\frac{1}{f_1^2} - \frac{1}{f_2^2}\right) DM \tag{5.1}$$

where $K = \frac{e^2}{2\pi mc} = \frac{1}{2.410331\times10^{-4}}$ MHz^2 cm^3 s pc^{-1} (see e.g. Backer *et al.*

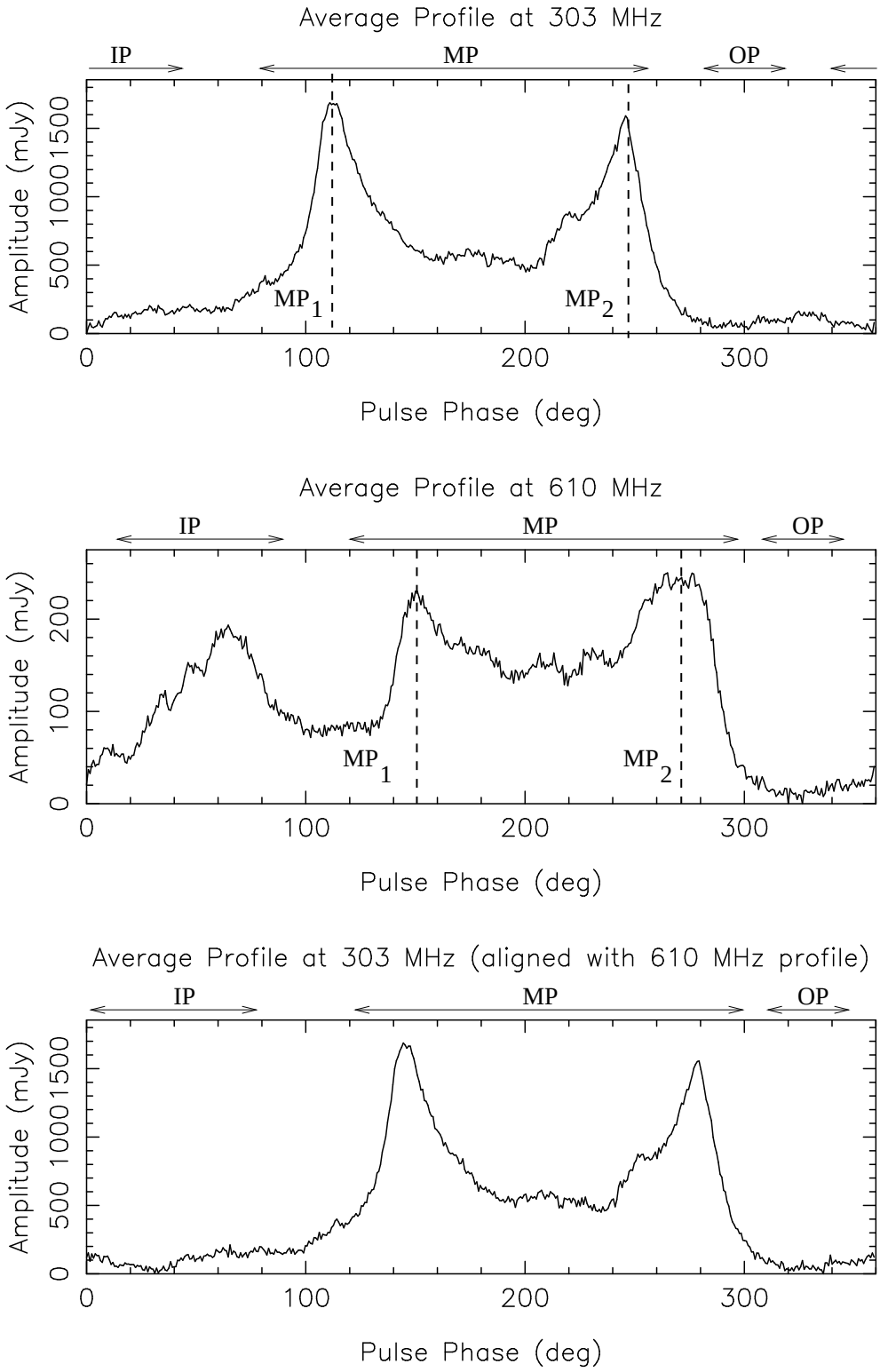

Figure 5.6: Average profiles for PSR B0826-34 at 303 and 610 MHz (upper two panels) from simultaneous dual frequency observations on 26/10/2003. The third panel shows the 303 MHz profile, aligned to the 610 MHz profile after correction for the dispersion delay. MP, IP and OP refer to main pulse, inter pulse and off pulse, respectively (as described in the text); MP_1 and MP_2 refer to the two peaks of the MP. The pulse amplitude is in mJy.

(1993)) and f_1 , f_2 are the reference frequencies with respect to which dedispersion has been done for the two bands: f_1=311 MHz, f_2=626 MHz.

As shown in Ahuja *et al.* (2005), the measured time delay (Δt) can be expressed as,

$$\Delta t = (N \times P) + P_\epsilon \tag{5.2}$$

where N is the integer number of pulsar period delay, P_ϵ is the delay within a pulse period and P is the Doppler corrected pulsar period. N is estimated using the observing frequencies, the pulsar period and a first guess DM value. For DM values around 52, it is easy to show that N is equal to 1 for our frequency combination.

P_ϵ is estimated from the position difference of the fiducial point between 303 and 610 MHz pulse profiles. To determine the position of the fiducial points at either of the two frequencies, we first estimate the position of the two peaks of the MP, by fitting second order polynomial functions. Here, the errors in the estimation of the location of the peaks, σ_{MP_1} and σ_{MP_2}, are smaller at 303 MHz, as compared to the corresponding values at 610 MHz, corresponding to the more complex structure of the profile peaks at 610 MHz (Fig.5.6). Using the inferred location of the fiducial points at the two frequencies, P_ϵ is estimated as 161.1 ms. The error in this estimate depends on the error in the estimate of the fiducial point ($\sigma_{x_{FP}}$), which follows from the error associated with the estimation of the position of MP_1 and MP_2 at the individual frequencies:

$$\sigma^2_{P_\epsilon} = \sigma^2_{x_{FP_{303}}} + \sigma^2_{x_{FP_{610}}}, \;\; \sigma^2_{x_{FP}} = \sigma^2_{MP_1} + \sigma^2_{MP_2} \tag{5.3}$$

Using these relationships, and a Doppler corrected period of 1.84881 s, we obtain a value of 52.2 pc/cm^3 for the DM of this pulsar, with an error of $\pm$ 0.6pc/cm^3. The comparison of these results with the other DM values in the literature is discussed in Sect. 5.4(c).

(d) Study of the pulsar in null state

Both short ($\sim$ few pulses) and long duration ($\sim$ few hundred pulses or more) nulls are present in our simultaneous dual frequency data. Fig. 5.7 shows the subpulse patterns at 303 and 610 MHz. For the initial 750 pulses, the pulsar was mostly in an active state except for a few short duration nulls

which appear to be simultaneous at the two frequencies (e.g. pulse # 250 to pulse # 260, pulse # 414 to pulse # 421, pulse # 613 to pulse # 621 and pulse # 683 to pulse # 691, in Fig. 5.7).

After the first 750 pulses, the pulsar goes into a long, apparently null state, and this happens simultaneously at both the frequencies. The pulsar remains in this state for the rest of the observations (about 1373 pulses). We obtain the average profile of the active state by integrating the first 750 pulses. Similarly, an average profile of the apparent null state of comparable duration is obtained from the next 750 pulses (see Fig.5.8). We see that during the null state, there is no evidence of any emission that matches with the active state average profile for the MP or IP regions, at either of the two frequencies. The mean power level in the null state profiles is comparable to the mean level of the OP region of the corresponding active state profiles. The fluctuations of the signal level in the null state profiles, though not completely Gaussian noise-like (probably due to low-level unexcised interference and other sources of "red" noise), show no correspondence with the features in the active state profiles. Furthermore, these features in the null state profiles have no resemblance or correlation between the simultaneous data at 303 and 610 MHz, indicating that these are not genuine profile features. In order to further check for any short duration bursts of strong emission in the null state, we divide the data (the first $\sim$1500 pulses in the observation) into 20 blocks and compared the average profiles from these blocks. For the first 10 blocks, during which the pulsar is in the active state, we see the characteristic pulse profile at either of the frequencies. For the next 10 blocks, during which the pulsar is in the null state, we do not see any systematic signature of emission, at either of the two frequencies, in any one of the 10 blocks. Fig. 5.11 shows a similar plot with the data divided in 8 blocks, where for first four blocks the characteristic pulsar profile was seen and for the rest the pulsar nulls.

For a more thorough investigation of the null state, we compare the rms values for the MP, OP and full pulse (FP) windows of the integrated pulse profiles (see Table 5.1). The rms during the pulsar null state is similar for all the windows (MP, OP and FP) and is also similar to the rms of the OP region of the pulsar active state. These rms values are much smaller than the rms of the MP window of the active state, and their ratios to the corresponding mean values are, to first order, consistent with thermal noise statistics. This

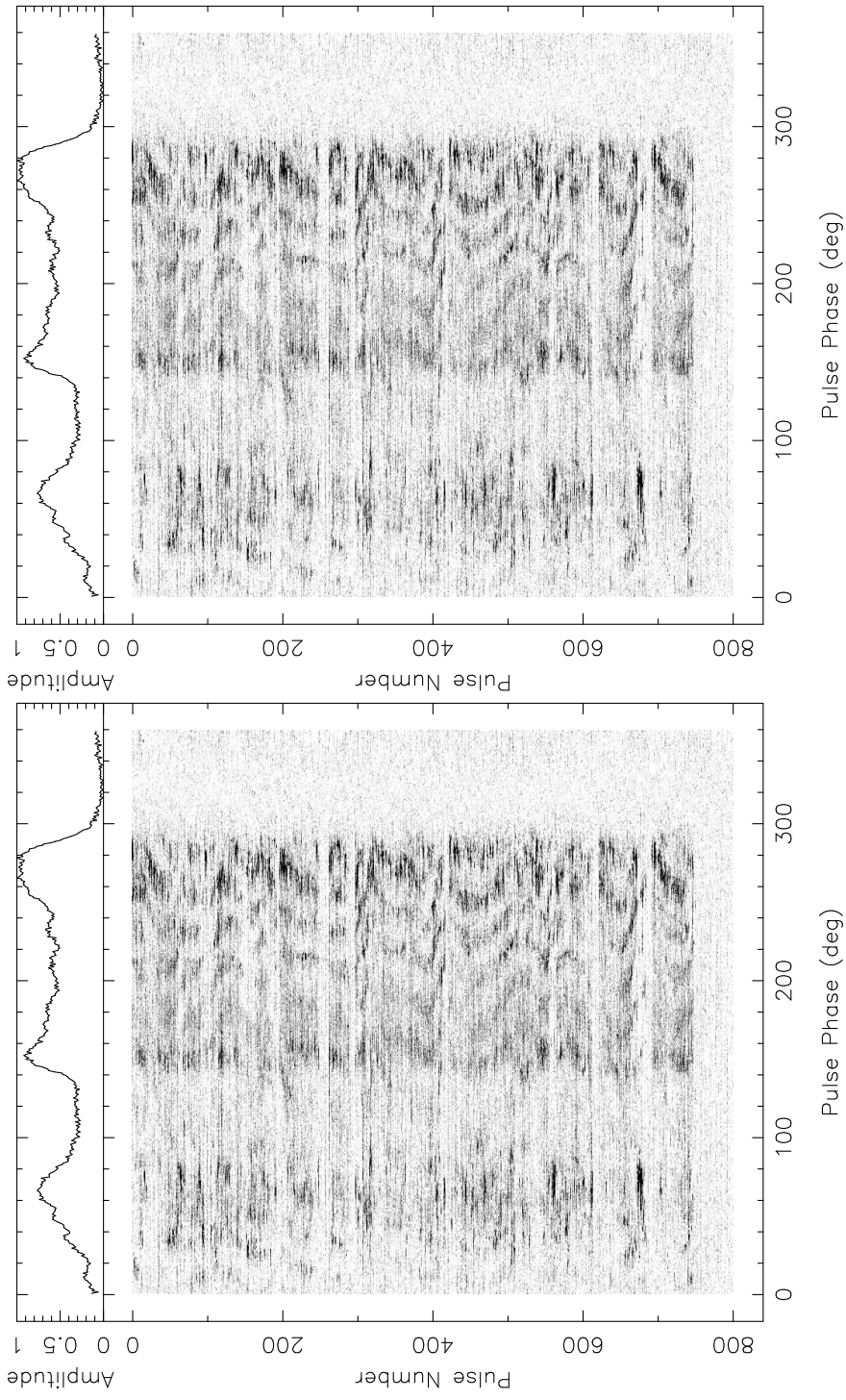

Figure 5.7: Gray scale plot of single pulse data for first 800 pulses, from the simultaneous dual-frequency observations on 26 October 2003, at 303 (left panel) and 610 MHz (right panel).

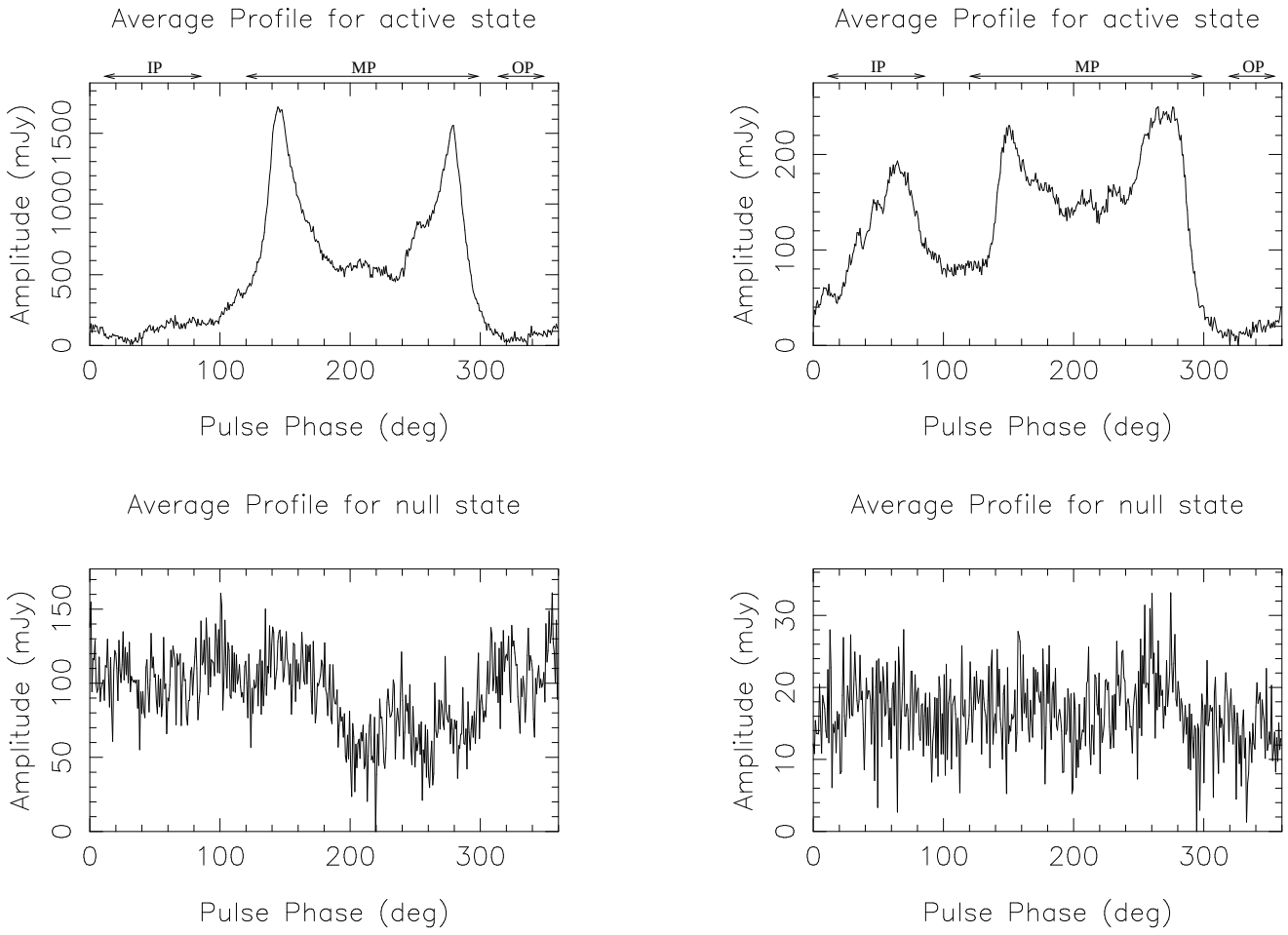

Figure 5.8: Average profiles in the active and null states, from the simultaneous dual-frequency observations on 26 October 2003, at 303 (left panel) and 610 MHz (right panel). The amplitude scale is in mJy.

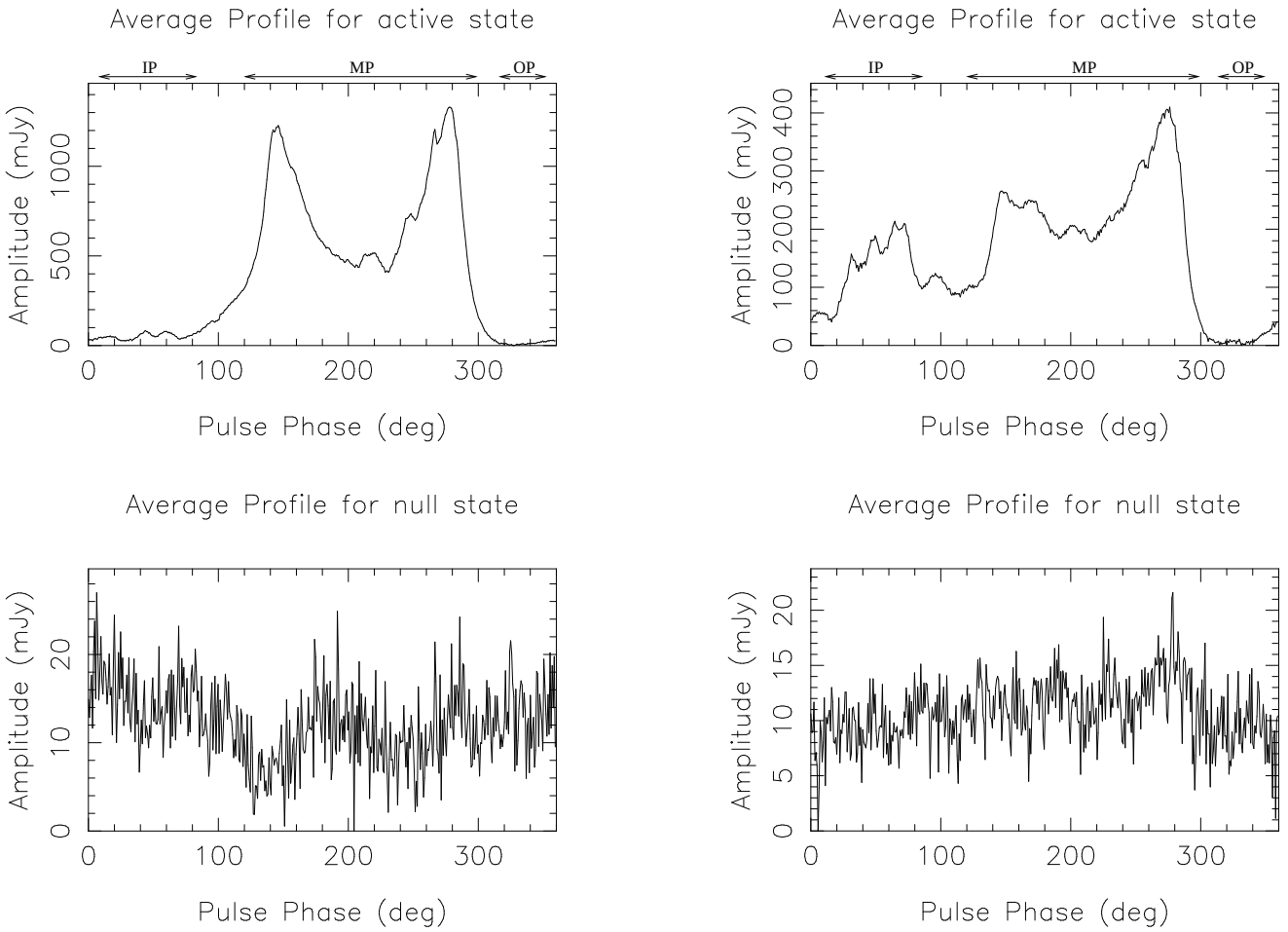

Figure 5.9: Same as Fig. 5.8 from higher sensitivity single frequency observations on 12 December 2005 at 325 (left panel) and on 13 December 2006 at 610 MHz (right panel).

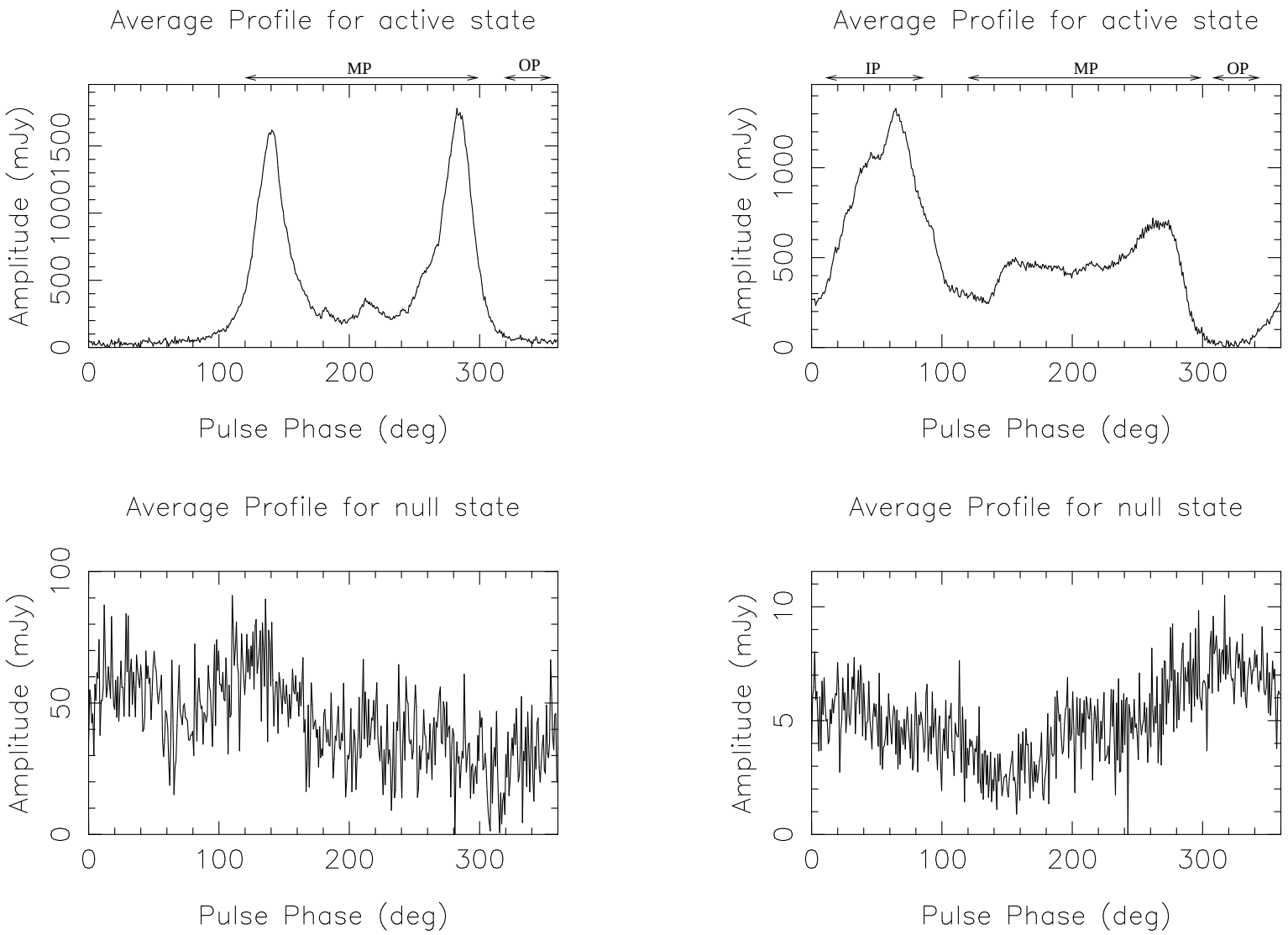

Figure 5.10: Same as Fig. 5.8 from higher sensitivity single frequency observations on 12 December 2006 at 157 (left panel) and on 18 November 2006 at 1060 MHz (right panel).

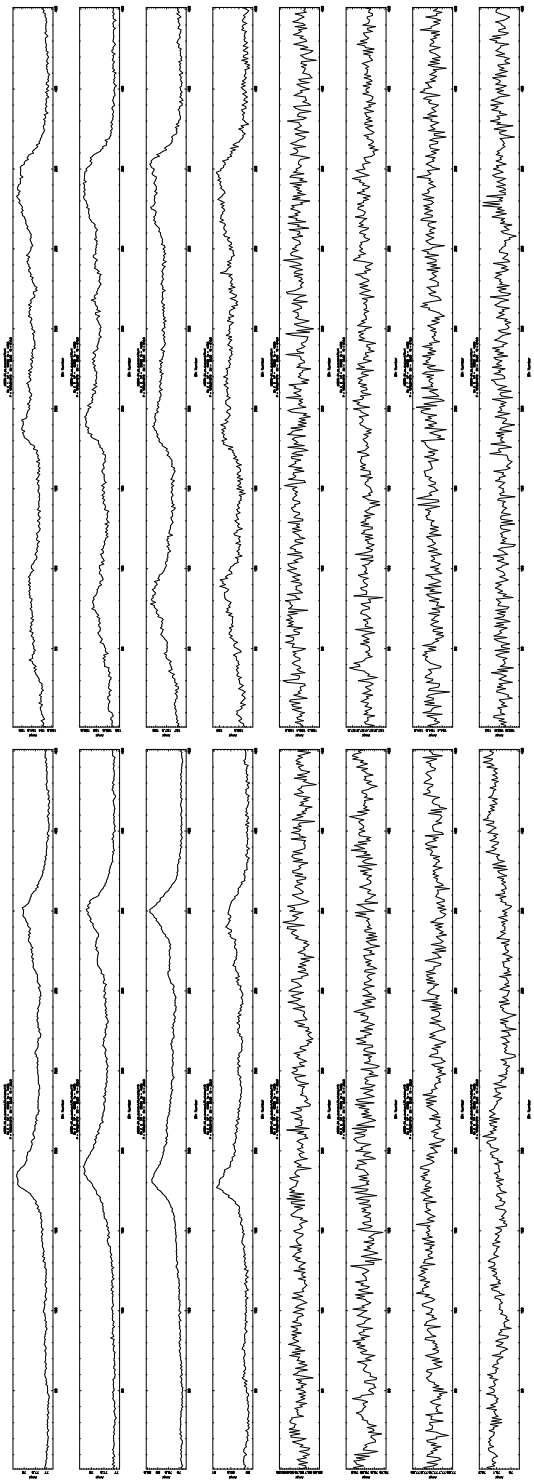

Figure 5.11: Average profiles in the active and null states with the data divided in 8 blocks from simultaneous dual frequency observations on 26 October 2003. The data is divided in 8 blocks at 303 (left panel) and 610 MHz (right panel), for the first four blocks the pulsar is in active state and then the pulsar is null state. We do not see any systematic signature of emission, at either of the frequencies.

behavior is consistent for both the frequencies, indicating that the null state signal is similar to the OP region of the pulsar's active state, and contains no detectable level of emission from the pulsar. To further constrain the above conclusion, we integrated the profile data to a time resolution of 20.048 ms, which is a reasonable compromise between integrating all of the pulsar's signal into a few bins and retaining enough time resolution to detect any large scale emission structure. Comparing the peak deflection in the active state profiles with three times rms of the fluctuations in the null state profiles, we conclude that there is no emission in the null state down to a level of $\sim$ 2% of the peak in the active state, for either frequency.

The dual frequency observations used a limited number of antennas at each frequency and are not very sensitive. In order to achieve better sensitivity, we use the results from the single frequency observations carried out with larger number of antennas in phased array mode. Fig. 5.9 and Fig. 5.10 show the active and null state profiles from these observations. Whereas the active and null state profiles for the 325 MHz observations are from different days, those for the 157, 610 and 1060 MHz observations are cases where the pulsar transited from the active to null state during the same observing session.

As can be seen, there is no evidence for systematic emission from the pulsar in the null state at any of the frequencies. Non-random features in the null state profiles, where seen, have no correspondence between different frequencies, or even for the same frequency at different epochs.

Comparing the peak deflection in the active state profile with three times the rms of the fluctuations in the null state average profile at a time resolution of 20.048 ms, we conclude that at 610 MHz there is no emission in the null state down to a level of $\sim$ 0.5 % of the peak in the active state. At 1060 MHz no signature of emission is seen in the null state profile down to $\sim$ 1.2% of the peak in the active state. Similarly, at 157 MHz the limit is $\sim$ 1.3%.

From the absolute flux calibration available, we determine the flux of the peak for 610 MHz active state to be $\sim$ 403 mJy, and the 3-sigma non-detection limit in the null state corresponds to about 2.3 mJy. Similarly, from the absolute flux calibration available for the null state observations at 325 MHz, we find the 3-sigma non-detection limit at this frequency to be $\sim$ 7 mJy. For the cases where we do not have any flux calibrator source

observed, we follow a relative calibration procedure, using the knowledge of the observing parameters and the background sky temperature near the source. As a crosscheck we find that, for the single frequency 610 MHz observations, the flux values estimated with absolute and relative calibration are similar. In Table 5.1 we list the flux at the peak and the mean flux for FP, MP and IP regions at different frequencies. From simultaneous dual frequency observations we see that the FP and MP has quite steep spectral index $\alpha_{fp}\sim$ -1.9 and $\alpha_{mp}\sim$ -2.2 whereas the IP has flatter spectral index, $\alpha_{ip}\sim$ 0.1 (where α is defined by $I \propto \nu^{\alpha}$). These are similar to the results reported by Biggs *et al.* (1985) between 408 and 645 MHz. From single frequency observations at 610 and 1060 MHz, the calculated spectral indexes are, $\alpha_{fp}\sim$ 2.2, $\alpha_{mp}\sim$ 1.3, $\alpha_{ip}\sim$ 3.4. Hence, the spectral index α for this pulsar is different for different profile components and also evolves with frequency. This can be easily visualized in Fig. 5.12.

To summarize, our results show similar limits ($\sim$ 1% of peak of active state profile, or better) of non-detection of emission in the null state, at frequencies of 157, 303, 325, 610 and 1060 MHz. These results are in apparent disagreement with those obtained at 1374 MHz by Esamdin *et al.* (2005), who report presence of weak emission in the apparent null state. We discuss the implications of this in Sect. 5.4(d).

(e) Study of subpulse emission

We align the 303 and 610 MHz data from the simultaneous dual frequency observations, by removing the initial 2009 ms of data (corresponding to the dispersion delay) from the 303 MHz data. This allows us to directly compare the corresponding single pulses from these two frequencies.

Pulse energy correlation

To study the correlation of pulse energy fluctuations as a function of frequency and pulse lag, we compute the correlation of the total energy under the MP (hereafter TE_{mp}), for different pulse lags, individually at 303 and 610 MHz, as well as between these two frequencies. For a train of single pulses with pulse number k, $1 \leq k \leq M$, the correlation function is given by

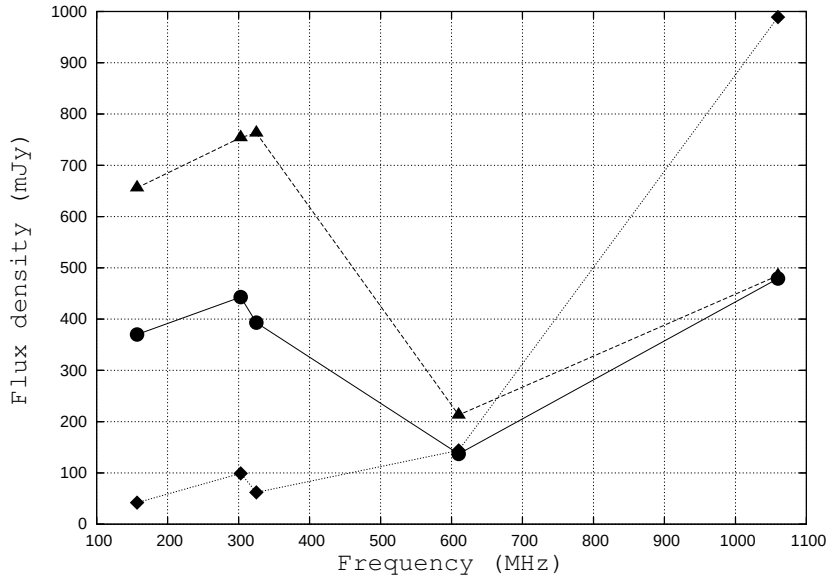

Figure 5.12: Spectra from calculated mean flux densities (Table 5.1) for FP (solid), MP (dashed), IP (dotted).

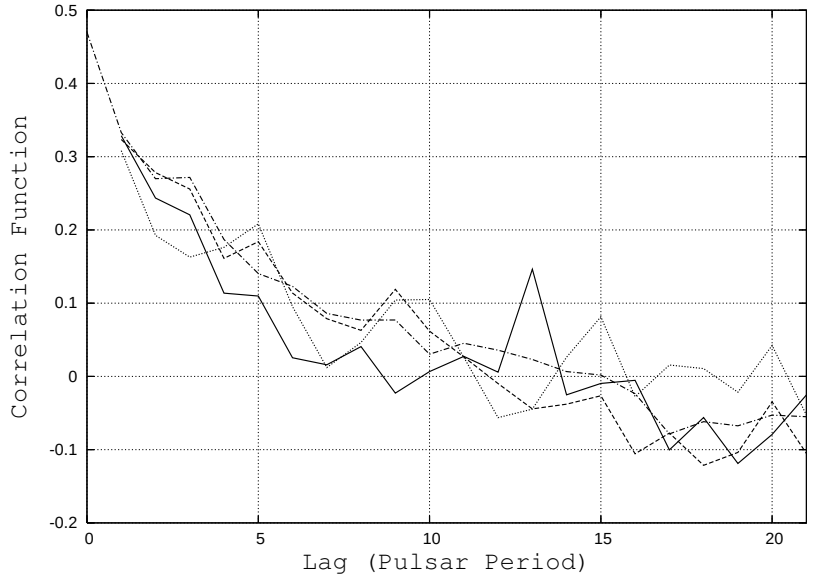

Figure 5.13: Plot of correlation function versus pulse lag from simultaneous dual frequency observations on 26/10/2003: autocorrelation function of TE_{mp} for 303 MHz (solid), same for 610 MHz (dashed), autocorrelation function of TE_{ip} at 610 MHz (dotted), cross correlation functions of the TE_{mp} between 303 and 610 MHz (dash-dot). The plot for the autocorrelation function starts from unit lag for all the three cases.

(Bartel, 1981),

$$C(l) = \frac{\frac{1}{M-l}\sum_{k=1}^{M-l}(I_{f_i}(k) - \langle I_{f_i}\rangle)(I_{f_j}(k+l) - \langle I_{f_j}\rangle)}{(\sigma_{f_i}^2\sigma_{f_j}^2)^{1/2}} \tag{5.4}$$

where i, j denote the concerned frequencies (303 or 610 MHz); $I_{f_i}(k)$ and $I_{f_j}(k)$ are the TE$_{mp}$ of the k th pulse for frequencies i and j, respectively; $\langle I_{f_i}\rangle$, $\langle I_{f_j}\rangle$ are the mean energies, and σ_{f_i}, σ_{f_j} are the variances for TE$_{mp}$ over M pulses. A similar procedure is adopted for the IP, where applicable. Fig. 5.13 shows the correlation function (for pulse number 1 to 750), for autocorrelation of TE$_{mp}$ at 303 and 610 MHz, autocorrelation of TE$_{ip}$ at 610 MHz and cross correlation of TE$_{mp}$ between 303 and 610 MHz, as a function of increasing pulse lag. The TE$_{mp}$ for the active state (pulse number 1 to 750), with zero pulse lag (i.e. $l = 0$), is 47% correlated between 303 and 610 MHz. Moreover, this level is very similar to the correlation at each of the two frequencies. All these three curves (as well as that for the autocorrelation of the IP at 610 MHz), follow very similar shapes with pulse lag, and show positive correlations out to fairly large lags: about 11 periods. Similar results are obtained from correlation studies of the higher sensitivity single frequency data. Furthermore, from the single frequency data, we find a crosscorrelation between TE$_{mp}$ and TE$_{ip}$ of about 22% at 610 MHz and 17% at 1060 MHz. In the autocorrelation function for 303 MHz (Fig. 5.13), and also in the autocorrelation of the 610 MHz data from the single frequency observations (not shown in Fig. 5.13) a secondary maximum is present at pulse lag $l = 13$, which is not consistently seen in all correlation functions. These different aspects of the correlation results, including comparison with existing results for other pulsars, are covered in Sect. 5.4(e).

Study of subpulse drifting

Drifting subpulses observed simultaneously at 303 and 610 MHz (e.g. Fig. 5.7), broadly reproduce the features reported by earlier studies at various individual frequencies (Biggs *et al.* (1985), Gupta *et al.* (2004) and Esamdin *et al.* (2005)). For a closer investigation of the simultaneous subpulse behavior, we zoom into a sequence of 200 pulses (pulse # 400 to pulse # 600) as shown in Fig. 5.14. At any given time, the simultaneous multiple subpulses present in the main pulse window follow the same drift rate and sign,

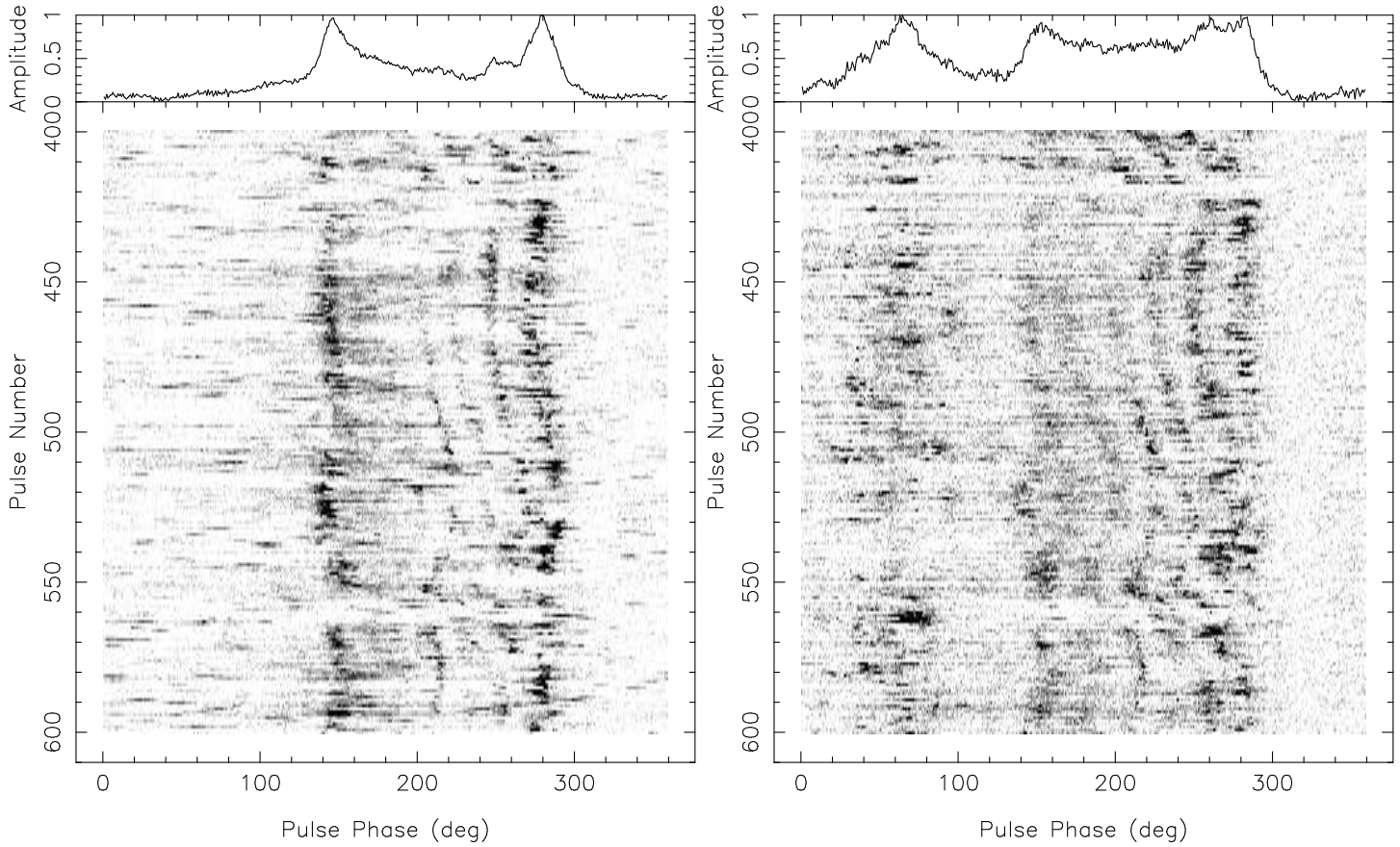

Figure 5.14: Gray scale plot of single pulse data for pulse number 400 to 600, from the simultaneous dual-frequency observations on 26 October 2003, at 303 (left panel), and 610 MHz (right panel).

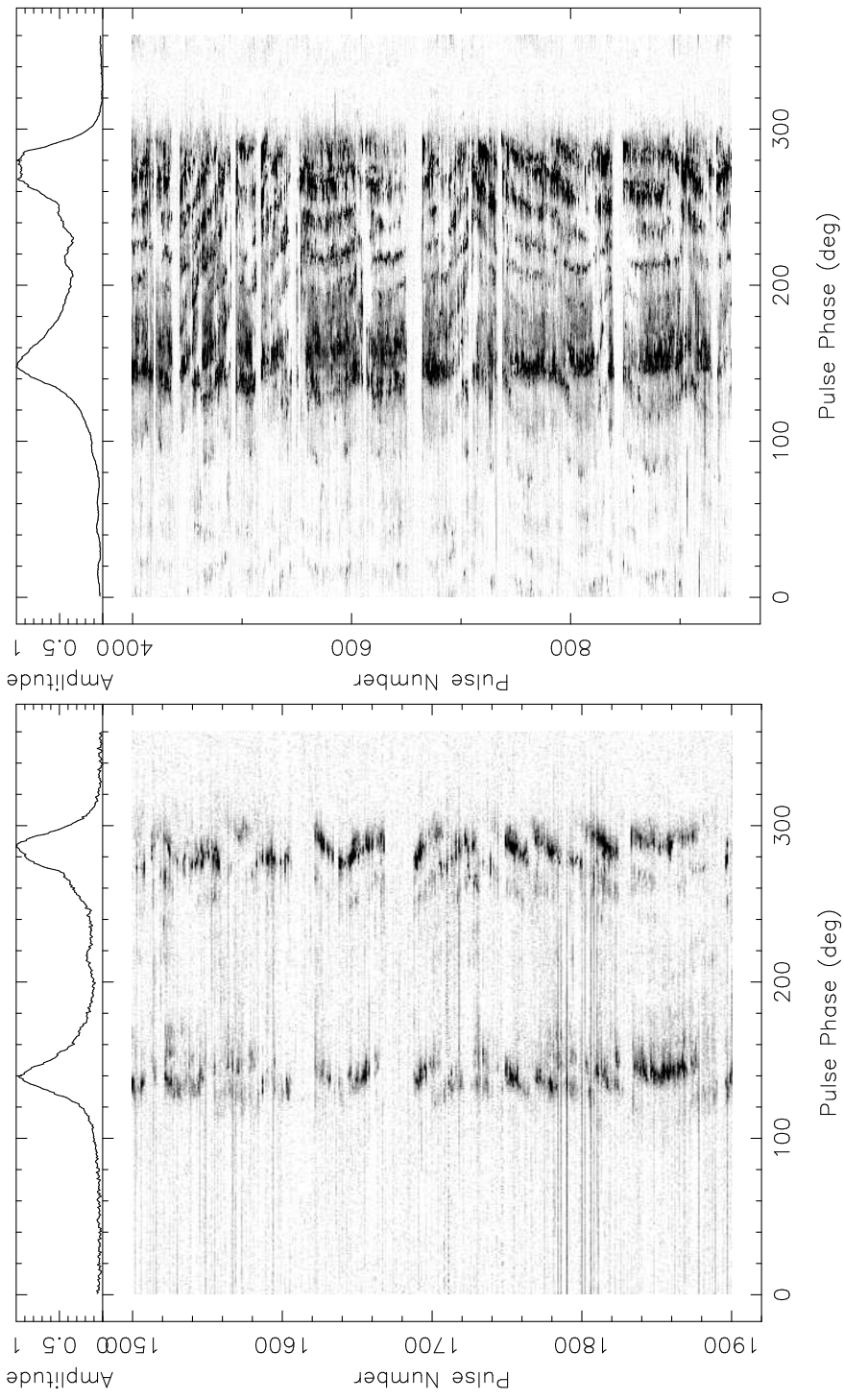

Figure 5.15: Gray scale plot of single pulse data from single frequency observations on 12 December 2006 at 157 (left panel) and on 12 December 2005 at 325 MHz (right panel).

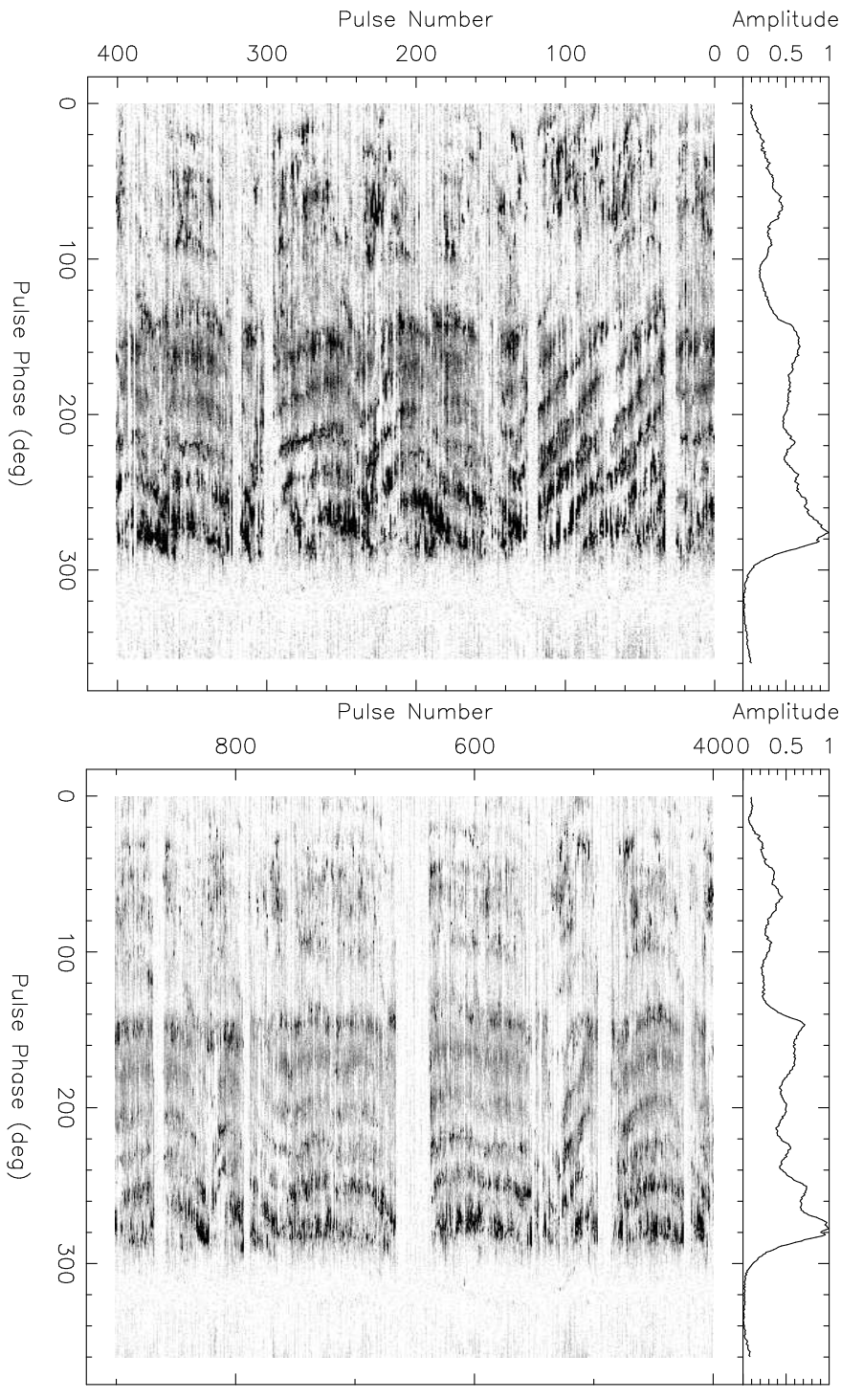

Figure 5.16: Gray scale plot of single pulse data from single frequency observations on 13 December 2006 at 610 MHz, for pulse number 1 to 400 (left panel) and pulse number 400 to 900 (right panel).

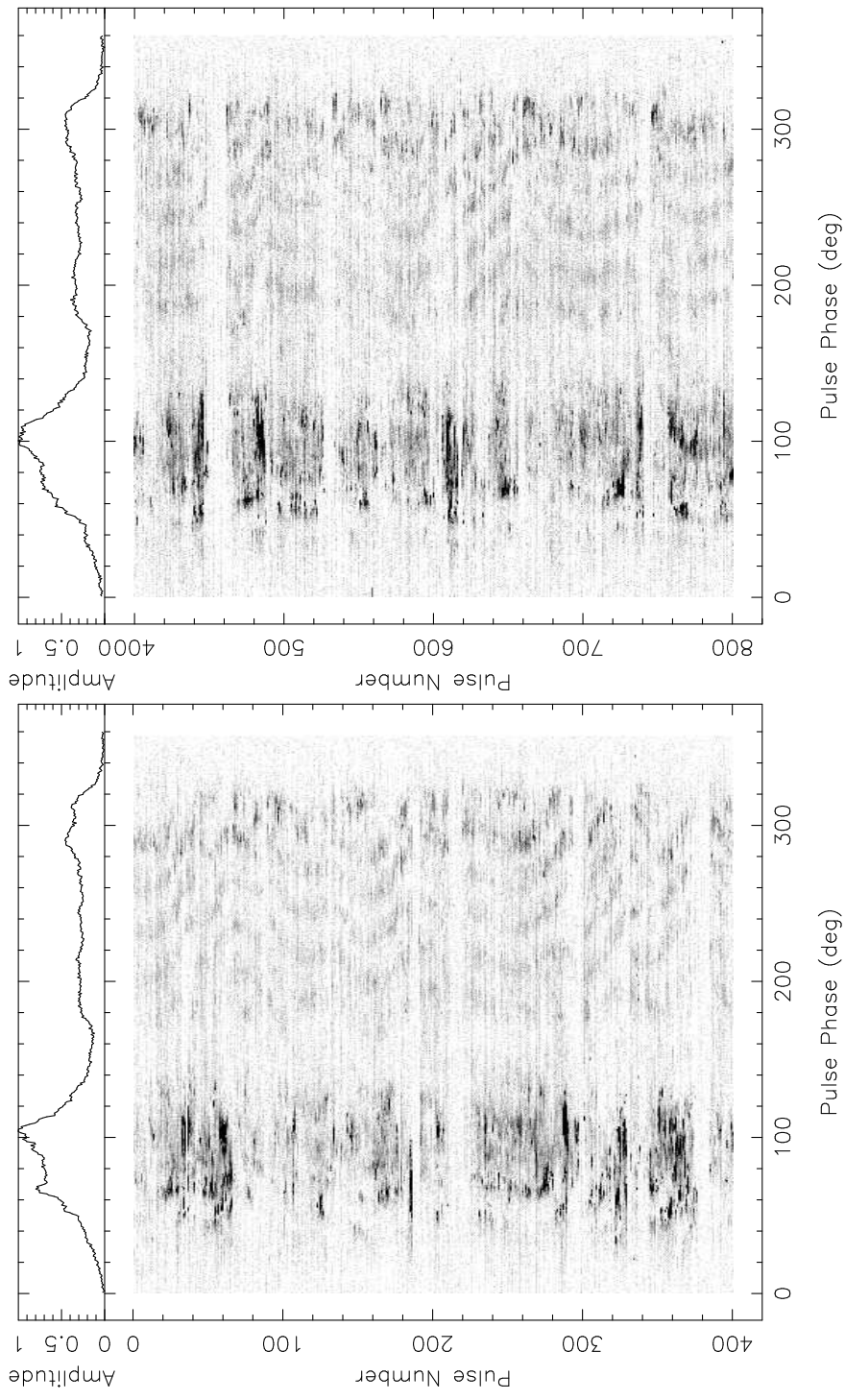

Figure 5.17: Gray scale plot of single pulse data from single frequency observations on 18 November 2006 at 1060 MHz, for pulse number 1 to 400 (left panel) and pulse number 400 to 800 (right panel).

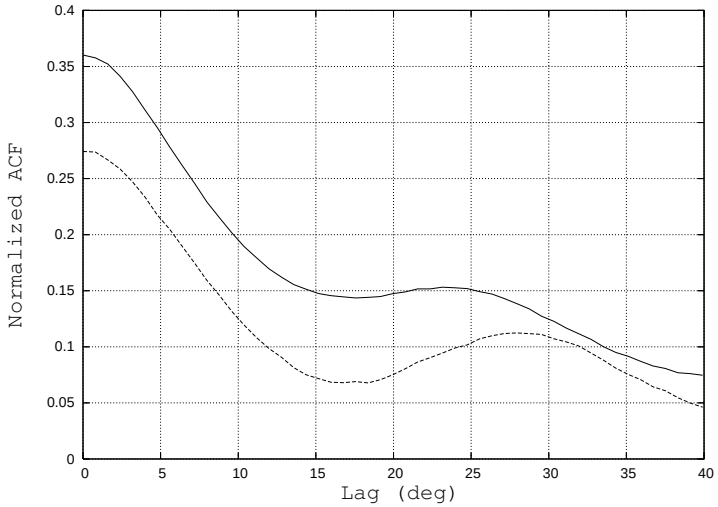

Figure 5.18: Figure for determination of P_2^m of PSR B0826−34 from simultaneous dual frequency observations on 26/10/2003 at 303 and 610 MHz. Autocorrelation results for section of profile for the MP (longitude 120 deg to 300 deg), calculated with one pulse offset, for pulse # 1 to 750 at 303 (solid) and at 610 MHz (dash). Secondary maximum of the autocorrelation function for 303 MHz is 22.6 deg and 610 MHz is 27.9 deg.

at both the frequencies. The pulse regions showing different drift rates of opposite signs are always connected by a region showing smooth transition of drift rate, as reported by Gupta *et al.* (2004). Such transitions, seen in pulse numbers 440 to 460, 500 to 520, 540 to 560 and 570 to 590, also occur simultaneously at 303 and 610 MHz. The gray scale plot of the single pulses from the higher sensitivity 157, 325, 610 and 1060 MHz single frequency observations (Fig. 5.15, 5.16, 5.17) show coherent drifting in the MP and IP regions (wherever seen), with approximately 6 drift bands in the MP and 4 drift bands in the IP. Subpulse drifting is observed under the two peaks of the MP at 157 MHz (Fig. 5.15). No IP emission is observed at 157 MHz. At 325 MHz 6 to 7 drift bands are seen in the MP window, and faint drift bands are observed in the IP window (Fig. 5.15). The MP and the IP emissions are locked in phase. Around 6 drift bands are in the MP and 3 to 4 drift bands in IP, with the MP and IP emission locked in phase are observed, at 610 and 1060 MHz (Fig. 5.16, 5.17). Though the drifting subpulses show very similar structure in our simultaneous dual frequency observations, there are subtle differences such as changes in the separations and widths of the

subpulse as a function of frequency. To investigate the change of drift band separation, we compute P_2^m from the autocorrelation function of the single pulses, averaged over the 750 pulses in the active state. In order to clearly see the secondary maximum in the correlation function (which will give us the P_2^m value), we correlate adjacent pulses with different longitude lags, rather than the same pulse (which is the traditionally correct procedure). This one pulse offset method suppresses a large amount of the correlation within the same subpulse, and as a consequence the secondary peak becomes stronger and easily detectable. This can be seen by comparing Fig.4 of Gupta *et al.* (2004) with our Fig. 5.18. We find $P_2^m = 22.6 \pm 0.8$ deg at 303 MHz and 27.9 ± 0.8 deg at 610 MHz. Thus, the value of P_2^m evolves with frequency. Any doubt about epoch dependent variations of P_2^m manifesting as variation of P_2^m with frequency can clearly be ruled out with these simultaneous dual frequency results. Further frequency evolution of P_2^m is obtained from our single frequency observations at different frequencies, the results from which are summarized in Table 5.4. In addition, we find $P_2^m \sim 20$ deg for the IP region, from 610 and 1060 MHz single frequency observations.

To study the longitude evolution of P_2^m, we repeat the correlation analysis over few chosen windows (~ 32 deg wide) of pulse longitude which are shifted systematically over a selected portion of main pulse window, in steps of 8 deg. Fig. 5.19 is a sample plot of correlation functions for 7 different pulse windows at 303 MHz and 610 MHz. For 303 MHz we observe a smooth trend for variation of P_2^m across the pulse window, with a minimum of 20.4 deg to a maximum of about 25 deg, which is compatible with the mean of 22.6 deg we obtained from the full main pulse. P_2^m increases from the center towards the edge of the MP, similar to the variation reported by Gupta *et al.* (2004) at 318 MHz. For 610 MHz, the variation is from a minimum of 26.3 deg to a maximum of 30.3 deg, again with a tendency to be lower in the middle of the MP, though the results are not as clear as for 303 MHz.

To study the variation of subpulse width, $\Delta\Phi_s$, with frequency, we compute the autocorrelation function (without any pulse offset) and find the full width at half maximum (FWHM). Average value for $\Delta\Phi_s$ is found to be 17.4 deg at 303 MHz, and 14.2 deg at 610 MHz, again confirming a frequency evolution. We collect values of $\Delta\Phi_s$ at different frequencies, from our observations as well as from literature, in Table 5.5. We observe longitude

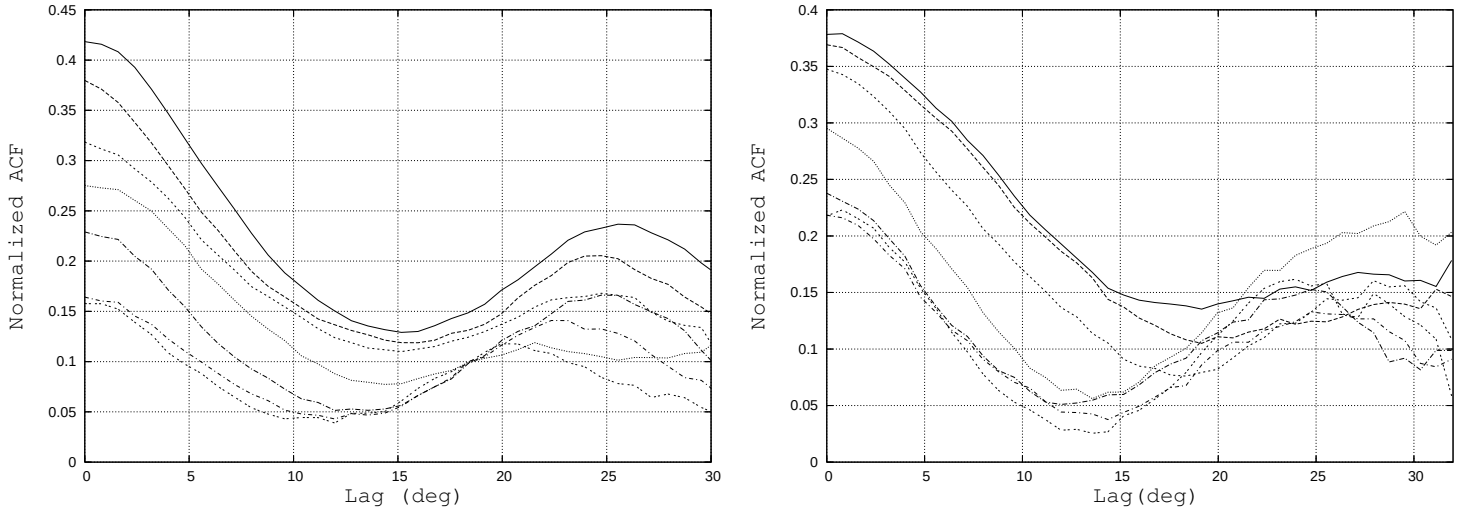

Figure 5.19: Figure for the study of evolution of P_2^m with pulse longitude of PSR B0826−34 from simultaneous dual frequency observations on 26 October 2003 at 303 and 610 MHz. Autocorrelation function for narrow pulse longitude windows at 303 MHz (left panel) and same at 610 MHz (right panel). Curves are for 7 different window locations: centered at 268 deg (solid), 260 deg (long dash), 252 deg (short dash), 244 deg (dot), 237 deg (long dash-dot), 229 deg (short dash-dot) and 221 deg (double dot).

Table 5.2: DM values of PSR B0826−34 from the literature survey.

Reference	DM value quoted (pc/cm^3)	DM determination method
Durdin *et al.* (1979)	52	Not described
EPN database (Gould & Lyne (1998) & D'Amico *et al.* (1998))	47	Not described
Taylor *et al.* (1993)	47±4	Timing analysis
Gupta *et al.* (2004)	47	Not described
Hobbs *et al.* (2004)	52.9±0.6	Timing analysis
Esamdin *et al.* (2005)	65.6	Not described
This chapter	52.2±0.6	Simultaneous dual frequency observations are used

evolution of $\Delta\Phi_s$: for region I (from 118 deg to 197 deg pulse longitude) $\Delta\Phi_s$ is significantly more than that for region II (from 197 deg to 276 deg pulse longitude) for all the frequencies. For a more detailed study of the longitude evolution of $\Delta\Phi_s$ within the MP, we followed a window scheme, similar to that employed for the P_2^m variation study. We find, $\Delta\Phi_s$ varies smoothly over the pulse window, in a manner that is somewhat similar to that of P_2^m variation with longitude, lower $\Delta\Phi_s$ values in the middle part of the MP and higher values towards the edges ($\Delta\Phi_s$ values near MP_1 being more than those near MP_2).

5.4 Discussions and Summary

(a) Average profile evolution with frequency

Values of $\Delta\Phi$ determined by us are in the same ballpark to the values reported by earlier studies of this pulsar (Biggs *et al.* (1985) and Gupta *et al.* (2004)). $\Delta\Phi$ varies with frequency as $\Delta\Phi \propto \nu^{-p}$, with average p value of 0.2, for different combinations of frequencies (refer to Table 5.4). Evolution of $\Delta\Phi$ with frequency follows the general trend of "radius to frequency mapping", seen in majority of pulsars. From our investigation of another wide profile pulsar, PSR B0818−41, we reported similar frequency evolution of $\Delta\Phi$ (see Chapter 2).

Very wide pulse profile observed for PSR B0826−34, indicate towards nearly aligned viewing geometry (i.e. very small values of α and β), which is supported by the PA fitting results from Biggs *et al.* (1985) and Gupta *et al.* (2004) and also reconfirmed by our study. Rankin (1993) have classified this pulsar as a "M-type" pulsar, i.e. a pulsar where the LOS and the emission geometry are such that multiple cones of emission are visible along with the central core component. It is confirmed by our analysis of drifting subpulses that the emission is entirely conal and there is no associated core emission present at least at 325 MHz and subsequent higher frequencies. The radiation pattern is interpreted to be created by the intersection of our LOS with two conal rings on the polar cap of a fairly aligned rotator (Gupta *et al.* (2004) and Esamdin *et al.* (2005)). Fig. 5.20 illustrates the possible LOS cuts at different frequencies. At lower frequencies (e.g. 157 or 325 MHz) LOS mostly sees the inner ring and that gives rise to the MP emission. The LOS

Table 5.3: Correlation of pulse energies between different frequencies of observations.

Pulsar	Frequency range MHz	Correlation Coefficient	Pulse Lag up to which correlation is positive	Reference
B0031−07	275 415	70%	-	Taylor *et al.* (1975)
B0031−07	102 406	50%	10†	Izvekova *et al.* (1993)
B0329+54	327 2695	75%	2†	Bartel & Sieber (1978)
B0329+54	102 1720	50±30%	4†	Bartel *et al.* (1981)
B0809+74	275 415	70%	-	Taylor *et al.* (1975)
B0809+74	102 1720	30±10%	4†	Bartel *et al.* (1981)
B0826−34	303 610	47%	11	This chapter
B0834+06	275 415	70%	-	Taylor *et al.* (1975)
B1133+16	275 415	78%	-	Taylor *et al.* (1975)
B1133+16	327 2695	75%	2†	Bartel & Sieber (1978)
B1508+55	102 1720	30±20%	1†	Bartel *et al.* (1981)

- : indicate that value for the corresponding parameter is not known

† : values obtained from visual inspection of plots for cross correlation coefficients vs pulse lag from respective references

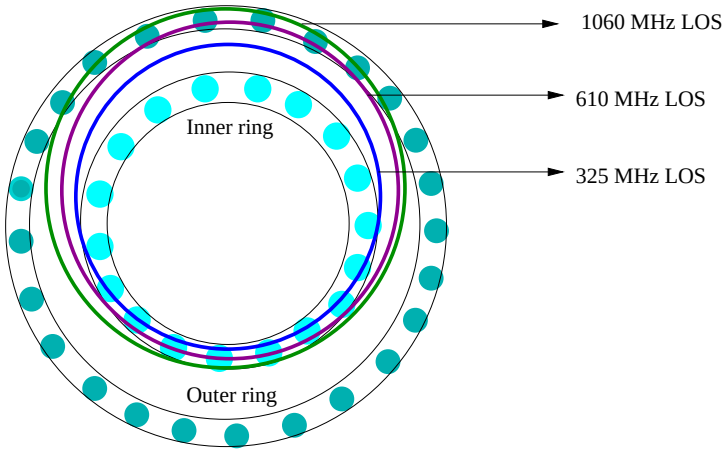

Figure 5.20: Possible LOS cuts at different frequencies for PSR B0826−34; 325 (blue), 610 (purple), 1060 (green).

is sufficiently further than the outer ring of emission at these frequencies and almost no inter pulse emission is observed. As frequency increases (e.g. 610 or 1060 MHz), one starts seeing emission coming from the second outer ring as well. As a consequence the IP emission becomes dominant with increasing frequency. Hence, the conal model (Rankin, 1993) naturally explains the observed profile evolution with the frequency. However, it is difficult to explain the observed evolution of profile with the frequency using the patchy beam model (Lyne & Manchester, 1988). We also note that IP is nearer to MP_1 and farther to MP_2 (refer to Fig. 5.1), which can be achieved by considering the sparks circulating around the local surface magnetic pole (instead of the magnetic dipole) as shown in Fig. 1 of Gupta *et al.* (2004).

(b) Polarization study

We report significant linear polarization in the inside edges and depolarization in the outside edges of the MP at 325 and 610 MHz. OPM jump observed at the edges of the MP (at 325 and 610 MHz), is the reason of the abrupt decrease of linear polarization near the edges of the profile. Depolarization in the outside edges associated with OPM jumps are commonly observed for quite a few pulsars (Gould & Lyne, 1998). For another wide profile pulsar PSR B0818−41 we observe similar orthogonal polarization mode change at

the edge of the profile, resulting in sharp fall of the linear polarization (refer to Sect. 2.5 of Chapter 2). The circular polarization observed in PSR B0826−34 changes sign near the center of the MP region. The sense reversal of circular polarization are commonly associated with the core components and argues in favor of the classification of the profile type of PSR B0826−34 as "M-type". But from our analysis of the drifting subpulse pattern it is implied that the MP is coming from the LOS cut of one single conal ring of emission and the IP is coming from the LOS cut of a second, outer ring of emission (Fig. 5.20). This stresses the fact that the sign reversal of the circular polarization observed in the central part of MP is not at all associated with the core emission for PSR B0826−34. Hence, the results from our study support the argument in Gupta *et al.* (2004), that the sense reversing of circular polarization can also be observed in conal components, if the related subpulses are quasi-stationary in phase (Gil *et al.*, 1995). Circular polarization associated with conal component is also observed in PSR B0818−41 for 1060 MHz (Sect. 2.5 of Chapter 2). We observe a correlation between sign change of circular polarization and the sense of the PA sweep for PSR B0826−34: right hand circular polarization accompanying increasing PA, which is also observed for PSR B0818−41 at 1060 MHz (Chapter 2). Han *et al.* (1998) reported similar correlation between the sense of PA sweep and the sense of circular polarization, using the polarization data of 20 conal-double pulsars.

The fact that the observed PA sweep (at 325 and 610 MHz) under the peaks of the MP are quite flat, is compatible with a positive sense of the impact angle β (Narayan & Vivekanand, 1982). In Fig. 5.5 we compare the PA curves at 325 and 610 MHz with the RVM fits from the geometries suggested for this pulsar in literature and also from our work. From the RVM fit to the PA data, Biggs *et al.* (1985) obtained best fit for $\alpha \sim 53$ deg and $\beta \sim 75$ deg. In addition, for $\alpha \sim 7.6$ deg and $\beta \sim 10$ deg they had a reasonable fit. We note that, while $\alpha \sim 53$ deg and $\beta \sim 75$ deg provides good fit only for the central region of the PA sweep of the MP, $\alpha \sim 7.6$ deg and $\beta \sim 10$ deg is a good fit for the outer regions of the PA sweep of the MP (Fig. 5.5). RVM with $\alpha \sim 7.6$ deg and $\beta \sim 10$ deg also satisfy part of the PA under the IP. On the other hand, RVM with $\alpha \sim 53$ deg and $\beta \sim 75$ deg is far from satisfying any part of PA sweep under the IP. In addition, to produce

as wide a profile as observed for PSR B0826−34, one needs fairly aligned geometry. $\alpha \sim 53$ deg and $\beta \sim 75$ from Biggs *et al.* (1985) fails to satisfy that criterion. Hence, according to us, RVM with $\alpha \sim 53$ deg and $\beta \sim 75$ deg is not a good fit to PA sweep, whereas, $\alpha \sim 7.6$ deg and $\beta \sim 10$ deg can be a plausible geometry. Investigating the PA sweep versus pulse longitude plot in Fig. 6 of Biggs *et al.* (1985), we note that sensitivity is relatively less under the two peaks of the MP, which could be the reason for which they found, $\alpha \sim 53$ deg and $\beta \sim 75$ deg, as the best fits to the RVM. Gupta *et al.* (2004) utilised the gradient of the PA sweep and the information for the separation between the peaks of the double peaked profile to converge to $\alpha \sim 2.5$ deg and $\beta \sim 1$ deg. Since this geometry is derived from the gradient of the PA sweep at the middle of the profile, RVM with corresponding α, β values satisfy the PA sweep in the central region, but not in the outer region (e.g. under the peaks of the profile the fit is not good). However, RVM with this geometry satisfy the same part of the PA sweep under the IP as was satisfied by $\alpha \sim 7.6$ deg and $\beta \sim 10$ deg. We obtain a reasonable RVM fit to the PA for $\alpha \sim 9.8$ deg and $\beta \sim 3.2$ deg. We note that the corresponding PA sweep derived with RVM (for this geometry) is very similar to that with $\alpha \sim 7.6$ deg and $\beta \sim 10$ deg, and satisfy the PA sweep under most of the MP and part of the IP. Because of flatter PA sweep in the central region and relatively steeper sweep in the outer region and even more flatter (almost horizontal) sweep under the edges of the profile, and the OPM jumps, it is difficult to converge on unique combination of α, β values.

(c) Determination of accurate DM value

Table 5.2 compares our result for the DM value of PSR B0826−34 with other available values from the literature − these cover a wide range, with the two most recent papers (Gupta *et al.* (2004) and Esamdin *et al.* (2005)) using values of 47 and 65.6 pc/cm^3. It is clear that, unlike most normal pulsars, DM determination for this pulsar is a difficult and trick exercise, mainly because the profile is quite complex, very wide and strongly evolving with frequency. Given our more accurate method of determining the DM, we believe that either of the extreme values are unlikely to be correct. We note that our DM result is closest to value obtained by Hobbs *et al.* (2004), using multi epoch timing. The accuracy of both these methods depends on the choice

of fiducial point. The fact that the results obtained match within the error bars implies that the fiducial point issues are probably well accounted for in both cases. The advantage of our method of DM determination is that observations at a single epoch are self sufficient for obtaining the DM value at that epoch, without requiring any absolute timing information. Our method of DM determination can facilitate the determination of DM values of other complex and wide profile pulsars.

(d) Study of the pulsar in null state

We see short duration nulls of a few pulses, which appear to be simultaneous over the frequency range of 303 to 610 MHz. In addition, this pulsar exhibits long durations of what is apparently a null state, which also appears to be broad band over this frequency range. However, we find no evidence for any weak emission in these long, apparently null states of the pulsar. Non-detection of any correlated emission structure in the null state profiles from the simultaneous dual frequency observations (at 303 and 610 MHz) are a clear proof of this. For frequencies above (up to 1060 MHz) and below (down to 157 MHz) also, we see no evidence for any weak emission. Our best limits on this non-detection are comparable to, or a few times better, than the level of detection (2%) that Esamdin *et al.* (2005) report for the null state of this pulsar, at 1374 MHz. These comparisons are all with respect to the peak of the emission profile in the active state. We have also obtained absolute flux limits for the non-detection at various frequencies, which should be a useful comparison standard for any more sensitive studies in the future.

What could be the reason for the difference between our results and those of Esamdin *et al.* (2005)? It could be a case of frequency dependent nulling, as reported by Bhat *et al.* (2007) for PSR B1133+16 where the pulsar exhibits cases of short duration nulls at lower frequencies like 325, 610 and 1400 MHz, while there is visible emission at 4850 MHz. This explanation appears somewhat difficult, given that we see no evidence for emission till the frequency of 1060 MHz, coupled with the fact that the emission properties of this pulsar appear to be significantly correlated over an octave range in frequency.

(e) Study of subpulse emission

(i) Pulse energy correlations :

Our result that the fluctuations of the main pulse energies at 303 and 610 MHz are correlated up to 47% level, indicates that the emission process generating the single pulses has a high degree of correlation over a octave bandwidth. What is equally noteworthy is that this level of correlation is pretty much the same as that at each of these individual frequencies, indicating that there is practically no loss of correlation over this range of frequency. Table 5.3 lists the correlation coefficient of pulse energies for different pulsars between two different observing frequencies, reported in the literature. All the pulsars listed there show significantly high correlation, supporting the case for the broad band nature of pulsar radio emission. At the same time, the significantly lower correlation between the main pulse and inter-pulse energies at 610 and 1060 MHz, implies that the physical processes responsible for the MP and IP emission may be much more unrelated to each other.

The result that the intensity correlations are positive for large lags implies that there is some kind of memory in the underlying subpulse structure. That this memory is the longest for PSR B0826−34 (amongst all known cases), is quantified in column 4 of Table 5.3. This is likely to be related to the large number of subpulses (or drift bands) that each main pulse energy estimate encompasses. The memory could then correspond to the time taken for the emission from a given subpulse spark column to drift through the main pulse window.

The other memory that the main pulse intensity variations exhibit is the intriguing feature of the peak at lag 13 seen in some of the correlation results. This could be an indication of the total time for rotation, around the magnetic axis, of the pattern of drifting subpulses − the carousel rotation time. For example, in the 14 spark model presented by Gupta *et al.* (2004), the drift rate is such that one subpulse drifts to a location close to that of the adjacent subpulse in one pulsar rotation, leading to a carousel rotation time of $P_4 = 14P_1$. However, if we believe that there are 13 sparks, as indicated in the model given by Esamdin *et al.* (2005), with the same drift rate condition as proposed by Gupta *et al.* (2004), then we would have $P_4 = 13P_1$, matching with the secondary peak feature seen in our data.

Table 5.4: Frequency dependence of profile width and P_2^m for different pulsars.

Pulsar	Frequency (MHz)	Profile width $\Delta\Phi^{\diamond}$ (deg)	P_2^m (deg)	Comments	Reference
B0031−07	60	75	20.6	$P_2^m \propto \nu^{-0.05}$	Izvekova *et al.* (1993)
	102	65	19.8	$\Delta\Phi \propto \nu^{-0.4}$	
	406	40	18.7		
B0031−07	157	44±5	18.9±1.2	P_2^m evolution	Smits *et al.* (2005)
A-mode	243	39.5±1.5	24±4	does not follow	
	325	39.4±0.3	19.8±1.0	definite trend	
	607	32±4	21±3		
	840	32.2±0.8	10±3		
	1167	25±6	14±5		
	4850	23.6±0.6	14±2		
B0031−07	157	46.3±1.4	19.2±0.7	P_2^m decreases	Smits *et al.* (2005)
B-mode	243	42.3±0.6	18.7±1.6	or remains unchanged	
	325	40.3±0.12	18.7±0.6	with increasing	
	607	39.3±0.9	18.7±0.6	frequency	
	840	43±0.9	14±1.6		
	1167	38±5	12±3		
B0320+39	102	11	3.8	$P_2^m \propto \nu^{-0.15}$	Izvekova *et al.* (1993)
	406	8.5	3.1	$\Delta\Phi \propto \nu^{-0.4}$	
B0809+74	102	34.8	14.7	see Sect.(e)	Davies *et al.* (1984)
	406	26.0	10.8		
	1412	29.8	8.6		
	1720	27.2^b	8.1		Bartel *et al.* (1981)
B0826−34	157	140±4†	23 ±0.8		This chapter
	303	132±4†	22.6±0.8	$\Delta\Phi \propto \nu^{-0.2}$	This chapter
	318	134±4†	24.9±0.8	P_2^m increases with	Gupta *et al.* (2004)
	610	116±4†	27.9±0.8	increasing frequency	This chapter
	645	112±4†	29±2.0	from 303 to 645 MHz	Biggs *et al.* (1985)
	1060	117±4†	28.7±0.8		This chapter
	1374	-	27.5		Esamdin *et al.* (2005)
B1237+25	430	16^a	10.6±2	$P_2^m \propto \nu^{-0.16}$	Wolszczan *et al.* (1981)
	1700	14.5^b	9.1±1.5	$\Delta\Phi \propto \nu^{-0.07}$	
B2016+28	102	20	8.5	$P_2^m \propto \nu^{-0.1}$	Izvekova *et al.* (1993)
	406	15	6.2	$\Delta\Phi \propto \nu^{-0.2}$	
	1412	15	5.5		
B2020+28	430	17^a	28.3±4	P_2^m increases with	Wolszczan *et al.* (1981)
	1700	16.2^b	51.4±7	frequency	

$\diamond$: Profile width at 10% intensity level

a : average profile width at 400 MHz from Gould & Lyne (1998)

b : average profile width at 1600 MHz from Gould & Lyne (1998)

I,II : left and right part of MP respectively, see Fig.1 of Biggs *et al.* (1985)

†: separation between two components of main pulse

(ii) Phase locked drifting in main pulse and inter pulse

PSR B0826−34 is an wide profile pulsar for which presence of simultaneous multiple drift regions are observed. For this pulsar the main pulse and the inter pulse emission are interpreted to be coming from two concentric rings of emission (Fig. 5.20). Single pulse gray scale plots in Sect. 5.3(e) illustrates in-phase drifting in the MP and IP region. For example Fig. 5.16 presents the gray scale plot of the single pulses from PSR B0826−34 at 610 MHz. This plot shows phase locked drifting in the MP ($\sim$ 5 to 6 drift bands) and IP ($\sim$ 3 to 4 drift bands) region. Esamdin *et al.* (2005) applied the method of phase tracking to the single pulse data and detected in total 13 drift bands in the pulse window. PLR between the inner and outer rings is evident from their results (Fig. 6 of Esamdin *et al.* (2005)). For PSR B0826−34 we observe frequent nulling and changes of drift rates which are simultaneous for both the inner and outer rings. In addition, we observe significant correlation between total energy of the main pulse and the inter pulse. With increasing pulse lag this correlation follows similar trend as the auto correlation of total energy of the main pulse or the inter pulse. This indicate that the conditions of the magnetosphere are similar for inner and outer rings of emission. We have already discussed about phase locked drifting between the inner and the outer rings for PSR B0818−41 in Sect. 3.4(b). Our finding of PLR between the emission from the inner and the outer rings (for all the pulsars for which drifting in both the rings are observed) in Chapter 3, as well as in this chapter, can be explained by considering that the pulsar emission as a pan magnetospheric phenomenon.

(iii) P_2^m evolution with frequency

PSR B0826−34 exhibits substantial variations of P_2^m at different frequencies, usually reported at different observing epochs (Table 5.4). The different values of P_2^m determined from the simultaneous data at 303 and 610 MHz strongly supports the claim that these are genuine variations with frequency, and not due to some time dependent phenomenon. The collected results in Table 5.4 are consistent with a scenario where P_2^m increases with frequency from 157 to 645 MHz, but then appears to saturate or even turn over at the higher frequencies like 1060 and 1374 MHz. For the low frequency range, we find that this frequency evolution ($P_2^m \propto \nu^{0.3}$) is of opposite sense to that for

the profile width, as measured by the separation between two components of the MP ($\Delta\Phi \propto \nu^{-0.2}$). Only two other pulsars in Table 5.4 show such an abnormal behavior : PSR B2020+28 shows a clear opposite sense (though only 2 frequency points are available) and PSR B0031−07 in the A-mode shows erratic increases and decreases of P_2^m with increasing frequency.

For most pulsars, though both P_2^m and the average profile width decrease with increasing frequency, the evolution of these two quantities with frequency does not exactly match (see Table 5.4). Izvekova *et al.* (1993) showed in detail that P_2^m is, in general, less dependent on frequency, as compared to the profile width − this is reflected in our Table 5.4 as well. This has been explained (see Gil & Krawczyk (1996) and Gil *et al.* (2002)) to be a natural consequence of the conal model of pulsar beams (e.g. Rankin (1993)) : the subpulse enhancement follows a narrow bundle of dipole field lines, while the mean enhancement corresponding to the peaks of mean profile components, is distributed over a cone (or a number of nested cones) of dipole field lines. Thus, the frequency dependence of subpulses and pulse widths should in general be different. However, these models do not appear to explain the opposite sense that we see in PSR B0826−34.

Another pulsar with anomalous frequency variations of profile width and P_2^m is PSR B0809+74. Rankin *et al.* (2005) analysed the P_2^m variations between 40 to 1400 MHz for this pulsar, and showed that they arise from incoherent superposition of two orthogonal modes of polarization. It will be interesting to see if detailed polarization studies of PSR B0826−34 can throw some light on the P_2^m variations with frequency.

The other interesting result is the variation of P_2^m with pulse longitude, where we confirm the behavior first reported by Gupta *et al.* (2004) at 318 MHz (a variation from 21.5 deg to 27 deg within the MP), and also find some signs for a similar effect at 610 MHz. Similarly, Esamdin *et al.* (2005) reported that at 1374 MHz, P_2^m varies from 26.8 deg to 28 deg within the MP. Gupta *et al.* (2004) have provided an explanation of this in terms of the geometrical effect of the way our LOS traverses the polar cap.

(iv) $\Delta\Phi_s$ evolution with frequency

$\Delta\Phi_s$ determined in this work is compared to the result quoted by Biggs *et al.* (1985) and Esamdin *et al.* (2005) at 645 and 1374 MHz respectively in Table

Table 5.5: Frequency and longitude dependence of subpulse width ($\Delta\Phi_s$) of PSR B0826−34.

Frequency (MHz)	$\Delta\Phi_s$ (deg)				Reference
	MP	I	II	IP	
157‡	15.8§	22.1§	10.2§	–	This chapter
303†	17.4§	28.4§	12.6§	–	This chapter
610†	14.2§	22§	12.6§	12.6§	This chapter
610‡	14.2§	22.9§	12.6§	12.6§	This chapter
645	–	14*	5.9*	4 *	Biggs *et al.* (1985)
1060‡	14.2§	20.5§	12.6§	17.4§	This chapter
1374	13.1±1.9	–	–	19±3.5	Esamdin *et al.* (2005)

† : From simultaneous dual frequency observing session
‡ : From single frequency observing session
I : 118 deg to 197 deg pulse longitude
II : 197 deg to 276 deg pulse longitude
∗ : Lag corresponding to half width at half maximum (HWHM) values
§ : Error associated in determination of $\Delta\Phi_s$ is ±1.6 deg

5.5. $\Delta\Phi_s$ is observed to be frequency dependent, average $\Delta\Phi_s$ at 303 MHz is more than 610 MHz value (see Sect. 5.3(e)). In addition, $\Delta\Phi_s$ is observed to be longitude dependent: $\Delta\Phi_s$ in region I is more than region II (Table 5.5). Similar longitude evolution of $\Delta\Phi_s$ within the MP is reported by Biggs *et al.* (1985) and Esamdin *et al.* (2005).

To summarize, using results from high sensitivity single pulse observations simultaneously at 303 and 610 MHz, and individually at 157, 325, 610 and 1060 MHz, we have investigated different aspects of PSR B0826−34: (1) average profile evolution with frequency, (2) polarization properties, (3) precise value of DM, (4) emission properties of the long duration null states and (5) simultaneous subpulses and details of the drifting behavior.

CHAPTER 6

Preliminary study of single pulse properties of six other pulsars

"No being exists or can exist which is not related to space in some way."
– Isaac Newton

6.1 Introduction

In the earlier chapters of this thesis we concentrated on detailed study of drifting and nulling properties of two wide profile drifting pulsars, PSR B0818−41 and PSR B0826−34. Our study illustrates that, due to almost aligned viewing geometry, one observes simultaneous multiple drift bands in the wide profile pulsars which can provide extra insights about the conditions of the magnetosphere. In this chapter we choose a sample of six relatively less studied pulsars with variety of profile shapes. While three, out of the six chosen pulsars have relatively wide pulse profiles (with conal double, multiple and triple profile structures), other three have typical narrow pulse profiles (with core single, core triple and conal single profile structures). This will in turn imply a range of viewing geometries, including the LOS cuts through the core and the conal components. This sample of pulsars were chosen based on the criterion that single pulses with sufficient SNR will be visible with the GMRT. Current single pulse studies report that the single pulse properties such as drifting and nulling are commonly seen only for the conal components and not for the core components. In this chapter, we aim to study the single pulse properties of the selected pulsars in both core and conal components in general and look for possible signature of drifting and nulling under the core components in particular.

6.2 Observations

We performed total intensity observations of the chosen sample of six pulsars at 325 and 610 MHz with the GMRT, using the phased array mode of observations. We put more antennas at the 610 MHz to get desired sensitivity, because of the fact that pulsars are intrinsically weaker at 610 MHz than at 325 MHz. Relatively slower dephasing at 610 MHz compared to 325 MHz allow us to choose far away arm antennas of the GMRT array for 610 MHz observations. Pulsar observations using the GMRT is explained in Sect. 1.5 of Chapter 1. Details of the observations, such as the epochs of observations, frequencies of observations, number of antennas used and number of pulses recorded for respective pulsars are summarized in Table 6.1. The raw data was recorded with 0.512 ms sampling interval. During offline analysis we further integrated the raw data to achieve the final time resolution of 2.048 ms. The raw data were first dedispersed with the respective DM values quoted for the individual pulsars. Then the bad data points were filtered out from the dedispersed data. The final average pulse profile for each pulsar was obtained by synchronous folding of this data with the available topocentric pulsar period. We determine the flux of the pulsars, following a relative calibration procedure, using the knowledge of the observing parameters and the background sky temperature near the source (similar to as done for PSR B0818−41 in Chapter 2 and for PSR B0826−34 in Chapter 5). The mean flux determined by us are similar to the values quoted in the literature for these pulsars.

6.3 Analysis and results

(a) PSR B0540+23:

Background:

Lyne & Manchester (1988) classified PSR B0540+23 as core single profile pulsar with partial cone. They also commented that the pulse profile of this pulsar changes very little over large frequency ranges. Rankin (1986) has classified the profile of this pulsar as core single. Nowakowski (1991) studied drifting subpulses from this pulsar at 430 MHz and according to him emission is coming from the core and two conal components. He reported

Table 6.1: Summary Table for the observations and the results

Pulsar	Frequency (MHz)	Date of observation	No of antennas used	Number of pulses	Pulsar Period (s)	α (deg)	β (deg)	Pulsar Flux[a] (mJy)	Fluctuation feature[a] (P_3^m)	Profile class[a]	Profile width[‡a] (deg)
B0540+23	325	24 February 2004	15	4500	0.246	38	–	20.2	9.8 P_1	Core single[b]	31
	610	25 February 2004	20	5600				11.9	9.8 P_1	Triple[a]	31
B1541+09	325	24 February 2004	16	3050	0.748	5[b]	0[b]	83.2	20 P_1	Triple[b]	55
	610	25 February 2004	25	3030		5.8[c]	0.8[c]	12.2		Multiple[a]	107
B1818−04	325	24 February 2004	17	3175	0.598	65[b]	3.5[b]	237	4 P_1	Triple[b]	16
	610	25 February 2004	25	3100				34	4 P_1	Triple[a]	15
B1819−22	325	28 January 2005	16	1216	1.874	17[c]	4.2[c]	28.5	16.6 P_1	Triple[a]	19
	610	11 January 2005	22	611				6.5	16.6 P_1		18
B1831−04	325	24 February 2004	18	4500	0.290	7.9[c]	1.6[c]	69.3	–	Multiple[b]	130
	610	25 February 2004	25	2290		10[b]	2[b]	20.9		Multiple[a]	130
B1839−04	610	1 January 2007	20	175	1.84	–	10.9	–	11.9 P_1	Double[a]	82

a result from this work, *b* : result from Rankin (1993), *c* : result from Lyne & Manchester (1988), † :simultaneous dual frequency observations, ‡ : 10% width of the profile.

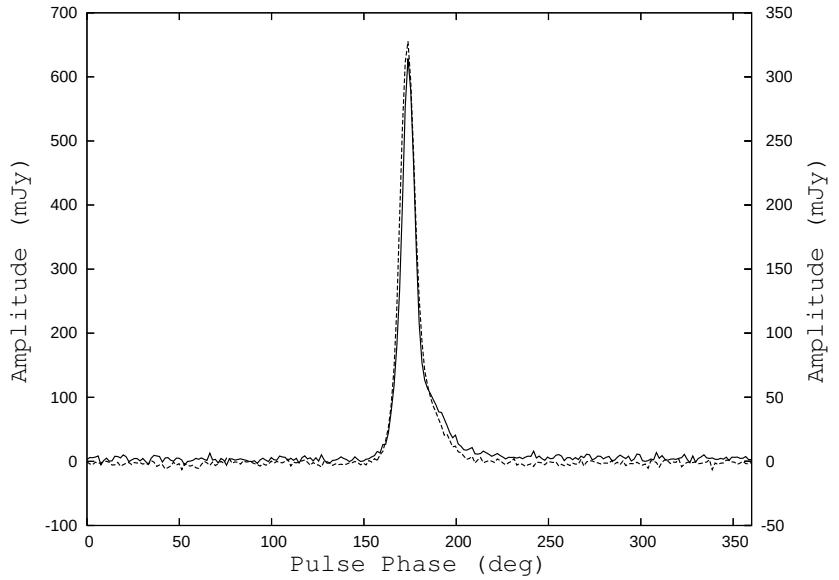

Figure 6.1: Average profile of PSR B0540+23 at 325 (solid line, with amplitude in the left y-scale) and 610 MHz (dashed line, with amplitude in the right y-scale). The pulse amplitude is in mJy. Core single profile with partial cones. 325 and 610 MHz profile are almost identical.

sporadic drift of subpulses for this pulsar. Although for most pulsars drifting is typically observed from the conal components and not from the core components, Nowakowski (1991) reported that for PSR B0540+23 the middle component − which is believed to be core emission − exhibit sporadic but very well organized drift in either direction with different rates. No preferred drift direction is reported. We observed this pulsar to investigate the nature of subpulse drifting in the core component.

Results:

Fig. 6.1 plots the average profile of PSR B0540+23 at 325 and 610 MHz. Core single profile at 325 and 610 MHz are almost identical. This supports the observations of Lyne & Manchester (1988) that profile changes very little with frequency. Fig. 6.2 presents the stack plots of the single pulses at 610 MHz. Sporadic drifting is evident in the stack plot, some such sequences are marked in Fig. 6.2. We observe occasional nulling in between sporadic drifting (e.g pulse # 1400 to 1450 in Fig. 6.2). Though such long nulls are not very commonly seen for this pulsar, relatively shorter nulls (typically $\sim$ 2 to 5 P_1 long) are quite frequently observed for this pulsar. This observation is

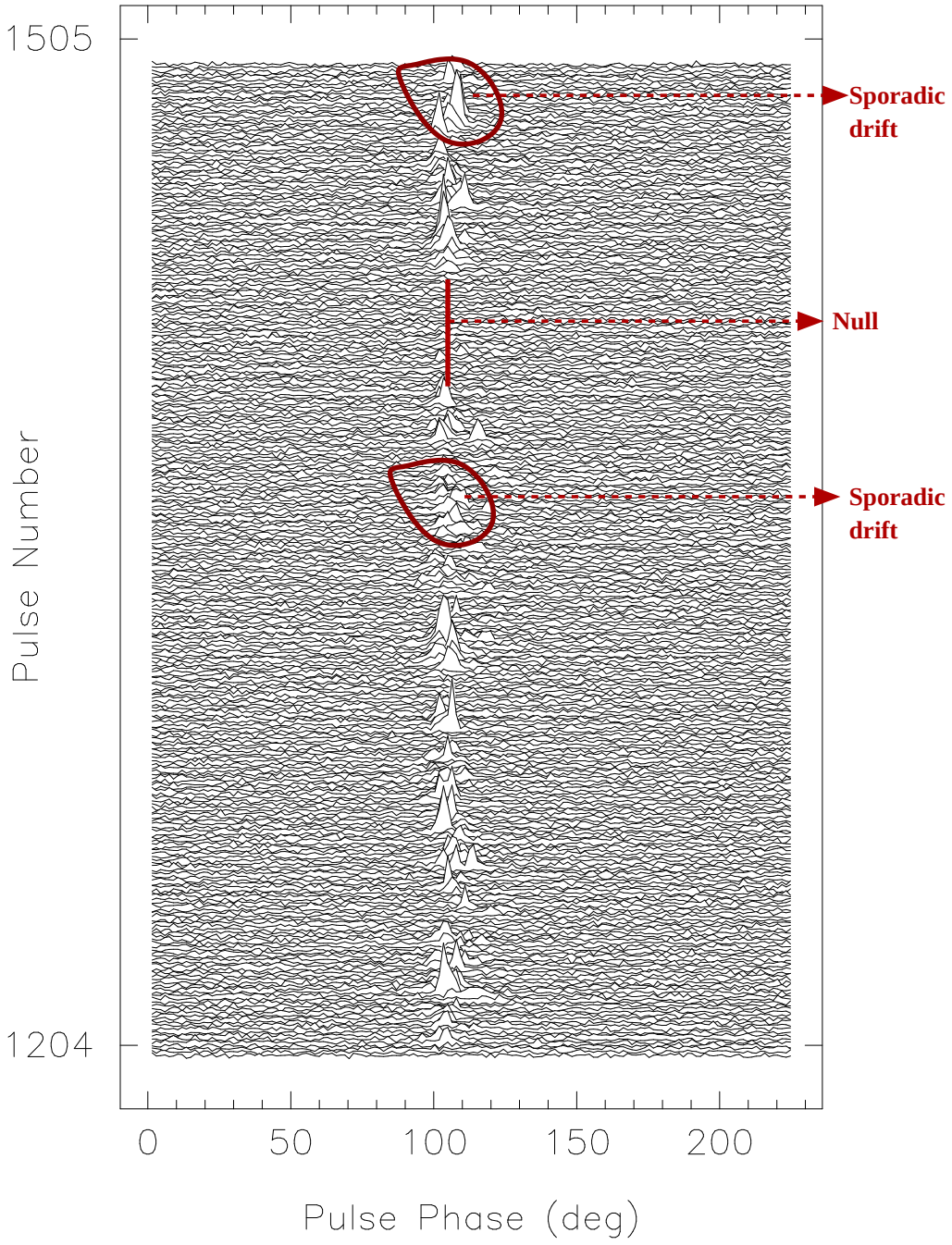

Figure 6.2: Stack plot of single pulse data of PSR B0540+23 at 610 MHz.

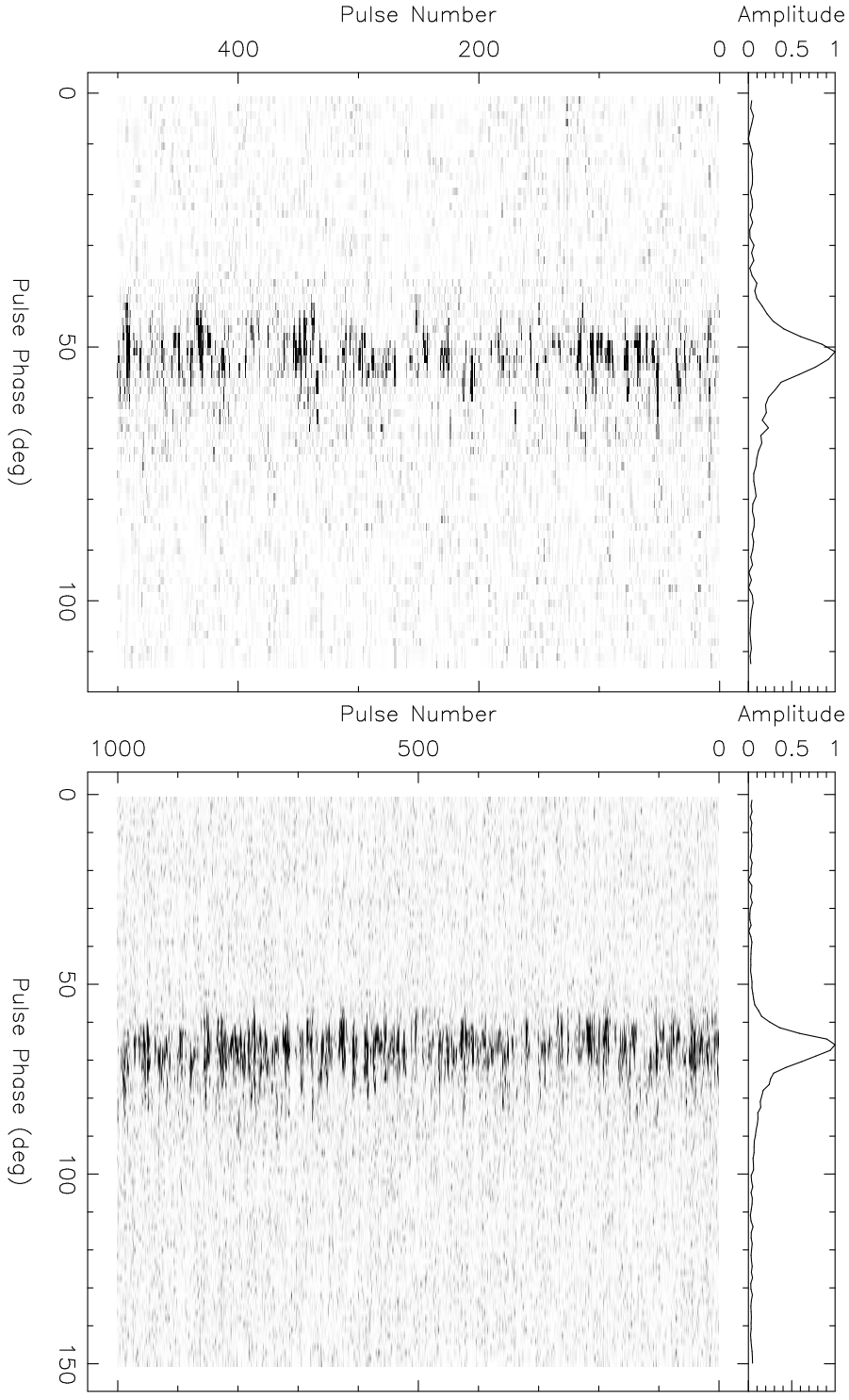

Figure 6.3: Gray scale plot of single pulse data of PSR B0540+23 at 325 MHz (left panel) and 610 MHz (right panel), with the average profile shown on top.

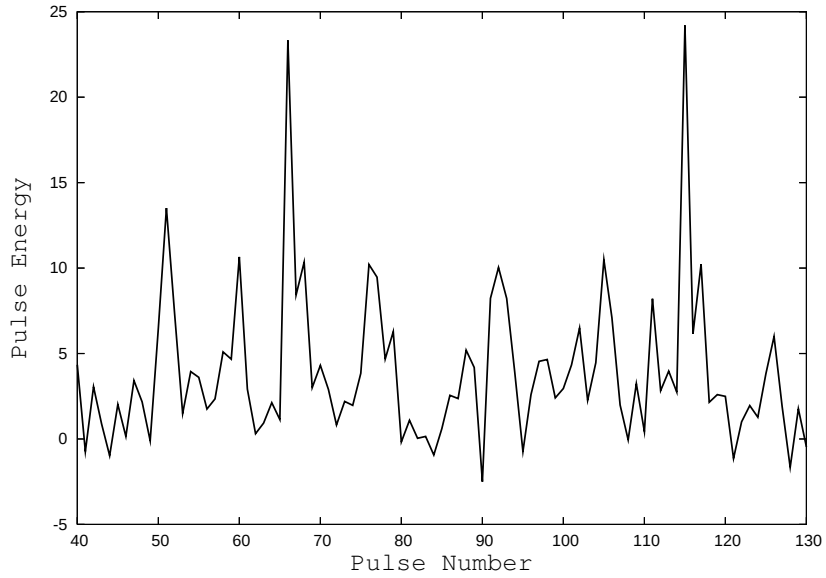

Figure 6.4: Pulse number versus pulse energy of PSR B0540+23 for pulse # 40 to 130 at 325 MHz. Note a periodicity at approximately 10 P_1.

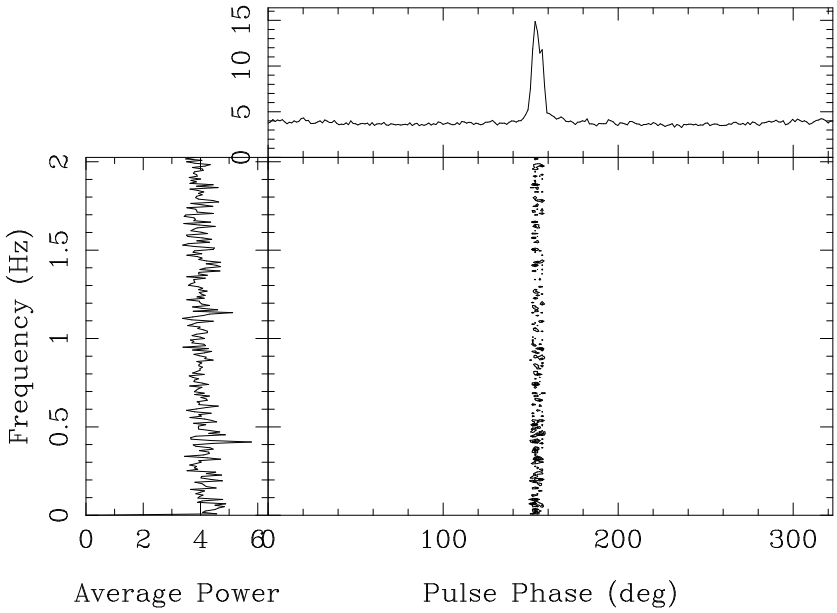

Figure 6.5: The contour plot of the power spectrum of the flux as a function of pulse phase during a sequence of 500 pulses (pulse # 1−500) for PSR B0540+23 at 325 MHz. The left panel shows the power spectrum integrated over the entire pulse longitude. The upper panel shows the power integrated over fluctuation frequency. Though some amount of power is present for all the frequencies displayed, maximum fluctuation power corresponds to a feature at 9.8 P_1.

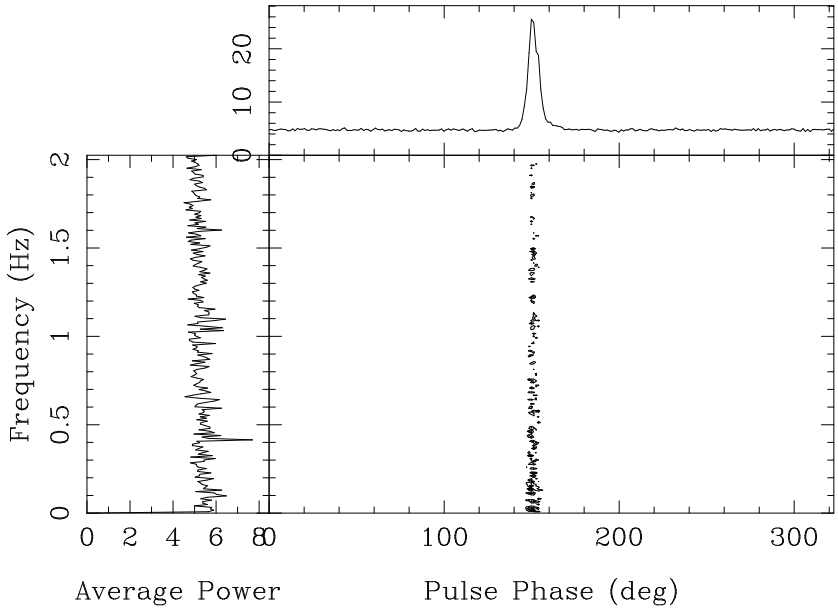

Figure 6.6: Same as Fig. 6.5, but at 610 MHz for pulse # 1 to 1000. Note a feature at 9.8 P_1.

important in the sense that nulls are not commonly seen in the core components. However, our results are in contrary to Nowakowski (1991), who has reported about not seeing any null from this pulsar during their observations. Fig. 6.3 presents the single pulse gray scale plots at 325 and 610 MHz. Sporadic drifting and occasional nulling are observed for both the frequencies. Some example of well organized drifting are observed with a typical duration being about 10 pulses. After that the drift may stop, change direction, or the subpulse may appear at a new phase and start drifting. These observations of ours are in agreement to what has been reported by Nowakowski (1991). Pulse energy under the on pulse window versus pulse number for 325 MHz observations is plotted in Fig. 6.4. We note a periodicity at approximately 10 P_1. Similar periodicity is seen in the pulse energy versus pulse number plot for 610 MHz. Fluctuation spectrum for 325 and 610 MHz are plotted in Fig. 6.5 and Fig. 6.6 respectively. Some amount of power is present for all the frequencies displayed, but maximum fluctuation power corresponds to a feature at 9.8 P_1.

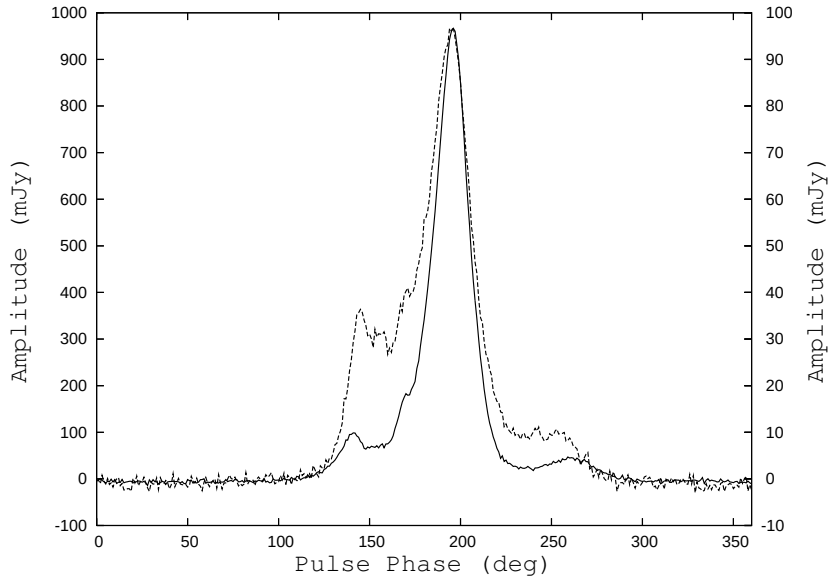

Figure 6.7: Average profile of PSR B1541+09 at 325 MHz (solid line, with amplitude in the left y-scale) and 610 MHz (dashed line, with amplitude in the right y-scale). The pulse amplitude is in mJy.

(b) PSR B1541+09:

Background:

Rankin (1986) classified this pulsar as triple and interpreted the emission to be coming from both core and conal components. Lyne & Manchester (1988) claimed to see five components in the profile. For this pulsar, fluctuation features around 12-15 P_1 are reported by Taylor & Huguenin (1971). The core component of this pulsar clearly shows leading edge absorption at 430 MHz (Rankin, 1993). The LOS traverse pass very close to the magnetic axis, e.g. with $\alpha \sim 6$ deg (Lyne & Manchester, 1988) or $\alpha \sim 5$ deg (Rankin, 1993). In addition, Lyne & Manchester (1988) also reported, $\beta \sim 0.8$ deg.

Results:

Fig. 6.7 presents the average profile of PSR B1541+09 at 325 and 610 MHz. Core component and one conal component on each side of core are evident. However, there is hint of a second cone, specially in the leading side, this makes it a five component pulsar. The conal components becomes relatively stronger at 610 MHz and hence the profile width is more at 610 MHz and less at 325 MHz (Table 6.1). Fig. 6.8 plots the stack plot of the single pulses

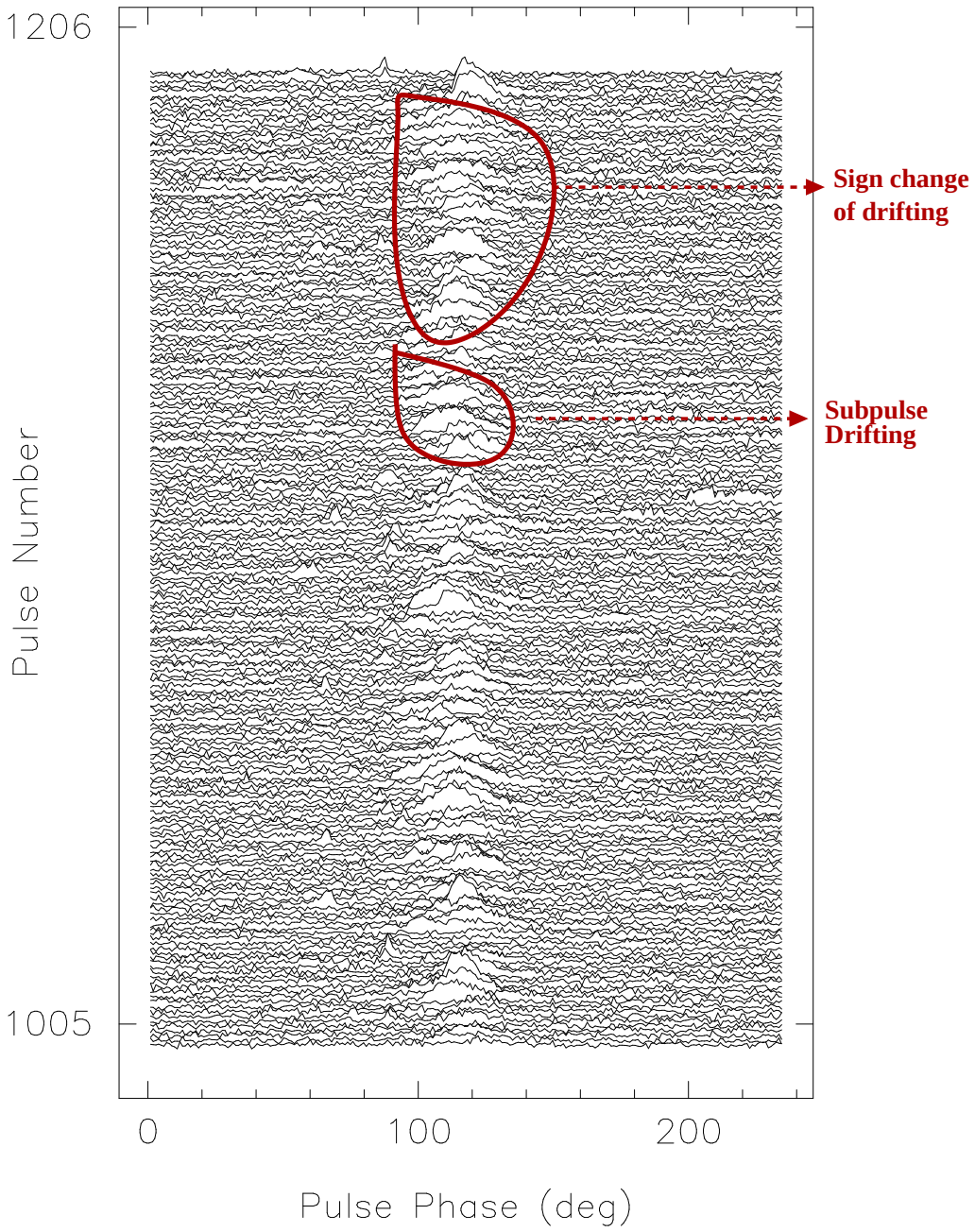

Figure 6.8: Stack plot of single pulse data (pulse # 1000 to 1200) of PSR B1541+09 at 325 MHz.

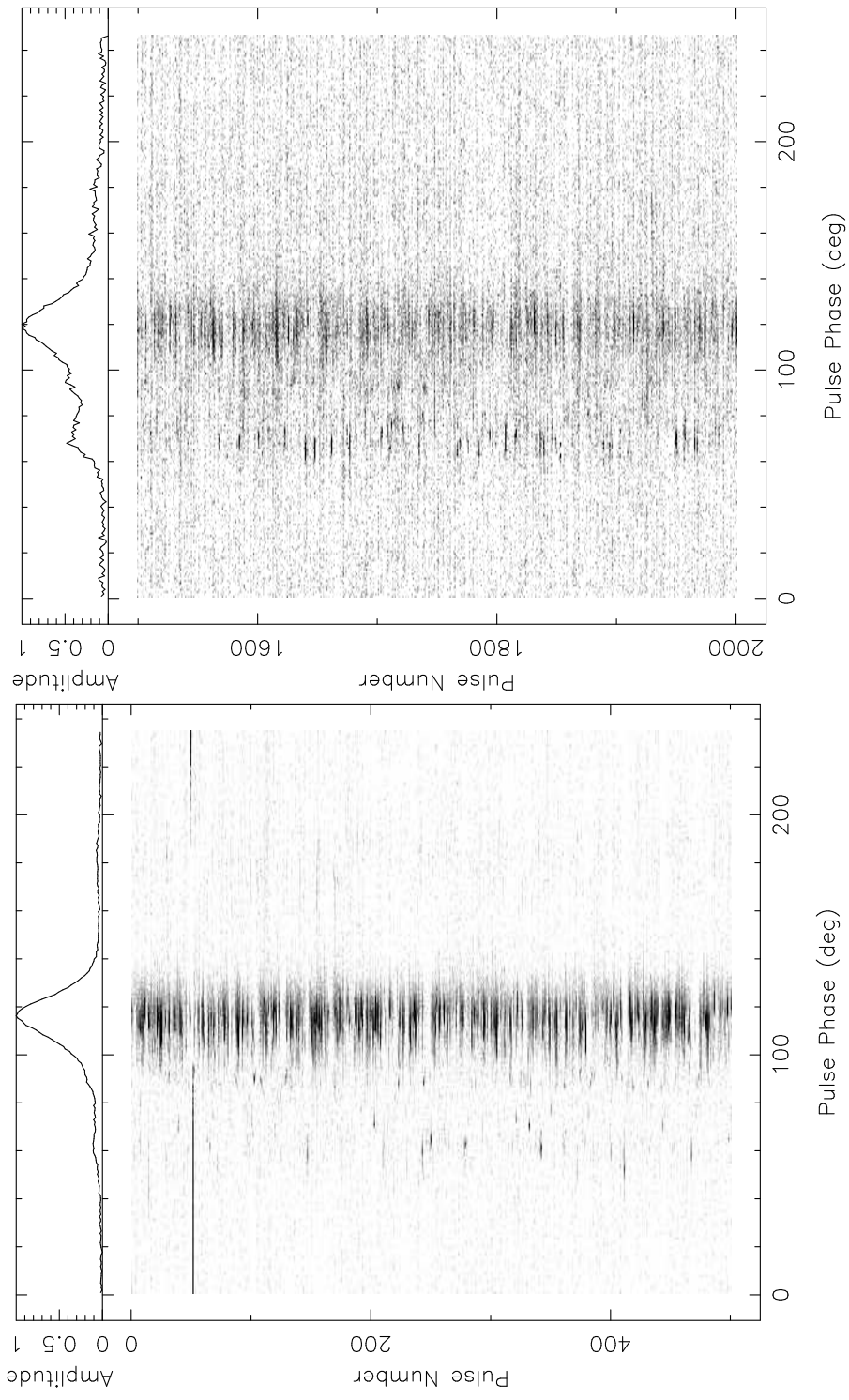

Figure 6.9: Gray scale plot of single pulse data of PSR B1541+09 at 325 MHz (left panel) and 610 MHz (right panel), with the average profile shown on top.

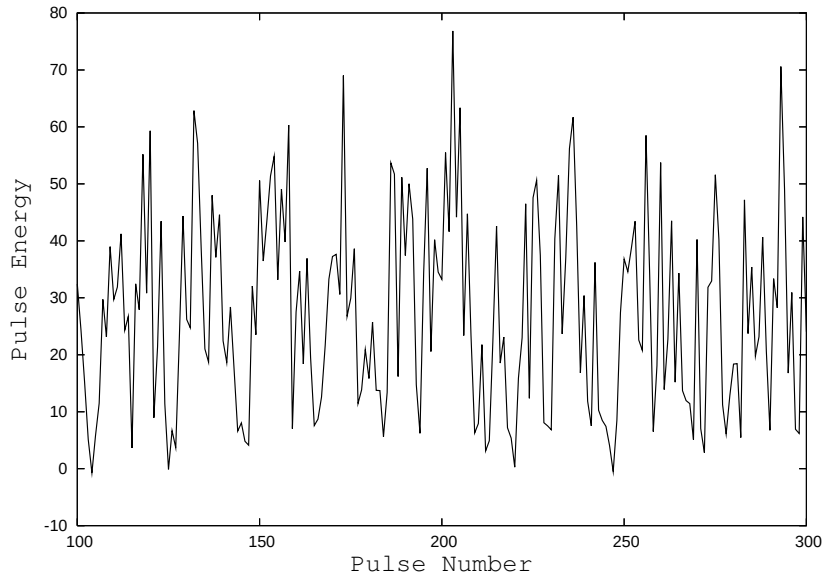

Figure 6.10: Pulse number versus pulse energy of the core component of PSR B1541+09 for pulse # 100 to 300 at 325 MHz. Some periodicity at 20 P_1 interval is observed.

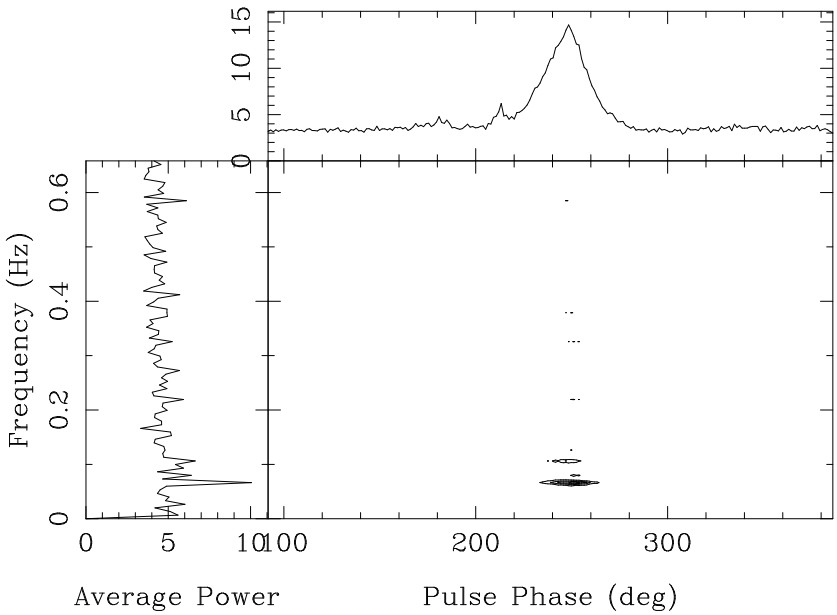

Figure 6.11: The contour plot of the power spectrum of the flux as a function of pulse phase for a sequence of 200 pulses (pulse # 1000−1200) for PSR B1541+09 at 325 MHz. The left panel shows the power spectrum integrated over the entire pulse longitude. The upper panel shows the power integrated over fluctuation frequency. Fluctuation feature is seen at 20 P_1.

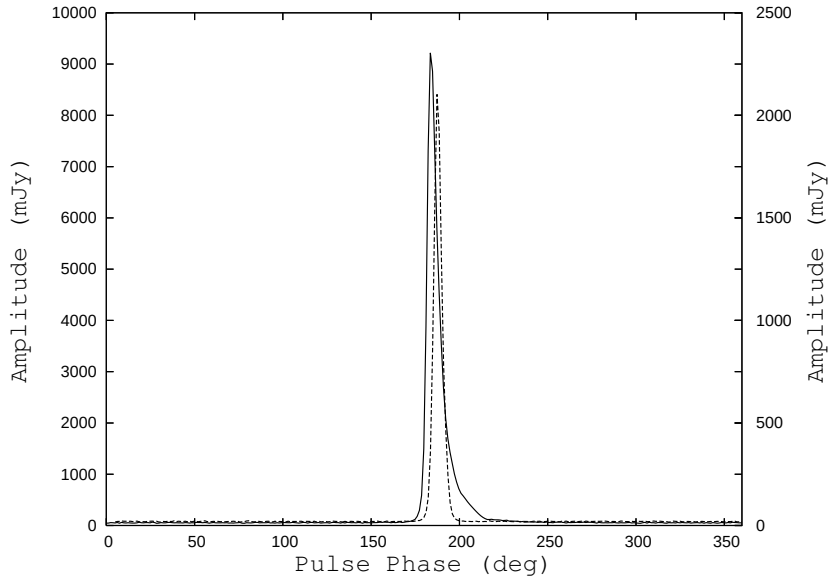

Figure 6.12: Average profile of PSR B1818−04 at 325 MHz (solid line, with amplitude in the left y-scale) and 610 MHz (dashed line, with amplitude in the right y-scale). The pulse amplitude is in mJy.

at 325 MHz. Most of the single pulses from this pulsar have only one subpulse, which are generally quite wide and have different structures. Drifting of the subpulses is evident in Fig. 6.8. Drift direction changes quite often. Fig. 6.9 plots the single pulse gray scale plot at 325 and 610 MHz. Strong single pulses with sporadic drifting is observed. But occasional strong pulses are observed under the conal peak in the leading side, which becomes more prominent at 610 MHz. Fig. 6.10 plots the total energy under the core component. Periodicity around 20 P_1 is evident in this figure. Fig. 6.11 plots the fluctuation spectrum at 325 MHz for pulse # 1000 to 1200. We observe a peak corresponding to P_3^m at $20P_1$. Short duration nulls (of the order of 5 to 10 pulses) are observed in the pulsar quite frequently, which possibly has some periodicity associated with it. This provides a rare example for nulling under the core components.

(c) PSR B1818−04:

Background:

Rankin (1993) had classified the profile as triple − the central component (apparently the core component) is sandwiched between two relatively weaker

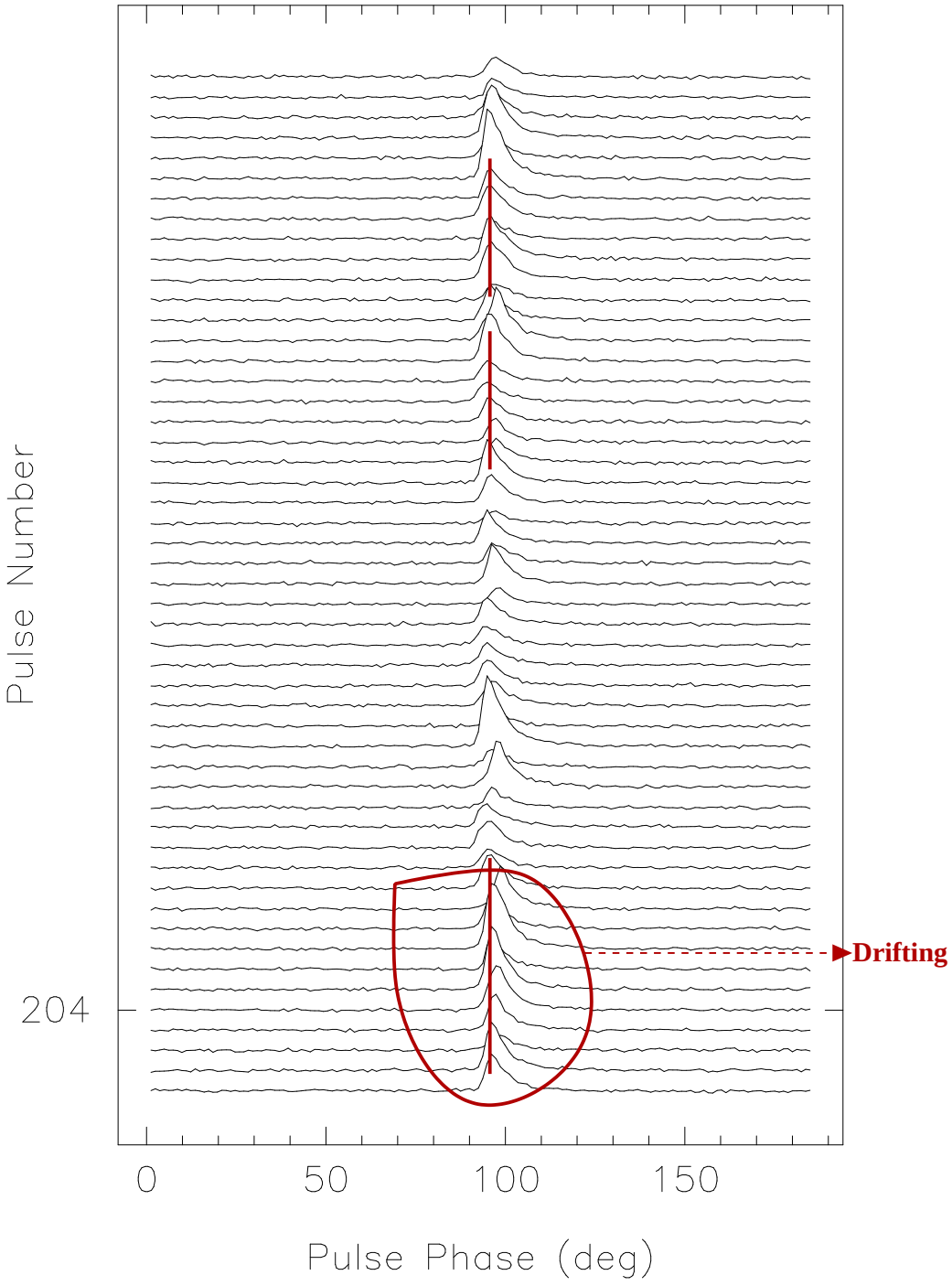

Figure 6.13: Stack plot of single pulse data (pulse # 200 to 250) of PSR B1818−04 at 325 MHz.

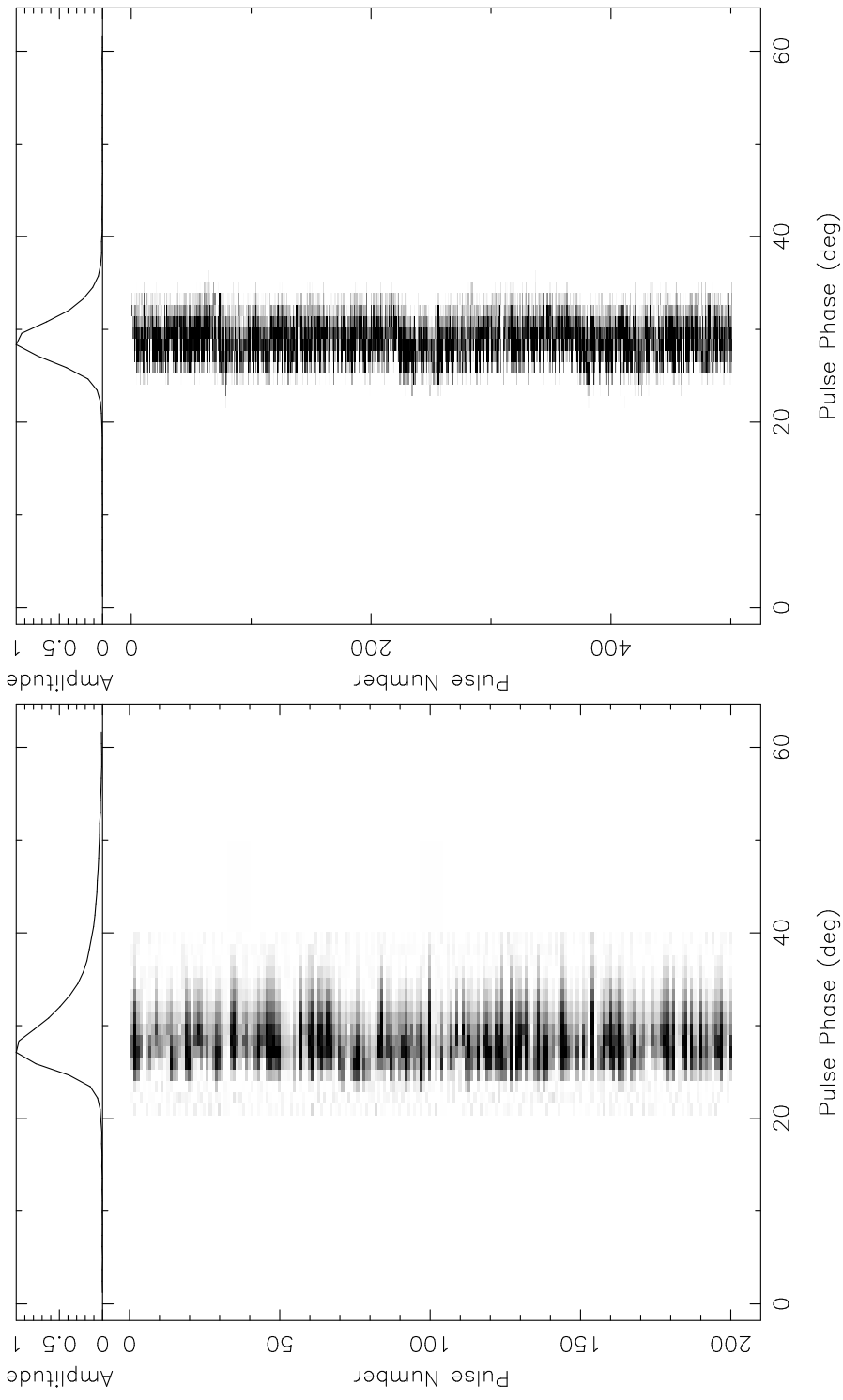

Figure 6.14: Gray scale plot of single pulse data of PSR B1818−04 at 325 MHz (left panel) and 610 MHz (right panel), with the average profile shown on top.

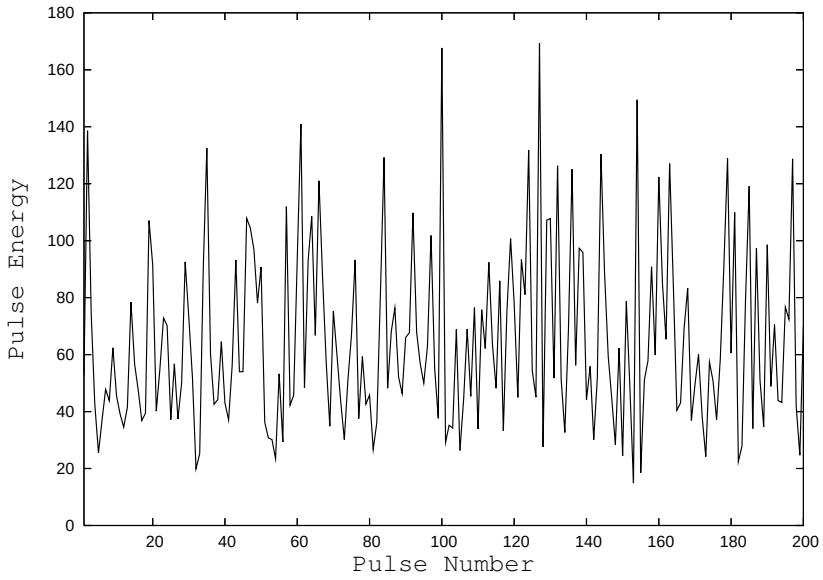

Figure 6.15: Pulse number versus pulse energy of B1818−04 for pulse # 1 to 200 at 325 MHz, note a periodicity at approximately 4 P_1.

conal components. She reported $\alpha \sim 65$ deg and $\beta \sim 3.5$ deg for this pulsar.

Results:

Fig. 6.12 plots the average profile of PSR B1818−04 at 325 and 610 MHz. Profile shape is similar at 325 and 610 MHz. Fig. 6.13 shows stack plot of the single pulses from PSR B1818−04 at 325 MHz. All the single pulses from this pulsar contain only one subpulse. In this context, the idea of core component sandwiched between the conal components can be given a rethought. Drifting of the subpulses are quite evident in this figure, some such sequences are marked in the figure. Very slow apparent drifting is continued for few pulses, and then the drifting starts from a different phase (generally earlier phase) in the pulse window. Fig. 6.14 presents the single pulse gray scale plot at 325 and 610 MHz. Clear signature of drifting is observed. Direction of drift is from earlier to later longitude, then suddenly the subpulse is back to earlier longitudes and drift resumes. Fig. 6.15 plots the pulse energy versus pulse number for pulse # 1 to 200 at 325 MHz. The consecutive peaks are roughly at 4 P_1 interval.

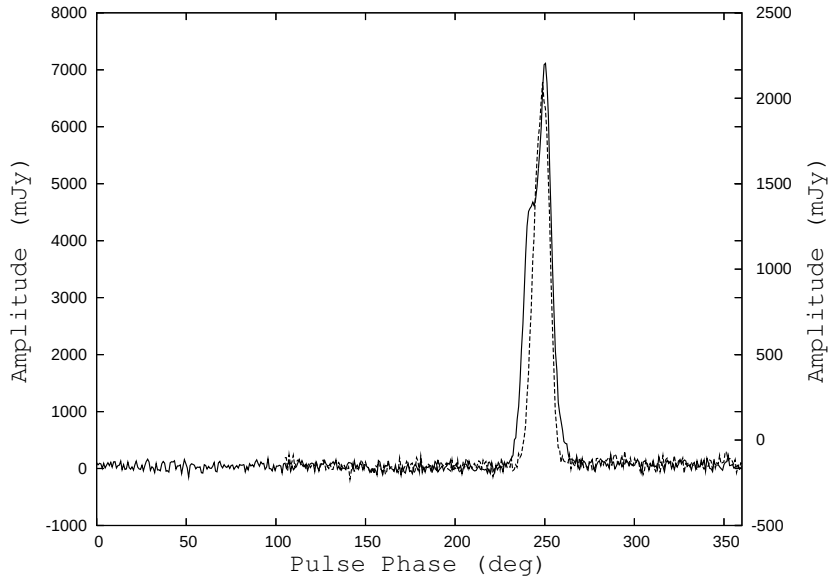

Figure 6.16: Average profile of PSR B1819−22 at 325 MHz (solid line, with amplitude in the left y-scale) and 610 MHz (dashed line, with amplitude in the right y-scale). The pulse amplitude is in mJy.

(d) PSR B1819−22:

Background:

Weltevrede *et al.* (2006) discovered the drifting property of B1819−22 with the WSRT at 1420 MHz. They reported that the fluctuation spectra of this pulsar very clearly shows a drift feature at 325 and 1420 MHz.

Results:

Fig. 6.16 presents the average profiles at 325 and 610 MHz. There is a component in the leading side at 325 MHz which is absent at 610 MHz. Fig. 6.17 presents the stack plot of the single pulses at 325 MHz. Generally simultaneous two subpulses are observed, which exhibit regular drifting. Fig. 6.18 presents subpulse drifting at 325 and 610 MHz. Simultaneous two drift bands are observed at both the frequencies. We observe some kind of mode changing between stronger and weaker modes with changes of drift rates, which are probably associated with frequent nulling observed in this pulsar. P_2^m values are calculated form the autocorrelation function of the single pulses, averaged over the total number of pulses. In Fig. 6.19, the secondary peak is due to the correlation between the adjacent drift bands and

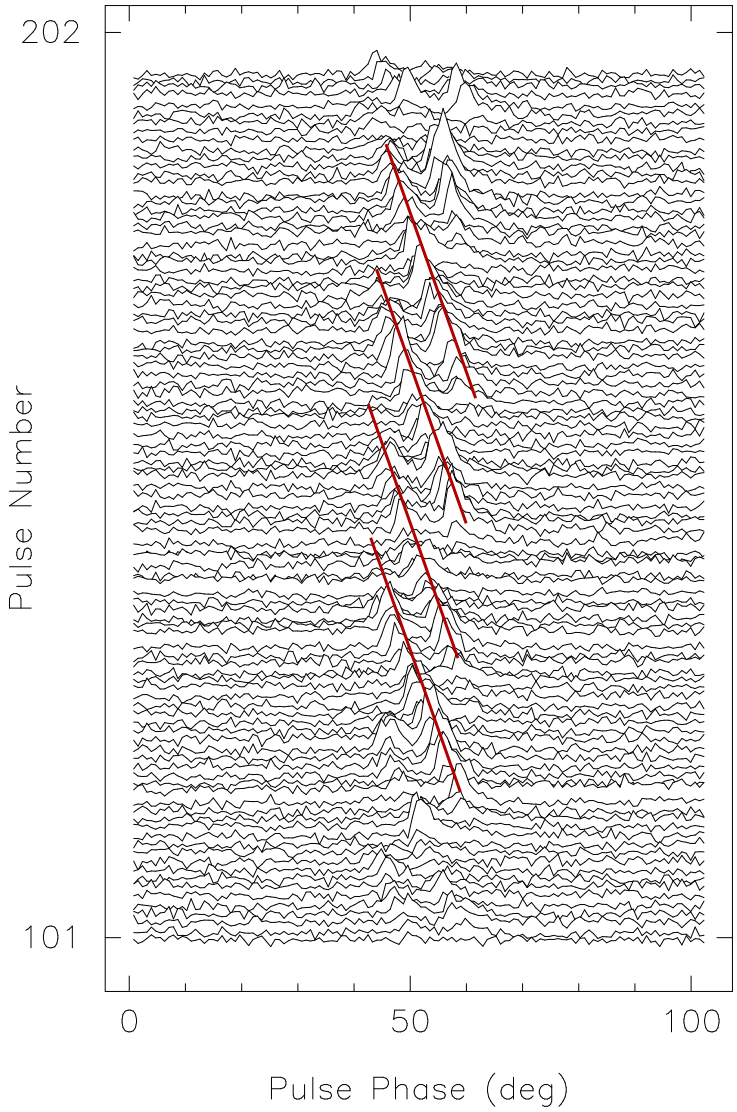

Figure 6.17: Gray scale plot of single pulse data (pulse # 1 to 500) of PSR B1819−22 at 325 MHz.

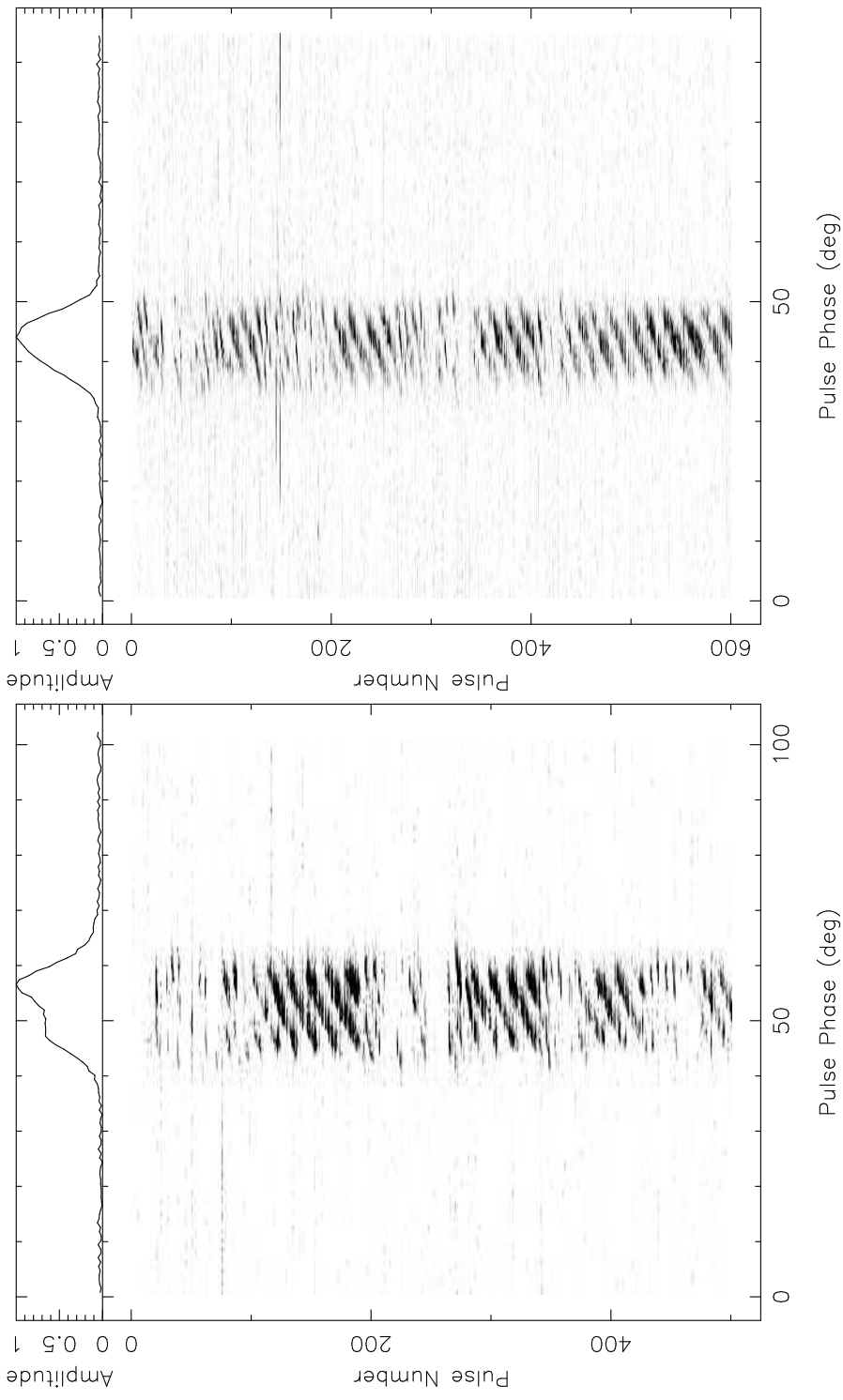

Figure 6.18: Gray scale plot of single pulse data of PSR B1819−22 at 325 MHz (left panel) and 610 MHz (right panel), with the average profile shown on top.

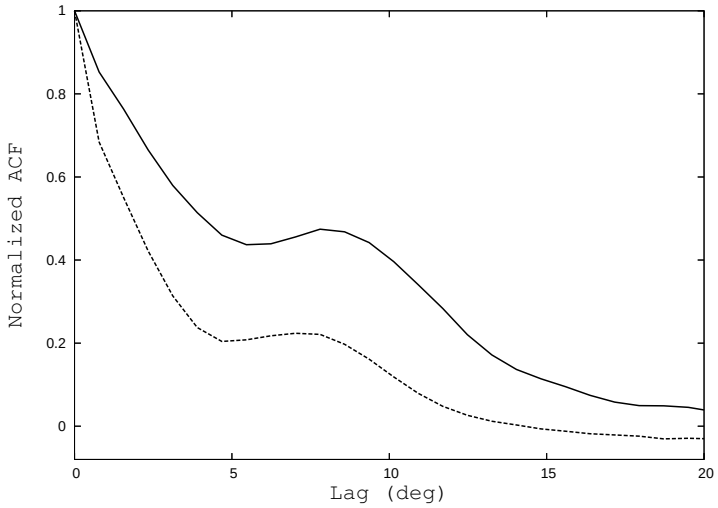

Figure 6.19: Autocorrelation for the on pulse window for PSR B1819−22 at 325 (solid curve) and 610 MHz (dashed curve). The secondary maximum of the auto correlation function is around 8.3 deg at 325 MHz and 7.8 deg for 610 MHz.

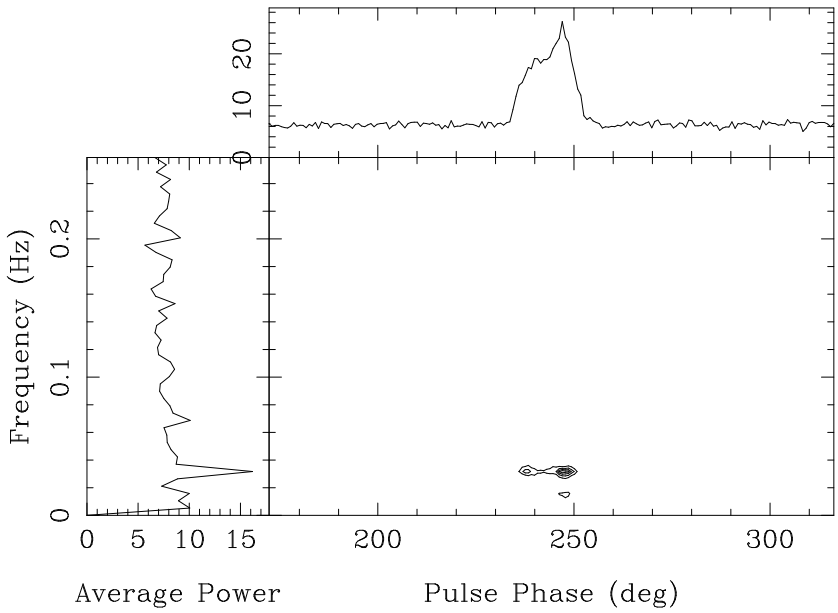

Figure 6.20: The contour plot of the power spectrum of the flux as a function of pulse phase during a sequence of 200 pulses (pulse # 100−200) for PSR B1819−22 at 325 MHz. The left panel shows the power spectrum integrated over the entire pulse longitude. The upper panel shows the power integrated over fluctuation frequency. Fluctuation feature is seen at 16.6 P_1.

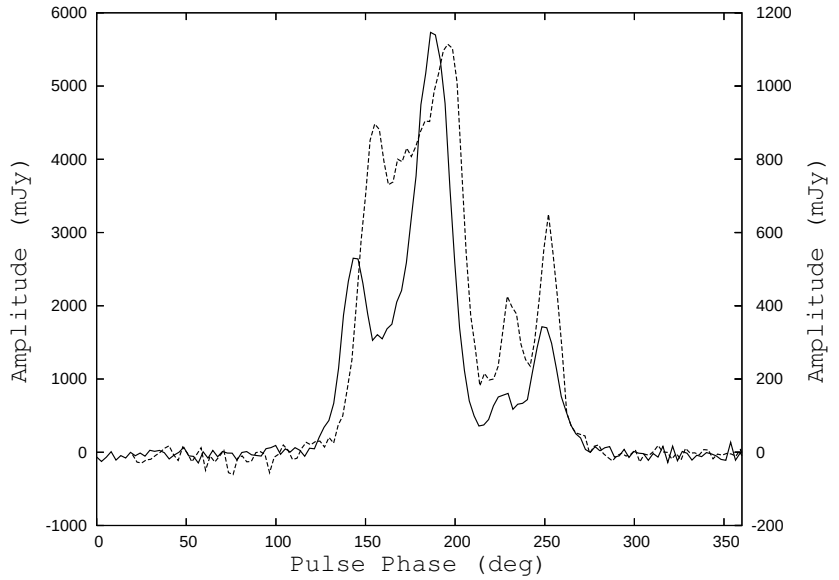

Figure 6.21: Average profile of PSR B1831−04 at 325 MHz (solid line, with amplitude in the left y-scale) and 610 MHz (dashed line, with amplitude in the right y-scale). The pulse amplitude is in mJy.

the corresponding P_2^m values are 8.3 deg and 7.8 deg at 325 and 610 MHz respectively. The fluctuation feature will be effected by mode changes. So we performed the fluctuation analysis for only the stronger mode, plotted in Fig. 6.20 for 325 MHz, and determined that $P_3^m \sim 16.6\ P_1$. Similarly, from fluctuation spectrum at 610 MHz for sequence of pulses in stronger mode, we determine $P_3^m \sim 16.6\ P_1$. This is similar to the result reported by Weltevrede *et al.* (2006) and (2007) at 325 MHz ($P_3^m \sim 16\ P_1$). However, at 1420 MHz they have reported a feature at 9.8 P_1. In our view this change in P_3^m over frequency is caused by the presence of weaker mode with changed drift rate. It would be interesting to investigate if the weaker drift mode dominates at higher frequencies.

(e) PSR B1831−04:

Background:

According to Lyne & Manchester (1988) and Rankin (1993), PSR B1831−04 have both core and cone emission. Both the works predicted a nearly aligned geometry for this pulsar (values of α, β are listed in Table 6.1).

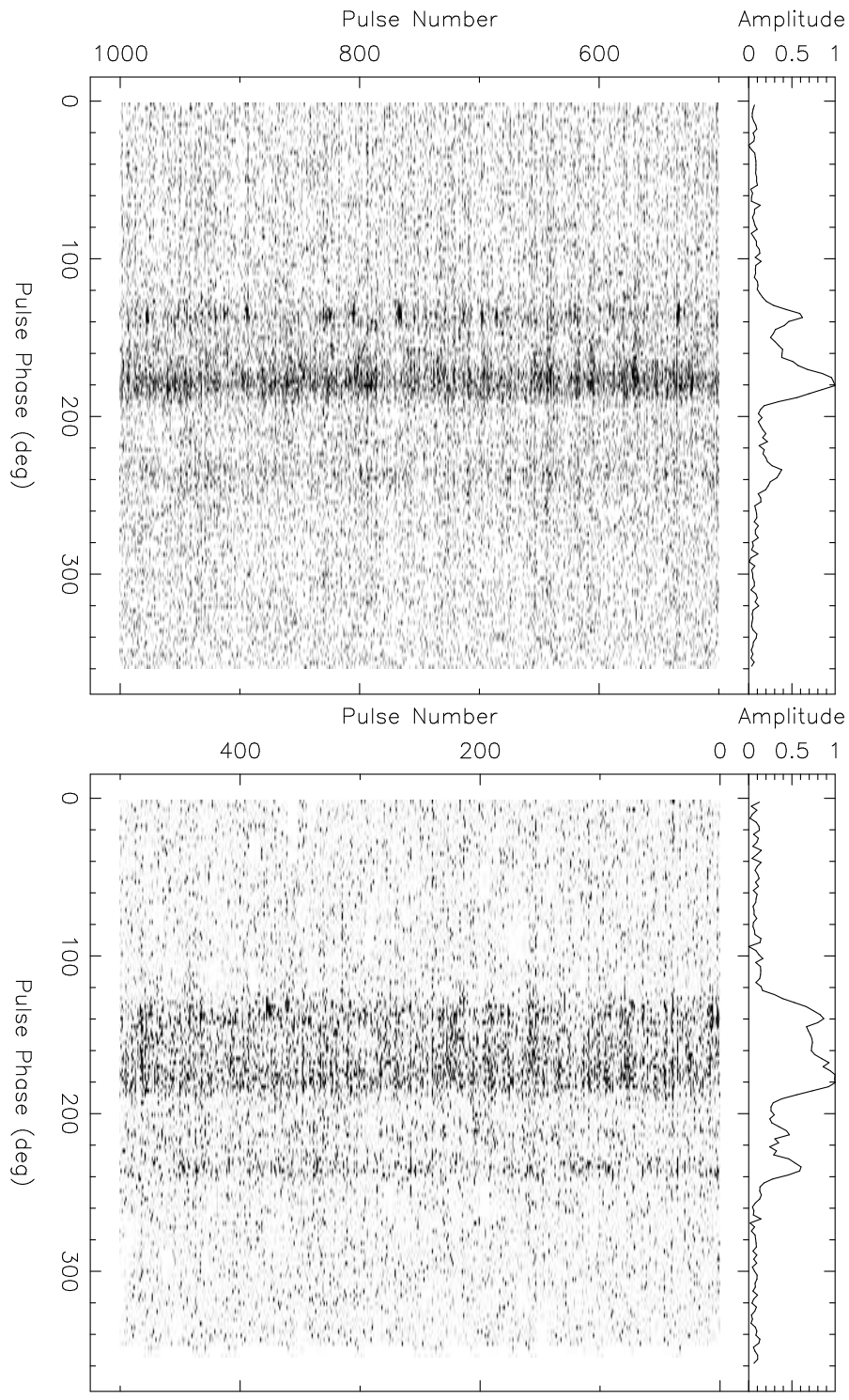

Figure 6.22: Gray scale plot of single pulse data of PSR B1831−04 at 325 MHz (left panel) and 610 MHz (right panel), with the average profile shown on top.

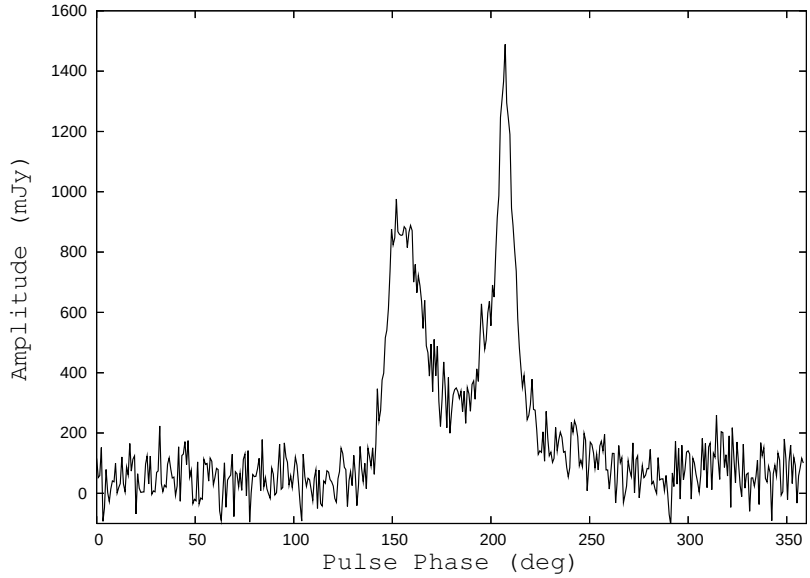

Figure 6.23: Average profile of PSR B1839−04 at 610 MHz. The pulse amplitude is in mJy.

Results:

Fig. 6.21 presents the average profile at 325 and 610 MHz. The relative strength of the conal components and the intensity of the saddle region between two components are more at 610 MHz than at 325 MHz. Fig. 6.22 plots the single pulse gray scale plot at 325 and 610 MHz. Single pluses are clearly visible in the central and also in the leading outer region. Faint single pulses are seen in the trailing outer region. More sensitive observations of this pulsar can provide information about the relation between the core and cone emission.

(f) PSR B1839−04:

Background:

Weltevrede *et al.* (2006) discovered the drifting property of PSR B1839−04 with the WSRT at 1420 MHz. They claimed that the slope of the drift bands in the two drift regions are mirrored and the drift bands are roughly in phase. They compared this pulsar with PSR B0815+09 which exhibits unique "by drifting" pattern (Qiao *et al.*, 2004).

Results:

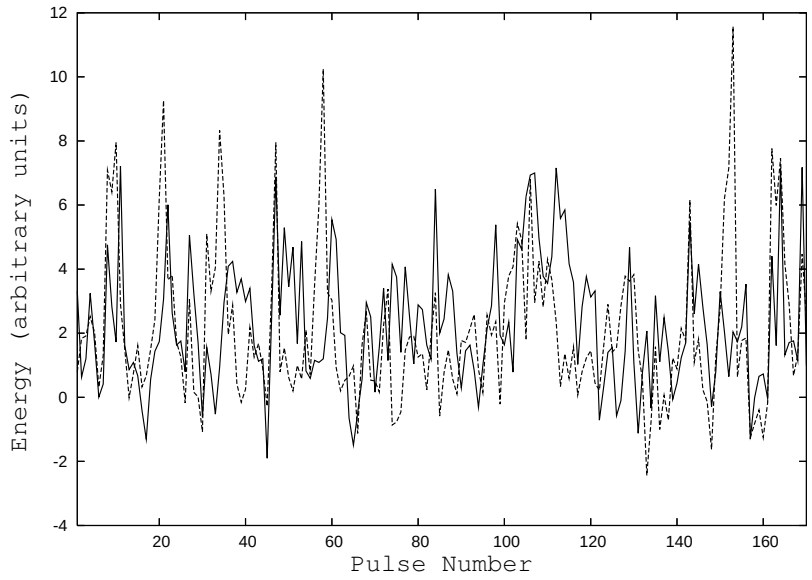

Figure 6.24: Pulse number versus pulse energy under the leading peak (solid line) and the trailing peak (dashed line) for PSR B1839−04 for pulse # 1 to 170 at 610 MHz.

The profile of PSR B1839−04, shown in Fig. 6.23, is steep sided, double peaked and fairly wide (≈ 82 deg). The trailing peak is significantly more intense than the leading peak, and the peaks are joined by a saddle region. The profile is very similar to PSR B0818−41 (the unique wide profile drifting pulsar discussed in Chapter 2, 3 and 4). We observed this pulsar for very short duration (≈ 5min ∼ 170 pulses) with the GMRT during a testing run. Fig. 6.25 shows the single pulse gray scale plot from our observations. Subpulse drifting is observed under the two peaks of the double peaked structure. However, signal to noise of the data is poor in the inner saddle region and we do not see single pulses in this region. There is a phase relation present between the emission under the two peaks. But the claim of Weltevrede *et al.* (2006) that the components are mirrored and have opposite drift direction is not obvious from our study. Fig. 6.24 shows the variation of energy under the leading and the trailing peaks with pulse number. This plot shows that the emission from the leading and the trailing peaks are almost in phase. Fig. 6.26 shows the fluctuation spectra for the same sequence of pulses with a peak at 11.9 P_1. This is in agreement with P_3^m equal to $12P_1$, determined by Weltevrede *et al.* (2006).

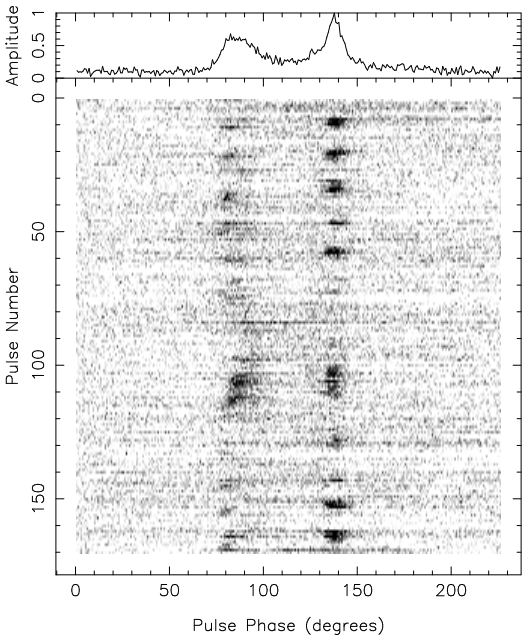

Figure 6.25: Gray scale plot of single pulse data (pulse # 1 to 170) of PSR B1839−04 at 610 MHz.

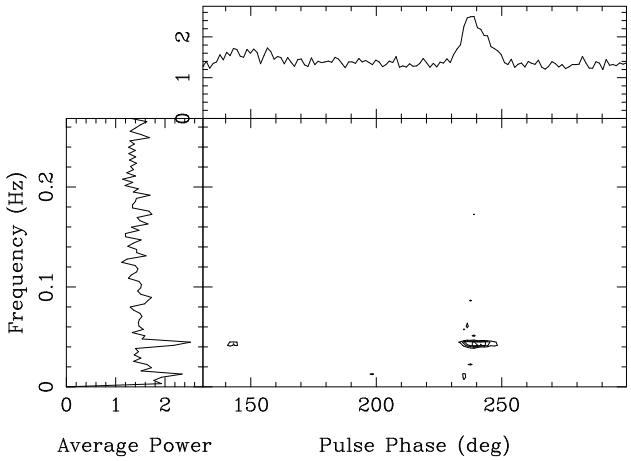

Figure 6.26: The contour plot of the power spectrum of the flux as a function of pulse phase during a sequence of 200 pulses (pulse # 1−170) for PSR B1839−04 at 610 MHz. The left panel shows the power spectrum integrated over the entire pulse longitude. The upper panel shows the power integrated over fluctuation frequency. Fluctuation feature is seen at 12 P_1.

6.4 Summary

In the following we highlight the outcome from our investigation of individual pulsars:

B0540+23:

• Presence of core as well as conal component in the profile
• Sporadic drifting in core component
• Determined P_3^m=9.8 P_1
• Periodicity ∼10 P_1, in the pulse energy versus pulse number plot
• Presence of nulling in core component

B1541+09:

• Presence of core component and two conal components on each side of the core
• Wide pulse profile − relative strengths of the conal components compared to the central component are more for 610 MHz profile
• Strong single pulses with sporadic drifting in core component
• Determined P_3^m=20 P_1
• Periodicity ∼20 P_1, in the pulse energy versus pulse number plot
• Frequent nulling in both core and conal components

B1818−04:

• Presence of core component and two conal components on each side of the core
• Profile do not evolve much with frequency
• Clear signature of drifting in the core component
• Direction of drift occasionally changes from positive to negative
• Periodicity of 4 P_1, in the pulse energy versus pulse number plot
• Occasional nulling in core and conal components

B1819−22:

• Conal triple profile, less evolution of profile with frequency
• Very strong drifting, with simultaneous two drift bands observed at both 325 and 610 MHz
• Two different modes of drifting is observed

• Changing drift rates between the stronger and weaker drift modes probably associated with the nulls
• Horizontal separation between the drift bands P_2^m is equal to 8.3 deg at 325 MHz and 7.8 deg at 610 MHz.
• Determined P_3^m=16.6 P_1 for the stronger drift mode at 325 and 610 MHz

B1831−04:
• Very wide profile : core surrounded by two cones
• Relative strength of conal components are more at 610 MHz
• Single pulses from core and conal components are seen with less SNR

B1839−04:
• Steep sided double peaked, fairly wide pulse profile
• Subpulse drifting observed under the two peaks of the profile
• Determined P_3^m=11.9 P_1
• Periodicity of 12 P_1, in the pulse energy versus pulse number plot
• Emission from leading and trailing peaks probably in phase

To summarize, we have presented the results from preliminary study of six relatively less studied pulsars with diverse profiles, corresponding to different emission as well as viewing geometries. We observe signatures of drifting in five pulsars and determine P_3^m for each of them. We report drifting and nulling corresponding to core components. This is noteworthy, as drifting and nulling are not commonly seen in the core components. Interaction between the drifting and nulling observed by us for one of the pulsars may help to probe emission mechanism. Therefore, this study, having potential to provide new insight about pulsar emission process, warrants more detailed follow-up investigations.

CHAPTER 7

Determination of the orbital parameters of binary pulsars

"It is clear to everyone that astronomy at all events compels the soul to look upwards, and draws it from the things of this world to the other."
– Plato

7.1 Introduction

Apart from the study of single pulse properties of the pulsars as described in the earlier Chapters, I got interested in developing a novel method for determining orbital parameters of binary pulsars. This work was triggered by the discovery of a binary pulsar PSR J0514−4002 (the first known pulsar in the globular cluster NGC 1851) at the GMRT in 2004 (Freire *et al.*, 2004). Though, the first orbital solution by Freire *et al.* (2004), was by more conventional methods, data from binary pulsar PSR J0514−4002 formed the motivation for this work and was used to test our method. In this chapter we provide a detailed description of this method.

With the movement of the binary pulsar in its orbit around the center of mass, the projected velocity of the pulsar in the line of sight direction (v_l) changes and as a consequence the observed pulsar period (P_{obs}) changes. The modulation in v_l (i.e. in P_{obs}) is governed by the orbital parameters of the binary system. So it is possible to get information about the orbit by studying the evolution of P_{obs}. Five orbital parameters, namely, the binary orbital period (P_b), orbital eccentricity (e), projection of the semi major axis on the line of sight ($a_1 sin\, i$, i being the angle between the orbit and the sky plane), longitude of periastron (ω) and the epoch of periastron passage (T_o) can be determined from radial velocity/observed pulsar period data in the

Newtonian, i.e non-relativistic regime (Fig. 7.1). These orbital parameters of binary pulsar systems can be determined by fitting a Keplerian model to the pulsar period versus epoch of observation data. The usual methods require simultaneous fit to many parameters and need an initial guess. Such methods need dense sampling of period measurements at different epochs during the pulsar orbital period. Overcoming some of these factors, Freire, Kramer & Lyne (2001) proposed a new method for determination of the orbital parameters of binary pulsars. They utilised information on periods and period derivatives at multiple observing epochs of the kind used in surveys, and extracted orbital parameter values. They successfully determined the orbital parameters of binary pulsars with nearly circular orbits.

We present an alternative approach to orbital parameter determination using the observing epoch versus pulsar period data, without requiring information about pulsar period derivatives. We demonstrate the method by estimating the orbital parameters of the binary pulsar PSR J0514−4002A, the first known pulsar in the globular cluster NGC 1851 (Freire *et al.*, 2004), and PSR J0024−7204, a binary pulsar in globular cluster 47 Tucanae, referred to as 47 Tuc T hereafter (Camilo *et al.*, 2000). In Sect. 7.2 we describe the method for preliminary determination of the orbital parameters. Sect. 7.3 presents a method for refinement of the determined orbital parameters. In Sect. 7.4 we compare the orbital parameters determined in this work with those available in the literature and discuss the advantages of our method.

7.2 Preliminary determination of orbital parameters

(a) Binary orbital period (P_b)

The observed pulsar period (P_{obs}) versus epoch of observation data set is folded with wide range of trial orbital periods (P_b). Corresponding to each trial value of P_b, we get, P_{obs} versus orbital phase ($\phi = 2\pi t/P_b$, t being the time measured from the periastron). For every set of folded data we calculate a parameter − roughness (R) − which we define as the summation of squared

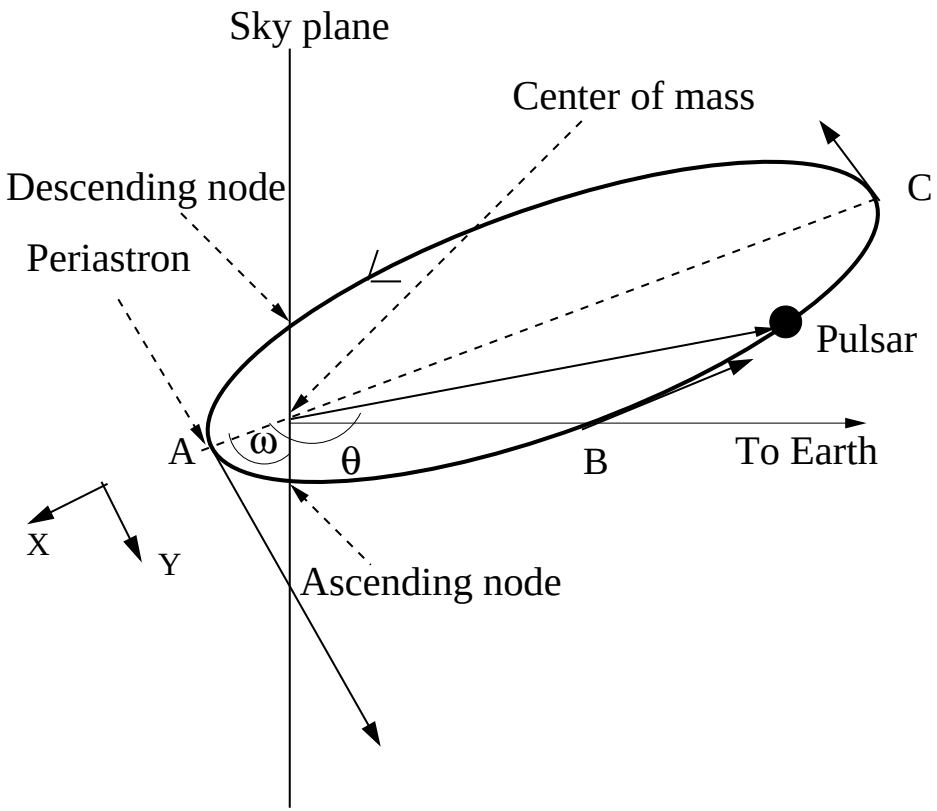

Binary orbit projected to a plane containing the direction of Earth and line of nodes

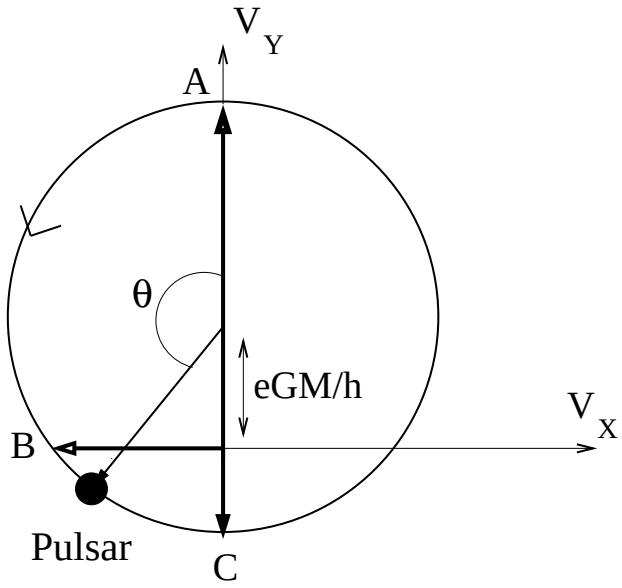

Orbit of binary pulsar in velocity space

Figure 7.1: Binary orbit (ω and θ are measured in the orbital plane and not in the projection shown).

differences of P_{obs} between the adjacent pairs of ϕ. Therefore,

$$R = \sum_{i=1}^{n} (P_{obs}(i) - P_{obs}(i+1))^2 \tag{7.1}$$

where n represents the total number of data points sorted in order of orbital phase. For the optimal choice of the trial folding period P_b, the plot of P_{obs} versus ϕ is expected to be the smoothest and hence the corresponding roughness parameter (R) will be minimum. In the search of P_b the increment (ΔP_b) must be chosen to cause small orbital phase shift (i.e. $\Delta\omega_b\, T << 1$) over the full data length T (i.e. $(2\pi/P_b^2)\Delta P_b T << 1$).

As a crosscheck, we apply this method on a simulated Keplerian orbit. First, we simulate sparsely and randomly sampled epoch of observation versus radial velocity data points with a set of arbitrarily chosen P_b, e, ω and T_o values (refer to Eqn. 7.6 of Sect. 7.2(b) for details). Using this kind of randomly generated radial velocity data, spanning over widely separated epochs, as input we apply the smoothness criterion described in Eqn. 7.1 and the true binary orbital period is recovered. There are few local minimas where R is lower than the adjacent values but there is no comparable minimum as to the strongest minimum corresponding to true P_b. The method worked for Keplerian orbits generated with various sets of P_b, e, ω and T_o values, and we could reproduce the true periodicity. Hence, to obtain a unique solution for P_b, one need to search for P_b within a wide range which includes the actual P_b with small enough step size determined by the criterion $(2\pi/P_b^2)\Delta P_b T << 1$. For preliminary determination of P_b of PSR J0514−40, we used P_{obs} versus epoch of observation data from the GMRT observations. We used 31 such data points, collected over six months, which are similar to the data used by Freire *et al.* (2004). For the known binary pulsars in globular clusters the orbital periods lie in the range $P_b \sim$ few hours to 256 days (refer to Table 1.1 of Freire (2000)). Initially we try P_b starting from few hours and up to 300 days with step size satisfying the criterion $(2\pi/P_b^2)\Delta P_b T << 1$, and determine R using Eqn.7.1. Then we narrowed down our search of the P_b around the lowest R. Though there are few local minima where R is lower than the adjacent values, we observe the strongest and rather flat minimum for a range of nearby values of P_b s around 18.79 days, no comparable minimum is observed in the range from few hours to 300 days. Fig. 7.2 presents the

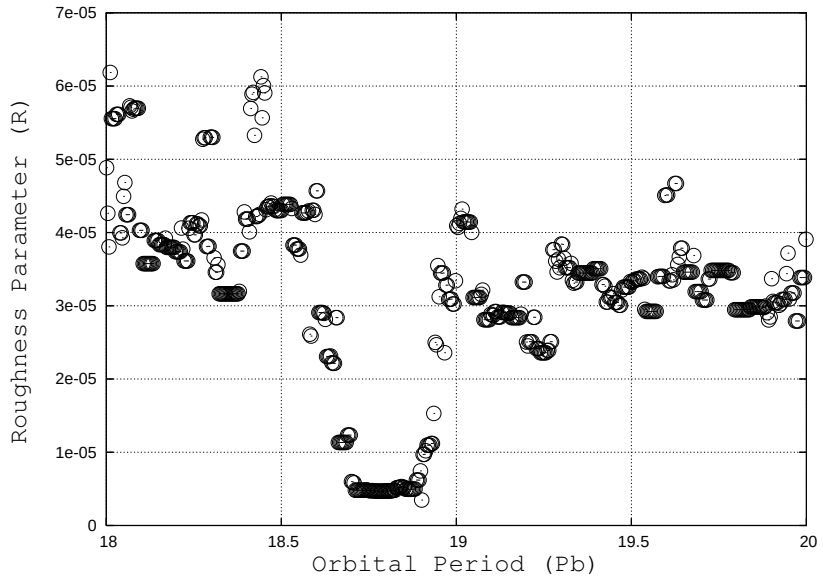

Figure 7.2: Roughness parameter (R) plotted against orbital period (P_b) for PSR J0514−4002A (a zoomed region near minimum R).

plot of the trial P_b against the corresponding R, zoomed into a region where R is minimum. For P_b=18.791 days, R is minimum. We fold the data with P_b=18.791 days to generate P_{obs} versus ϕ data set, which is plotted in Fig. 7.3. We notice quite smooth nature of the plot and abrupt change of the pulsar period corresponding to the periastron passage, around orbital phase equal to 0.4.

For the determination of orbital period of 47 Tuc T we utilised the 9 data points (provided in Freire, Kramer & Lyne (2001)) of P_{obs} versus epoch of observation. We determine P_b=1.1 days which is close to the value estimated by Freire, Kramer & Lyne (2001).

(b) Other orbital parameters from the hodograph

Basic principle

The left panel of Fig. 7.1 shows the orbit of a binary pulsar around the center of mass of the system, projected in a plane containing the direction of Earth and the line of nodes (line of intersection of orbital plane and the sky plane). 'A' denotes the periastron position and θ is the angle of the pulsar to the periastron, also known as 'true anomaly'. 'B' and 'C' are two other points in the binary orbit. A rather geometric picture of the Kepler's laws

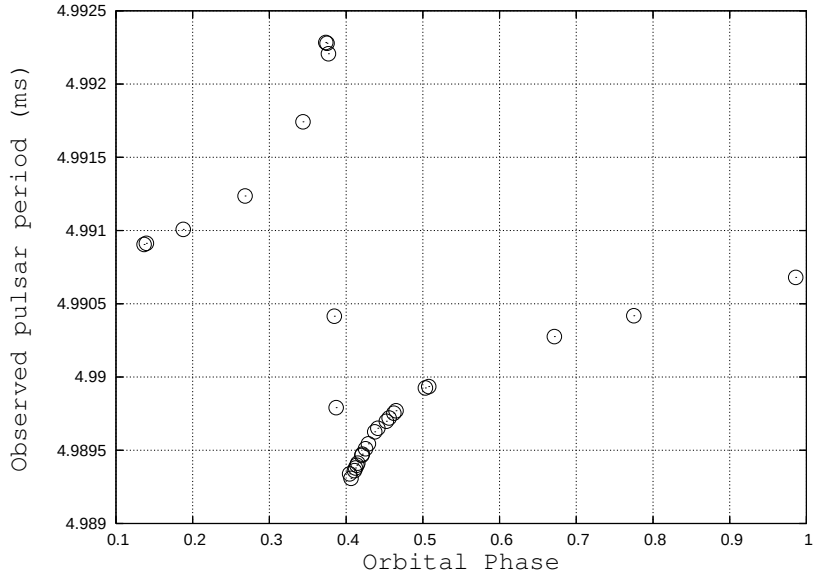

Figure 7.3: Orbital phase (ϕ) versus observed pulsar period (P_{obs}) of PSR J0514−4002A after folding the data with P_b=18.791 days.

using the idea of velocity space is due to Hamilton (1987). It is not often used and hence described briefly below. According to Newton's laws for the path of the vector $(\vec{r}_{pulsar}(t) - \vec{r}_{companion}(t))$ (i.e. for the relative orbit of the pulsar with respect to the companion star), the relative velocity,

$$\Delta \mathbf{v} = -\left(\frac{GM}{r^2}\right) \Delta t \, \hat{\mathbf{r}} \tag{7.2}$$

where G is the Gravitational constant and M is the total mass of the pulsar and the companion star.
From the conservation of angular momentum,

$$\Delta\theta = \frac{h}{r^2} \, \Delta t \tag{7.3}$$

where h is angular momentum per unit mass.
Dividing the absolute value of Eqn. 7.2 by Eqn. 7.3 we get,

$$\frac{|\Delta \mathbf{v}|}{\Delta\theta} = \left(\frac{GM}{h}\right) = constant \tag{7.4}$$

The path followed by the velocity vector of a particle is called the hodograph.

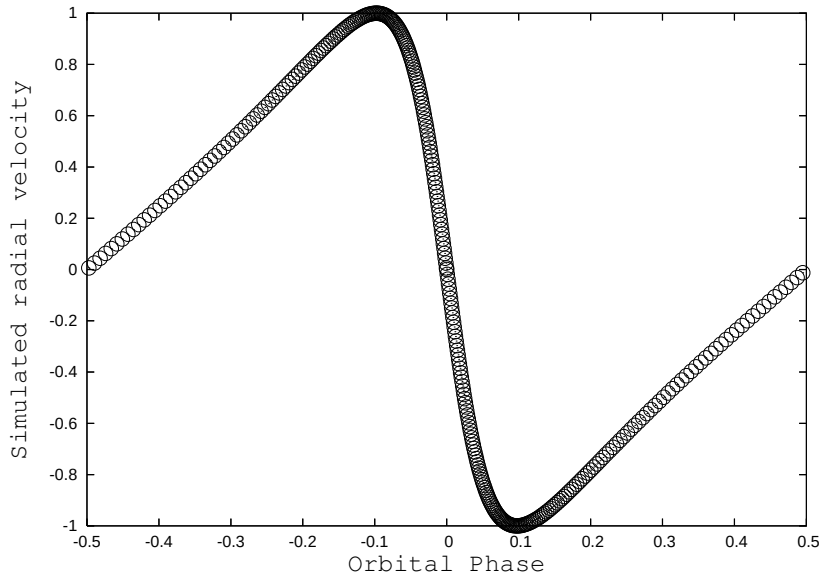

Figure 7.4: Simulated radial velocity versus orbital phase for $e = 0.5$, $\omega = 90$ deg, antisymmetric function.

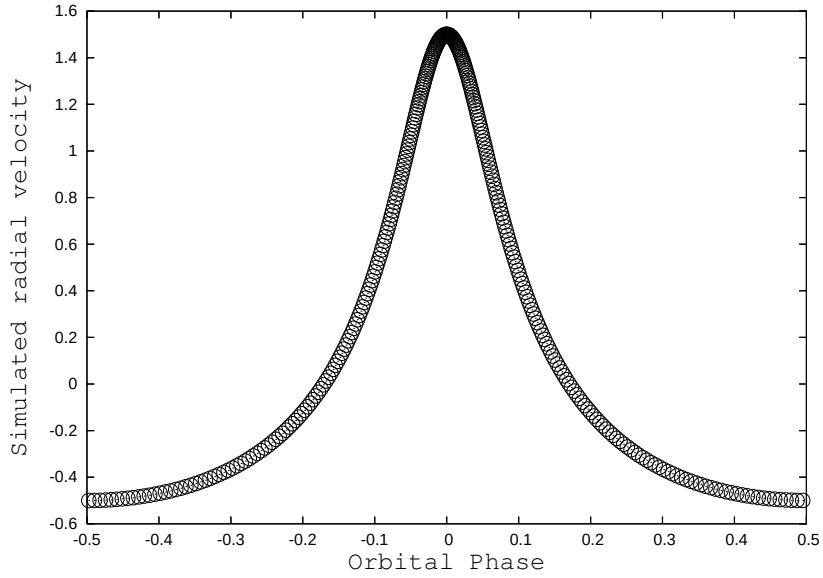

Figure 7.5: Simulated radial velocity versus orbital phase for $e = 0.5$, $\omega =$ 0deg, symmetric function.

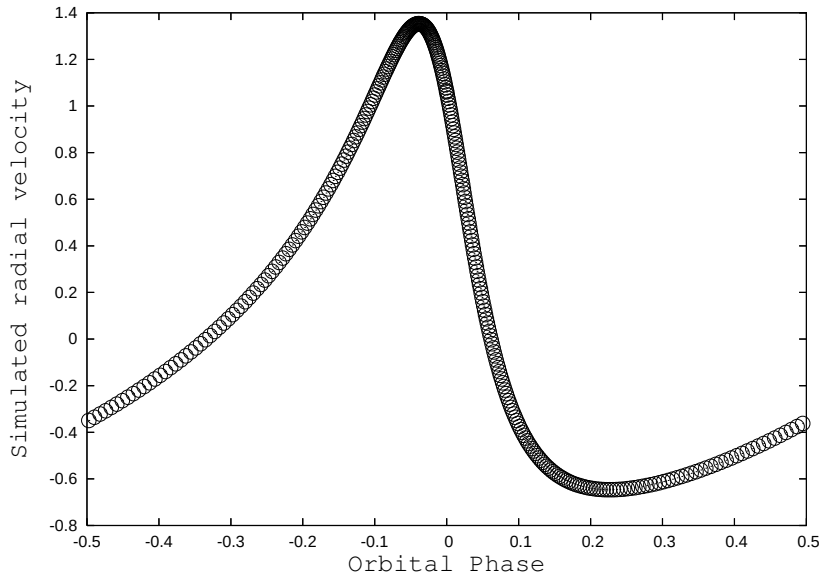

Figure 7.6: Simulated radial velocity versus orbital phase for $e = 0.5$, $\omega = 45$ deg, combination of antisymmetric and symmetric function.

$\Delta\mathbf{v}$ is the arc length and $\Delta\theta$ is the angle traversed by the pulsar in velocity space. The ratio $(|\Delta\mathbf{v}|/\Delta\theta)$ is the radius of curvature of the hodograph. Since the radius of curvature is constant, the hodograph is a circle for Keplerian motion. The right panel of Fig.7.1 shows the corresponding hodograph of the elliptical binary orbit that is shown in the left panel. The center of the circle is offset from the origin by (eGM/h) and the radius of the circle is (GM/h). For a particular eccentricity (e) and longitude of periastron (ω), the x and y component of velocity are given by,

$$v_x = -\frac{GM}{h} sin\,\theta;\; v_y = \frac{GM}{h}(cos\,\theta + e) \tag{7.5}$$

Hence, the relative radial velocity along the projection of the line of sight into the orbital plane is given by,

$$\begin{aligned} v_r &= (v_x\, cos\,(\pi/2 - \omega) + v_y\, sin\,(\pi/2 - \omega)) \\ &= \left(\frac{GM}{h}\right)(sin\,\theta\; sin\,\omega + (cos\,\theta + e)\; cos\,\omega) \\ &= \left(\frac{GM}{h}\right) v_{rs} \end{aligned} \tag{7.6}$$

For $\omega = 90$ deg the observed velocity will be antisymmetric (odd) as a function of θ or time measured from periastron (Fig. 7.4). Similarly, for $\omega = 0$ deg the observed velocity will be symmetric (even), as in Fig. 7.5. For other intermediate values of ω the observed velocity will be a combination of antisymmetric and symmetric parts in the ratio of $sin\,\omega/cos\,\omega$, as shown in Fig. 7.13. Plot of the antisymmetric versus the symmetric part will be an ellipse and the parameters of the ellipse will provide preliminary values of the orbital parameters. As a crosscheck, we apply this method on simulated Ke-

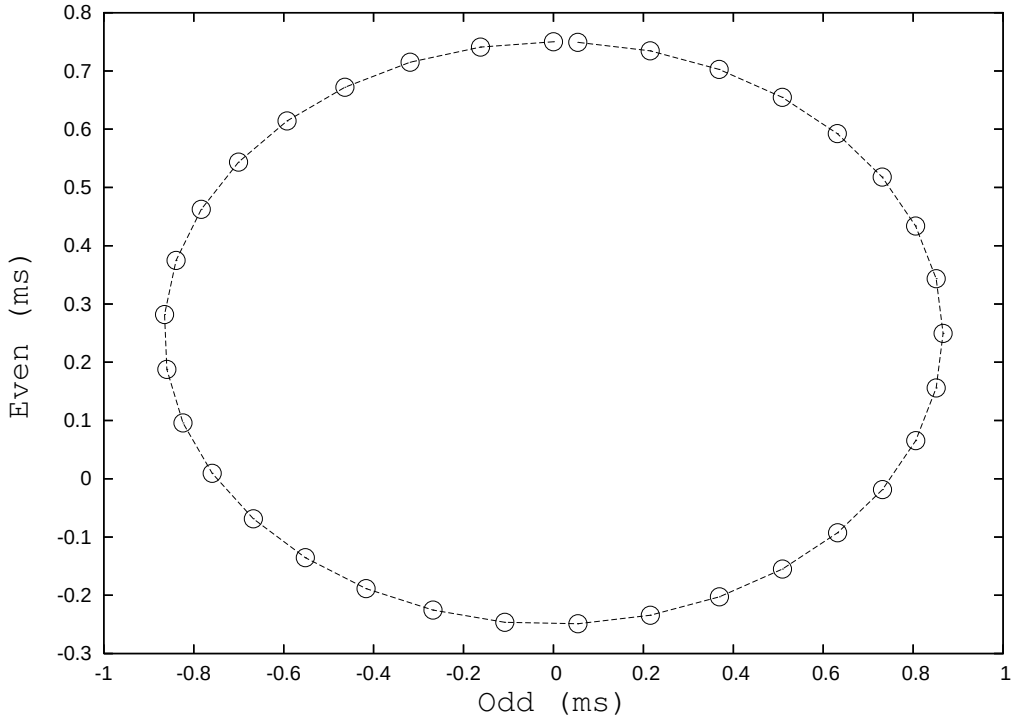

Figure 7.7: $v_{r_s}^{odd}$ versus $v_{r_s}^{even}$ (generated for simulated Keplerian orbit with $e = 0.5, \omega = 60$ deg) and the fitted ellipse for correct choice of T_o.

plerian orbits. We simulate v_{rs} for trial value of e, ω and T_o. Corresponding to each v_{rs} value at a particular orbital phase (ϕ), we determine the v_{rs} at conjugate phase ($2\pi - \phi$), using Lagrange's interpolation method with three points. The even and odd parts are defined as follows,

$$v_{r_s}^{even} = (v_{rs}(\phi) + v_{rs}(2\pi - \phi))/2 \tag{7.7}$$

$$v_{r_s}^{odd} = (v_{rs}(\phi) - v_{rs}(2\pi - \phi))/2 \tag{7.8}$$

Plot of $v_{r_s}^{odd}$ versus $v_{r_s}^{even}$ should be an ellipse, for correct choice of T_o (Fig.7.7). The ratio of major and the minor axes of the ellipse gives, $tan\,\omega$, and the shift of the origin of the ellipse gives e. Using the method illustrated at the end of this section, we fit an ellipse to the $v_{r_s}^{odd}$ versus $v_{r_s}^{even}$ data. ω and e are recovered from the parameters of the best fit ellipse.

Since v_{r_s} and the observed pulsar period (P_{obs}) will have similar modulations, we construct antisymmetric and symmetric parts from the P_{obs}. Corresponding to each P_{obs} value at a particular orbital phase (ϕ), we determine the P_{obs} at conjugate phase ($2\pi - \phi$) using Lagrange's interpolation method with three points. The even and the odd parts are defined as follows,

$$P_{obs}^{even} = (P_{obs}(\phi) + P_{obs}(2\pi - \phi))/2 \tag{7.9}$$

$$P_{obs}^{odd} = (P_{obs}(\phi) - P_{obs}(2\pi - \phi))/2 \tag{7.10}$$

The plot of P_{obs}^{odd} versus P_{obs}^{even} should be an ellipse for correct choice of the periastron passage (T_o).

Method for ellipse Fitting

In the following we describe the ellipse fitting method, which will be used for determination of orbital parameters. For fitting an ellipse to a set of points (P_{obs}^{even} versus P_{obs}^{odd}) we use the information that the origin of the ellipse will be at (0, $(eGM/h)\,cos\,\omega$), and the major and minor axis of the ellipse will be $(GM/h)\,sin\omega$ and $(GM/h)cos\omega$. Using this information we get an expression which is linear in parameters and hence is easy to fit. The ellipse will be of the form,

$$\frac{X^2}{\left(\frac{GM}{h}\ sin\,\omega\right)^2} + \frac{\left(Y - e\frac{GM}{h}cos\,\omega\right)^2}{\left(\frac{GM}{h}\ cos\,\omega\right)^2} = 1 \tag{7.11}$$

Replacing $(GM/h)\ sin\,\omega = a$, $(GM/h)\ cos\,\omega = b$, $(eGM/h)\ cos\,\omega = d$ we have,

$$\frac{X^2}{a^2} + \frac{\left(Y - d\right)^2}{b^2} = 1 \tag{7.12}$$

Which can easily be simplified to the form,

$$AX^2 + BY^2 + CY = 1 \tag{7.13}$$

Where $A = (1/a^2)/(1 - b^2/d^2), B = (1/b^2)/(1 - b^2/d^2), C = -(2d/b^2)/(1 -$

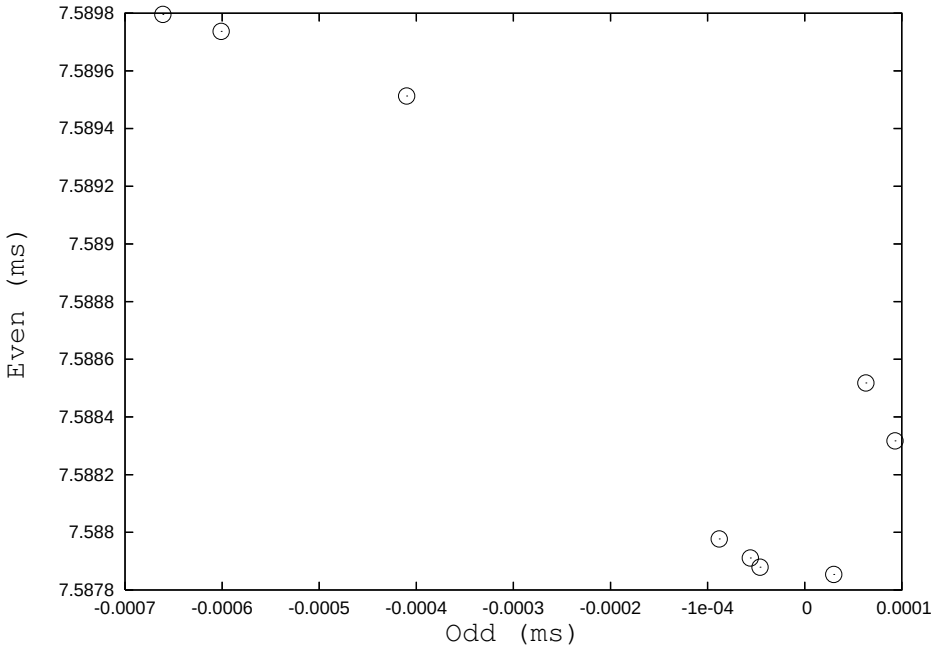

Figure 7.8: P_{obs}^{odd} versus P_{obs}^{even} for 47 Tuc T for arbitrary choice of T_o.

b^2/d^2). We use the singular value decomposition method, as described by Press *et al.* (1992) (Freire, Kramer & Lyne (2001) have also used this method) to determine A, B and C.[1] χ^2 in this case is defined as,

$$\chi^2 = \sum_{i=1}^{N}((A\,(P_{obs}^{odd})_i^2 + B\,(P_{obs}^{even})_i^2 + C(P_{obs}^{even})_i) - 1)^2 \qquad (7.14)$$

Here, χ^2 means deviations of the points normal to the ellipse. Criterion of minimising the χ^2 value gave us satisfactory results. From parameters of the fitted ellipse (A, B and C) we determine a, b and c and obtain e, ω values as, $e = d/b$ and $\omega = tan^{-1}(a/b)$.

Determination of the orbital parameters: We vary T_o, corresponding P_{obs}^{odd} versus P_{obs}^{even} are generated, and fit an ellipse to the P_{obs}^{odd} versus P_{obs}^{even} plot, using the method described above . Fig. 7.8 is the plot of P_{obs}^{odd} versus P_{obs}^{even} for real data of 47 tuc T with arbitrary choice of T_o. Fig. 7.9 is the plot of P_{obs}^{odd} versus P_{obs}^{even} for real data of 47 tuc T with optimal choice of T_o

[1]While doing the ellipse fitting for the real data we used P_{obs}^{odd} versus mean subtracted P_{obs}^{even} data to avoid numerical problems.

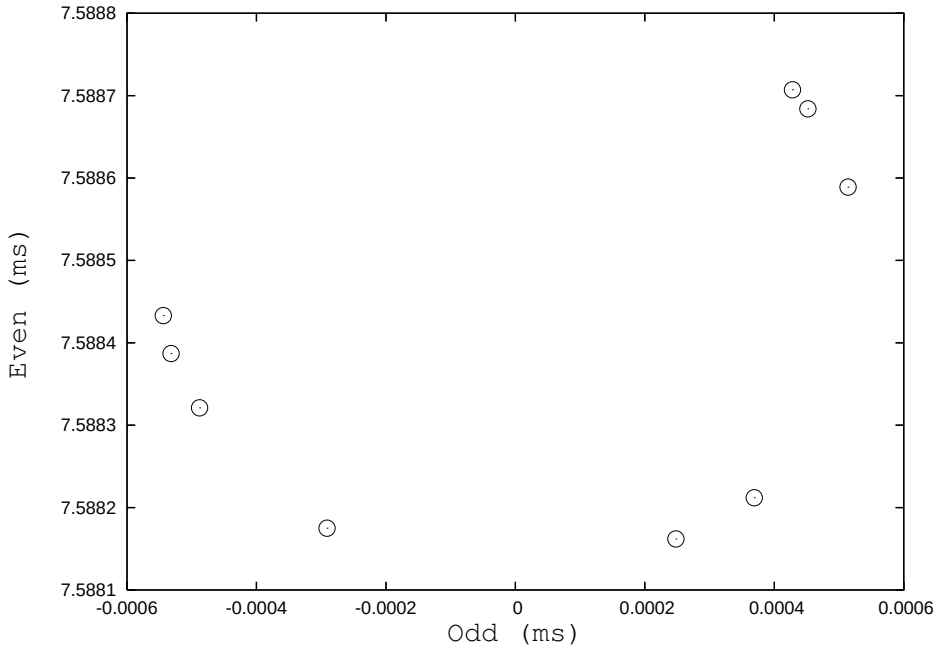

Figure 7.9: P_{obs}^{odd} versus P_{obs}^{even} for 47 Tuc T for correct choice of T_o with minimum χ^2.

(T_o for which χ^2 is minimum after ellipse fitting). Preliminary values of e, ω are obtained from the parameters of the best fit ellipse.

7.3 Refinement of the determined orbital parameters

In this section we take the preliminary determined orbital parameters as the initial guess in a linear least squares fit. This is now computationally efficient since only a small range of the parameters, near the first guess values, has to be searched. P_{obs} is determined by the relation,

$$P_{obs} = P_o\ (1 + \frac{v_l}{c}) \tag{7.15}$$

where P_o is the rest frame period of the binary pulsar, v_l is the projected velocity of the pulsar in the line of sight direction and c is the velocity of light. This relationship is valid provided v_l is small compared to c.

Now we explain the straight line nature of P_{obs} versus v_{rs} plot and interpret the slope and intercept in terms of the orbital parameters. We consider the binary orbit of the pulsar, where m_p and v_p are the mass and velocity of the pulsar and m_c and v_c are the same for the companion. a is the semi major axis of the pulsar orbit relative to the companion and a_1 is the semi major axis of the pulsar relative to the center of mass. Using the standard relation between mass and specific angular momentum in a Kepler orbit we make the following illustrations for the relative orbit of the pulsar with respect to the companion.

$$\frac{GM}{h} = \frac{G(m_p + m_c)}{\sqrt{a(1-e^2)G(m_p + m_c)}} \tag{7.16}$$

$$v_r = (v_p - v_c) = \frac{m_p + m_c}{m_c} v_p \tag{7.17}$$

$$a = a_1 \frac{m_p + m_c}{m_c} \tag{7.18}$$

Substituting GM/h (from Eqn. 7.18) in Eqn. 7.6,

$$v_r = \sqrt{\frac{G(m_p + m_c)}{a(1-e^2)}} \times v_{rs} \tag{7.19}$$

Therefore velocity of the pulsar v_p can be obtained from Eqn. 7.19 as,

$$v_p = \frac{m_c}{m_p + m_c} \sqrt{\frac{G(m_p + m_c)}{a(1-e^2)}} \times v_{rs} \tag{7.20}$$

Projected velocity of the pulsar in the line of sight direction (v_l) is given by,

$$v_l = v_p \times sin\, i = \frac{m_c}{m_p + m_c} \sqrt{\frac{G(m_p + m_c)}{a(1-e^2)}} \times v_{rs} \times sin\, i \tag{7.21}$$

Therefore, v_l versus v_{rs} is a straight line with slope (S),

$$S = \frac{m_c}{m_p + m_c} \sqrt{\frac{Gm_c}{a_1(1-e^2)}} sin\, i \tag{7.22}$$

So P_{obs} versus v_{rs} will also be a straight line with slope (S_{fit}),

$$S_{fit} = \frac{P_o}{c} \times S \tag{7.23}$$

But P_b and a_1 are related by,

$$P_b{}^2 = \frac{4\pi^2 a_1{}^3}{G} \left(\frac{(m_p + m_c)^2}{m_c{}^3} \right) \tag{7.24}$$

Therefore, from Eqn. 7.23 and Eqn. 7.24,

$$(a_1 sin\ i)^2 = \frac{P_b^2 S_{fit}^2 (1 - e^2) c^2}{4\pi^2 P_o^2} \tag{7.25}$$

Scheme for determination of orbital parameters

Following are the steps for determination of orbital parameters:

1. We simulate orbital phase (ϕ) versus scaled radial velocity (v_{rs}) with trial values P_b, e, ω, T_o (using Eqn. 7.6).

2. To compare the simulated data with the observations we need to find out the simulated v_{rs} at those orbital phase points for which P_{obs} is available. v_{rs} at observed orbital phases is obtained by using Lagrange's interpolation method with three points.

3. Next we fit a straight line to P_{obs} versus v_{rs} and calculate χ^2.

We repeat this procedure for all the trial combinations of orbital parameters. For the right choice of the orbital parameters, the plot of P_{obs} versus v_{rs} will be a straight line (see Eqn. 7.23). Hence, the set of orbital parameters, P_b, e, ω, T_o, for which the straight line fit is best, i.e. χ^2 value is minimum, will correspond to the optimal choice of orbital parameters. χ^2 is minimised so that the expected value for N independent data points is N. A change of 1 then corresponds to a 68% confidence limit (page 694, Press *et al.* (1992)). Given the above criterion for change in χ^2, the optimal grid for any parameter (keeping all the other parameter fixed) would have about three points in an interval over which the minimum χ^2 ($\chi^2{}_{min}$) increases by 1 σ ($\sigma \sim \chi^2{}_{min}$/N). This is the criterion that decide the step size used for different trial combinations of the orbital parameters. The search for each orbital parameter was continued till the χ^2 becomes about 1000 σ on each side of the minima, keeping all the other parameters fixed. It is possible to

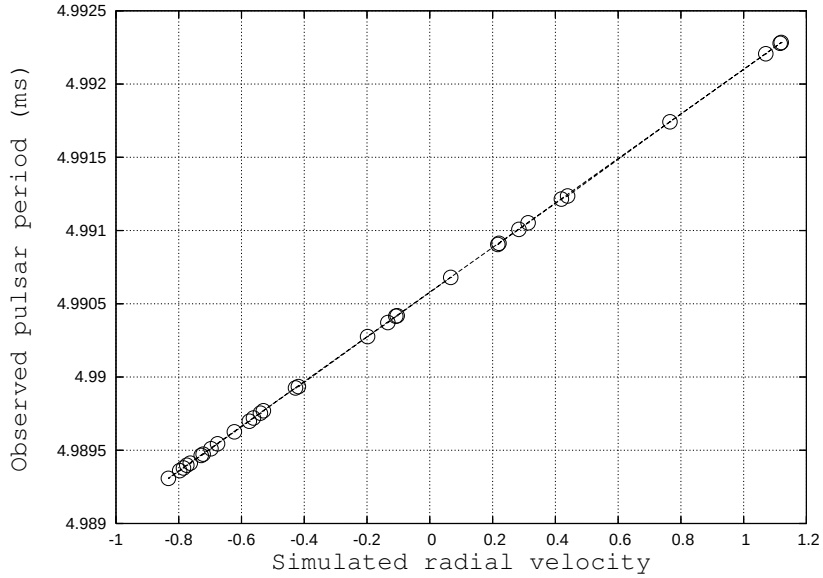

Figure 7.10: Simulated radial velocity (v_{rs}) interpolated at each observing epoch is plotted against observed pulsar period (P_{obs}) for PSR J0514−4002.

use this method to determine the orbital parameters, with out assuming the preliminary values. But in that case one has to search a wide range for each of the orbital parameters which would be computationally expensive. The intercept of the fitted straight line will give the value of P_o. Substituting the values of P_b, e, P_o and the slope of the fitted straight line S_{fit}, in Eqn. 7.25, we can determine the projected semi major axis in light seconds, $a_1 sin(i)/c$.

Implementation of the method

(1) J0514−4002 :

Fig.7.10 presents the plot of P_{obs} versus v_{rs} (generated with the optimal choice of orbital parameters) and the corresponding straight line fit. Fig. 7.4 is the plot of the calculated residual for each data point as a function of ϕ for the best straight line fit. The residuals are quite small (almost negligible) for all the measurements, indicating successful fitting and orbital parameter determination. Table 7.2 lists the determined orbital parameter values of PSR J0514−4002. The step size used for the different sets of trial of orbital parameters, P_b, e, ω and T_o, are also listed in Table 7.2. The uncertainty on the values of each of the orbital parameters are calculated from the change of orbital parameter values required for 1σ change in the χ^2 value, keeping

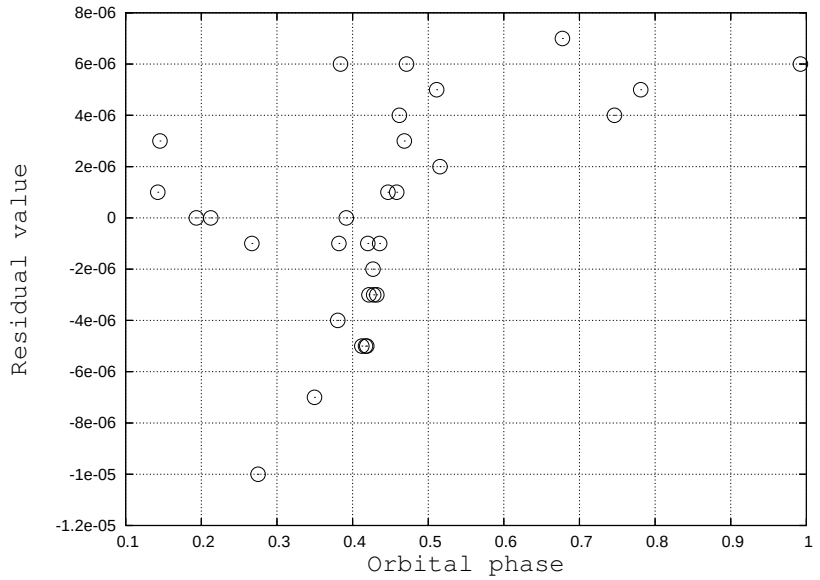

Figure 7.11: Residual from the best fit straight line as a function of orbital phase (ϕ), for PSR J0514−4002.

all the other parameters fixed. The uncertainty quoted in the bracket is on the last significant digit of the concerned parameter.

(2) 47 Tuc T : Fig. 7.12 plots the P_{obs} versus the optimal v_{rs}. Fig. 7.13 shows that the simulated and observed radial velocity plotted as a function of pulse phase matches very well. From Fig. 7.12 and Fig. 7.13 it is evident that the observational data is well reproduced by simulation with the derived orbital parameters. Determined orbital parameter values and the associated errors are listed in Table 7.3.

7.4 Discussion

The orbital parameters determined in this chapter and those determined by Freire *et al.* (2004) and Freire *et al.* (2007) for PSR J0514−4002 are listed in Table 7.2. For PSR J0514−4002, we have used similar data to those used by Freire *et al.* (2004) (Sect. 7.2). The orbital parameters determined by us are close to their determination within the error quoted by them. But our results are more accurate and are close to the values obtained by Freire *et al.* (2007) who have used a much longer data stretch from regular observations with the GBT for about two years. Table 7.3 compare the orbital parameters

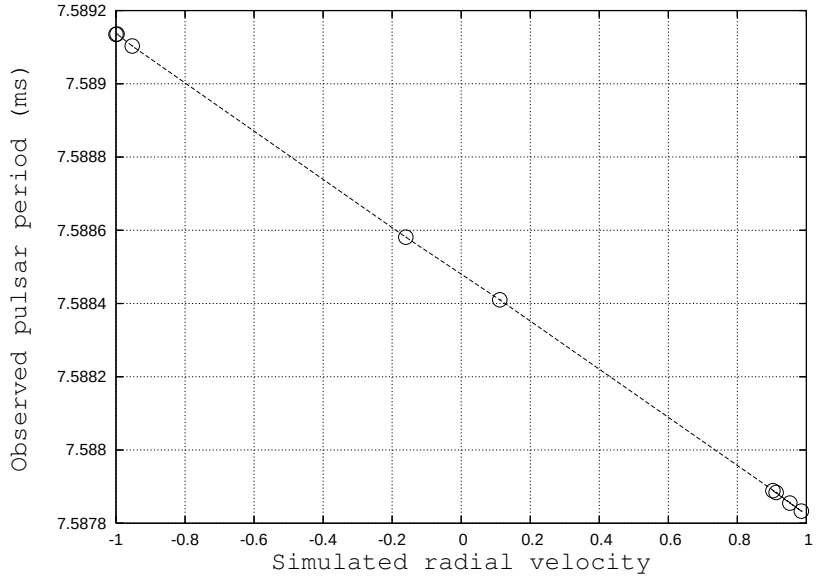

Figure 7.12: Same as Fig. 7.7, but for 47 Tuc T.

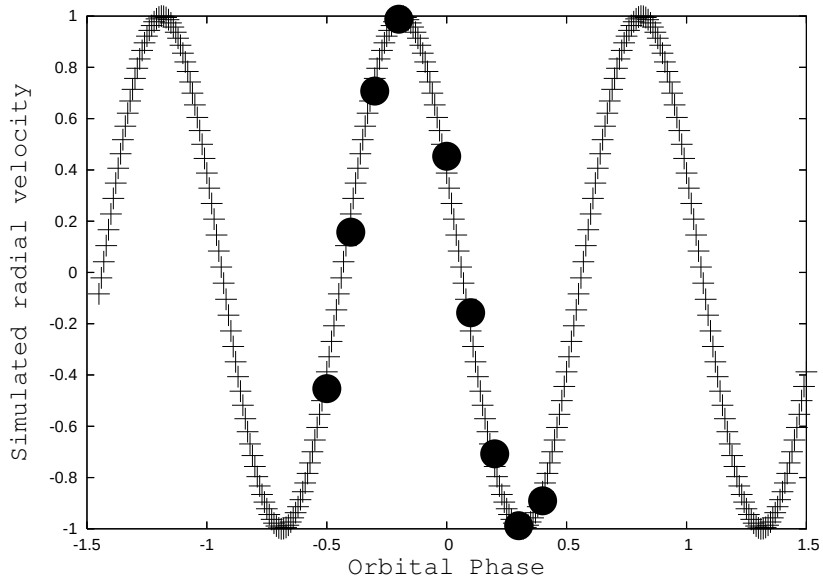

Figure 7.13: Radial velocity with simulation with derived orbital parameters (plus sign) and from the observations calculated from the observed pulse period (solid circles) plotted as a function of orbital phase, for for 47 Tuc T.

determined by us with those obtained by, Freire, Kramer & Lyne (2001) and Camilo *et al.* (2000) for 47 Tuc T. Our result agree with Freire, Kramer & Lyne (2001), but are more accurate and closer to the values predicted by Freire *et al.* (2007), who used coherent timing analysis for orbital parameter determination. Note that the small eccentricity of 47 Tuc T could only be found from the coherent timing solution. Our method of orbital parameter determination has the following features :

(1) The procedure for determination of binary orbital parameters outlined in this chapter utilises the measurements of P_{obs} at given observing epoch and does not require any information about the period derivatives in contrast to the method described by Freire, Kramer & Lyne (2001). It may at first sight be surprising that period derivatives do not help to constrain the final orbital solution. This can be understood by examining the accuracy of the measurement which is limited by the period variation over the length of a single observing session. Clearly, the period derivatives implied by the P_{obs} versus ϕ curves already have smaller errors than this, since one is looking at period variations over the P_b time scale. However, period derivatives clearly plays a role in the work by Freire, Kramer & Lyne (2001) in determining orbital phases and P_b, which in our method comes from the roughness search.

(2) Unlike the method used by Freire, Kramer & Lyne (2001), which works for nearly circular binary orbits, this method works for binary orbit with any eccentricity. For example, our method worked well for the binary orbit with highest known eccentricity (PSR J0514−4002 with $e \sim 0.888$), and also for an orbit with lower eccentricity (PSR 47 Tuc T with $e \sim 0$).

(3) The accuracy of the determined orbital parameter values are subject to the sampling of the binary orbit. Our method works with random sampling of the orbit. A small number of data points are required for determination of orbital parameters in our method. In case of PSR J0514−4002, our method converged even for 5 random data points.

(4) The computation involves only one dimensional searches and linear least square fits [2].

[2]The code we have used consists of several stand alone programs in the 'octave' (matlab like) language. These programs have not been linked to make up a pipeline. Readers interested in the code may contact me

Table 7.1: Epoch of observation versus measured periods for PSR J0514−4002

T (MJD)	P_{obs} (ms)
53015.8	4.99090524
53015.9	4.990913
53016.8	4.9910076
53019.7	4.99174228
53020.8	4.9893395
53020.9	4.9893085
53021.7	4.98969759
53021.8	4.98972017
53025.9	4.9902763
53027.8	4.99041771
53031.8	4.99068
53039.8	4.9893607
53039.8	4.989398
53040.7	4.9897533
53040.8	4.98977
53058.6	4.989379
53058.6	4.989412
53058.7	4.98946454
53074.7	4.991236
53076.6	4.992284
53076.7	4.99227832
53077.5	4.98947338
53077.6	4.98951
53077.7	4.989544
53095.5	4.99220733
53095.6	4.990415
53095.7	4.989791
53135.4	4.9899248
53135.5	4.9899355
53228.2	4.9896262
53228.2	4.98965

Table 7.2: Orbital parameters of PSR J0514−4002

Parameter	Freire *et al.* (2004) (Coherent timing analysis)	Freire *et al.* (2007) (Coherent timing analysis)	This work
Orbital period (P_b) (days)	18.7850(8)	18.7851915(4)	18.7851(1) [0.00003]‡
Eccentricity (e)	0.889(2)	0.8879773(3)	0.8879(2) [0.000005]‡
Longitude of periastron (ω) (deg)	82(1)	82.266550(18)	82.20(6) [0.002]‡
Semi major axis of the orbit projected along LOS ($a_1 sin(i)/c$) (light-seconds)	36.4(2)	36.2965(9)	36.28(1)
Pulsar period (P_o) (ms)	4.990576(5)	4.990575114114(3)	4.990575(4)
Epoch of periastron passage (T_o) (MJD)	52984.46(2)	-	52984.5(1) [0.02]‡

† : The uncertainty quoted in the bracket is on the last significant digit of the concerned parameter.
‡ : The step size used for comparing the simulation with the observation (Sect. 7.3).

Table 7.3: Orbital parameters of 47 Tuc T

Parameter	Freire, Kramer & Lyne (2001)	Camilo *et al.* (2000) (Coherent timing analysis)	This work
Orbital period (P_b) (days)	1.12(3)	1.126176785(5)	1.126175(2) [0.0000005]‡
Eccentricity (e)	-	0.00038(2)	0.0000(8) [0.0001]‡
Longitude of periastron (ω) (deg)	-	63(3)	63.0(1) [0.03]‡
Semi major axis of the orbit projected along LOS ($a_1 sin(i)/c$) (light-seconds)	1.33(4)	1.33850(1)	1.337(2)
Pulsar period (P_o) (ms)	7.588476(4)	7.588479792132(5)	7.58848(2)
Epoch of periastron passage (T_o) (MJD)	51000.3173(2)	51000.317049(2)	51000.317(2) [0.0001]‡

† : The uncertainty quoted in the bracket is on the last significant digit of the concerned parameter.
‡ : The step size used for comparing the simulation with the observation (Sect. 7.3).

CHAPTER 8

Conclutions and Future Prospects

"The most incomprehensible thing about the universe is that it is comprehensible."
– Albert Einstein

The main aim of this thesis was to investigate the dynamics of pulse emitting regions of radio pulsars, wide profile pulsars were used as a probe. During the thesis period, I have mainly concentrated on the study of single pulse properties of two wide profile drifting pulsars, PSR B0818−41 and PSR B0826−34. For both the pulsars, we observe simultaneous multiple drift regions and interpret the emission to be coming from two concentric conal rings. We report that, subpulse drifting for multiple rings of emission are always locked in phase, which naturally puts constraints on the theoretical models. Portion of the thesis is devoted to the development of a novel method for determining orbital parameters of binary pulsars. In this chapter we present the main conclusions from the individual projects and then discuss about some of the possible future prospects of the current work that will enrich the present understanding of the radio radiation mechanism of the pulsars.

8.1 Results from individual projects

In the following, the main projects that were undertaken for the thesis, and the important results form the individual works are described in some details,

(a) Exploration of the remarkable subpulse drift and polarization properties of PSR B0818−41

We report the discovery of a remarkable subpulse drift pattern for PSR B0818−41 at 325 MHz: simultaneous occurrence of three drift regions with two different drift rates, an inner region with steeper apparent drift rate flanked on each side by a region of slower apparent drift rate. The closely spaced drift bands always maintain a constant phase relationship. Changes of drift rates including curved and straight drift bands are commonly observed for this pulsar. Investigating 10,000 pulses from two different epochs of observations at 325 MHz, we observe frequent occurrences of small changes in drift rates, seven transitions from negative to stationary drift rates, five transitions from stationary to negative drift rates, and two possible signatures of curved drift bands. Changes in drift rates are always associated with nulling. In addition to 325 MHz, we also report subpulse drifting at 244 and 610 MHz: at 244 MHz we observe drifting in the outer regions but not in the inner region, whereas at 610 MHz subpulse drift is observed in both inner and outer regions. We determine P_2^m, P_3^m and $\Delta\Phi_s$, for the inner and outer drift regions at all the frequencies. Though P_3^m is the same ($\sim 18\ P_1$) for all the drift regions, P_2^m and $\Delta\Phi_s$ values are different. Significant linear polarization with depolarization at the edge of the profile is observed at 325, 610 and 1060 MHz. OPM jumps are observed at the two edges of the pulse profile at 325 MHz. Circular polarization changes sign near the middle of the pulse profile at 1060 MHz, which is not observed at 325 and 610 MHz. Remarkable evolution of polarization angle is observed between 325 and 610 MHz, which is not generally observed in other pulsars. We obtain best fit of the RVM model to the PA curve, at 325 MHz, with $\alpha \sim$175.4 deg and $\beta \sim -6.9$ deg.

- We interpret the unique drift pattern of this pulsar as being created by the intersection of our LOS with two conal rings on the polar cap of a fairly aligned rotator. We propose two possible viewing geometries, **G-1** ($\alpha \sim$11 deg, $\beta \sim -5.4$ deg, which incidentally reproduces the middle part of the PA sweep at 610 MHz) and **G-2** ($\alpha \sim$175.4 deg, $\beta \sim -6.9$ deg, geometry derived from RVM fit to 325 MHz PA sweep). We present results from simulations of the radiation pattern using the inferred parameters, that support our interpretations and reproduce

the average profile as well as the observed features in the drift pattern quite well for both **G-1** and **G-2**. However, **G-2** fits the PA sweep much better than **G-1**.

- The peak emission from the leading and the trailing outer regions are in phase at a pulse offset of $\sim 9\ P_1$. We utilise this information to resolve the aliasing problem and argue that drifting is first order aliased with corresponding carousel rotation period $P_4 \sim 10$ s. This makes it the fastest rotating carousel, proposed so far.

- Drifting from two different rings are phase locked for PSR B0818−41. This phase locked relation is maintained even during the sequences of irregular drifting or nulling. This indicates common electrodynamic control for both the rings.

(b) Investigation of the unique nulling properties of PSR B0818−41

The unique nulling properties of PSR B0818−41 were hitherto unexplored. Following are some of the important new results from our study,

- We identify a strong trend in the intensity fluctuations of the inner region of the individual pulses immediately before and after the nulls for PSR B0818−41. Our investigations bring out the fact that the nature of the transitions from bursts to nulls are different from the transitions from nulls to bursts. Switching off of pulsar radiation during nulling for PSR B0818−41 is not abrupt, but is gradual, whereas the transitions from null to burst are found to be rather abrupt for the inner drift region. This effect is not prominent in the outer drift regions. Although, the inner region of the last active pulses before nulls are dimmer, the first active pulses after the nulls outshines the normal ones.

- Intensity of the inner region is maximum for the average profile from the first active pulse immediately after the nulls, and then the intensity gradually goes down. This is consistent with the behavior of the individual nulls described above. But the leading peak attains its maximum intensity for the average profile from the second or third active

pulse immediately after the nulls, and the trailing peak attains its maximum for the average profile from the fourth active pulse immediately after the nulls.

- The average profile from the first active pulse immediately after the nulls follows similar shape as the normal profile but shows increased intensity (in the form of a bump) in the inner region which is not present in the normal average profile. In addition, the average profile from the first active pulse after the nulls has equally intense leading and trailing peaks, while for the normal profile, trailing peak is significantly more intense.

- Width of the average profile from the active pulses immediately after the nulls are more than the width of normal average profile of PSR B0818−41. Profile width increases more in the trailing side than in the leading side. The wider profiles immediately after the nulls can be explained by considering that the emission is coming from higher height in the magnetosphere or from the outer field lines.

- It is very striking that, all the above results are remarkably similar between the different epochs of observations. The fact that the average profiles of the first active pulses immediately after the nulls are very similar between two epochs of observations for PSR B0818−41, is very unique and has not been reported for any other pulsar. This demands similar conditions of magnetosphere immediately after individual nulls. Our investigation brings out that the phenomenon of nulling is not abrupt or random, but some systematic energy distribution is happening in the magnetosphere immediately after the nulls. This favors some mechanism enabling persistent memory of the condition of the magnetosphere after the nulls, as part of the pulsar radiation process. Such result have potential to probe the connection of nulling with the pulsar emission mechanism and is not investigated for any other pulsar so far.

(c) Results from multi-frequency study of PSR B0826−34

We studied PSR B0826−34 using the GMRT, simultaneously at 303 and 610 MHz, and individually at 157, 325, 610 and 1060 MHz. Some of the

important new results are highlighted in the following.

- Accurate estimate of dispersion measure (DM) was not hitherto available for PSR B0826−34. The DM determination of PSR B0826−34 becomes tricky because of the fact that, the pulse profile is quite complex, very wide and strongly evolving with frequency. In the literature we notice the use of different DM values, in the range of 47 to 65 pc/cm^3. In our scheme of DM determination, simultaneous dual frequency observations of B0826−34 with the GMRT at 303 and 610 MHz are used. The position difference of the fiducial point at different frequencies, reflects the dispersion delay of pulse arrival between those frequencies, and provides the basis of DM determination. We estimate the DM value of PSR B0826−34 to be 52.2±0.6 pc/cm^3.

- Contrary to the earlier study by Esamdin *et al.* (2005), we find no evidence of weak emission during the typical long null state of this pulsar, simultaneously at 303 and 610 MHz, as well as from non simultaneous observations at 157, 325, 610 and 1060 MHz at separate epochs. We have also obtained absolute flux limits for the non-detection at various frequencies, which should be a useful comparison standard for any more sensitive studies in the future.

- Significant correlation in the total intensity of the individual pulses between 303 and 610 MHz is reported from the simultaneous dual frequency observations, which is indicative of the broad-band nature of the emission.

- Though we find the drift pattern to be very similar in the simultaneous 303 and 610 MHz data, we observe that the drift band separation (P_2^m) evolves significantly between these two frequencies, and in a manner opposite to the average profile evolution. In addition, we confirm the dependence of P_2^m on pulse longitude at 303 MHz and find indications for the same at 610 MHz.

- Significant linear polarization is observed in the MP, which drops abruptly at the edges. Two OPM jumps are seen at the edges of the MP at 325 and 610 MHz. Significant circular polarization with a sense reversal near the central part of MP is observed. The sense reversal of circular

polarization are commonly associated with the core components, however our study stresses that this can also be observed in conal components. At 610 MHz, we observe somewhat non orthogonal mode jumps near the edges of the IP window. The PA curve shows typical "S" shaped swing (though there is some hint of a kink in the central part of the PA curve). RVM fit to the PA curve is obtained with $\alpha \sim 9.8$ deg, $\beta \sim 3.2$ deg, at both 325 and 610 MHz.

(d) Phase relation between simultaneous multiple drift regions

We investigated multiple drift regions with their drift phase related to each other, for PSR B0818−41 and PSR B0826−34. For PSR B0818−41, the emission from inner and outer drift regions are observed to be in fixed phase: inner drift bands start almost halfway between two drift bands in the leading outer region and always remain connected with the drift bands from trailing outer region. This PLR does not get perturbed by nulling or irregular drifting and is maintained even during sequences of irregular drifting as well as after nulling. Furthermore, nulling and changing drift rates are observed to be simultaneous in both the regions. For PSR B0826−34 we observe two separate drift regions corresponding to main pulse and inter pulse emissions. Subpulse drift from these two regions are observed to be locked in phase. Frequent nulling and changes of drift rates, observed for B0826−34, are simultaneous for both the rings. In addition, we observe significant correlation of total energy in the main pulse and inter pulse region. Simultaneous multiple drift regions, are known in only a few other pulsars, namely, B0815+09 by McLaughlin *et al.* (2000), and B1839−04 by Weltevrede *et al.* (2006) (also in Chapter 6 of this thesis). For both of these pulsars PLR between the drift regions are observed. Thus observed multiple drift regions are always locked in phase.

We interpret that the inner and outer drift regions are coming from two concentric rings of emission for PSR B0818−41. Similarly for PSR B0826−34 phased locked emission in the main pulse and the inter pulse region are considered to be coming from two concentric rings of emission. However, the mirrored drift bands for B0815+09 are explained in the sparking gap model as emission coming from an inner core gap (we refer as vacuum gap) and

inner annular gap (Qiao *et al.*, 2004). Our study imply that the emission from the inner and outer rings are always in phase. No counter examples are observed. The phase locked relation imply that, inner and outer rings drift with the same angular rate, emissions from the two rings are not independent and conditions responsible for drifting are similar in both rings. This puts constrains to the theoretical models and demands common electrodynamic control of the emission from the concentric rings.

(e) Preliminary study of single pulse properties of six other pulsars

In this thesis, we have presented interesting new results from the single pulse study of six other pulsars. Following are some of the important new results,

- We observed occasional nulling in between sporadic drifting corresponding to the core component for PSR B0540+23. This observation is important in the sense that nulls are not commonly seen in the core components for other pulsars. However, Nowakowski (1991) have reported that they have not seen any nulling for this pulsar during their observations. We determine P_3^m=9.8 P_1 for this pulsar at 325 and 610 MHz.

- We report the observations of irregular drifting with frequent changes of drift directions for PSR B1541+09. We determine P_3^m=20P_1, at 325 and 610 MHz.

- Drifting of the subpulses are quite evident for B1818−04, from our study. The pulse energy time series shows a 4 P_1 periodicity.

- We observe simultaneous two drift bands for B1819−22 at 325 and 610 MHz. We observe some kind of mode changing between stronger and weaker modes with changes of drift rates, which are probably associated with occasional nulling observed in this pulsar. We calculated P_2^m equal to 8.3 deg at 325 MHz and 7.8 deg at 610 MHz. $P_3^m \sim 16.6\ P_1$ is calculated for both the frequencies from fluctuation spectrum analysis.

- For PSR B1839−04 subpulse drifting is observed under the two peaks of the profile. The emission under the leading and trailing peaks appear to be in phase. We determined P_3^m=11.9 P_1.

(f) Determination of the orbital parameters of binary pulsars

Apart from the above work, we developed a new method for determination of the orbital parameters of the binary pulsars. This work was triggered by the discovery of a binary pulsar PSR J0514−4002 (the first known pulsar in the globular cluster NGC 1851) by the GMRT in 2004. We present a novel method for determination of the orbital parameters of binary pulsars, using data on the pulsar period at multiple observing epochs in contrast to the method described by Freire *et al.* (2001) which requires both pulsar period and period derivatives at particular observing epochs. This method uses the circular nature of the velocity space orbit of Keplerian motion and produces preliminary values based on two one dimensional searches. Preliminary orbital parameter values are then refined using a computationally efficient linear least square fit. This method works for random and sparse sampling of the binary orbit. Unlike the method used by Freire *et al.* (2001), which works for nearly circular binary orbits, this method works for binary orbit with any eccentricity. We demonstrate the technique on (a) the highly eccentric binary pulsar PSR J0514−4002 (the first known pulsar in the globular cluster NGC 1851) and (b) 47 Tuc T, a binary pulsar with a nearly circular orbit. Our result agrees with the earlier determination of the orbital parameters of the binary pulsars done with coherent multi-epoch timing (Freire *et al.* (2004) and Freire *et al.* (2007)). In our method the computation involves only one dimensional searches and linear least square fits.

8.2 Future Prospects

(a) Follow-ups from this thesis

In this thesis we have made detailed study of single pulse properties of two wide profile pulsars : PSR B0818−41 and B0826−34. In addition, we have also reported interesting new results from single pulse study of a selected sample of pulsars. However, some aspects of investigation of these pulsars presented in this thesis warrants further followup. Few of the suggested follow-ups will require more sensitive observations, which will be possible

with the existing and upcoming telescopes (e.g. the GMRT with its upgradation with the Software back-end and increased band width, GBT, LOFAR, Parkes).

PSR B0818−41 :

- This pulsar exhibits remarkable subpulse drift pattern, with simultaneous inner and outer drift regions, which we believe is originated from intersection of our LOS with two respective rings of emission (as described in Chapter 3). In addition to the remarkable subpulse drifting observed at 325 MHz, we report subpulse drifting at 244 and 610 MHz. At 244 MHz we observe drifting in the outer regions, but not in the inner region, whereas at 325 and 610 MHz subpulse drift is observed in both the inner and outer regions. As we have argued in Chapter 3, the absence of the inner drift region at 244 MHz can be interpreted as the LOS missing the emission from the inner ring. However, more sensitive single pulse observations of this pulsar is required to rule out the possibility of low level drifting in the inner region. Moreover, sensitive single pulse observations at both higher and lower frequencies (e.g. at 150 and 1420 MHz), will provide the information about how the LOS cut evolves with the frequency.

- We report significant evolution of PA sweep between 325, 610 and 1060 MHz for PSR B0818−41 (in Chapter 2), which is not generally observed for the other pulsars. Investigation of the possible cause for the observed remarkable evolution of PA with frequency may provide clue towards some frequency dependent nature of magnetic field structure in the polar cap.

- In Chapter 4, we investigated the unique null state properties of the pulsar at 325 and 610 MHz. Our investigation brings out remarkable similarity between the emission after the nulls for the observations at different epochs, which is a very unique property and is not reported for any other pulsar. This investigation is worth repeating for more epochs of observations, as well as at other frequencies. In addition, investigation of nulling, simultaneously at different frequencies will put more light to the scenario.

PSR B0826−34 :

- Our investigations of PSR B0826−34 (in Chapter 5) report that P_2^m evolves significantly with frequencies, and in a manner opposite to the average profile evolution. Existing models do not appear to explain this opposite sense of frequency evolution between the average profile and P_2^m. This aspect warrants further investigation.

- Esamdin *et al.* (2005) claim the presence of weak emission, at 1374 MHz, during the long duration nulls of this pulsar. However, we do not find any evidence of weak emission during nulling (Chapter 5). More sensitive single pulse study of this pulsar simultaneously at multiple frequencies will be insightful, in this regard.

- Our investigations of PSR B0826−34 in Chapter 5 brings out significant evolution of the average profile with frequency. It appears that the MP reduces in strength compared to the IP systematically, as one goes from lower to the higher frequencies. The IP dominates over the MP at frequencies above 1 GHz. It will be interesting to study average profile and the single pulse properties of this pulsar at even higher frequencies. This will help to probe the relation between the MP and the IP emission in more detail.

Follow-up investigations of the selected sample of pulsars:
In Chapter 6 we presented interesting new results from the single pulse study of few pulsars. Some (if not all), among those pulsars warrants follow-up study.

- PSR B0540+23 warrants further investigation of nulling in the core components, which is reported by us.

- More sensitive single pulse observations of PSR B1541+09 and B1831−04 may put some light on the relation of core and conal emission.

- Observed single pulse drifting seemed quite interesting for PSR B1818−04 and require follow-up investigations.

- Presence of different drift modes and their association with nulls need to be investigated in PSR B1819−22.

- More sensitive single pulse observations of PSR B1839−04 will enable to study the phase relation between the drift bands.

(b) Probing pulsar emission mechanism via an in-depth study of subpulse drifting and nulling:

Though it has been recently shown that subpulse drifting may be fairly common among the pulsars (Weltevrede *et al.* (2006) and (2007)), a thorough study has not been done for a majority of them. Discovery of remarkable drift patterns with phase relation between simultaneous multiple drift regions observed for PSR B0818−41 and B0826−34 (as discussed in Chapter 3 and 5), and the follow-up interpretations of polar cap configuration brings out the fact that the pulsar emission mechanism is a pan magnetospheric phenomena. This exemplify that constraints provided by the drifting pulsars can have far reaching implications on the theoretical models.

- Subpulse drifting : Determination of the drift parameters of more pulsars, simulation of their radiation patterns using the inferred parameters (as is done in Chapter 3) and reproduction of the observed drift patterns, will provide empirical knowledge about the polar cap configuration (e.g. dipolar versus non dipolar magnetic field structure, radius of emission ring, separation between sparks, aliased versus unaliased drifting, carousel rotation time etc). Subpulse drifting is an excellent example of under-sampling, and often we observe aliased drift rate rather than true drift rate. Phase relation between multiple drift regions can be used to resolve aliasing, similar to as is done in Chapter 3 of this thesis. Quantitative results from the observations, e.g. the carousel rotation period (P_4), compared against the predictions of theoretical models put constraints to the models. Our investigation brings out that for all the pulsars for which drifting is known from multiple rings (PSR B0818−41 and B0826−34), the subpulse drift is phase locked between the rings (as discussed in Chapter 3 and 5). This will favor a pan magnetospheric emission mechanism as discussed in this thesis. More sensitive single pulse observations may increase the number of pulsars for which drifting is seen for multiple rings of emission which will put more light to the scenario.

- Nulling : In Chapter 4 we report systematic intensity distribution around the nulls for PSR B0818−41. Intensity modulation around nulls are been investigated for five pulsars, namely PSR B0031−07, B0818−13, B0809+74, B1944+17 and B0818−41. Out of these for three pulsars (B0809+74, B1944+17, and B0818−41) relatively dim pulses just before nulls and outshining pulses just after the nulls are observed. In addition, for two of the pulsars (B0818−41 and B1944+17) the transitions from burst to null is gradual, where as the transitions from null to bursts are random. Follow-up studies of intensity modulation around the nulls will help to prove association of nullling with emission mechanism. Observed similarity of the average profile immediately after the nulls between different epochs, for PSR B0818−41 (as in Chapter 4), favors that emission mechanism should have persistent memory. Investigation of the same for other pulsars assumes importance. In addition, study of presence of possible weak emission during the nulls (Esamdin *et al.*, 2005) (also in Chapter 5), periodicity in the nulls (Rankin & Wright, 2008) and interactions between drifting and nulling will act as important probes to the possible relation between the pulsar emission mechanism and nulling.

(c) Exploring polarization properties of pulsars:

It is emphasized in this thesis that study the polarization properties of pulsars is required to get a complete idea about the emission. As discussed in Chapter 1, viewing geometry can be determined from RVM fit to PA curve. Though characteristic PA curve for many pulsars hints towards possible dipolar magnetic field, there are pulsars for which strong deviation from RVM is observed. The PA curve for B0818−41 at 610 MHz has different slopes in different parts of the profile and is an example of non RVM PA sweep (Chapter 2). A systematic investigation of the pulsars with non RVM PA curves, and the nature of deviation from the RVM is crucial for the knowledge of the magnetic field structure of the pulsars. Generally, the PA curve does not evolve much with frequency, but there are cases like PSR B0818−41, for which significant evolution of PA sweep is observed across the frequency band (Chapter 2). This warrants thorough investigation and may provide clues towards frequency dependent emission modes. Orthogonal polarization

modes (OPM) are quite common in pulsars. For example for PSR B0818−41 and B0826−34 we observe OPM at the edges of the pulse profile as reported in Chapter 2 and 5 of this thesis. We investigated published polarization profiles of pulsars and observed that, OPM jumps occur mainly at the middle and the edge of the profile. It will be interesting to investigate if there is any preferred pulse longitude for OPM jumps. Investigation of whether or not the OPMs depends on profile class of pulsars will also be interesting.

(d) Determination of binary orbital parameters:

In Chapter 7 we developed a unique method for determination of the orbital parameters of the binary pulsars. Following seems to be some of the logical follow-ups of this work:

• Development of a user friendly pipeline of the method

• Application of the method to determine the orbital parameters of a larger range of binaries

• Extension of this method for determining the orbital parameters of x-ray binaries

• Extension of this method to determine the non Keplerian orbital parameters

Bibliography

Ahuja, A. L., Gupta, Y., Mitra, D. & Kembhavi, A. K. 2005 . *MNRAS* **357**, 1013.

Asgekar, A. & Deshpande, A. A. 2001 . *MNRAS* **326**, 1249.

Asgekar, A. & Deshpande, A. A. 2005 . *MNRAS* **357**, 1105.

Baade, W. & Zwicky, F. 1934 . *PNAS* **20**, 254.

Backer, D. C. 1970*a* . *Nature* **228**, 1297.

Backer, D. C. 1970*b* . *Nature* **228**, 42.

Backer, D. C. 1973 . *ApJ* **182**, 245.

Backer, D. C. 1976 . *ApJ* **209**, 895.

Backer, D. C., Hama, S., Hook, S. V. & Foster, R. S. 1993 . *ApJ* **404**, 636.

Bartel, N. 1981 . *A&A* **97**, 384.

Bartel, N. & Sieber, W. 1978 . *A&A* **70**, 260.

Bartel, N., Sieber, W., Wielebinski, R., Kardashev, N. S., Ia., N. N., Popov, M. V., Soglasnov, V. A., Kuzmin, A. D., Smirnova & V., T. 1981 . *A&A* **93**, 85.

Bhat, N. D. R., Gupta, Y., Kramer, M., Karastergiou, A., Lyne, A. G. & Johnston, S. 2007 . *A&A* **462**, 257.

Bhattacharyya, B., Gupta, Y., Gil, J. & Sendyk, M. 2007 . *MNRAS* **377L**, 10B.

Biggs, J. D. 1992 . *ApJ* **394**, 574.

Biggs, J. D., McCulloch, P. M., Hamilton, P. A., Manchester, R. N. & Lyne, A. G. 1985 . *MNRAS* **215**, 281.

Camilo, F., Lorimer, D. R., Freire, P., Lyne, A. G. & Manchester, R. N. 2000 . *ApJ* **535**, 975.

Cheng, A. F. & Ruderman, M. 1979 . *ApJ* **229**, 348.

Cheng, A. F. & Ruderman, M. A. 1980 . *ApJ* **235**, 576.

D'Amico, N., Stappers, B. W., Bailes, M., Martin, C. E., Bell, J. F., Lyne, A. G. & Manchester, R. N. 1998 . *MNRAS* **297**, 28.

Davies, J. G., Lyne, A. G., Smith, F. G., Izvekova, V. A., Kuzmin, A. D. & Shitov, Y. P. 1984 . *MNRAS* **211**, 57.

Deich, W. T. S., Cordes, J. M., Hankins, T. H. & Rankin, J. M. 1986 . *ApJ* **300**, 540.

Deshpande, A. A. & Rankin, J. M. 1999 . *ApJ* **524**, 1008.

Deshpande, A. A. & Rankin, J. M. 2001 . *MNRAS* **322**, 438.

Drake, F. D. & Craft, H. D. 1968 . *Nature* **220**, 231.

Durdin, J. M., Large, M. I., Little, A. G., Manchester, R. N., Lyne, A. G. & Taylor, J. H. 1979 . *MNRAS* **186**, 39P.

Esamdin, A., Lyne, A. G., Graham-Smith, F., Kramer, M., Manchester, R. N. & Wu, X. 2005 . *MNRAS* **356**, 59.

Everett, J. E. & Weisberg, J. M. 2001 . *ApJ* **553**, 341.

Filippenko, A. V. & Radhakrishnan, V. 1982 . *ApJ* **263**, 828.

Freire, P. C. 2000 . PhD thesis, University of Manchester.

Freire, P. C., Gupta, Y., Ransom, S. M. & Ishwara-Chandra, C. H. 2004 . *ApJ L* **606**, L53.

Freire, P. C., Kramer, M. & Lyne, A. G. 2001 . *MNRAS* **322**, 885.

Freire, P. C., Kramer, M., Lyne, A. G., Camilo, F., Manchester, R. N. & D'Amico, N. 2001 . *ApJ L* **557**, L105.

Freire, P. C., Ransom, S. M. & Gupta, Y. 2007 . *ApJ* **662**, 1177.

Gangadhara, R. 1997 . *A&A* **327**, 155.

Gangadhara, R. T. & Gupta, Y. 2001 . *ApJ* **555**, 31.

Gil, J., Gupta, Y., Gothoskar, P. B. & Kijak, J. 2002 . *ApJ* **565**, 500.

Gil, J., Kijak, J., Maron, O. & Sendyk, M. 1995 . *A&A* **301**, 177.

Gil, J. & Krawczyk, A. 1996 . *MNRAS* **280**, 143.

Gil, J., Melikidze, G. & Zang, B. 2006 . *A&A* **457**, L5.

Gil, J., Melikidze, G. I. & Geppert, U. 2003 . *A&A* **407**, 315.

Gil, J. & Mitra, D. 2001 . *ApJ* **550**, 383.

Gil, J. A. & Sendyk, M. 2000 . *ApJ* **541**, 351.

Gould, D. M. & Lyne, A. G. 1998 . *MNRAS* **301**, 235.

Gupta, Y. & Gangadhara, R. T. 2003 . *ApJ* **584**, 418.

Gupta, Y., Gil, J., Kijak, J. & Sendyk, M. 2004 . *A&A* **426**, 229.

Gupta, Y., Gothoskar, P., Joshi, B. C., Vivekanand, M., Swain, R., Sirothia, S. & Bhat, N. D. R. 2000 . *ASP* **202**, 277.

Hamilton, W. R. 1987 . *Proceedings of the Royal Irish Academy* **3**, 344.

Han, J. L., Manchester, R. N., Xu, R. X. & Qiao, G. J. 1998 . *MNRAS* **300**, 373.

Herfindal, J. L. & Rankin, J. M. 2007 . *MNRAS* **380**, 430.

Hewish, A., Bell, S. J., Pilkington, J. D. H., Scott, P. F. & Collins, R. A. 1968 . *Nature* **217**, 709.

Hobbs, G., Faulkner, A., Stairs, I. H., Camilo, F., Manchester, R. N., Lyne, A. G., Kramer, M., D'Amico, N., Kaspi, V. M., Possenti, A., McLaughlin, M. A., Lorimer, D. R., Burgay, M., Joshi, B. C. & Crawford, F. 2004 . *MNRAS* **352**, 1439.

Hobbs, G., Lyne, A. G., Kramer, M., Martin, C. E. & Jordan, C. 2004 . *MNRAS* **353**, 1311.

Huguenin, G. R., Taylor, J. H. & Troland, T. H. 1970 . *ApJ* **162**, 727.

Izvekova, V. A., Kuz'min, A. D., Lyne, A. G., Shitov, Y. P. & Graham Smith, F. 1993 . *MNRAS* **261**, 865.

Janssen, G. H. & van Leeuwen, J. 2004 . *A&A* **425**, 255.

Johnston, S. & Weisberg, M., J. 2006 . *MNRAS* **368**, 1856.

Kaspi, V. M. & Stinebring, D. R. 1992 . *ApJ* **392**, 530.

Kijak, J. & Gil, J. 2003 . *ApJ* **397**, 969.

Kramer, M., Xilouris, K. M., Lorimer, D., Doroshenko, O., Jessner, A., Wielebinski, R., Wolszczan, A. & Camilo, F. 1998 . *ApJ* **501**, 270.

Lyne, A. G. & Ashworth, M. 1983 . *MNRAS* **204**, 519.

Lyne, A. G. & Manchester, R. N. 1988 . *MNRAS* **234**, 477.

Malofeev, V. M., Gil, J. A., Jessner, A., Malov, I. F., Seiradakis, J. H., Sieber, W. & Wielebinski, R. 1994 . *A&A* **285**, 201.

Manchester, R. N., Lyne, A. G., Taylor, J. H., Durdin, J. M., Large, M. I. & Little, A. G. 1978 . *MNRAS* **185**, 409.

Maron, O., Kijak, J., Kramer, M. & Wielebinski, R. 2000 . *A&AS* **147**, 195.

McLaughlin, M., Cordes, J. M. & Arzoumanian, Z. 2000 . *ASP Conf. Ser. 202: IAU Colloq. 177: Pulsar Astronomy - 2000 and Beyond* p. 41.

Michel, F. C. 1987 . *Nature* **329**, 310.

Mitra, D. & Deshpande, A. A. 1999 . *A&A* **346**, 906.

Mitra, D. & Rankin, J. M. 2008 . *MNRAS* **385**, 606.

Mitra, D., Rankin, J. M. & Gupta, Y. 2007 . *MNRAS* **379**, 932.

Narayan, R. & Vivekanand, M. 1982 . *A&A* **113**, L3.

Nowakowski, L. A. 1991 . *ApJ* **377**, 581.

Press, W. H., Teukolsky, S. A., Vetterling, W. T. & Flannery, B. P. 1992 . *2nd edn, Cambridge Univ. Press, Cambridge* .

Qiao, G. J., Lee, K. J., Zhang, B., Xu, R. X. & Wang, H. G. 2004 . *ApJ* **616**.

Qiao, G. J., Manchester, R. N., Lyne, A. G. & Gould, D. M. 1995 . *MNRAS* **274**, 572.

Radhakrishnan, V. & Cooke, D. J. 1969 . *APL* **3**, 225.

Radhakrishnan, V. & Rankin, J. M. 1990 . *ApJ* **352**, 258.

Rankin, J. M. 1983 . *ApJ* **274**, 333.

Rankin, J. M. 1986 . *ApJ* **301**, 901.

Rankin, J. M. 1990 . *ApJ* **352**, 247.

Rankin, J. M. 1993 . *ApJ* **405**, 285.

Rankin, J. M., Ramachandran, R. & Suleymanova, S. A. 2005 . *A&A* **447**, 235.

Rankin, J. M. & Suleymanova, S. A. 2006 . *A&A* **453**, 679.

Rankin, J. M., Suleymanova, S. A. & Deshpande, A. A. 2003 . *MNRAS* **340**, 1076.

Rankin, J. M. & Wright, G. A. E. 2007 . *MNRAS* **379**, 507.

Rankin, J. M. & Wright, G. A. E. 2008 . *MNRAS* **385**, 1923.

Rickett, B. J. 1990 . *ARA&A* **28**, 561.

Ritchings, R. T. 1976 . *MNRAS* **176**, 249.

Ruderman, M. 1976 . *ApJ* **203**, 206.

Ruderman, M. A. & Sutherland, P. G. 1975 . *ApJ* **196**, 51.

Smits, J. M., Mitra, D. & Kuijpers, J. 2005 . *A&A* **440**, 683.

Smits, J. M., Mitra, D., Stappers, B. W., Kuijpers, J., Weltevrede, P., Jessner, A. & Gupta, Y. 2007 . *A&A* **465**, 575.

Swarup, G., Ananthakrishnan, S., Subrahmanya, C. R., Rao, A. P., Kulkarni, V. K. & Kapahi, V. K. 1997 . *High Sensitivity Radio Astronomy, ed. N.Jackson and R.J. Davis (Cambridge: Cambridge University Press)* .

Taylor, J. H. & Huguenin, G. R. 1971 . *ApJ* **167**, 273.

Taylor, J. H., Manchester, R. N. & Huguenin, G. R. 1975 . *ApJ* **195**, 513.

Taylor, J. H., Manchester, R. N. & Lyne, A. G. 1993 . *ApJS* **88**, 529.

Usov, V. V. & Melrose, D. B. 1996 . *ApJ* **464**, 306.

van Leeuwen, A. G. J., Stappers, B. W., Ramachandran, R. & Rankin, J. M. 2003 . *A&A* **399**, 223.

Vivekanand, M. 1995 . *MNRAS* **274**, 785.

Vivekanand, M. & Joshi, B. C. 1999 . *ApJ* **515**, 398.

Vivekanand, M. & Joshi, V. 1997 . *ApJ* **477**, 431.

Weltevrede, P., Edwards, R. T. & Stappers, B. W. 2006 . *A&A* **445**, 243.

Wolszczan, A., Bartel, N. & Sieber, W. 1981 . *A&A* **100**, 91.

Wright, G. A. E. 2003 . *MNRAS* **344**, 1041.